Heavy quark physics on the lattice with improved nonrelativistic actions

Stefan Meinel

Dissertation submitted for the degree of
Doctor of Philosophy
at the University of Cambridge

Department of Applied Mathematics and Theoretical Physics
and
St John's College

21 December 2009

UNIVERSITY OF
CAMBRIDGE

Declaration

This dissertation is the result of my own work and includes nothing which is the outcome of work done in collaboration, except where specifically indicated in the text. No part of this dissertation has been previously submitted for a degree or any other qualification.

Stefan Meinel
21 December 2009

Abstract

Hadrons containing heavy quarks, in particular b quarks, play an important role in high energy physics. Measurements of their electroweak interactions are used to test the Standard Model and search for new physics. For the comparison of experimental results with theoretical predictions, nonperturbative calculations of hadronic matrix elements within the theory of quantum chromodymanics are required.

Such calculations can be performed from first principles by formulating QCD on a Euclidean spacetime grid and computing the path integral numerically. Including b quarks in lattice QCD calculations requires special techniques as the lattice spacing in present computations usually can not be chosen fine enough to resolve their Compton wavelength.

In this work, improved nonrelativistic lattice actions for heavy quarks are used to perform calculations of the bottom hadron mass spectrum and of form factors for heavy-to-light decays. In heavy-to-light decays, additional complications arise at high recoil, when the momentum of the light meson reaches a magnitude comparable to the cutoff imposed by the lattice. Discretisation errors at high recoil can be reduced by working in a frame of reference where the heavy and light mesons move in opposite directions. Using a formalism referred to as moving nonrelativistic QCD (mNRQCD), the nonrelativistic expansion for the heavy quark can be performed around a state with an arbitrary velocity.

This dissertation begins with a review of the fundamentals of lattice QCD. Then, the construction of effective Lagrangians for heavy quarks in the continuum and on the lattice is discussed in detail. A highly improved lattice mNRQCD action is derived and its effectiveness is demonstrated by nonperturbative tests involving both heavy-heavy and heavy-light mesons at several frame velocities.

This mNRQCD action is then used in combination with a staggered action for the light quarks to calculate hadronic matrix elements relevant for rare B decays, including $B \to K^*\gamma$ and $B \to K\ell\ell$. A major contribution to the uncertainty of the results also comes from statistical errors. The effectiveness of random-wall sources to reduce these errors is studied.

As another application of a nonrelativistic heavy quark action, the spectrum of bottomonium is calculated and masses of several bottom baryons are predicted. In these computations, the light quarks are implemented with a domain wall action.

Contents

Chapter 1

Introduction

The existence of a third generation of quarks was predicted by Kobayashi and Maskawa in 1973 to explain the phenomenon of CP violation [1]. Their prediction was confirmed by the discovery of the Υ meson [2], a bound state of a bottom quark and its antiquark, in 1977 at Fermilab.

The $\Upsilon(4S)$ resonance can decay through the strong interaction into pairs of B mesons, which were first observed at the electron-positron storage ring CESR in 1983 [3]. B mesons allow the study of weak interactions of the b quark, and thereby provide some of the most stringent tests of the Standard Model of elementary particle physics.

A wealth of experimental results for decays and mixing processes of B mesons has been obtained, most recently by the experiments BaBar at SLAC and Belle at KEK. World-averages of heavy-hadron properties can be found in [4].

In many cases, the experimental results for exclusive decays, where a definite final state is considered, are more precise than those for inclusive decays. The comparison of theory and experiment for exclusive processes requires knowledge of the structure of the hadrons, described by decay constants and form factors. These quantities are governed by the non-perturbative dynamics of the strong interaction at low energies.

The theory of the strong interactions is quantum chromodynamics (QCD). Nonperturbative calculations in QCD can be performed from first principles by formulating the theory on a Euclidean spacetime grid [5] and computing the path integral numerically. With several improvements in the lattice actions and numerical algorithms, and with the enormous growth in available computer power, lattice QCD now allows accurate predictions of many hadronic properties. One major step towards this success was the inclusion of vacuum polarisation effects from the light quarks [6]. Reviews of recent progress in lattice QCD with dynamical quarks can be found in [7, 8].

A lattice with side length L and lattice spacing a can accommodate physics at energy scales between approximately $1/L$ and $1/a$. To minimise finite-volume effects, it is required that $m_\pi L \gg 1$, where m_π is the mass of the lightest propagating particle in the theory, the pion. With the limited resources available, it is usually not possible to achieve $m_b\, a \ll 1$ at the same time. In other words, the lattices are not fine enough to accurately resolve the Compton wavelength of the b quark.

For this reason, special techniques are required when the b quark is to be included in lattice QCD calculations. One possibility is the non-relativistic treatment of the b quark, which is based on the observation that fluctuations in the b-quark's momentum are of order $\Lambda_{QCD} \ll m_b$ in heavy-light hadrons and $m_b v_{\text{orb.}} \ll m_b$ in bottomonium. Here, Λ_{QCD} is the intrinsic scale of QCD, which governs the dynamics of the light degrees of freedom (light quarks and gluons) in a heavy-light hadron, and $v_{\text{orb.}}$ is the internal speed of the b quarks inside bottomonium ($v_{\text{orb.}}^2 \approx 0.1$).

One particular nonrelativistic technique for b quarks is lattice NRQCD [9, 10], which can be applied to both heavy-heavy and heavy-light systems. Lattice NRQCD has been used in [11] to calculate form factors for the decay $B \to \pi\ell\nu$. The form factors are functions of $q^2 = (p - p')^2$, where p and p' are the four-momenta of the B meson and pion, respectively. In [11], the B meson was taken to be at rest in the lattice frame. The momentum $\mathbf{p}'$ of the pion in the lattice calculation is limited by the requirement that $|\mathbf{p}'|a \ll 1$, which means that only the low-recoil region (large q^2) is accessible. However, experimental data cover the entire range of recoil momenta [12, 13, 14]. The problem is more severe for the radiative decay $B \to K^*\gamma$ [15, 16, 17, 18], which has $q^2 = 0$, corresponding to $|\mathbf{p}'|$ close to $M_B/2$ in the B rest frame. This decay is rare because it proceeds through a loop-suppressed flavour-changing neutral-current $b \to s$ transition, which also makes it very sensitive to possible contributions from physics beyond the Standard Model. In contrast to $B \to \pi\ell\nu$, for rare three-body decays like $B \to K\ell^+\ell^-$ and $B \to K^*\ell^+\ell^-$ the shape of the form factors is not known well from experiment, and lattice QCD calculations for a wide range of q^2 are desirable.

For a given q^2, the momentum $\mathbf{p}'$ of the final meson and hence discretisation errors can be reduced by giving the B meson a non-zero momentum in the direction opposite to $\mathbf{p}'$. To substantially reduce $|\mathbf{p}'|$, the momentum of the B meson has to be very large, so that NRQCD would no longer be able to describe the b quark inside it due to relativistic and lattice spacing errors. However, fluctuations of the momentum of the heavy quark inside the B meson are much smaller than the momentum of the meson itself. Therefore, to reduce errors, instead of discretising the momentum of the b quark itself, one can discretise

its fluctuations inside the moving B meson. The formalism which achieves this is known as lattice moving NRQCD (mNRQCD). In mNRQCD, the nonrelativistic expansion is performed around a state where the heavy quark is moving with a velocity $\mathbf{v}$, the frame velocity.

The idea of mNRQCD goes back to [19] and was developed further in [20, 21, 22]. Numerical tests of mNRQCD with a simple $\mathcal{O}(1/m_b)$ action and with quenched gauge field configurations (i.e. without dynamical quarks) were reported in [22, 23, 24, 25]. In this dissertation I extend this work as follows:

- I independently derive a moving NRQCD action of order $\mathcal{O}(1/m_b^2, v_{\mathrm{orb.}}^4)$. My derivation gives a result that differs slightly from the one reported in [21, 22, 23].
- I perform a wide range of numerical tests of the full $\mathcal{O}(1/m_b^2, v_{\mathrm{orb.}}^4)$ lattice mNRQCD action in realistic lattice QCD with 2+1 flavours of light dynamical quarks. The accuracy through order $v_{\mathrm{orb.}}^4$ is crucial as I use calculations with bottomonium mesons to determine renormalisation parameters nonperturbatively.

I then apply moving NRQCD to the calculation of form factors for semileptonic and radiative B decays:

- I compute the heavy-light three-point and two-point correlation functions necessary to extract all semileptonic and radiative B/B_s decay form factors, using the full $\mathcal{O}(1/m_b^2, v_{\mathrm{orb.}}^4)$ lattice mNRQCD action for the b quark and an improved staggered action for the light quarks.
- I test a "random-wall source" method for the reduction of statistical errors.
- I analyse the data and obtain preliminary results for form factors describing $B \to K$ and $B \to K^*$ decays.

In this dissertation I also present my work on a second project, the calculation of the heavy-hadron spectrum in lattice QCD with dynamical domain wall fermions. Here I implement the b quark with standard lattice NRQCD. The domain wall fermion action [26, 27, 28] used here for the light quarks has an approximate chiral symmetry that becomes exact, even at finite lattice spacing, when the extent of an auxiliary fifth dimension is taken to infinity. My work on the heavy-hadron spectrum includes the following:

- I first calculate the spectrum of the bottomonium system, including radial/orbital excitations and spin-dependent energy splittings. These calculations serve as tests of the lattice methods and also allow precise determinations of the lattice scale.

- I then calculate the masses of B/B_s mesons, singly-bottom baryons and doubly-bottom baryons, using a domain-wall action for the light valence quarks. I also perform the first lattice QCD calculation of the mass of the Ω_{bbb} baryon. Currently, bottom baryons are the focus of intense experimental studies at the Tevatron, and further discoveries are possible with the Large Hadron Collider. Therefore, lattice QCD predictions of their masses are highly desirable.

This dissertation is organised as follows. In Chapter 2, I give an introduction to the theoretical foundations of lattice QCD, including the fascinating topic of chiral symmetry on the lattice. At the end of this chapter, I briefly review relativistic lattice methods for heavy quarks. Chapter 3 contains derivations of effective Lagrangians for heavy quarks in the continuum and a discussion of the power-counting. In particular, I derive the $\mathcal{O}(1/m_b^2, v_{\text{orb.}}^4)$ mNRQCD Lagrangian and show how the Euclidean actions for quarks and antiquarks are related to each other. Two different approaches exist for the lattice discretisation of nonrelativistic heavy-quark Lagrangians. The first, known as lattice HQET, is only applicable to hadrons containing a single heavy quark, but has the advantage that the continuum limit can be taken. It is discussed briefly in Chapter 4. The second approach, lattice (moving) NRQCD, is applicable to systems containing any number of heavy quarks. In Chapter 5, I construct a highly improved lattice discretisation of the full $\mathcal{O}(1/m_b^2, v_{\text{orb.}}^4)$ moving NRQCD action. I also discuss the mNRQCD energy shift and the renormalisation of the external momentum. I then report on my nonperturbative tests of lattice moving NRQCD in Chapter 6. These tests include the calculation of renormalisation parameters, meson energy splittings and decay constants at several frame velocities. Chapter 7 is an interlude; it contains my work on the calculation of the heavy-hadron spectrum. I return to the subject of moving NRQCD in Chapter 8, which deals with the calculation of form factors for rare B decays. There, I briefly review the physics of electroweak decays of B mesons, define the form factors and show how they can be extracted from Euclidean correlation functions. I discuss the necessary operator matching of the heavy-light currents and estimate the optimal choice for the frame velocity as a function of q^2. I then give the details of the calculation of the two-point and three-point functions and compare numerical results obtained with random-wall sources and point sources. I examine different fitting strategies and present preliminary results for the form factors. Chapter 9 contains the conclusions and an outlook to future work.

Chapter 2

Lattice QCD

In this chapter, the fundamentals of lattice QCD will be reviewed. I used the textbooks [29, 30, 31, 32, 33, 34] in preparing this chapter; additional references will be given where appropriate.

Lattice QCD is based on the nonperturbative regularisation of the Euclidean path integral obtained by defining the fields only on the points or links of a spacetime grid. This corresponds to a momentum cutoff of the order of the inverse lattice spacing, without any reference to perturbation theory. Furthermore, as we will see in Sec. 2.3, exact gauge invariance can be implemented in a beautiful way on the lattice [5].

It turns out that the lattice discretisation of fermions is more involved than for gauge fields, due to the so-called doubling problem. This is related to chiral symmetry and the axial anomaly. Section 2.4 is devoted to this rich topic.

When considering a lattice of finite volume, the path integral turns into an ordinary multidimensional integral, which, thanks to the Euclidean weighting factor e^{-S_E} and the positivity of S_E, becomes calculable numerically by Monte-Carlo methods.

As usual for interacting quantum field theories, to obtain physical results, renormalisation is required. This will be discussed briefly in Sec. 2.6. In practice, the number of lattice points is limited by the available computing resources, and one has to make careful choices for the lattice spacings, volumes, and quark masses. Usually, extrapolations in all these parameters are required to extract physical results, and these extrapolations can be guided by predictions from effective field theories, as reviewed in Sec. 2.7.

Finally, in Sec. 2.8 I briefly discuss relativistic lattice methods for heavy quarks.

2.1 Euclidean path integral

As the Euclidean path integral is the starting point for lattice QCD, we will discuss it in some detail in the following sections. We begin with a derivation of the Euclidean path integral for a scalar field in Sec. 2.1.1, starting from the canonical formalism. This clearly exposes the relation to the operators on the Hilbert space, gives us a prescription for obtaining the Euclidean action, and shows how a non-zero temperature is introduced. Remarks on fermions and gauge fields will be made in Secs. 2.1.2 and 2.1.3.

2.1.1 Real scalar field

We consider a real scalar field $\phi(t, \mathbf{x})$ with Minkowski space action

$$S = \int \mathrm{d}t\, \mathrm{d}^3x\, \mathcal{L} \qquad \text{with} \qquad \mathcal{L} = \frac{1}{2}(\partial_t\phi)^2 - \frac{1}{2}(\boldsymbol{\nabla}\phi)^2 - \frac{1}{2}m^2\phi^2 - V(\phi), \tag{2.1}$$

where $V(\phi)$ is a polynomial. The conjugate momentum field is then $\Pi = \partial\mathcal{L}/\partial(\partial_t\phi) = \partial_t\phi$, and the Hamilton functional becomes

$$H = \int \mathrm{d}^3x\, \mathcal{H} \qquad \text{with} \qquad \mathcal{H} = \frac{1}{2}\Pi^2 + \frac{1}{2}\left(\boldsymbol{\nabla}\phi\right)^2 + \frac{1}{2}M^2\phi^2 + V\left(\phi\right). \tag{2.2}$$

We denote the Heisenberg field operators associated with ϕ, Π by $\mathsf{\Phi}$ and $\mathsf{\Pi}$, respectively. These satisfy the canonical commutation relations $[\mathsf{\Phi}(0,\mathbf{x}), \mathsf{\Pi}(0,\mathbf{y})] = i\,\delta^3(\mathbf{x}-\mathbf{y})$. We also introduce zero-time "position space" and "momentum space" eigenstates $|\varphi\rangle$, $|\pi\rangle$, satisfying

$$\mathsf{\Phi}(0,\mathbf{x})|\varphi\rangle = \varphi(\mathbf{x})|\varphi\rangle, \qquad \mathsf{\Pi}(0,\mathbf{x})|\pi\rangle = \pi(\mathbf{x})|\pi\rangle. \tag{2.3}$$

Note that their scalar product is $\langle\varphi|\pi\rangle = \exp\left\{i\int \mathrm{d}^3x\, \varphi(\mathbf{x})\pi(\mathbf{x})\right\}$.

The Hamilton operator H is obtained by replacing the classical fields ϕ, Π in (2.2) by the corresponding field operators. We are interested in the quantum-mechanical transition amplitude between two field eigenstates, $\langle\varphi'|e^{-i\,t\,\mathsf{H}}|\varphi\rangle$. The transition to Euclidean space is obtained by inserting $t = -i\tau$ with $\tau > 0$. To derive the path integral representation for the Euclidean matrix element $\langle\varphi'|e^{-\tau\,\mathsf{H}}|\varphi\rangle$, we split the Euclidean time interval τ into N pieces of length $a = \tau/N$, and insert complete sets of position space and momentum space eigenstates after each step:

$$\begin{aligned}\langle\varphi'|e^{-\tau\mathsf{H}}|\varphi\rangle \;\; = \;\; & \int \prod_{k=1}^{N-1} \mathrm{d}[\varphi_k] \int \prod_{l=1}^{N} \frac{\mathrm{d}[\pi_l]}{2\pi} \\ & \times\; \langle\varphi'|e^{-a\mathsf{H}}|\pi_N\rangle\langle\pi_N|\varphi_{N-1}\rangle\langle\varphi_{N-1}|e^{-a\mathsf{H}}|\pi_{N-1}\rangle\cdots\langle\pi_1|\varphi\rangle. \end{aligned} \tag{2.4}$$

Next, note that for $a \to 0$, we have

$$\begin{aligned}\langle\varphi_k|e^{-a\mathsf{H}}|\pi_k\rangle &\underset{a\to 0}{=} (1 - aH[\varphi_k,\pi_k])\,\langle\varphi_k|\pi_k\rangle \\ &\underset{a\to 0}{=} \exp\left\{-a\int \mathrm{d}^3x\left[\mathcal{H}(\varphi_k,\pi_k) - i\frac{\varphi_k\,\pi_k}{a}\right]\right\}. \end{aligned} \tag{2.5}$$

Thus, for $N \to \infty$, Eq. (2.4) becomes

$$\begin{aligned}\langle\varphi'|e^{-\tau\mathsf{H}}|\varphi\rangle &= \lim_{N\to\infty}\int\prod_{k=1}^{N-1}\mathrm{d}[\varphi_k]\int\prod_{l=1}^{N}\frac{\mathrm{d}[\pi_l]}{2\pi} \\ &\quad\times\ \exp\left\{-a\sum_{j=1}^{N}\int\mathrm{d}^3x\left[\mathcal{H}(\varphi_j,\pi_j) - i\frac{\pi_j(\varphi_j-\varphi_{j-1})}{a}\right]\right\} \end{aligned} \tag{2.6}$$

with $\varphi_0 = \varphi$ and $\varphi_N = \varphi'$. The limit $N \to \infty$ replaces the sum in (2.6) by an integral over $[0,\tau]$ and we can write

$$\langle\varphi'|e^{-\tau\mathsf{H}}|\varphi\rangle = \int\mathcal{D}[\Pi_E]\int_{\varphi}^{\varphi'}\mathcal{D}[\phi_E]\,\exp\left\{-\int_0^\tau\mathrm{d}\tau'\int\mathrm{d}^3x\big[\mathcal{H}(\phi_E,\Pi_E) - i\Pi_E\,\partial_{\tau'}\phi_E\big]\right\}. \tag{2.7}$$

The functional integrals $\int\mathcal{D}[\Pi_E]\int\mathcal{D}[\phi_E]$ in (2.7) are over Euclidean fields $\Pi_E(\tau',\mathbf{x})$ and $\phi_E(\tau',\mathbf{x})$, subject to the boundary conditions $\phi_E(0,\mathbf{x}) = \varphi(\mathbf{x})$ and $\phi_E(\tau,\mathbf{x}) = \varphi'(\mathbf{x})$. The integral over Π_E is Gaussian and can be performed explicitly by completing the square. This gives[1]

$$\langle\varphi'|e^{-\tau\,\mathsf{H}}|\varphi\rangle = \int_{\varphi}^{\varphi'}\mathcal{D}[\phi_E]\ e^{-S_E[\phi_E]} \tag{2.8}$$

with the Euclidean action

$$S_E[\phi_E] = \int\mathrm{d}\tau\int\mathrm{d}^3x\ \left[\frac{1}{2}(\partial_\tau\phi_E)^2 + \frac{1}{2}(\boldsymbol{\nabla}\phi_E)^2 + \frac{1}{2}m^2\phi_E^2 + V(\phi_E)\right]. \tag{2.9}$$

By comparing (2.1) and (2.9), we find that the Euclidean action $S_E[\phi_E]$ can be obtained from the Minkowski space action $S[\phi]$ in the following formal way: first, replace $\phi(t,\mathbf{x})$ by $\phi_E(\tau,\mathbf{x})$. Subsequently, replace every remaining t by $-i\tau$, so that the integration measure and derivatives become $\mathrm{d}t \to (-i)\mathrm{d}\tau$, $\partial_t \to i\partial_\tau$. Finally, multiply the action by $(-i)$.

Having derived Eq. (2.8), the next step is to obtain a path integral representation for correlation functions. For simplicity we only consider the two-point function; the generalisation to higher correlation functions is straightforward.

[1] In (2.8) we have absorbed the constant factor from the Π-integration by redefining the integration measure $\mathcal{D}[\phi_E]$.

Let $|0\rangle$ be the vacuum state. For $\tau > 0$, the Euclidean two-point function (Schwinger function) is

$$C(\tau, \mathbf{x}) = \langle 0|\, e^{\tau \mathsf{H}}\, \Phi(0,\mathbf{x})\, e^{-\tau \mathsf{H}}\, \Phi(0,\mathbf{0})\, |0\rangle. \tag{2.10}$$

First, note that $C(\tau, \mathbf{x})$ may be written as

$$C(\tau, \mathbf{x}) = \lim_{L_\tau \to \infty} \frac{\mathrm{Tr}\left[e^{-L_\tau \mathsf{H}}\, e^{\tau \mathsf{H}}\, \Phi(0,\mathbf{x})\, e^{-\tau \mathsf{H}}\, \Phi(0,\mathbf{0})\right]}{\mathrm{Tr}\left[e^{-L_\tau \mathsf{H}}\right]}. \tag{2.11}$$

To show (2.11), we use an orthonormal basis of energy eigenstates $|n\rangle$:

$$C(\tau, \mathbf{x}) = \lim_{L_\tau \to \infty} \frac{\sum_{n,m} \langle n|e^{-L_\tau \mathsf{H}}|m\rangle \langle m|\, e^{\tau \mathsf{H}}\, \Phi(0,\mathbf{x})\, e^{-\tau \mathsf{H}}\, \Phi(0,\mathbf{0})|n\rangle}{\sum_n \langle n|e^{-L_\tau \mathsf{H}}|n\rangle}. \tag{2.12}$$

Provided that the theory has a mass gap, in the limit $L_\tau \to \infty$ only the lowest-energy state $|0\rangle$ remains, and the factor of $\langle 0|e^{-L_\tau \mathsf{H}}|0\rangle$ cancels.

We may also evaluate the traces in (2.11) using field eigenstates:

$$\begin{aligned} C(\tau, \mathbf{x}) &= \lim_{L_\tau \to \infty} \frac{\int \mathrm{d}[\varphi]\, \langle \varphi|\, e^{-(L_\tau - \tau)\mathsf{H}}\, \Phi(0,\mathbf{x})\, e^{-\tau \mathsf{H}}\, \Phi(0,\mathbf{0})\, |\varphi\rangle}{\int \mathrm{d}[\varphi]\, \langle \varphi|\, e^{-L_\tau \mathsf{H}}\, |\varphi\rangle} \\ &= \lim_{L_\tau \to \infty} \frac{\int \mathrm{d}[\varphi] \int \mathrm{d}[\varphi']\, \langle \varphi|\, e^{-(L_\tau - \tau)\mathsf{H}}\, |\varphi'\rangle \varphi'(\mathbf{x}) \langle \varphi'|\, e^{-\tau \mathsf{H}}\, |\varphi\rangle \varphi(\mathbf{0})}{\int \mathrm{d}[\varphi]\, \langle \varphi|\, e^{-L_\tau \mathsf{H}}\, |\varphi\rangle}. \end{aligned} \tag{2.13}$$

Finally, using Eq. (2.8) to express the matrix elements in (2.13) as path integrals, we obtain

$$C(\tau, \mathbf{x}) = \left\langle \phi_E(\tau,\mathbf{x})\, \phi_E(0,\mathbf{0}) \right\rangle \equiv \lim_{L_\tau \to \infty} \frac{\int \mathcal{D}[\phi_E]\;\; \phi_E(\tau,\mathbf{x})\, \phi_E(0,\mathbf{0})\;\; e^{-S_E[\phi_E]}}{\int \mathcal{D}[\phi_E]\;\; e^{-S_E[\phi_E]}} \tag{2.14}$$

where the functional integral is over the Euclidean field ϕ_E with the periodic boundary conditions $\phi_E(L_\tau, \mathbf{x}) = \phi_E(0, \mathbf{x})$. The generalisation of the above derivation to n-point correlation functions is straightforward.

Note that for finite L_τ, Eq. (2.11) is a thermal expectation value of the operator $e^{\tau \mathsf{H}}\, \Phi(0,\mathbf{x})\, e^{-\tau \mathsf{H}}\, \Phi(0,\mathbf{0})$ at the temperature $1/L_\tau$. Thus, for the Euclidean path integral with periodic boundary conditions in the time direction a finite temporal extent corresponds to a non-zero temperature $1/L_\tau$. The limit $L_\tau \to \infty$ is a zero-temperature limit.

2.1.2 Dirac field

The Minkowski space action for a Dirac field with mass m is

$$S = \int \mathrm{d}t\, \mathrm{d}^3x\;\; \overline{\Psi}\, (i\hat{\gamma}^\mu \partial_\mu - m)\, \Psi \tag{2.15}$$

with $\{\hat{\gamma}^\mu, \hat{\gamma}^\nu\} = 2\, g^{\mu\nu}$. Note that $i\overline{\Psi}\hat{\gamma}^0$ is the conjugate momentum field for Ψ, and the Hamilton functional reads

$$H = \int \mathrm{d}^3x \;\overline{\Psi}\left(-i\hat{\gamma}^j\partial_j + m\right)\Psi. \tag{2.16}$$

Because the field operators $\overline{\Psi}$, Ψ obey the canonical anticommutation relations

$$\left\{\overline{\Psi}_\alpha(0,\mathbf{x}),\; \Psi_\beta(0,\mathbf{y})\right\} = \hat{\gamma}^0_{\alpha\beta}\,\delta^3(\mathbf{x}-\mathbf{y}), \tag{2.17}$$

the fields in the fermionic path integral have to be Grassmann-algebra-valued. The partition function can be written as a Berezin integral

$$\mathrm{Tr}\left[e^{-L_\tau \mathsf{H}}\right] = \int \mathcal{D}[\overline{\Psi}_E, \Psi_E]\; e^{-S_E[\Psi_E,\overline{\Psi}_E]} \tag{2.18}$$

over Euclidean Grassmann-valued fields with the antiperiodic boundary conditions

$$\begin{aligned} \Psi_E(0,\mathbf{x}) &= -\Psi_E(L_\tau,\mathbf{x}), \\ \overline{\Psi}_E(0,\mathbf{x}) &= -\overline{\Psi}_E(L_\tau,\mathbf{x}). \end{aligned} \tag{2.19}$$

The Euclidean action in (2.18) is

$$S_E[\Psi_E,\overline{\Psi}_E] = \int \mathrm{d}\tau \int \mathrm{d}^3x \;\overline{\Psi}_E\left[\hat{\gamma}^0\partial_\tau - i\hat{\gamma}^j\partial_j + m\right]\Psi_E. \tag{2.20}$$

Eq. (2.20) suggests the definition of Euclidean gamma matrices $\gamma^0 \equiv \hat{\gamma}^0$, $\gamma^j \equiv -i\hat{\gamma}^j$ which satisfy $\{\gamma^\mu, \gamma^\nu\} = 2\,\delta^{\mu\nu}$. Euclidean correlation functions can be computed from[2]

$$\begin{aligned} &\left\langle \Psi(x_1)...\Psi(x_n)\;\overline{\Psi}(y_1)...\overline{\Psi}(y_n)\right\rangle \\ &= \lim_{L_\tau\to\infty} \frac{\int \mathcal{D}[\overline{\Psi},\Psi]\;\Psi(x_1)...\Psi(x_n)\;\overline{\Psi}(y_1)...\overline{\Psi}(y_n)\; e^{-S[\Psi,\overline{\Psi}]}}{\int \mathcal{D}[\overline{\Psi},\Psi]\; e^{-S[\Psi,\overline{\Psi}]}}. \end{aligned} \tag{2.21}$$

Writing the Euclidean action as

$$S[\Psi,\overline{\Psi}] = \int \mathrm{d}^4x \int \mathrm{d}^4y \sum_{\alpha,\beta} \overline{\Psi}_\alpha(x)\, K_{\alpha\,\beta}(x,y)\,\Psi_\beta(y), \tag{2.22}$$

where the kernel K satisfies the correct boundary conditions, one obtains the following results from the rules of Grassmann integration:

$$\int \mathcal{D}[\overline{\Psi},\Psi]\; e^{-S[\Psi,\overline{\Psi}]} = \det K \tag{2.23}$$

[2] In the following, we drop the subscript E

and

$$\begin{aligned}&\left\langle \Psi_{\alpha_1}(x_1)...\Psi_{\alpha_n}(x_n)\,\overline{\Psi}_{\beta_1}(y_1)...\overline{\Psi}_{\beta_n}(y_n)\right\rangle \\ &= (-1)^{n(n-1)/2}\sum_{P\in S_n}(-1)^{\sigma(P)}K^{-1}_{\alpha_1\,\beta_{P(1)}}\big(x_1,y_{P(1)}\big)\;...\;K^{-1}_{\alpha_n\,\beta_{P(n)}}\big(x_n,y_{P(n)}\big)\end{aligned} \tag{2.24}$$

where K^{-1} denotes the inverse matrix of K with respect to both position and Dirac indices.

2.1.3 Gauge fields

Consider N_c copies of the Dirac field with Lagrangian (2.15). The resulting theory has a global symmetry

$$\Psi_a(x) \;\mapsto\; G_{ab}\,\Psi_b(x), \qquad \overline{\Psi}_a(x) \;\mapsto\; \overline{\Psi}_b(x)\,G^\dagger_{ba}. \tag{2.25}$$

with $G \in SU(N_c)$. In the following we shall not write out the indices $a, b, ...$ explicitly. The symmetry (2.25) can be promoted to a local gauge symmetry with position-dependent $G(x)$,

$$\Psi(x) \;\mapsto\; G(x)\Psi(x), \qquad \overline{\Psi}(x) \;\mapsto\; \overline{\Psi}(x)\,G^\dagger(x), \tag{2.26}$$

through replacing the derivative $\partial_\mu\Psi(x)$ in the Lagrangian by

$$D_\mu\Psi(x) \equiv \partial_\mu\Psi(x) + igA_\mu(x)\Psi(x). \tag{2.27}$$

The covariant derivative (2.27) contains a new field $iA_\mu(x) \in \mathfrak{su}(N_n)$ that changes under gauge transformations in the following way:

$$A_\mu(x) \;\mapsto\; G(x)A_\mu(x)G^\dagger(x) + \frac{i}{g}\left[\partial_\mu G(x)\right]G^\dagger(x). \tag{2.28}$$

The transformation law (2.28) ensures that $D_\mu\Psi$ transforms in the same way as Ψ. To obtain the complete theory, the following kinetic term for the gauge field is added to the action (in Minkowski space):

$$S_{YM} = -\frac{1}{2}\int \mathrm{d}^4x\;\mathrm{Tr}\left[F_{\mu\nu}F^{\mu\nu}\right], \tag{2.29}$$

where

$$F_{\mu\nu} \equiv \frac{1}{ig}[D_\mu,\,D_\nu] = \partial_\mu A_\nu - \partial_\nu A_\mu + ig[A_\mu,\,A_\nu]. \tag{2.30}$$

For a gauge theory, the derivation of the path integral is more complicated since the fields are only determined up to gauge transformations. The definition of a Hamiltonian and canonical quantisation require gauge fixing. However, in the nonperturbative lattice

formulation of the path integral the integration over redundant degrees of freedom does not cause problems. We shall therefore not derive the path integral in the continuum, but rather define it directly on the lattice in Sec. 2.3.

Note that the Euclidean action can be obtained from the Minkowski space action in the same way as described in Sec. 2.1.1, except that because ∂_t becomes $i\partial_\tau$ one also needs to replace A_0 by iA_0^E in order to achieve consistency with the gauge transformation law (2.28). The Euclidean action is

$$S_E = \int \mathrm{d}^4 x_E \left[\overline{\Psi}_E(x_E)(\gamma_\mu D_\mu + m)\Psi_E(x_E) + \frac{1}{2}\mathrm{Tr}\left[F_{\mu\nu}(x_E)F_{\mu\nu}(x_E)\right] \right]. \tag{2.31}$$

2.2 Extracting observables from Euclidean correlation functions

When Euclidean correlation functions are calculated numerically in lattice field theory, it is usually not possible to perform an analytic continuation back to Minkowski space. Thus, one has to extract results for physical observables directly from Euclidean correlators.

The energy spectrum of the theory can be extracted straightforwardly from two-point functions, as can already be seen from Eq. (2.12). Consider a set of Euclidean fields O_i associated with the Minkowski space operators O_i. Using the Heisenberg equations of motion and $\mathsf{H}|0\rangle = \mathsf{P}|0\rangle = 0$ we have for $\tau > 0$ and $L_\tau = \infty$

$$\begin{aligned} C_{ij}(\tau, \mathbf{p}) &\equiv \int \mathrm{d}^3 x \ \langle O_i(\tau, \mathbf{x}) O_j^\dagger(0)\rangle \ e^{-i\mathbf{p}\cdot\mathbf{x}} \\ &= \int \mathrm{d}^3 x \ \langle 0|\mathsf{O}_i(0) e^{-\mathsf{H}\tau + i\mathsf{P}\cdot\mathbf{x}} \mathsf{O}_j^\dagger(0)|0\rangle \ e^{-i\mathbf{p}\cdot\mathbf{x}}. \end{aligned} \tag{2.32}$$

Now, let $|X\rangle$ denote an eigenstate of H with zero momentum, and let $|X_\mathbf{k}\rangle$ denote the boost of $|X\rangle$ to momentum $\mathbf{k}$. Then we have the completeness relation

$$\mathsf{I} = |0\rangle\langle 0| + \sum_X \int \frac{\mathrm{d}^3 k}{(2\pi)^3} \frac{1}{2E(X_\mathbf{k})} |X_\mathbf{k}\rangle\langle X_\mathbf{k}|, \tag{2.33}$$

where $\sum_X$ denotes the sum/integration over all zero-momentum eigenstates (except the

vacuum) of H. Inserting (2.33) into (2.32), we get[3]

$$\begin{aligned} C_{ij}(\tau,\mathbf{p}) &= \sum_X \int \frac{\mathrm{d}^3k}{(2\pi)^3}\frac{1}{2E(X_\mathbf{k})}\int \mathrm{d}^3x\ \langle 0|\mathsf{O}_i(0)|X_\mathbf{k}\rangle\langle X_\mathbf{k}|\mathsf{O}_j^\dagger(0)|0\rangle e^{-E(X_\mathbf{k})\tau}e^{-i(\mathbf{p}-\mathbf{k})\cdot\mathbf{x}} \\ &= \sum_X \int \mathrm{d}^3k \frac{1}{2E(X_\mathbf{k})}\langle 0|\mathsf{O}_i(0)|X_\mathbf{k}\rangle\langle X_\mathbf{k}|\mathsf{O}_j^\dagger(0)|0\rangle e^{-E(X_\mathbf{k})\tau}\delta^3(\mathbf{p}-\mathbf{k}) \\ &= \sum_X \frac{1}{2E(X_\mathbf{p})}\langle 0|\mathsf{O}_i(0)|X_\mathbf{p}\rangle\ \langle 0|\mathsf{O}_j(0)|X_\mathbf{p}\rangle^*\ e^{-E(X_\mathbf{p})\tau}. \end{aligned} \tag{2.34}$$

Thus, the energies of the states $|X_\mathbf{p}\rangle$ with non-zero overlap $\langle 0|\mathsf{O}_i(0)|X_\mathbf{p}\rangle$ can be extracted from a multi-exponential fit to (2.34). For large τ, the lowest-energy state with a non-zero overlap dominates, and a single-exponential fit will be sufficient to obtain its energy.

From such a fit, one also obtains the amplitudes $\langle 0|\mathsf{O}_i(0)|X_\mathbf{p}\rangle$. Consider the case of QCD, with $O_1 = J_5^\mu = \overline{u}\hat{\gamma}^\mu\hat{\gamma}_5 d$ and $O_2 = \overline{u}\hat{\gamma}_5 d$. Then the lowest-energy state contributing to (2.34) is a charged pion at momentum $\mathbf{p}$ and we obtain

$$\langle 0|\ \overline{\mathsf{u}}(0)\hat{\gamma}^\mu\hat{\gamma}_5\mathsf{d}(0)\ |\pi^-(\mathbf{p})\rangle = -if_\pi\, p^\mu. \tag{2.35}$$

Thus, the pion decay constant f_π, which is relevant for the leptonic decay $\pi \to \ell\nu$, can be extracted. Similarly, from Euclidean three-point correlation functions, one can straightforwardly extract form factors for electroweak decays with a single hadron in both the initial and final state, such as $B \to \pi\ell\nu$. This will be explained in Sec. 8.4.

In contrast, hadron-hadron scattering processes can not be calculated directly from Euclidean correlation functions in infinite volume, except at kinematic thresholds [35]. There is a way around this: by studying the volume-dependence of multi-particle energy levels in a finite box one can compute elastic scattering phase shifts [36, 37].

2.3 Gauge fields and naive fermions on the lattice

We will now discretise the theory with action (2.31) on a hypercubic lattice with points $x = an$, $n \in \mathbb{Z}^4$. Since we will work exclusively with the Euclidean theory, we drop the subscript "E" in the following.

Let us consider the Dirac action without the gauge field first. The derivative $\partial_\mu\Psi$ must be replaced by a difference quotient[4]:

$$\frac{1}{2a}\left[\Psi(x+a\hat{\mu}) - \Psi(x-a\hat{\mu})\right], \tag{2.36}$$

[3] We assume $\langle 0|\mathsf{O}_i|0\rangle = 0$. Otherwise, take the connected 2-point function.

[4] The symmetric difference is chosen to give a Hermitian Hamiltonian

where $\hat{\mu}$ denotes the unit-vector in μ-direction. Expression (2.36) is not covariant under gauge transformations, since $\Psi(x+a\hat{\mu})$ and $\Psi(x-a\hat{\mu})$ transform differently under (2.26). Thus, the fields must be parallel-transported to the same lattice point x first. The covariant derivative may be written as

$$\Delta_\mu^{(\pm)}\Psi(x) \equiv \frac{1}{2a}\left[U_\mu(x)\Psi(x+a\hat{\mu}) - U_{-\mu}(x)\Psi(x-a\hat{\mu})\right], \tag{2.37}$$

where $U_\mu(x)$, $U_{-\mu}(x) \in SU(N_c)$ and $U_{-\mu}(x) = U_\mu^\dagger(x-a\hat{\mu})$. These *link variables* must transform under gauge transformations as

$$U_\mu(x) \mapsto G(x)U_\mu(x)G^\dagger(x+a\hat{\mu}) \tag{2.38}$$

in order to guarantee the exact gauge invariance of the lattice Dirac action

$$S_F^{\text{lat.}}[\overline{\Psi},\Psi,U] = a^4 \sum_{x\in a\mathbb{Z}^4} \overline{\Psi}(x)\left[\gamma^\mu\Delta_\mu^{(\pm)} + m\right]\Psi(x). \tag{2.39}$$

When defining $A_\mu^{\text{lat.}}$ by

$$U_\mu(x) = \exp\left(iagA_\mu^{\text{lat.}}(x)\right) = \mathbb{1} + iagA_\mu^{\text{lat.}}(x) + \mathcal{O}(a^2), \tag{2.40}$$

we see that for sufficiently smooth fields in the limit $a \to 0$ the lattice expressions approach the continuum expressions,

$$\begin{aligned} \lim_{a\to 0}\Delta_\mu^{(\pm)}\Psi(x) &= D_\mu\Psi(x), \\ \lim_{a\to 0}A_\mu^{\text{lat.}}(x) &= A_\mu(x), \end{aligned} \tag{2.41}$$

and the gauge transformation law for the link variables, (2.38), becomes equivalent to (2.28).

What is still missing is a lattice discretisation of the kinetic term for the gauge field. For this, a lattice definition of the gauge field strength tensor is needed. Mathematically speaking, the field strength is the curvature associated with the gauge connection. Thus, it can be obtained from parallel transport around a small closed loop. The smallest possible loop on the lattice is the *plaquette*

$$U_{\mu\nu}(x) \equiv U_\mu(x)U_\nu(x+a\hat{\mu})U_\mu^\dagger(x+a\hat{\nu})U_\nu^\dagger(x). \tag{2.42}$$

Inserting (2.40), we find

$$U_{\mu\nu}(x) = \mathbb{1} + iga^2F_{\mu\nu}(x) + \mathcal{O}(a^3). \tag{2.43}$$

Thus, a possible choice for the lattice field strength would be

$$\frac{i}{ga^2}(\mathbb{1} - U_{\mu\nu}(x)). \tag{2.44}$$

Since the continuum $F_{\mu\nu}$ is Hermitian, one may also choose the Hermitian conjugate of (2.44) to represent $F_{\mu\nu}$. To obtain a real and positive lattice action, the natural choice is to take the product of (2.44) and its Hermitian conjugate as the lattice discretisation of $F_{\mu\nu}F_{\mu\nu}$ in the action:

$$\begin{aligned} S_G^{\text{lat.}}[U] &= a^4 \sum_{x\in a\mathbb{Z}^4} \sum_{\mu,\nu} \frac{1}{2} \operatorname{Tr}\left\{ \frac{i}{ga^2}\big(\mathbb{1} - U_{\mu\nu}(x)\big) \left[\frac{i}{ga^2}\big(\mathbb{1} - U_{\mu\nu}(x)\big)\right]^\dagger \right\} \\ &= \sum_{x\in a\mathbb{Z}^4} \sum_{\mu,\nu} \frac{1}{2g^2} \operatorname{Tr}\Big[2\cdot\mathbb{1} - U_{\mu\nu}(x) - U_{\mu\nu}^\dagger(x)\Big] \\ &= \beta \sum_{x\in a\mathbb{Z}^4} \sum_{\mu<\nu} \left[1 - \frac{1}{N_c} \operatorname{Re}\operatorname{Tr} U_{\mu\nu}(x)\right] \end{aligned} \tag{2.45}$$

with $\beta = 2N_c/g^2$. Eq. (2.45) is the plaquette action, as introduced by Wilson in [5]. For smooth fields, the deviation to the continuum action (2.31) is of order $\mathcal{O}(a^2)$.

The total lattice action $S^{\text{lat.}}[\overline{\Psi}, \Psi, U]$ for the Dirac field coupled to the gauge field is of course the sum of (2.39) and (2.45). The path integral for an observable $O[\overline{\Psi}, \Psi, U]$ depending on the fermion and gauge fields is then defined as

$$\langle O\rangle = \frac{\int \mathcal{D}[U] \int \mathcal{D}[\overline{\Psi}, \Psi] \;\; O[\overline{\Psi}, \Psi, U] \;\; e^{-S^{\text{lat.}}[\overline{\Psi}, \Psi, U]}}{\int \mathcal{D}[U] \int \mathcal{D}[\overline{\Psi}, \Psi] \;\; e^{-S^{\text{lat.}}[\overline{\Psi}, \Psi, U]}}, \tag{2.46}$$

where $\int \mathcal{D}[\overline{\Psi}, \Psi]$ stands for the Grassmann integrations over all colour/spin components of $\overline{\Psi}$ and Ψ at all lattice points, and $\int \mathcal{D}[U] = \int \prod_x \prod_\mu \mathrm{d}U_\mu(x)$ denotes the integrations over all link variables $U_\mu(x)$ with the Haar measure. The group-multiplication invariance of the latter leads to the gauge invariance of the path integral. In local coordinates $\{\omega^a\}$ on $SU(N_c)$ the Haar measure is given by

$$\mathrm{d}U = C\sqrt{\det A} \prod_{a=1}^{N_c^2-1} \mathrm{d}\omega^a, \tag{2.47}$$

where C is a normalisation factor so that $\int \mathrm{d}U = 1$, and A is the metric on $SU(N_c)$,

$$A_{ab} = -2 \operatorname{Tr}\big[(U^{-1}\partial_a U)(U^{-1}\partial_b U)\big] = 2 \operatorname{Tr}\big[\partial_a U \, \partial_b U^\dagger\big]. \tag{2.48}$$

(From [30]). The fermion measure $\mathcal{D}[\overline{\Psi}, \Psi]$ is gauge-invariant because $\det G(x) = 1$ for gauge transformations $G(x) \in SU(N_c)$.

Using the results (2.23) and (2.24), the Grassmann integrations can be performed explicitly. This gives

$$\langle O \rangle = \frac{\int \mathcal{D}[U] \;\; O\big[K^{-1}[U],\, U\big] \;\det\left(K[U]\right) \;\; e^{-S_G^{\text{lat.}}[U]}}{\int \mathcal{D}[U] \det\left(K[U]\right) \; e^{-S_G^{\text{lat.}}[U]}} \tag{2.49}$$

where K is the kernel of the lattice Dirac action. For the naive action (2.39), the kernel is

$$K(x,\, x') = \sum_{\mu=0}^{3} \frac{1}{2a}\, \gamma^\mu \;\big[U_\mu(x)\delta_{x',\, x+a\hat{\mu}} - U_{-\mu}(x)\delta_{x',\, x-a\hat{\mu}}\big] + m\, \delta_{x',\, x}. \tag{2.50}$$

On a finite lattice, (2.49) is an ordinary multidimensional integral over real numbers (local coordinates on $SU(N_c)$), and can be calculated numerically by Monte-Carlo methods, as explained in Sec. 2.5.

2.4 More about lattice fermions

2.4.1 Naive fermions

The lattice fermion action defined in (2.39) is called the *naive* fermion action, for reasons that will become clear when considering the resulting free (= without gauge fields) propagator in momentum space:

$$\begin{aligned} K^{-1}(p) &= \big[i\gamma_\mu \sin(a\, p_\mu)/a + m\big]^{-1} \\ &= \frac{-i\gamma_\mu \sin(a\, p_\mu)/a + m}{\sum_{\mu=0}^{3} \sin^2(a\, p_\mu)/a^2 + m^2}. \end{aligned} \tag{2.51}$$

Note that the lattice momentum p is restricted to the periodic Brillouin zone, which is a 4-dimensional torus, with $-\pi < ap_\mu \leq \pi$. The sine functions in (2.51) vanish at the 16 points $p^{(1)} = (0,0,0,0)$, $p^{(2)} = (\pi,0,0,0)/a$, ... $p^{(16)} = (\pi,\pi,\pi,\pi)/a$ of the Brillouin zone, and for momenta close to these points one can expand them in a Taylor series to obtain the continuum limit $a \to 0$. Writing $p = p^{(n)} + k$ (modulo $2\pi/a$), this gives

$$K^{-1}(p^{(n)} + k) = \frac{-i\gamma_\mu^{(n)} k_\mu + m}{k^2 + m^2} + \mathcal{O}(a) \tag{2.52}$$

with

$$\gamma_\mu^{(n)} = \gamma_\mu \, \cos(a\, p_\mu^{(n)}) = \pm\gamma_\mu. \tag{2.53}$$

For $a \to 0$, (2.52) has a pole at $k_0 = i\sqrt{\mathbf{k}^2 + m^2}$, and hence (2.51) has 16 such poles in the continuum limit. The matrices $\gamma_\mu^{(n)}$ in (2.53) can be written as

$$\gamma_\mu^{(n)} = S_{(n)}^\dagger \gamma_\mu S_{(n)} \tag{2.54}$$

with unitary $S_{(n)}$, see [31]. The transformation

$$\Psi'_{(n)}(x) = e^{-ip^{(n)}\cdot x} S_{(n)} \Psi(x), \qquad \overline{\Psi}'_{(n)}(x) = \overline{\Psi}(x) S^{\dagger}_{(n)} e^{ip^{(n)}\cdot x} \tag{2.55}$$

brings the action for the n-th doubler to its standard form.

The interpretation of the doublers as corresponding to individual Dirac fields called *tastes* can be made more explicit by transforming to a spin-taste basis, as will be explained in Sec. 2.4.3. It turns out that the fermion doubling is related to chiral symmetry. This is discussed in Sec. (2.4.4).

2.4.2 Wilson fermions

One way to remove the 15 unwanted doublers is to modify the lattice action by a term that gives them infinite "mass" in the continuum limit, so that they decouple from the theory. Wilson suggested the following action:

$$S_F^{\mathrm{W}}[\overline{\Psi}, \Psi, U] = a^4 \sum_{x \in a\mathbb{Z}^4} \overline{\Psi}(x) \left[\gamma_\mu \Delta_\mu^{(\pm)} - \frac{1}{2} a \Delta_\mu^{(+)} \Delta_\mu^{(-)} + m \right] \Psi(x), \tag{2.56}$$

so that

$$K_W(x, x') = -\sum_{\mu=0}^{3} \frac{1}{2a} \left[(1-\gamma^\mu) U_\mu(x) \delta_{x',\, x+a\hat{\mu}} + (1+\gamma^\mu) U_{-\mu}(x) \delta_{x',\, x-a\hat{\mu}} \right] + \left(m + \frac{4}{a} \right) \delta_{x',\, x}. \tag{2.57}$$

This gives the free propagator

$$K_W^{-1}(p) = \frac{-i\gamma_\mu \sin(a\, p_\mu)/a + \tilde{m}(a,p)}{\sum_{\mu=0}^{3} \sin^2(a\, p_\mu)/a^2 + \tilde{m}^2(a,p)}, \tag{2.58}$$

with $\tilde{m}(a,p) = m + \frac{2}{a} \sum_{\mu=0}^{3} \sin^2(a p_\mu/2)$. The behaviour near $p = 0$ is unaltered but the doublers disappear. However, the new term in the action explicitly breaks the chiral symmetry that one would have for $m = 0$. This results in an additive mass renormalisation and more severe complications related to operator mixing.

2.4.3 Staggered fermions

Starting from the naive fermion action (2.39), we perform a unitary transformation $\Psi(x) = \Omega(x)\Psi'(x)$, $\overline{\Psi}(a) = \overline{\Psi}'(x)\Omega^\dagger(x)$ with[5]

$$\Omega(x) = \gamma_0^{x_0} \gamma_1^{x_1} \gamma_2^{x_2} \gamma_3^{x_3}. \tag{2.59}$$

[5]From now on, we use lattice units with $a = 1$.

Then, using

$$\Omega^\dagger(x)\gamma_\mu\Omega(x+\hat{\mu}) = \underbrace{(-1)^{x_0+\ldots+x_{\mu-1}}}_{\equiv\eta_\mu(x)}\,\mathbb{1}, \tag{2.60}$$

the action becomes

$$S_F = \sum_{x\in\mathbb{Z}^4} \overline{\Psi}'(x)\left[\eta_\mu(x)\Delta_\mu^{(\pm)} + m\right]\Psi'(x). \tag{2.61}$$

This is now diagonal in spin-space, and we see that the four components of Ψ' interact independently and equally.

The staggered fermion action is then constructed by keeping only one of the components of Ψ', e.g. the first, Ψ'_1. The physical content of the resulting action can be analysed by grouping the values of the one-component field Ψ'_1 from the 16 corners of each hypercube of the lattice into a new field $Q_{\alpha\beta}$, living on a lattice with the double lattice spacing. Let us consider the free case without gauge fields for simplicity. The coordinates of the original lattice can be written as $x = 2y+\rho$ with $y\in\mathbb{Z}^4$ and $\rho_\mu = 0,1$. Then, one defines

$$Q_{\alpha\beta}(y) = \frac{1}{8}\sum_\rho \Omega_{\alpha\beta}(\rho)\Psi'_1(2y+\rho), \qquad \overline{Q}_{\alpha\beta}(y) = \frac{1}{8}\sum_\rho \overline{\Psi}'_1(2y+\rho)\Omega^\dagger_{\alpha\beta}(\rho). \tag{2.62}$$

The index α is the spinor index, while the index β turns out to label the tastes. Reintroducing the lattice spacing, the action becomes

$$\begin{aligned} S_F^{\text{stag.}} \;=\; & (2a)^4 \sum_{y\,\in\,2a\mathbb{Z}^4}\sum_{\mu=0}^{3} \overline{Q}(y)\Big[(\gamma_\mu\otimes\mathbb{1})\Delta_\mu^{(\pm)} + a(\gamma_5\otimes\gamma_\mu^T\gamma_5^T)\Delta_\mu^{(-)}\Delta_\mu^{(+)}\Big]Q(y) \\ & + (2a)^4 \sum_{y\,\in\,2a\mathbb{Z}^4} m\,\overline{Q}(y)\Big[\mathbb{1}\otimes\mathbb{1}\Big]Q(y), \end{aligned} \tag{2.63}$$

where the notation is "spin $\otimes$ taste" and derivatives are now understood with the double lattice spacing:

$$\Delta_\mu^{(+)}Q = \frac{1}{2a}\left[Q(y+2a\hat{\mu}) - Q(y)\right] \qquad \text{etc.} \tag{2.64}$$

In the new basis, (2.63) gives the following propagator (with $b = 2a$):

$$K^{-1}_{\text{stag.}}(p) = \frac{\frac{1}{b}\sum_{\mu=0}^3\left[-i(\gamma_\mu\otimes\mathbb{1})\sin(b\,p_\mu) + (\gamma_5\otimes\gamma_\mu^T\gamma_5^T)\sin^2\frac{b\,p_\mu}{2}\right] + m\mathbb{1}\otimes\mathbb{1}}{\sum_{\mu=0}^3\frac{4}{b^2}\sin^2\frac{b\,p_\mu}{2} + m^2}. \tag{2.65}$$

Since the lattice spacing for $Q_{\alpha\beta}$ is $b = 2a$, the momenta are restricted to $-\pi/b < p_\mu \le \pi/b$, and the sine function in the denominator vanishes only at $p = 0$. In the continuum limit, (2.65) reduces to the correct propagator describing four Dirac fields of the same mass. At non-zero lattice spacing, the term $a(\gamma_5\otimes\gamma_\mu^T\gamma_5^T)\Delta_\mu^{(-)}\Delta_\mu^{(+)}$ in (2.63) breaks the taste symmetry.

As we have seen at the beginning of this section, a naive fermion field is equivalent to be four identical copies of staggered fermion fields. Thus, the above calculations also show that the naive action corresponds to 16 tastes in the continuum limit.

Rooted staggered fermions

In the continuum limit, the staggered fermion action describes four identical copies of a Dirac field, which means that the corresponding fermion operator can be written as

$$K = (\not{D} + m) \otimes \mathbb{1}_{4\times 4}, \tag{2.66}$$

where $\not{D}$ is the continuum Dirac operator. This was shown in the previous section for the free case without gauge fields. The path integral for a continuum theory with action (2.66) contains the determinant

$$\det\left[(\not{D} + m) \otimes \mathbb{1}_{4\times 4}\right] = \left[\det(\not{D} + m)\right]^4. \tag{2.67}$$

The determinant is responsible for the loops of virtual fermions, i.e. the sea quarks in QCD. Hence, for such a continuum theory, one can reduce the number of sea quarks to one by taking the positive 4-th root of the fermion determinant in the path integral[6]:

$$\det(\not{D} + m) = \left(\det\left[(\not{D} + m) \otimes \mathbb{1}_{4\times 4}\right]\right)^{1/4}. \tag{2.68}$$

For rooted staggered fermions, the same procedure is done at non-zero lattice spacing. At non-zero lattice spacing, the taste-symmetry is broken and the resulting theory is non-local [38]. However, there is evidence that the continuum limit is still correct [39, 40, 41]. It is crucial to take this limit before the chiral limit, so that the taste splittings always remain smaller than the Goldstone pion mass.

The use of rooted staggered fermions has been criticised in particular by M. Creutz [42, 43, 44], and this criticism has been refuted in [45, 46, 47, 48].

2.4.4 Fermion doubling and chiral symmetry

The naive fermion action (2.39), which suffers from doubling, has a $U(1)$ chiral symmetry at $m = 0$,

$$\Psi' = e^{i\alpha\gamma_5}\Psi, \qquad \overline{\Psi}' = \overline{\Psi}e^{i\alpha\gamma_5}. \tag{2.69}$$

Equivalently, the naive lattice fermion matrix (2.50) with $m = 0$ satisfies $\{K,\, \gamma_5\} = 0$. On the other hand, in the Wilson action (2.56), the fermion doublers are removed by including the operator $\frac{1}{2}a\Delta_\mu^{(+)}\Delta_\mu^{(-)}$, which breaks the chiral symmetry.

[6] the determinant is positive for $m > 0$, since $\left\{\not{D}, \gamma_5\right\} = 0$ and $\not{D}$ is anti-Hermitian

An important observation can be made about the chirality of the doublers. Starting from the naive lattice action, let us try to restrict the theory to, say, the left-handed components

$$\Psi_L(x) = \tfrac{1}{2}(1-\gamma_5)\Psi, \qquad \overline{\Psi}_L(x) = \overline{\Psi}\tfrac{1}{2}(1+\gamma_5). \tag{2.70}$$

Due to the chiral symmetry, the left-handed components are not coupled to the right-handed components, and so we can set the latter to zero. However, for half of the tastes, the transformation (2.55) which was used to obtain the correct form of the action, changes the handedness:

$$S_{(n)}\tfrac{1}{2}(1+\gamma_5)S^{\dagger}_{(n)} = \tfrac{1}{2}(1\pm\gamma_5) \tag{2.71}$$

with a minus sign for 8 of the 16 tastes. Thus, by doing the projection (2.70) one obtains a theory of 8 left-handed and 8 right-handed fermions.

The number of doublers in the naive action, $2^4 = 16$, is due to the hypercubic symmetry. Wilczek [49] suggested the following action that breaks hypercubic symmetry at non-zero lattice spacing

$$K(p) = i\sum_{j=1}^{3}\gamma_j\frac{1}{a}\sin(a\,p_j) + i\gamma_0\left[\frac{1}{a}\sin(a\,p_0) + \lambda\sum_{j=1}^{3}\frac{1}{a}\sin^2\left(\tfrac{1}{2}a\,p_j\right)\right]. \tag{2.72}$$

This is chirally symmetric and has zeros only at $p = (0,0,0,0)$ and $p = (\pi/a,0,0,0)$. By doing the projection (2.70) one obtains a theory of a single left-handed and a single right-handed fermion, i.e. a theory with the degrees of freedom of a single Dirac fermion[7].

In [50], actions of the general form $K(x,y) = \sum_{\mu=0}^{3}\gamma_\mu F_\mu(x,y)$ that satisfy translation invariance (i.e. $F(x,y) = F(x-y)$), Hermiticity (i.e. $F^*(z) = F(-z)$), and $|z|^4F(z) \to 0$ for $|z| \to \infty$, are considered. These properties imply that the Fourier transform $F_\mu(p)$ is a continuous real vector field on the Brillouin zone, which is a 4-dimensional torus T^4. The Poincaré-Hopf theorem states that for a compact manifold the sum of the indices at the zeros of F_μ is equal to the Euler characteristic of the manifold, which is zero for T^4. This implies that there is always an equal number of left-handed and right-handed fermions.

Very general proofs of the existence of an equal number of left-handed and right-handed fermions were given by Nielsen and Ninomiya in [51, 52, 53].

The fermion doubling is also related to the axial anomaly. In the continuum theory of a massless Dirac field coupled to a gauge field, the axial current $J^\mu_A = \overline{\Psi}\gamma^\mu\gamma_5\Psi$ is no longer conserved after quantisation:

$$\langle\,\partial_\mu J^\mu_A(x)\,\rangle = \frac{g^2}{16\pi^2}\epsilon_{\mu\nu\rho\lambda}\left\langle\,\mathrm{Tr}[F^{\mu\nu}(x)F^{\rho\lambda}(x)]\,\right\rangle. \tag{2.73}$$

[7]However, breaking hypercubic invariance leads to other complications.

As Fujikawa has shown [54], this can be explained by the non-invariance of the fermion path integral measure, when properly regulated in a gauge-invariant way, under the transformation (2.69). However, on the lattice the fermion measure is in fact invariant under (2.69) due to $\mathrm{Tr}\,\gamma_5 = 0$. The naive lattice action (2.39) at $m = 0$ is also invariant, and hence with naive fermions the lattice axial current

$$J_A^{\mu\,(\mathrm{lat.})} = \frac{1}{2}\left[\overline{\Psi}(x)U_\mu(x)\gamma_\mu\gamma_5\Psi(x+\hat{\mu}) + \overline{\Psi}(x+\hat{\mu})\gamma_\mu\gamma_5 U_\mu^\dagger(x)\Psi(x)\right] \tag{2.74}$$

is still exactly conserved in the quantum theory: $\langle \Delta_\mu^{(-)} J_A^{\mu\,(\mathrm{lat.})}\rangle = 0$. This can be viewed as a cancellation between the contributions to the axial anomaly from the left-handed and right-handed doublers [55]. Note that in the spin-taste basis introduced in Sec. 2.4.3, the transformation (2.69) reads

$$Q \mapsto e^{i\alpha(\gamma_5\otimes\gamma_5)}Q, \qquad \overline{Q} \mapsto \overline{Q}e^{i\alpha(\gamma_5\otimes\gamma_5)}, \tag{2.75}$$

and it is therefore identified as a taste-non-singlet symmetry. The taste-*singlet* axial transformation generated by $\gamma_5 \otimes \mathbb{1}$ is not an exact symmetry of the action at non-zero lattice spacing, and the associated current is in fact anomalous [56, 57].

For Wilson fermions, the action is not invariant under (2.69) due to the Wilson term. In this case the current (2.74) has the correct anomaly [55].

2.4.5 The Ginsparg-Wilson relation

In the last section we have established the following: on the lattice, the path integral measure is invariant under the transformation (2.69). With the naive lattice action, which is also invariant under (2.69), unphysical fermion doublers appear, turning this transformation into a non-singlet symmetry which therefore is non-anomalous.

On the other hand, the Wilson action is not invariant under (2.69), so that the doublers disappear and the axial anomaly is generated. However, for a theory with multiple *physical* quark flavours, the Wilson term also breaks all non-singlet chiral symmetries, which makes renormalisation of the lattice theory very difficult.

There is, however, a more continuum-like way of generating the axial anomaly on the lattice, which avoids doublers but leaves the non-singlet chiral symmetries for multiple physical flavours intact. In this approach, the definition of the chiral transformation is modified for non-zero lattice spacing, but reduces to the usual form for $a \to 0$. The simplest definition of the infinitesimal transformation reads [58]

$$\delta\Psi = i\alpha\gamma_5\left(1 - \frac{a}{2r_0}K\right)\Psi, \qquad \delta\overline{\Psi} = i\alpha\overline{\Psi}\left(1 - \frac{a}{2r_0}K\right)\gamma_5, \tag{2.76}$$

where K is the lattice Dirac operator. Flavour non-singlet transformations can be defined by including a flavour-group generator. The action is invariant under (2.76) if K satisfies the relation

$$\{\gamma_5,\, K\} = \frac{a}{r_0}\, K\, \gamma_5\, K. \tag{2.77}$$

Eq. (2.77) had already been derived by Ginsparg and Wilson [59] as the remnant of continuum chiral symmetry obtained after a blocking transformation. Explicit solutions for K will be given in Secs. 2.4.6 and 2.4.7. By multiplying (2.77) from both the left and right with K^{-1} we find the following relation for the propagator K^{-1}:

$$\left\{\gamma_5,\, K^{-1}(x,\, x')\right\} = \frac{a}{r_0}\, \gamma_5\, \delta_{x,\, x'}, \tag{2.78}$$

that is, the propagator is chirally invariant in the usual sense at all non-zero distances.

It turns out that the path integral measure transforms under the flavour-singlet chiral rotation (2.76) in precisely the right way to generate the axial anomaly [58]. As it should be, the measure is invariant under flavour-non-singlet transformations.

Starting from a lattice Dirac operator K satisfying the Ginsparg-Wilson relation, a mass m can be introduced in the following way:

$$K(m) = \left(1 - \frac{am}{2r_0}\right) K + m. \tag{2.79}$$

2.4.6 Overlap fermions

An explicit example of a lattice Dirac operator satisfying (2.77) is the overlap operator [60, 61, 62]

$$K = \frac{r_0}{a}\left[1 + \gamma_5\ \mathrm{sgn}(H)\right] \tag{2.80}$$

where the simplest choice is $H = \gamma_5\, K_W$ with the Wilson fermion operator (2.57) with negative mass $-r_0/a$. In (2.80), the function $\mathrm{sgn}(H)$ is the matrix sign function: for Hermitian H, one has $\mathrm{sgn}(H) = H/\sqrt{H^2}$. In numerical simulations, the sign function is implemented by some iterative approximation.

2.4.7 Domain wall fermions

Chiral fermions in 4 dimensions can also be obtained as zero-modes localised at domain walls in 5-dimensional theories. Following [63], let us consider the 5-dimensional continuum Dirac equation with a position-dependent mass term,

$$\left[\not{D} + \gamma_5 \partial_s + M(s)\right] \Psi(x, s) = 0, \tag{2.81}$$

where s is the 5-th coordinate, $\not{D}$ is the 4-dimensional massless Dirac operator and

$$M(s) = \begin{cases} +M, & s > 0 \\ -M, & s < 0 \end{cases} \qquad (M > 0). \tag{2.82}$$

Since (2.81) is separable, we can write $\Psi(x, s)$ as a linear combination of products of the form[8]

$$\Psi(x, s) = \sum_n \left[f_n(s) P_R + g_n(s) P_L \right] \psi_n(x), \tag{2.83}$$

where $P_{R/L} = \frac{1}{2}(1 \pm \gamma_5)$ and

$$\begin{aligned} \left[\partial_s + M(s)\right] f_n(s) &= \mu_n \, g_n(s), \\ \left[-\partial_s + M(s)\right] g_n(s) &= \mu_n \, f_n(s), \\ \not{D} \, \psi_n(x) &= -\mu_n \, \psi_n(x). \end{aligned} \tag{2.84}$$

The functions f_0 and g_0 with eigenvalue $\mu = 0$ have the form

$$\begin{aligned} f_0(s) &= F \, e^{-\int_0^s M(s') \, \mathrm{d}s'} = F \, e^{-M|s|}, \\ g_0(s) &= G \, e^{+\int_0^s M(s') \, \mathrm{d}s'} = G \, e^{+M|s|}, \end{aligned} \tag{2.85}$$

with constants F and G. Since $g_0(s)$ is not normalisable for $G \neq 0$, we must have $G = 0$. Thus, the massless mode is right-handed (for $M < 0$, a left-handed mode is obtained). One expects that all other eigenvalues are of order $|\mu_n| \gtrsim \mathcal{O}(M)$, and so the low-energy effective theory consists of a 4-dimensional right-handed massless fermion.

For a compact fifth dimension with periodic boundary conditions (and hence with a kink and an anti-kink in $M(s)$), in the absence of gauge fields one finds a massless left-handed mode localised at one of the domain walls and a massless right-handed mode localised at the other domain wall. However, interactions with gauge fields lead to a coupling of the left-handed and right-handed modes and hence a breaking of exact chirality and the appearance of a residual mass. This coupling vanishes as the length of the fifth dimension is taken to infinity, and exact chirality is restored.

The appearance of chiral modes bound to domain walls can be used to construct chiral lattice fermion actions [26]. A domain wall action commonly used in current simulations was introduced in [27] and [28]. In lattice units, it is given by

$$S_{DW} = \sum_x \sum_{s=1}^{L_s} \overline{\Psi}(x, s) \left[\Psi(x, s) - P_L \Psi(x, s+1) - P_R \Psi(x, s-1) + \sum_{x'} K_W(x, x') \Psi(x', s) \right] \tag{2.86}$$

[8] This may also include integration over a continuous part of the spectrum.

where K_W is the Wilson fermion operator (2.57) with negative mass $-M_5 = -r_0$ and the gauge fields in K_W are independent of the 5-th coordinate s. The 5-dimensional fermion fields are subject to the boundary conditions

$$\begin{aligned} P_L\,\Psi(x,\,L_s+1) &= -\,m\,P_L\,\Psi(x,\,1), \\ P_R\,\Psi(x,\,0) &= -\,m\,P_R\,\Psi(x,\,L_s). \end{aligned} \tag{2.87}$$

The Dirac mass turns out to be proportional to m. Left-handed and right-handed four-dimensional fermion fields can be defined as

$$\begin{aligned} q_L(x) &= \Psi_L(x,\,1), & q_R(x) &= \Psi_R(x,\,L_s), \\ \overline{q}_L(x) &= \overline{\Psi}_L(x,\,1), & \overline{q}_R(x) &= \overline{\Psi}_R(x,\,L_s), \end{aligned} \tag{2.88}$$

where $\Psi_{L/R} = P_{L/R}\Psi$ and $\overline{\Psi}_{L/R} = \overline{\Psi}P_{R/L}$. For $m = 0$ and in the limit $L_s \to \infty$ the left-handed and right-handed fields decouple completely.

Note that in order to cancel the contributions from the heavy fermion modes in the bulk, one has to introduce additional 5-dimensional bosonic pseudofermion fields (also referred to as Pauli-Villar fields) in the partition function. A commonly used choice for their kernel is [64]

$$K_{PV} = K_{DW}\Big|_{m=1}\,, \tag{2.89}$$

where K_{DW} is the 5-dimensional domain wall operator defined by (2.86, 2.87). Performing the Gaussian integrals over the fermion and pseudofermion fields in the partition function, one obtains a factor of

$$\frac{\det K_{DW}}{\det K_{PV}}. \tag{2.90}$$

As shown in [65], this ratio of determinants can be written as a single determinant of a 4-dimensional *truncated overlap* operator that becomes an exact overlap operator in the limit $L_s \to \infty$.

At finite L_s, a small residual chiral symmetry breaking remains. See Ref. [66] for a detailed discussion of the choice of L_s in practical simulations.

2.5 Numerical calculations

Numerical calculations in lattice QCD usually start from Eq. (2.49), where the Grassmann integrals over the fermion fields have been performed explicitly. A set of gauge field configurations $\{U_1, U_2, ..., U_N\}$ is created via a Markov process such that for large N this

set is distributed with the probability density

$$p[U_i] \propto \Big(\prod_f \det K_f[U_i] \Big) e^{-S_G[U_i]}, \tag{2.91}$$

where K_f are the lattice fermion actions for the various flavours of dynamical quarks[9]. The expectation value of an observable O is then approximated as the ensemble-average

$$\langle O \rangle \approx \frac{1}{N} \sum_{i=1}^{N} O\Big[\Big\{ K_f^{-1}[U_i] \Big\}, U_i \Big]. \tag{2.92}$$

For this to make sense, the product of the fermion determinants in (2.91) must be positive. This is satisfied e.g. for Ginsparg-Wilson fermions. More generally, when a fermion action satisfies γ_5-Hermiticity, it follows that the corresponding determinant is real:

$$(\det K)^* = \det K^\dagger = \det(\gamma_5 K \gamma_5) = \det K. \tag{2.93}$$

Then, if mass-degenerate pairs of flavours are used, (2.91) will be positive. In many numerical calculations, the u- and d- quarks are taken to have equal mass.

With rooted staggered fermions (see Sec. 2.4.3), one can take $\left[\det\ K^\dagger K|_{\mathrm{ee}}\right]^{1/4}$ for each flavour, where the subscript "ee" denotes the restriction of the matrix $K^\dagger K$ to the even sublattice ($K^\dagger K$ is block-diagonal in terms of even and odd sites).

The algorithms used to update the gauge fields according to the distribution (2.91) usually require the repeated (iterative) solution of equations like $K\,G = S$, which makes the inclusion of dynamical fermions computationally expensive.

2.6 Renormalisation and continuum limit

The asymptotic freedom of QCD (for a sufficiently small number of flavours) implies that the continuum limit of lattice QCD corresponds to the limit where the bare gauge coupling is taken to zero.

In numerical computations, one chooses a value for the bare gauge coupling and then "measures" the corresponding lattice spacing. This is done by computing some physical quantity (in lattice units) and comparing the result to the experimental value. The bare quark masses can be set by requiring that the lattice results for a few "input" hadron masses agree with experiment (this may not be directly feasible; see Sec. 2.7.2).

[9] For heavy flavours, depending on the problem considered it can be a good approximation to neglect the effects of pair creation and set the corresponding determinant to 1.

When reducing the lattice spacing, the number of lattice sites in each direction has to be increased accordingly to keep the physical box size fixed. One also has to take the infinite volume limit, by doing the calculations with several physical box sizes. Extrapolations in the lattice spacing, the volume and the quark masses can be performed with the help of effective field theories [67]; this will be discussed in Sec. 2.7. It is also possible to reduce cutoff effects at non-zero lattice spacing by including additional higher-dimension operators to the lattice action (cf. Sec. 2.7.1).

While hadron masses can be obtained directly from the exponential decay of correlation functions, the values of matrix elements of certain operators require further renormalisation. They may depend on the scale and renormalisation scheme, and it may be necessary to convert the results to a continuum scheme like $\overline{\mathrm{MS}}$ in order to make contact with experiment. The same applies for the definition of the renormalised gauge coupling and renormalised quark masses.

In general, the renormalisation is simplified when symmetries are preserved exactly by the regulator. As an example, for flavour- and chirally symmetric lattice actions, one finds $Z_V = Z_A = 1$ for the conserved vector- and axial vector currents.

One method to relate lattice and continuum schemes is lattice perturbation theory, which has the advantage that analytic results can be obtained. The mismatch between the lattice and the continuum theories lies in the ultraviolet where the coupling is small, so that perturbation theory may be a good approximation. However, a systematic uncertainty due to neglected higher-order terms and nonperturbative effects remains.

Methods for nonperturbative renormalisation include the regularisation-independent (RI) scheme [68] and the Schrödinger functional method. Applications of the Schrödinger functional method include the renormalisation of the gauge coupling [69, 70] and quark masses [71], as well as the matching of heavy-quark effective theory (see Sec. 4) to QCD [72].

2.7 Lattice artefacts and effective field theories

2.7.1 Non-zero lattice spacing effects

Errors due to a non-zero lattice spacing can be analysed be means of the *Symanzik effective field theory*, where the lattice theory is modelled by a continuum theory with Lagrangian

$$\mathcal{L}_{\mathrm{Sym}} = \mathcal{L}_{\mathrm{QCD}} + \mathcal{L}_I, \tag{2.94}$$

where $\mathcal{L}_I$ describes the lattice artefacts. It contains all higher-order local operators O_i that are not forbidden by the symmetries of the lattice action,

$$\mathcal{L}_I = \sum_i a^{\dim O_i - 4}\, c_i\, O_i, \tag{2.95}$$

with dimensionless short-distance coefficients c_i depending on the couplings in the lattice action and the renormalisation scale. Using this framework, one can predict the functional dependence of lattice results on a, allowing a controlled continuum extrapolation. Note that for the fermionic part of the action, the possible operators of dimension 5, like the Wilson term (2.56), break chiral symmetry. Thus, if the lattice action has an exact chiral symmetry, these dimension-five operators will be forbidden in the Symanzik effective Lagrangian, so that chiral actions can not have $\mathcal{O}(a)$ errors.

Using the Symanzik effective theory, one can not only analyse non-zero lattice spacing errors, but can also reduce them by adjusting the couplings in the lattice action so that some of the coefficients c_i in (2.95) get smaller or vanish. This requires the inclusion of the corresponding higher-order operators in the lattice action.[10] As the CPU time needed to generate statistically independent gauge configurations with a fixed physical volume grows like $a^{-(4+z)}$, where $z > 0$ accounts for critical slowing down,[11] it can be much more cost-effective to use Symanzik-improvement rather than reduce a [76].

Consider for instance a lattice derivative operator

$$\Delta_\mu^{(\pm)} = \frac{\exp(aD_\mu) - \exp(-aD_\mu)}{2a} = D_\mu + \frac{a^2}{6}(D_\mu)^3 + \frac{a^4}{120}(D_\mu)^5 + ... \tag{2.96}$$

For smooth fields, the order a^2 error in (2.96) can be removed by taking the improved derivative

$$\widetilde{\Delta}_\mu^{(\pm)} = \Delta_\mu^{(\pm)} - \frac{a^2}{6}\Delta_\mu^{(+)}\Delta_\mu^{(\pm)}\Delta_\mu^{(-)} \tag{2.97}$$

instead. However, at one-loop level, (2.97) still leads to $\mathcal{O}(\alpha_s a^2)$ errors due to radiative corrections. These errors can be reduced by adjusting the coefficient in (2.97), but it is difficult to find the correct value. A simple method of reducing radiative corrections is *tadpole improvement* [77], which is based on the following observation. In lattice perturbation theory, the gauge link $U_\mu(x)$ is given in terms of the vector potential A_μ^{lat} as an expansion in powers of a:

$$U_\mu(x) = 1 + iagA_\mu^{\text{lat}}(x) + \frac{1}{2}(iag)^2\left[A_\mu^{\text{lat}}(x)\right]^2 + ... \tag{2.98}$$

[10] For off-shell quantities, also the interpolating fields in correlation functions must be improved.

[11] Critical slowing down is particularly severe for topological modes, where the autocorrelation time grows rapidly [73], possibly exponentially [74, 75], when a is reduced.

Consider the expectation value

$$u_0 = \frac{1}{N_c} \langle \mathrm{Tr}\, U_\mu \rangle \,, \tag{2.99}$$

(the mean link) defined in Landau gauge. At tree-level, $u_0 = 1$, and the one-loop result is still close to 1, while the nonperturbative result for u_0 is significantly smaller. It turns out that higher-order terms in the expansion (2.98) are actually not suppressed by powers of a, since the contractions of A_μ^{lat} with itself (leading to "tadpole" diagrams) produce UV-divergences proportional to the same power of $1/a$. The large tadpole renormalisations in lattice operators can be taken care of through rescaling the links by a factor of $1/u_0$, where u_0 can be measured nonperturbatively.

Finally, note that for heavy quarks ($am \gtrsim 1$) the usual Symanzik effective theory breaks down. Following [67], we consider operators like $\sum_\mu (-\gamma^\mu D_\mu)^n$ (these describe deviations from Lorentz/Euclidean invariance). The time derivative is of the order of the heavy-quark mass,

$$a^n (-\gamma^0 D_0)^n \Psi \sim (am)^n \Psi, \tag{2.100}$$

and hence powers of a are accompanied by powers of m, spoiling the convergence of the expansion. The physical interpretation is that the lattice can not resolve the Compton wavelength of heavy quarks when the grid is too coarse. Hence, the standard relativistic fermion actions develop large discretisation errors for $am \gtrsim 1$. The discussion of relativistic heavy quarks in lattice QCD will be continued in Sec. 2.8.

2.7.2 Unphysical quark masses

The CPU time in dynamical lattice QCD calculations also grows like some inverse power of the light quark mass, as the condition number of the fermion matrix is proportional to $(am_q)^{-1}$. In addition, lighter quark masses require larger volumes to keep finite-size effects under control (see Sec. 2.7.3). Thus, most present computations are done at larger-than-physical u- and d- quark masses, and extrapolations are required.

For many observables, the functional form of the dependence on the light quark masses can be predicted using chiral perturbation theory (χPT); see e.g. [78, 79] for an introduction. In QCD with N_f massless quarks, the $SU(N_f)_L \times SU(N_f)_R$ chiral flavour symmetry turns out to be spontaneously broken to $SU(N_f)_V$ by a non-zero vacuum expectation value $\langle \overline{q}_R^f q_L^{f'} \rangle = v\delta^{ff'}$. Fluctuations in the vacuum expectation value along the broken symmetry directions, which do not change the potential energy, correspond to $\dim[SU(N_f)] = N_f^2 - 1$ massless Goldstone bosons (pions). One can introduce an effective $SU(N_f)$-valued field

$\Sigma(x) = \exp(2i\Phi/f)$ (with traceless and Hermitian Φ) for them, with Lagrangian

$$\mathcal{L}_{\chi\mathrm{PT}} = \frac{f^2}{8}\,\mathrm{Tr}(\partial_\mu\Sigma\partial^\mu\Sigma^\dagger) \quad + \quad \text{higher order terms.} \tag{2.101}$$

Since the operators in the chiral effective Lagrangian contain derivatives, the contributions from higher-order operators and from loops are suppressed by factors of p^2/f^2. This gives the theory its predictive power.

In nature, the u-, d- and possibly s- quark masses are small enough so that one has an approximate $SU(3)_L \times SU(3)_R$ symmetry. For $N_f = 3$, the field Φ can be parametrised as

$$\Phi = \begin{pmatrix} \pi^0/\sqrt{2} + \eta/\sqrt{6} & \pi^+ & K^+ \\ \pi^- & -\pi^0/\sqrt{2} + \eta/\sqrt{6} & K^0 \\ K^- & \bar{K}^0 & -2\eta/\sqrt{6} \end{pmatrix}. \tag{2.102}$$

To lowest order, non-zero quark masses can be included in the chiral Lagrangian through the term

$$-\frac{f^2}{4}\,B_0\mathrm{Tr}\left[M_q(\Sigma + \Sigma^\dagger)\right], \tag{2.103}$$

where B_0 is a new low-energy coefficient and $M_q = \mathrm{diag}(m_u, m_d, m_s)$. Expanding $\Sigma = \exp(2i\Phi/f)$ around $\Phi = 0$, Eq. (2.103) then gives a trivial constant term and, to quadratic order,

$$\begin{aligned} B_0\mathrm{Tr}\left[M_q\Phi^2\right] \;=\; & B_0\Big[(m_u+m_d)\pi^+\pi^- + (m_u+m_s)K^+K^- + (m_d+m_s)K^0\bar{K}^0 \\ & + \tfrac{1}{6}(4m_s+m_d+m_u)\,\eta\,\eta + \tfrac{1}{\sqrt{3}}(m_u-m_d)\,\eta\,\pi^0 + \tfrac{1}{2}(m_u+m_d)\pi^0\pi^0\Big], \end{aligned} \tag{2.104}$$

from which we can read off the leading-order masses of the 8 pseudo-Goldstone bosons,

$$m^2_{\pi^\pm} = B_0(m_u + m_d), \quad \text{etc.} \tag{2.105}$$

This is a first prediction from χPT. Calculations to order p^4 (this includes one-loop corrections) have been performed in [80]. At order p^4, there are new low-energy coefficients and the results for masses, decay constants etc. include logarithms of the form $\frac{m^2_{PS}}{(4\pi f)^2}\ln(m^2_{PS}/\mu^2)$ where m_{PS} is the mass of a Goldstone boson[12]. Like the chiral logs, the low-energy-coefficients also depend on the scale μ, so that the overall scale-dependence is cancelled.

[12]When dimensional regularisation is used, no power-law divergences appear. When a momentum cutoff (or a lattice) is used as a regulator, the power-law divergences can still be absorbed into the couplings of the given order.

With many lattice actions, chiral symmetry is broken explicitly by lattice artefacts, so that there will be additive terms in (2.105) that do not vanish for $m_q = 0$. The effects of non-zero lattice spacing can be systematically included in the χPT Lagrangian.

Note that it is also possible to study the interactions of (pseudo-)Goldstone bosons with heavy particles (e.g. baryons) in χPT, as long as the momenta of the Goldstone bosons involved are small compared to the scale of chiral symmetry breaking.

2.7.3 Finite-volume effects

As we have seen in Sec. 2.1.1, a finite temporal box size L_τ (with the correct boundary conditions) corresponds to a non-zero temperature. If one is interested in zero-temperature physics, one typically chooses L_τ about 2 - 4 times bigger than the spatial extent L. The dominant finite-volume errors then arise from the finite spatial size.

In a simplistic picture, a single hadron in a periodic box much larger than the hadron itself interacts with the infinite set of its mirror images. The interaction proceeds through the exchange of the lightest excitations, the pions (in computations with dynamical quarks), and so we expect the effect to be suppressed by $e^{-m_\pi L}$.

Finite-volume effects can be studied systematically in chiral perturbation theory, using the same chiral Lagrangian as in infinite volume but performing the effective-theory calculations in the finite box [81, 82]. The pion propagator then has to satisfy the periodic boundary conditions, and can be written as an infinite sum over shifted infinite-volume propagators.

As already mentioned in Sec. 2.2, the effects of finite volume can also be expressed in terms of scattering parameters, and can in turn be used to compute these parameters [36, 37].

2.8 Relativistic heavy quarks on the lattice

As seen in section 2.7.1, the usual relativistic lattice actions develop large discretisation errors when $am \gtrsim 1$. A possible remedy would be to simply reduce the lattice spacing a. For the charm quark, which has $m_c(\mu = m_c) = 1.27^{+0.07}_{-0.11}$ GeV in the $\overline{\text{MS}}$ scheme [83], this is already feasible today, in particular with the help of Symanzik improvement. An example is the Highly Improved Staggered Quark (HISQ) action [84], which allows calculations up to about $am \sim 0.5$. In [85], the HISQ action has been used to make precision calculations of the D and D_s leptonic decay constants. With this approach, the same action can be

used for the charm quarks and the light quarks, and a partially conserved current can be employed to calculate the decay constants.

In [86], the application of the HISQ action to bottom quarks is explored. The b quark mass is $m_b(\mu = m_b) = 4.20^{+0.17}_{-0.07}$ GeV [83]. The MILC collaboration [87] have generated gauge configurations with lattice spacings in the range from $a \approx 0.18$ fm ($a^{-1} \approx 1.1$ GeV) to $a \approx 0.045$ fm ($a^{-1} \approx 4.4$ GeV). Even with HISQ, this is still not fine enough to accommodate the b quark, and extrapolations in m_b are required which lead to additional systematic errors. Given that autocorrelation times grow dramatically as a is reduced [75, 73], it appears that in the near future fine enough lattices with low pion masses and large volumes will not be available.

One option for the inclusion of relativistic b quarks in lattice QCD is to use anisotropic lattices, choosing the temporal lattice spacing a_t much finer than the spatial lattice spacing a_s so that $a_t m \ll 1$ [88, 89]. From Eq. (2.100) one might expect that for heavy-light mesons at rest the errors only appear as powers of $a_t m$. However, it turns out that errors governed by $a_s m$ can still appear [90]. See also [91] for a more recent paper.

Alternatively, one can work with isotropic lattices, but tune the couplings of the temporal and spatial terms in the heavy-quark action separately so that the dispersion relation for the heavy quark is corrected [92]. This is known as the "Fermilab method". Additional higher-dimension operators need to be included in order to achieve good accuracy. The kernel for the simplest action has the form

$$\begin{aligned} K_{\mathrm{FNAL}}(x,\, x') \;=\; & \delta_{x',\,x} - \kappa_t \Big[(1-\gamma^0)U_0(x)\delta_{x',\,x+\hat{0}} + (1+\gamma^0)U_{-0}(x)\delta_{x',\,x-\hat{0}}\Big] \\ & - \kappa_s \sum_{j=1}^{3} \Big[(r_s-\gamma^j)U_j(x)\delta_{x',\,x+\hat{j}} + (r_s+\gamma^j)U_{-j}(x)\delta_{x',\,x-\hat{j}}\Big] \\ & + 2\, c_E\, \kappa_t\, [\gamma^0,\gamma^j]E_j(x)\, \delta_{x',\,x} \;+\; c_B\, \kappa_s\, \epsilon_{jkl}[\gamma^j,\gamma^k]B_l(x)\, \delta_{x',\,x} \end{aligned} \tag{2.106}$$

where for convenience the fields are normalised such that the coefficient of the first Kronecker-delta is 1. In (2.106), E_j and B_j are the chromoelectric and chromomagnetic components of a lattice discretisation of $F_{\mu\nu}$. The bare mass is $am_0 = 1/(2\kappa_t) - 1 - 3r_s\zeta$ with $\zeta = \kappa_s/\kappa_t$. The parameters r_s, ζ, c_E, c_B must be tuned as functions of am_0. Note that for $r_s = \zeta = 1$, $c_E = c_B = 0$, the Fermilab action reduces to the standard Wilson action.

Chapter 3

Effective Lagrangians for heavy quarks

Effective theories for heavy quarks are based on the separation of scales $|\mathbf{k}| \ll m$, where m is the mass of the heavy quark and $|\mathbf{k}|$ is the typical magnitude of the spatial momenta relevant for the system, defined in the rest frame of the hadron containing the heavy quark(s). One important consequence of this separation of scales is that the effects of heavy-quark pair production can be neglected or described by local effective operators. The power counting will be discussed in more detail in Sec. 3.2. It turns out to be different for hadrons containing more than one and hadrons containing only one heavy quark.

Heavy-quark effective theories can be used to analyse the behaviour of Wilson-like lattice fermion actions in the large-mass limit [93, 94, 95]. Alternatively, one can directly use a discretisation of a nonrelativistic effective Lagrangian to describe heavy quarks on the lattice. The latter method is used in this dissertation.

In this chapter, I shall review the derivation of the standard heavy-quark effective Lagrangians in the continuum. I will then perform an independent derivation of a "moving nonrelativistic QCD" (mNRQCD) Lagrangian, obtaining a new result slightly different from that reported previously in the literature. Two approaches to the lattice discretisation of heavy-quark effective theories will then be discussed in Chapters 4 and 5.

One way to derive an effective Lagrangian is to write down all local operators compatible with the symmetries and required for the physical system under consideration. The short-distance coefficients of the operators are adjusted so that the effective theory and QCD give the same results for on-shell physical observables to the given order. This approach is applied to heavy quarkonia in [9, 10] and goes back to [96]. If performed cor-

rectly, it has the advantage that no operators are missed out, but the method is technically not so straightforward.

Another derivation of a continuum effective Lagrangian, appropriate to heavy-light systems, is to "integrate out" the antiquark components of the theory in the path integral approach [97]. This is usually done at tree-level only, and a matching to full QCD is performed afterwards.

Here I will use the method of the Foldy-Wouthuysen-Tani (FWT) transformation, following [98], where the effective Lagrangian is obtained via a field transformation. This is a systematic procedure, which gives all operators bilinear in the heavy-quark fields together with their tree-level coefficients. By construction, it also gives the tree-level relation between the heavy quark fields in QCD and the ones in the effective Lagrangian.

3.1 Foldy-Wouthuysen-Tani transformation

In this section we derive a classical (tree-level) continuum effective Lagrangian for heavy quarks order by order in $1/m$ via the Foldy-Wouthuysen-Tani (FWT) transformation, which decouples the particle- and antiparticle components in the Dirac Lagrangian to a given order[1]. The particle/antiparticle projectors are

$$P_\pm = \frac{1}{2}(1 \pm \hat{\gamma}^0), \tag{3.1}$$

and hence the transformation should remove all terms from the Lagrangian that do not commute with $\hat{\gamma}^0$. In the following, we work in Minkowski space. Writing the Dirac Lagrange density as

$$\mathcal{L} = \overline{\Psi}(-m + i\hat{\gamma}^0 D_0 + i\hat{\gamma}^j D_j)\Psi, \tag{3.2}$$

we see that we must aim to cancel the $i\hat{\gamma}^j D_j$ term. To this end, we introduce the field redefinition

$$\begin{aligned} \Psi &= \exp\left(\frac{1}{2m}\, i\hat{\gamma}^j D_j\right) \Psi_{(1)}, \\ \overline{\Psi} &= \overline{\Psi}_{(1)} \exp\left(\frac{1}{2m}\, i\hat{\gamma}^j D_j\right) = \overline{\Psi}_{(1)} \exp\left(-\frac{1}{2m}\, i\hat{\gamma}^j \overleftarrow{D}_j\right), \end{aligned} \tag{3.3}$$

[1]The expansion parameter $1/m$ is purely formal at this stage. It turns out that for heavy-light hadrons, the expansion really is in $\Lambda_{\rm QCD}/m$ (cf. Sec. 3.2), and consequently the FWT method is particularly convenient for these. The method is also correct for heavy-heavy mesons, but there the power counting is different.

which does indeed cancel $i\hat{\gamma}^j D_j$, but also results in an infinite set of additional terms with higher powers of $1/m$. In terms of the new field $\Psi_{(1)}$, the Lagrangian reads

$$\mathcal{L} = \overline{\Psi}_{(1)}(-m + i\hat{\gamma}^0 D_0)\Psi_{(1)} + \sum_{n=1}^{\infty} \frac{1}{m^n} \overline{\Psi}_{(1)}\, O_{(1)n}\, \Psi_{(1)}. \tag{3.4}$$

The new terms $O_{(1)n}$ $(n \geq 1)$ still contain pieces with odd powers of spatial gamma matrices and thus do not commute with $\hat{\gamma}^0$. The order $1/m$ term is given by

$$\begin{aligned} O_{(1)1} &= -\frac{1}{2} D_j D^j - \frac{ig}{8}[\hat{\gamma}^\mu, \hat{\gamma}^\nu] F_{\mu\nu} \\ &= \underbrace{-\frac{1}{2} D_j D^j - \frac{ig}{8}[\hat{\gamma}^j, \hat{\gamma}^k] F_{jk}}_{=O^C_{(1)1}} \quad \underbrace{-\frac{ig}{2}\hat{\gamma}^j \hat{\gamma}^0 F_{j0}}_{=O^A_{(1)1}}. \end{aligned} \tag{3.5}$$

Here, we wrote $O_{(1)1} = O^C_{(1)1} + O^A_{(1)1}$, with $\left[O^C_{(1)1}\,,\ \hat{\gamma}^0\right] = 0$ and $\left\{O^A_{(1)1}\,,\ \hat{\gamma}^0\right\} = 0$. The anticommuting part $O^A_{(1)1}$ can now be cancelled by a second field redefinition, similar to (3.3),

$$\begin{aligned} \Psi_{(1)} &= \exp\left(\frac{1}{2m^2} O^A_{(1)1}\right) \Psi_{(2)}, \\ \overline{\Psi}_{(1)} &= \overline{\Psi}_{(2)} \exp\left(\frac{1}{2m^2} O^A_{(1)1}\right), \end{aligned} \tag{3.6}$$

which results in

$$\mathcal{L} = \overline{\Psi}_{(2)}(-m + i\hat{\gamma}^0 D_0)\Psi_{(2)} + \sum_{n=1}^{\infty} \frac{1}{m^n} \overline{\Psi}_{(2)}\, O_{(2)n}\, \Psi_{(2)} \tag{3.7}$$

with

$$\begin{aligned} O^C_{(2)1} &= O^C_{(1)1}, \\ O^A_{(2)1} &= 0, \\ O^C_{(2)2} &= -\frac{g}{8}\hat{\gamma}^0 \left(D^{\mathrm{ad}}_j F_{j0} - \frac{1}{2}[\hat{\gamma}^j,\, \hat{\gamma}^k]\,\{D_j,\, F_{k0}\}\right), \\ O^A_{(2)2} &= -\frac{i}{3}\hat{\gamma}^j \hat{\gamma}^k \hat{\gamma}^l D_j D_k D_l - \frac{g}{4}\hat{\gamma}^j [D_0, F_{j0}]. \end{aligned} \tag{3.8}$$

Next, to cancel $O^A_{(2)2}$, we write

$$\begin{aligned} \Psi_{(2)} &= \exp\left(\frac{1}{2m^3} O^A_{(2)2}\right) \Psi_{(3)}, \\ \overline{\Psi}_{(2)} &= \overline{\Psi}_{(3)} \exp\left(\frac{1}{2m^3} O^A_{(2)2}\right). \end{aligned} \tag{3.9}$$

The Lagrangian becomes

$$\mathcal{L} = \overline{\Psi}_{(3)}(-m + i\hat{\gamma}^0 D_0)\Psi_{(3)} + \sum_{n=1}^{\infty} \frac{1}{m^n} \overline{\Psi}_{(3)}\, O_{(3)n}\, \Psi_{(3)} \tag{3.10}$$

with

$$\begin{aligned} O^C_{(3)1} &= O^C_{(2)1}, \\ O^A_{(3)1} &= 0, \\ O^C_{(3)2} &= O^C_{(2)2}, \\ O^A_{(3)2} &= 0. \end{aligned} \tag{3.11}$$

Clearly, this procedure can be repeated to remove the $\hat{\gamma}^0$-anticommuting terms to arbitrarily high but finite order in $1/m$. Note that no additional time derivatives are introduced. We will only keep the terms up to order $1/m^2$ now.

As these terms commute with $\hat{\gamma}^0$ and there are no time derivatives other than $i\hat{\gamma}^0 D_0$, we can now remove the mass term[2] from the Lagrangian by redefining

$$\begin{aligned} \Psi_{(3)} &= \exp\left(-imx^0\hat{\gamma}^0\right)\tilde{\Psi}, \\ \overline{\Psi}_{(3)} &= \overline{\tilde{\Psi}} \exp\left(imx^0\hat{\gamma}^0\right). \end{aligned} \tag{3.12}$$

The resulting Lagrangian is

$$\begin{aligned} \mathcal{L} &= \overline{\tilde{\Psi}} \Bigg[i\hat{\gamma}^0 D_0 - \frac{1}{2m} D_j D^j - \frac{ig}{8m}[\hat{\gamma}^j, \hat{\gamma}^k] F_{jk} \\ &\quad - \frac{g}{8m^2}\hat{\gamma}^0 \left(D^{\mathrm{ad}}_j F_{j0} - \frac{1}{2}[\hat{\gamma}^j,\, \hat{\gamma}^k]\, \{D_j,\, F_{k0}\} \right) \Bigg] \tilde{\Psi} \;+\; \mathcal{O}(1/m^3). \end{aligned} \tag{3.13}$$

Using $[\hat{\gamma}^j, \hat{\gamma}^k] = -2i\epsilon_{jkl}\Sigma^l$ with

$$\Sigma^j \equiv \begin{pmatrix} \sigma^j & 0 \\ 0 & \sigma^j \end{pmatrix}, \tag{3.14}$$

and defining the chromoelectric and chromomagnetic components of the gluon field strength tensor as $E_j = F_{0j}$ and $B_j = -\frac{1}{2}\epsilon_{jkl}F_{kl}$, we obtain

$$\begin{aligned} \mathcal{L} &= \overline{\tilde{\Psi}} \left[i\hat{\gamma}^0 D_0 + \frac{\mathbf{D}^2}{2m} + \frac{g}{2m}\boldsymbol{\Sigma}\cdot\mathbf{B} + \frac{g}{8m^2}\hat{\gamma}^0 \left(\mathbf{D}^{\mathrm{ad}}\cdot\mathbf{E} + i\boldsymbol{\Sigma}\cdot(\mathbf{D}\times\mathbf{E} - \mathbf{E}\times\mathbf{D}) \right) \right] \tilde{\Psi} \\ &\quad + \mathcal{O}(1/m^3). \end{aligned} \tag{3.15}$$

[2]This step is not really necessary, since the mass term only corresponds to a trivial shift in the energy. In fact, a mass term is generated as a counterterm through renormalisation.

For later reference, we also summarise the field transformation:

$$\Psi(x) = T_{\rm FWT}\, e^{-imx^0\hat{\gamma}^0}\, \tilde{\Psi}(x) \tag{3.16}$$

with

$$\begin{aligned} T_{\rm FWT} \;=\;& \exp\left[\frac{1}{2m}\,(i\hat{\boldsymbol{\gamma}}\cdot\mathbf{D})\right] \\ & \times \exp\left[\frac{1}{2m^2}\left(-\frac{ig}{2}\hat{\gamma}^0\hat{\boldsymbol{\gamma}}\cdot\mathbf{E}\right)\right] \\ & \times \exp\left[\frac{1}{2m^3}\left(\frac{g}{4}\hat{\boldsymbol{\gamma}}\cdot(D_0^{\rm ad}\mathbf{E}) + \frac{1}{3}\,(i\hat{\boldsymbol{\gamma}}\cdot\mathbf{D})^3\right)\right] \\ & \times \left[1+\mathcal{O}(1/m^4)\right]. \end{aligned} \tag{3.17}$$

Next, introducing two-component fields ψ and ξ as

$$\tilde{\Psi} = \begin{pmatrix} \psi \\ \xi \end{pmatrix}, \qquad \overline{\tilde{\Psi}} = \left(\psi^\dagger, \quad -\xi^\dagger\right), \tag{3.18}$$

we find that the Lagrangian (3.15) can be written as

$$\begin{aligned} \mathcal{L} \;=\;& \psi^\dagger\left[iD_0 + \frac{\mathbf{D}^2}{2m} + \frac{g}{2m}\boldsymbol{\sigma}\cdot\mathbf{B} + \frac{g}{8m^2}\left(\mathbf{D}^{\rm ad}\cdot\mathbf{E} + i\boldsymbol{\sigma}\cdot(\mathbf{D}\times\mathbf{E} - \mathbf{E}\times\mathbf{D})\right)\right]\psi \\ +\;& \xi^\dagger\left[iD_0 - \frac{\mathbf{D}^2}{2m} - \frac{g}{2m}\boldsymbol{\sigma}\cdot\mathbf{B} + \frac{g}{8m^2}\left(\mathbf{D}^{\rm ad}\cdot\mathbf{E} + i\boldsymbol{\sigma}\cdot(\mathbf{D}\times\mathbf{E} - \mathbf{E}\times\mathbf{D})\right)\right]\xi \\ +\;& \mathcal{O}(1/m^3). \end{aligned} \tag{3.19}$$

As desired, the quark field ψ and the antiquark field ξ are separated. In our conventions, the field operator related to ψ annihilates a quark, whereas the field operator related to ξ creates an antiquark. Note that the antiquark action $S_\xi = \int \mathcal{L}_\xi\, \mathrm{d}^4x$ can be obtained from the quark action $S_\psi = \int \mathcal{L}_\psi\, \mathrm{d}^4x$ by making the following replacements:

$$\begin{aligned} \psi &\;\mapsto\; (\xi^\dagger)^T, \\ \psi^\dagger &\;\mapsto\; (\xi)^T, \\ iA_\mu &\;\mapsto\; (iA_\mu)^* = -\,(A_\mu)^T, \\ iE_j &\;\mapsto\; (iE_j)^* = -\,(E_j)^T, \\ iB_j &\;\mapsto\; (iB_j)^* = -\,(B_j)^T, \\ i\sigma^j &\;\mapsto\; \left(i\sigma^j\right)^* = -\left(\sigma^j\right)^T, \end{aligned} \tag{3.20}$$

where ^{T} denotes the transpose (in colour and/or spin space) and * complex conjugation, i.e. the antiquark field transforms under the complex conjugate representations in colour

and spin space. To see this, integrate by parts and take the transpose of the entire action (the latter also introduces an overall minus sign, since the Grassmann-valued fields ξ and $\xi^\dagger$ are interchanged).

It is important to make the following remark: In the quantum field theory functional integral, one integrates over arbitrary non-smooth fields. However, the FWT transformations e.g. contain derivative operators acting on these fields. Of course, the path integral is only defined with an ultraviolet regulator such as the lattice, but one can not expect that the field transformations commute with the UV regularisation and renormalisation. The form of the local operators obtained through the FWT transformation is still correct, but after (lattice) regularisation their coefficients must be renormalised away from their tree-level values to take into account the short-distance (UV) effects.

The derivation given here also misses out operators which are not bilinear in the heavy-quark fields, like four-fermion operators of the form

$$\psi^\dagger \, \xi \, \xi^\dagger \, \psi. \tag{3.21}$$

In perturbation theory, these operators arise at 1-loop level and therefore have coefficients suppressed by an additional factor of α_s^2 [10]. Hence, these operators are far less important than the bilinear operators, and can be neglected here.

3.2 Power counting and heavy-quark symmetries

3.2.1 Heavy-light hadrons

For mesons and baryons containing only a single heavy quark, the light degrees of freedom are governed by the nonperturbative gluon dynamics and are thus characterised by the scale $\Lambda_{\rm QCD}$. It follows that the typical momentum transfer between the heavy quark and the light degrees of freedom is also of order $\Lambda_{\rm QCD}$. Thus, if the hadron is at rest, the covariant derivative acting on the effective heavy-quark field is of order

$$|D_0| \sim |\mathbf{D}| \sim \Lambda_{\rm QCD}. \tag{3.22}$$

The gluon gauge potential is also determined by the light degrees of freedom, and hence, in a smooth gauge,

$$|gA_0| \sim |g\,\mathbf{A}| \sim \Lambda_{\rm QCD} \tag{3.23}$$

and

$$|g\,\mathbf{E}| \sim \Lambda_{\rm QCD}^2, \qquad |g\,\mathbf{B}| \sim \Lambda_{\rm QCD}^2. \tag{3.24}$$

By simple dimensional analysis it follows that for a heavy-light hadron at rest a term in the Lagrangian that comes with $1/m^n$ will be suppressed by a factor of

$$\left(\frac{\Lambda_{\rm QCD}}{m}\right)^n \tag{3.25}$$

relative to the leading term. Consequently, (3.19) is accurate up to corrections of order $(\Lambda_{\rm QCD}/m)^3$. In the *static limit*

$$m \to \infty \tag{3.26}$$

the effective Lagrangian (3.19) therefore reduces to

$$\mathcal{L} = \psi^\dagger \, iD_0 \, \psi, \tag{3.27}$$

(here we have set $\xi = 0$) and the heavy quark only acts as a static colour source. It is now obvious that the physics of the heavy-light hadron in this limit does not depend on the flavour or the spin of the heavy quark. This leads to the *heavy-quark flavour symmetry* and the *heavy-quark spin symmetry* [99, 97], which are broken by corrections proportional to $\Lambda_{\rm QCD}/m$ (the flavour symmetry breaking is proportional to $\Lambda_{\rm QCD}/m_1 - \Lambda_{\rm QCD}/m_2$ for two heavy-light hadrons with heavy quark masses m_1 and m_2).

3.2.2 Heavy-heavy mesons

The situation is different for heavy-heavy mesons (quarkonia). Naively speaking, the heavy quark and antiquark orbit around their centre of mass with some velocity $v_{\rm orb.}$. For bottomonium one has $v_{\rm orb.}^2 \approx 0.1$ and for charmonium $v_{\rm orb.}^2 \approx 0.3$ [9]. These estimates are obtained by assuming that the average kinetic energy is of the order of the $2S-1S$ energy splitting; the values for $v_{\rm orb.}^2$ calculated in this way are consistent with predictions from potential models.

The spatial momentum and the kinetic energy of the orbital motion are of order

$$|\mathbf{k}| \sim m \, v_{\rm orb.}, \qquad E_{\rm kin} \sim m \, v_{\rm orb.}^2. \tag{3.28}$$

It follows that the spatial covariant derivative acting on the heavy-quark field is of size

$$|\mathbf{D}| \sim m \, v_{\rm orb.}. \tag{3.29}$$

At the short distances relevant for quarkonium, the quark-antiquark potential is similar to the Coulomb potential. Thus, the kinetic energy is of the same order of magnitude as the potential energy, and so we have (in Coulomb gauge)

$$|g \, A_0| \sim |D_0| \sim E_{\rm kin} \sim m \, v_{\rm orb.}^2. \tag{3.30}$$

Using the Yang-Mills equations, one can then show [10] that the vector potential is of order

$$|g\,\mathbf{A}| \sim m\,v_{\text{orb.}}^3, \tag{3.31}$$

and hence

$$|g\,\mathbf{E}| \sim m^2 v_{\text{orb.}}^3, \qquad |g\,\mathbf{B}| \sim m^2 v_{\text{orb.}}^4. \tag{3.32}$$

We now see that the individual terms in the effective Lagrangian are suppressed by various powers of the internal velocity $v_{\text{orb.}}$, and this is the correct expansion parameter. All terms in (3.15) are of order $v_{\text{orb.}}^4$ or lower powers of $v_{\text{orb.}}$, but one term of order $v_{\text{orb.}}^4$ is missing. By expanding the expression for the relativistic kinetic energy in powers of the momentum $\mathbf{k}$,

$$\begin{aligned} E_{\text{kin}} &= \sqrt{\mathbf{k}^2 + m^2} - m \\ &= \frac{\mathbf{k}^2}{2m} - \frac{\mathbf{k}^4}{8m^3} + \frac{\mathbf{k}^6}{16m^5} - ... \end{aligned} \tag{3.33}$$

we see that we must include the term

$$\mathcal{L}_{\text{kin},m^{-3}} = \overline{\tilde{\Psi}}\,\frac{\mathbf{D}^4}{8m^3}\tilde{\Psi} \tag{3.34}$$

into the Lagrangian to obtain accuracy to order $v_{\text{orb.}}^4$. For more details of the heavy-heavy power counting, see [10].

3.3 Generalisation to a moving frame of reference

The effective Lagrangian obtained in section 3.1 can be used to describe a heavy quark with small spatial momentum $\mathbf{k}$, that is $|\mathbf{k}| \ll m$. Note that the *total* 4-momentum p_μ can be written in terms of the *residual* momentum k_μ as

$$p_\mu = m\,u_\mu + k_\mu \tag{3.35}$$

with the trivial 4-velocity $u = (1, 0, 0, 0)$. We will now work in a Lorentz-boosted frame of reference moving with an arbitrary velocity $\mathbf{v}$ so that $u = (\gamma,\, \gamma\mathbf{v})$ with $\gamma = 1/\sqrt{1-\mathbf{v}^2}$. Under the coordinate transformation

$$x'^\mu = \Lambda^\mu{}_\nu x^\nu, \tag{3.36}$$

the original Dirac field in (3.2) transforms as follows:

$$\Psi'(x') = S(\Lambda)\Psi(x), \tag{3.37}$$

where $S(\Lambda)$ is the Dirac-spinor representation of Λ. Writing $\Psi(x)$ in terms of the effective field $\tilde{\Psi}(x)$ using (3.16), we get

$$\Psi'(x') = S(\Lambda) \exp\left(\frac{1}{2m}\, i\hat{\gamma}^j D_j\right) \,...\, \exp\left(-imx^0\hat{\gamma}^0\right) \tilde{\Psi}(x), \tag{3.38}$$

where the ellipsis indicates the higher-order parts of the FWT transformation. Using

$$S(\Lambda)\, \hat{\gamma}^\mu = (\Lambda^{-1})^\mu{}_\nu\, \hat{\gamma}^\nu\, S(\Lambda), \tag{3.39}$$

the matrix $S(\Lambda)$ in (3.38) can be moved to the right:

$$\Psi'(x') = \exp\left(\frac{1}{2m}\, i(\Lambda^{-1})^j{}_\mu \hat{\gamma}^\mu D_j\right) \,...\, \exp\left(-imx^0(\Lambda^{-1})^0{}_\nu\hat{\gamma}^\nu\right)\; S(\Lambda)\, \tilde{\Psi}(x). \tag{3.40}$$

Next, we define a new field

$$\tilde{\Psi}'(x') \equiv S(\Lambda)\, \tilde{\Psi}(x), \tag{3.41}$$

and express (3.40) in terms of the coordinates x'. This finally gives

$$\begin{aligned}
\Psi'(x') &= \exp\left(\frac{1}{2m}\, i(\Lambda^{-1})^j{}_\mu \hat{\gamma}^\mu \Lambda^\nu{}_j D'_\nu\right) \,...\, \exp\left(-im\Lambda^0{}_\lambda x'^\lambda (\Lambda^{-1})^0{}_\rho \hat{\gamma}^\rho\right)\; \tilde{\Psi}'(x') \\
&= \exp\left(\frac{1}{2m}\, i(\not{D}' - \not{u}\, u\cdot D')\right) \,...\, \exp\left(-im\, u\cdot x'\; \not{u}\right)\; \tilde{\Psi}'(x'),
\end{aligned} \tag{3.42}$$

where $\not{u} \equiv u_\mu\hat{\gamma}^\mu$. In terms of the new field $\tilde{\Psi}'(x')$, the effective Lagrangian (3.13) reads, through order $1/m$,

$$\begin{aligned}
\mathcal{L} &= \overline{\tilde{\Psi}}\left(i\hat{\gamma}^0 D_0 - \frac{1}{2m} D_j D^j - \frac{ig}{8m}[\hat{\gamma}^j,\hat{\gamma}^k]F_{jk}\right)\tilde{\Psi} \\
&= \overline{\tilde{\Psi}'}\; S(\Lambda)\left(i\hat{\gamma}^0\Lambda^\mu{}_0 D'_\mu - \frac{1}{2m}\Lambda^\mu{}_j\Lambda^j{}_\nu D'_\mu D'^\nu - \frac{ig}{8m}[\hat{\gamma}^j,\hat{\gamma}^k]\Lambda^\mu{}_j\Lambda^\nu{}_k F'_{\mu\nu}\right) S^{-1}(\Lambda)\; \tilde{\Psi}' \\
&= \overline{\tilde{\Psi}'}\left(i\,\not{u}\, u\cdot D' - \frac{D'^2_\perp}{2m} - \frac{1}{4m}[\hat{\gamma}_\mu,\hat{\gamma}_\nu]D'^\mu_\perp D'^\nu_\perp\right)\tilde{\Psi}' \\
&= \overline{\tilde{\Psi}'}\left(i\,\not{u}\, u\cdot D' - \frac{\not{D}'^2_\perp}{2m}\right)\tilde{\Psi}'.
\end{aligned} \tag{3.43}$$

Here we have used the notation

$$D'^\mu_\perp \;\equiv\; D'^\mu - u^\mu\; u\cdot D'. \tag{3.44}$$

To separate the particle- and antiparticle components in (3.43), we now have to use the boosted projectors

$$P^{(u)}_\pm = S(\Lambda)\, P_\pm\, S^{-1}(\Lambda) = \frac{1 \pm \not{u}}{2}. \tag{3.45}$$

Defining $\tilde{\Psi}'_\pm \equiv P^{(u)}_\pm \tilde{\Psi}'$, we obtain

$$\mathcal{L} \;=\; \overline{\tilde{\Psi}'_+}\left(+i\,u\cdot D' - \frac{\not{D}'^2_\perp}{2m}\right)\tilde{\Psi}'_+ \;+\; \overline{\tilde{\Psi}'_-}\left(-i\,u\cdot D' - \frac{\not{D}'^2_\perp}{2m}\right)\tilde{\Psi}'_- \;+\; \mathcal{O}(1/m). \qquad (3.46)$$

The part with $\tilde{\Psi}'_+$ in (3.46) is the standard continuum HQET (heavy-quark effective theory) Lagrangian for a non-zero frame velocity [97].

3.4 Moving NRQCD Lagrangian

As a consequence of the Lorentz boost, the terms in the Lagrangian (3.43) commute with $\not{u}'$ rather than γ^0 and the spatial derivatives are now accompanied by temporal derivatives. For applications in lattice QCD, it is more convenient to introduce a different form of the boosted Lagrangian that retains commutativity with γ^0 and does not contain time derivatives in the $1/m$ correction terms [19, 20]. This formalism is called *Moving nonrelativistic QCD* (mNRQCD).

The commutativity with γ^0 can be restored by simply removing the factor $S(\Lambda)$ in the definition of the field $\tilde{\Psi}'$, Eq. (3.41), so that

$$\tilde{\Psi}'(x') \equiv \tilde{\Psi}(x). \qquad (3.47)$$

The relation between Ψ' and $\tilde{\Psi}'$ then reads

$$\Psi'(x') = S(\Lambda)\,\exp\left(\frac{1}{2m}\,i\gamma^j\Lambda^\mu{}_j D'_\mu\right)\,\ldots\,\exp\left(-im\,u\cdot x'\,\gamma^0\right)\tilde{\Psi}'(x'), \qquad (3.48)$$

and the Lagrangian becomes

$$\begin{aligned}\mathcal{L} \;=\; & \overline{\tilde{\Psi}'}\Bigg[i\gamma^0 u\cdot D' + \frac{(u\cdot D')^2 - D'^2}{2m} - \frac{ig}{8m}[\gamma^j,\gamma^k]\Lambda^\rho{}_j\Lambda^\sigma{}_k F'_{\rho\sigma} \\ & -\frac{g}{8m^2}\gamma^0\left(\Lambda^\nu{}_j\Lambda^\rho{}_j u^\sigma (D'^{\mathrm{ad}}_\nu F'_{\rho\sigma}) - \frac{1}{2}[\gamma^j,\,\gamma^k]\Lambda^\nu{}_j\Lambda^\rho{}_k u^\sigma\left\{D'_\nu,\,F'_{\rho\sigma}\right\}\right)\Bigg]\tilde{\Psi}' \\ & +\; \mathcal{O}(1/m^3). \end{aligned} \qquad (3.49)$$

Since we will work exclusively in the x' frame from now on, it is convenient to rename the coordinates such that

$$\begin{aligned} x' \;&\to\; x \\ x \;&\to\; x'. \end{aligned} \qquad (3.50)$$

This means that in (3.49) we rename $\tilde{\Psi}' \to \tilde{\Psi}$, $\overline{\tilde{\Psi}'} \to \overline{\tilde{\Psi}}$, $D'_\mu \to D_\mu$, $F'_{\mu\nu} \to F_{\mu\nu}$. With the new notation and after some additional algebraic steps we have

$$\begin{aligned}\mathcal{L} &= \overline{\tilde{\Psi}}\Big[i\hat{\gamma}^0 u\cdot D + \frac{(u\cdot D)^2 - D^2}{2m} + \frac{g}{2m}\mathbf{\Sigma}\cdot\mathbf{B}' \\ &\quad + \frac{g}{8m^2}\hat{\gamma}^0\left(D^{\rm ad}_\mu u_\nu F^{\mu\nu} + i\epsilon_{jkl}\Sigma^j\Lambda^\mu{}_k\left\{D_\mu,\, E'_l\right\}\right)\Big]\tilde{\Psi} \\ &\quad + \mathcal{O}(1/m^3). \end{aligned} \tag{3.51}$$

Here, we wrote $B'_j = -\frac{1}{2}\epsilon_{jkl}\Lambda^\mu{}_k\Lambda^\nu{}_l F_{\mu\nu}$ and $E'_j = \Lambda^\mu{}_j u^\nu F_{\mu\nu}$ where convenient to simplify the notation. In terms of the fields B_j and E_j, these relations read

$$\begin{aligned}\mathbf{B}' &= \gamma\left(\mathbf{B} - \mathbf{v}\times\mathbf{E} - \frac{\gamma}{1+\gamma}\mathbf{v}\,(\mathbf{v}\cdot\mathbf{B})\right), \\ \mathbf{E}' &= \gamma\left(\mathbf{E} + \mathbf{v}\times\mathbf{B} - \frac{\gamma}{1+\gamma}\mathbf{v}\,(\mathbf{v}\cdot\mathbf{E})\right). \end{aligned} \tag{3.52}$$

We now need to eliminate the time derivatives in the operators of order $1/m$ and $1/m^2$ in (3.51). This can be done via further field redefinitions [19, 22].

It is convenient to write the Lagrangian (3.51) in the following form,

$$\mathcal{L} = \gamma\,\overline{\tilde{\Psi}}\left[O_0 + \frac{1}{\gamma m}O_1 + \frac{1}{(\gamma m)^2}O_2\right]\tilde{\Psi} + \mathcal{O}(1/m^3), \tag{3.53}$$

with

$$\begin{aligned} O_0 &= i\hat{\gamma}^0(D_0 + \mathbf{v}\cdot\mathbf{D}), \\ O_1 &= \frac{1}{2}\left((u\cdot D)^2 - D^2\right) + \frac{g}{2}\mathbf{\Sigma}\cdot\mathbf{B}', \\ O_2 &= \frac{g}{8}\gamma\,\hat{\gamma}^0\left(D^{\rm ad}_\mu u_\nu F^{\mu\nu} + i\epsilon_{jkl}\Sigma^j\Lambda^\mu{}_k\left\{D_\mu,\, E'_l\right\}\right). \end{aligned} \tag{3.54}$$

We start by removing the time derivatives in O_1. To see how this can be done, we note that any field redefinition of the form

$$\begin{aligned}\tilde{\Psi} &= \exp\left(\frac{1}{\gamma m}U\right)\tilde{\Psi}_{(1)}, \\ \overline{\tilde{\Psi}} &= \overline{\tilde{\Psi}}_{(1)}\exp\left(\frac{1}{\gamma m}U\right), \end{aligned} \tag{3.55}$$

will result in

$$\mathcal{L} = \gamma\,\overline{\tilde{\Psi}}_{(1)}\left[O_0 + \frac{1}{\gamma m}O_{(1)1} + \frac{1}{(\gamma m)^2}O_{(1)2}\right]\tilde{\Psi}_{(1)} + \mathcal{O}(1/m^3), \tag{3.56}$$

with the new operators

$$\begin{aligned} O_{(1)1} &= O_1 + \{U,\, O_0\}\,, \\ O_{(1)2} &= O_2 + \{U,\, O_1\} + UO_0U + \frac{1}{2}\left\{U^2,\, O_0\right\}. \end{aligned} \tag{3.57}$$

Thus, we need to write $O_1 = O_{(1)1} - \{U,\, O_0\}$ with some operator U such that $O_{(1)1}$ does not contain time derivatives. This is indeed possible,

$$\begin{aligned} O_1 &= \frac{1}{2}\left[\gamma^2 D_0^2 + \gamma^2\left\{D_0,\, \mathbf{v}\cdot\mathbf{D}\right\} + \gamma^2(\mathbf{v}\cdot\mathbf{D})^2 - D_0^2 + \mathbf{D}^2\right] + \frac{g}{2}\boldsymbol{\Sigma}\cdot\mathbf{B}' \\ &= \underbrace{\frac{1}{2}\left[\mathbf{D}^2 - (\mathbf{v}\cdot\mathbf{D})^2\right] + \frac{g}{2}\boldsymbol{\Sigma}\cdot\mathbf{B}'}_{\equiv\, O_{(1)1}} \\ &\quad + \underbrace{\frac{1}{2}\left[(\gamma^2-1)D_0^2 + \gamma^2\left\{D_0,\, \mathbf{v}\cdot\mathbf{D}\right\} + (\gamma^2+1)(\mathbf{v}\cdot\mathbf{D})^2\right]}_{=\, -\,\{U,\, O_0\}}, \end{aligned} \tag{3.58}$$

and we can now read off the operator U:

$$U = \frac{i}{4}\hat{\gamma}^0\left[(\gamma^2-1)D_0 + (\gamma^2+1)\mathbf{v}\cdot\mathbf{D}\right]. \tag{3.59}$$

The next step is to remove the time derivatives (other than the adjoint time derivative, which acts on the gluon field strength only) in the new operator $O_{(1)2}$, given in (3.57).

Similarly to before, we use a field redefinition

$$\begin{aligned} \tilde{\Psi}_{(1)} &= \exp\left(\frac{1}{(\gamma m)^2}V\right)\tilde{\Psi}_{(2)}, \\ \overline{\tilde{\Psi}}_{(1)} &= \overline{\tilde{\Psi}}_{(2)}\exp\left(\frac{1}{(\gamma m)^2}V\right), \end{aligned} \tag{3.60}$$

now with an extra power of $1/(\gamma m)$, so that the lower order terms are unaffected. The transformation (3.60) results in

$$\mathcal{L} = \gamma\,\overline{\tilde{\Psi}}_{(2)}\left[O_0 + \frac{1}{\gamma m}O_{(2)1} + \frac{1}{(\gamma m)^2}O_{(2)2}\right]\tilde{\Psi}_{(2)} + \mathcal{O}(1/m^3) \tag{3.61}$$

with

$$\begin{aligned} O_{(2)1} &= O_{(1)1}, \\ O_{(2)2} &= O_{(1)2} + \{V,\, O_0\}\,. \end{aligned} \tag{3.62}$$

We need to write $O_{(1)2} = O_{(2)2} - \{V,\, O_0\}$ with some operator V such that $O_{(2)2}$ does not contain time derivatives. We will treat the terms in $O_{(1)2}$ (Eq. (3.57)) individually. Note

that the last term, $-\left\{-\frac{1}{2}U^2,\, O_0\right\}$, is already in the desired form. The time-derivative in the original O_2, defined in (3.54), can be treated as follows:

$$\begin{aligned}\frac{ig}{8}\gamma\,\hat{\gamma}^0\epsilon_{jkl}\Sigma^j\Lambda^0{}_k\left\{D_0,\, E_l'\right\} &= -\frac{ig}{8}\gamma\,\hat{\gamma}^0\epsilon_{jkl}\Sigma^j\Lambda^0{}_k\left\{\mathbf{v}\cdot\mathbf{D},\, E_l'\right\}\\ &\quad -\left\{-\frac{g}{8}\gamma\,\epsilon_{jkl}\Sigma^j\Lambda^0{}_k E_l',\;\; O_0\right\}. \end{aligned} \tag{3.63}$$

Next, using

$$U = \frac{1}{4}(\gamma^2-1)O_0 + \frac{i}{2}\hat{\gamma}^0\,\mathbf{v}\cdot\mathbf{D} \tag{3.64}$$

we obtain

$$\begin{aligned} UO_0U &= \frac{1}{2}\left\{U^2,\, O_0\right\} + \frac{1}{2}\left[U,\, [O_0,\, U]\right]\\ &= \frac{1}{2}\left\{U^2,\, O_0\right\} + \frac{1}{2}\left[U,\, \left[O_0,\, \frac{1}{4}(\gamma^2-1)O_0 + \frac{i}{2}\hat{\gamma}^0\,\mathbf{v}\cdot\mathbf{D}\right]\right]\\ &= \frac{1}{2}\left\{U^2,\, O_0\right\} + \frac{1}{2}\left[U,\, \left[i\hat{\gamma}^0(D_0+\mathbf{v}\cdot\mathbf{D}),\, \frac{i}{2}\hat{\gamma}^0\,\mathbf{v}\cdot\mathbf{D}\right]\right]\\ &= \frac{1}{2}\left\{U^2,\, O_0\right\} - \frac{1}{4}\left[U,\, [D_0, \mathbf{v}\cdot\mathbf{D}]\right]\\ &= \frac{1}{2}\left\{U^2,\, O_0\right\} - \frac{i}{16}\left[\hat{\gamma}^0\left((\gamma^2-1)D_0 + (\gamma^2+1)\mathbf{v}\cdot\mathbf{D}\right),\; ig\mathbf{v}\cdot\mathbf{E}\right]\\ &= -\left\{-\frac{1}{2}U^2,\, O_0\right\} + \frac{g}{16}\hat{\gamma}^0\left((\gamma^2-1)D_0^{\mathrm{ad}} + (\gamma^2+1)\mathbf{v}\cdot\mathbf{D}^{\mathrm{ad}}\right)(\mathbf{v}\cdot\mathbf{E}) \end{aligned} \tag{3.65}$$

and

$$\begin{aligned} \{U,\, O_1\} &= \left\{\frac{1}{4}(\gamma^2-1)O_0 + \frac{i}{2}\hat{\gamma}^0\,\mathbf{v}\cdot\mathbf{D},\, O_1\right\}\\ &= \left\{\frac{i}{2}\hat{\gamma}^0\,\mathbf{v}\cdot\mathbf{D},\, O_1\right\} - \left\{-\frac{1}{4}(\gamma^2-1)O_1,\, O_0\right\}\\ &= \left\{\frac{i}{2}\hat{\gamma}^0\,\mathbf{v}\cdot\mathbf{D},\, O_{(1)1}\right\} - \left\{\frac{i}{2}\hat{\gamma}^0\,\mathbf{v}\cdot\mathbf{D},\, \{U,\, O_0\}\right\} - \left\{-\frac{1}{4}(\gamma^2-1)O_1,\, O_0\right\}\\ &= \left\{\frac{i}{2}\hat{\gamma}^0\,\mathbf{v}\cdot\mathbf{D},\, O_{(1)1}\right\} + \left[U,\, \left[\frac{i}{2}\hat{\gamma}^0\,\mathbf{v}\cdot\mathbf{D},\, O_0\right]\right]\\ &\quad -\left\{\left\{\frac{i}{2}\hat{\gamma}^0\,\mathbf{v}\cdot\mathbf{D},\, U\right\} - \frac{1}{4}(\gamma^2-1)O_1,\, O_0\right\}. \end{aligned} \tag{3.66}$$

Let us now consider the nested commutator in (3.66):

$$\begin{aligned}\left[U,\, \left[\frac{i}{2}\hat{\gamma}^0\,\mathbf{v}\cdot\mathbf{D},\, O_0\right]\right] &= \left[U,\, \left[\frac{i}{2}\hat{\gamma}^0\,\mathbf{v}\cdot\mathbf{D},\, i\hat{\gamma}^0 D_0\right]\right]\\ &= \left[\frac{i}{4}\hat{\gamma}^0\left((\gamma^2-1)D_0 + (\gamma^2+1)\mathbf{v}\cdot\mathbf{D}\right), \frac{ig}{2}\mathbf{v}\cdot\mathbf{E}\right]\\ &= -\frac{g}{8}\hat{\gamma}^0\left((\gamma^2-1)D_0^{\mathrm{ad}} + (\gamma^2+1)\mathbf{v}\cdot\mathbf{D}^{\mathrm{ad}}\right)(\mathbf{v}\cdot\mathbf{E}). \end{aligned} \tag{3.67}$$

The adjoint time derivative $D_0^{\rm ad}\mathbf{E}$ acts only on the chromoelectric field and can be kept. We conclude from (3.57), (3.63), (3.65) and (3.66) that

$$V = -\frac{g}{8}\gamma\,\epsilon_{jkl}\Sigma^j{\Lambda^0}_k E_l' + \left\{\frac{i}{2}\hat\gamma^0\,\mathbf{v}\cdot\mathbf{D},\,U\right\} - \frac{1}{4}(\gamma^2-1)O_1 - U^2 \tag{3.68}$$

and

$$\begin{aligned} O_{(2)2} &= \frac{g}{8}\gamma\,\hat\gamma^0\Big(D_\mu^{\rm ad}u_\nu F^{\mu\nu} + i\epsilon_{jkl}\Sigma^j\Lambda^m{}_k\left\{D_m,\,E_l'\right\} - i\epsilon_{jkl}\Sigma^j{\Lambda^0}_k\left\{\mathbf{v}\cdot\mathbf{D},\,E_l'\right\}\Big) \\ &\quad -\frac{g}{16}\hat\gamma^0\left((\gamma^2-1)D_0^{\rm ad} + (\gamma^2+1)\mathbf{v}\cdot\mathbf{D}^{\rm ad}\right)(\mathbf{v}\cdot\mathbf{E}) \\ &\quad +\frac{i}{4}\hat\gamma^0\left\{\mathbf{v}\cdot\mathbf{D},\,\mathbf{D}^2-(\mathbf{v}\cdot\mathbf{D})^2+g\boldsymbol{\Sigma}\cdot\mathbf{B}'\right\} \\ &= \frac{g}{8}\gamma^2\hat\gamma^0\left(\mathbf{D}^{\rm ad}\cdot\mathbf{E}-\mathbf{v}\cdot(\mathbf{D}^{\rm ad}\times\mathbf{B})\right) + \frac{ig}{8}\gamma\hat\gamma^0\boldsymbol{\Sigma}\cdot\left(\mathbf{D}\times\mathbf{E}'-\mathbf{E}'\times\mathbf{D}\right) \\ &\quad -\frac{ig\gamma^2}{8(1+\gamma)}\hat\gamma^0\left\{\mathbf{v}\cdot\mathbf{D},\;\boldsymbol{\Sigma}\cdot(\mathbf{v}\times\mathbf{E}')\right\} + \frac{i}{4}\hat\gamma^0\left(\left\{\mathbf{v}\cdot\mathbf{D},\,\mathbf{D}^2\right\}-2(\mathbf{v}\cdot\mathbf{D})^3\right) \\ &\quad +\frac{ig}{4}\hat\gamma^0\left\{\mathbf{v}\cdot\mathbf{D},\;\boldsymbol{\Sigma}\cdot\mathbf{B}'\right\} + \frac{(2-\mathbf{v}^2)g\gamma^2}{16}\hat\gamma^0\left(D_0^{\rm ad}-\mathbf{v}\cdot\mathbf{D}^{\rm ad}\right)(\mathbf{v}\cdot\mathbf{E})\,. \end{aligned} \tag{3.69}$$

We have now achieved the goal of removing the time derivatives through $\mathcal{O}(1/m^2)$. Finally, we rescale the fields

$$\begin{aligned} \tilde\Psi_{(2)} &= \frac{1}{\sqrt{\gamma}}\Psi_v, \\ \overline{\tilde\Psi}_{(2)} &= \frac{1}{\sqrt{\gamma}}\overline{\Psi}_v, \end{aligned} \tag{3.70}$$

to remove the factor of γ in front of $\mathcal{L}$. We arrive at the following result for the tree-level moving NRQCD Lagrangian in Minkowski space:

$$\begin{aligned} \mathcal{L} &= \overline{\Psi}_v\Big[i\hat\gamma^0 D_0 + i\hat\gamma^0\mathbf{v}\cdot\mathbf{D} + \frac{\mathbf{D}^2-(\mathbf{v}\cdot\mathbf{D})^2}{2\gamma m} + \frac{g}{2\gamma m}\boldsymbol{\Sigma}\cdot\mathbf{B}' \\ &\quad + \frac{i}{4\gamma^2m^2}\hat\gamma^0\left(\left\{\mathbf{v}\cdot\mathbf{D},\,\mathbf{D}^2\right\}-2(\mathbf{v}\cdot\mathbf{D})^3\right) + \frac{g}{8m^2}\hat\gamma^0\left(\mathbf{D}^{\rm ad}\cdot\mathbf{E}-\mathbf{v}\cdot(\mathbf{D}^{\rm ad}\times\mathbf{B})\right) \\ &\quad + \frac{ig}{8\gamma m^2}\hat\gamma^0\,\boldsymbol{\Sigma}\cdot\left(\mathbf{D}\times\mathbf{E}'-\mathbf{E}'\times\mathbf{D}\right) - \frac{ig}{8(\gamma+1)m^2}\hat\gamma^0\left\{\mathbf{v}\cdot\mathbf{D},\;\boldsymbol{\Sigma}\cdot(\mathbf{v}\times\mathbf{E}')\right\} \\ &\quad + \frac{(2-\mathbf{v}^2)g}{16m^2}\hat\gamma^0\left(D_0^{\rm ad}-\mathbf{v}\cdot\mathbf{D}^{\rm ad}\right)(\mathbf{v}\cdot\mathbf{E}) + \frac{ig}{4\gamma^2m^2}\hat\gamma^0\left\{\mathbf{v}\cdot\mathbf{D},\;\boldsymbol{\Sigma}\cdot\mathbf{B}'\right\}\Big]\Psi_v \\ &\quad + \mathcal{O}(1/m^3). \end{aligned} \tag{3.71}$$

As before, all terms commute with $\hat\gamma^0$. We can therefore introduce 2-component fields $\psi_v(x)$ and $\xi_v(x)$,

$$\Psi_v = \begin{pmatrix}\psi_v\\ \xi_v\end{pmatrix}, \qquad \overline{\Psi}_v = \left(\psi_v^\dagger,\quad -\xi_v^\dagger\right), \tag{3.72}$$

to explicitly separate the Lagrangian into the quark and antiquark pieces (terms that do not contain a factor of $\hat{\gamma}^0$ in (3.71) appear with the opposite sign in the antiquark Lagrangian):

$$\begin{aligned}
\mathcal{L} \;=\; & \psi_v^\dagger \Bigg[iD_0 + i\mathbf{v}\cdot\mathbf{D} + \frac{\mathbf{D}^2 - (\mathbf{v}\cdot\mathbf{D})^2}{2\gamma m} + \frac{g}{2\gamma m}\boldsymbol{\sigma}\cdot\mathbf{B}' \\
& + \frac{i}{4\gamma^2 m^2}\left(\{\mathbf{v}\cdot\mathbf{D},\, \mathbf{D}^2\} - 2(\mathbf{v}\cdot\mathbf{D})^3\right) + \frac{g}{8m^2}\Big(\mathbf{D}^{\rm ad}\cdot\mathbf{E} - \mathbf{v}\cdot(\mathbf{D}^{\rm ad}\times\mathbf{B})\Big) \\
& + \frac{ig}{8\gamma m^2}\,\boldsymbol{\sigma}\cdot\big(\mathbf{D}\times\mathbf{E}' - \mathbf{E}'\times\mathbf{D}\big) - \frac{ig}{8(\gamma+1)m^2}\left\{\mathbf{v}\cdot\mathbf{D},\ \boldsymbol{\sigma}\cdot(\mathbf{v}\times\mathbf{E}')\right\} \\
& + \frac{(2-\mathbf{v}^2)g}{16m^2}\Big(D_0^{\rm ad} - \mathbf{v}\cdot\mathbf{D}^{\rm ad}\Big)(\mathbf{v}\cdot\mathbf{E}) + \frac{ig}{4\gamma^2 m^2}\left\{\mathbf{v}\cdot\mathbf{D},\ \boldsymbol{\sigma}\cdot\mathbf{B}'\right\}\Bigg]\psi_v \\
& + \xi_v^\dagger \Bigg[iD_0 + i\mathbf{v}\cdot\mathbf{D} - \frac{\mathbf{D}^2 - (\mathbf{v}\cdot\mathbf{D})^2}{2\gamma m} - \frac{g}{2\gamma m}\boldsymbol{\sigma}\cdot\mathbf{B}' \\
& + \frac{i}{4\gamma^2 m^2}\left(\{\mathbf{v}\cdot\mathbf{D},\, \mathbf{D}^2\} - 2(\mathbf{v}\cdot\mathbf{D})^3\right) + \frac{g}{8m^2}\Big(\mathbf{D}^{\rm ad}\cdot\mathbf{E} - \mathbf{v}\cdot(\mathbf{D}^{\rm ad}\times\mathbf{B})\Big) \\
& + \frac{ig}{8\gamma m^2}\,\boldsymbol{\sigma}\cdot\big(\mathbf{D}\times\mathbf{E}' - \mathbf{E}'\times\mathbf{D}\big) - \frac{ig}{8(\gamma+1)m^2}\left\{\mathbf{v}\cdot\mathbf{D},\ \boldsymbol{\sigma}\cdot(\mathbf{v}\times\mathbf{E}')\right\} \\
& + \frac{(2-\mathbf{v}^2)g}{16m^2}\Big(D_0^{\rm ad} - \mathbf{v}\cdot\mathbf{D}^{\rm ad}\Big)(\mathbf{v}\cdot\mathbf{E}) + \frac{ig}{4\gamma^2 m^2}\left\{\mathbf{v}\cdot\mathbf{D},\ \boldsymbol{\sigma}\cdot\mathbf{B}'\right\}\Bigg]\xi_v \\
& + \mathcal{O}(1/m^3). \qquad (3.73)
\end{aligned}$$

A moving NRQCD Lagrangian of this order had already been presented in [22, 21, 23], but my result (3.71, 3.73), which is published in [100], is slightly different.

For later reference, I now summarise the tree-level relation between the full QCD field $\Psi(x)$ and the 4-component moving NRQCD field (3.72). We have

$$\Psi(x) \;=\; S(\Lambda)\; T_{\rm FWT}\; e^{-im\,u\cdot x\,\hat{\gamma}^0}\; A_{D_t}\; \frac{1}{\sqrt{\gamma}}\,\Psi_v \qquad (3.74)$$

(and correspondingly for $\overline{\Psi}$) where $T_{\rm FWT}$ is the FWT transformation (3.17) expressed in the new frame of reference,

$$T_{\rm FWT} = \exp\left(\frac{i\hat{\gamma}^j \Lambda^\mu{}_j D_\mu}{2m}\right)\exp\left(\frac{ig\hat{\boldsymbol{\gamma}}\cdot\mathbf{E}'\hat{\gamma}^0}{(2m)^2}\right)\times\ldots\,, \qquad (3.75)$$

and A_{D_t} removes the unwanted time derivatives in the Lagrangian,

$$A_{D_t} = \exp\left(\frac{U}{\gamma m}\right)\exp\left(\frac{V}{(\gamma m)^2}\right)\times\ldots\ . \qquad (3.76)$$

The operators U and V in (3.76) were defined in Eqs. (3.59) and (3.68), respectively.

3.4.1 $\mathcal{O}(1/m^3)$ relativistic correction in moving NRQCD

As explained in section 3.2.2, for heavy-heavy mesons one needs to include an additional $\mathcal{O}(1/m^3)$ term in order to achieve accuracy to order $\mathcal{O}(v_{\text{orb.}}^4)$. Instead of performing all the field redefinitions to this order, we again obtain this term by expanding the kinetic energy expression in powers of the residual momentum $\mathbf{k}$,

$$\begin{aligned} E_{\text{kin}} &= \sqrt{(\gamma m\mathbf{v}+\mathbf{k})^2+m^2}-\gamma m \\ &= \mathbf{v}\cdot\mathbf{k}+\frac{1}{2\gamma m}\left(\mathbf{k}^2-(\mathbf{v}\cdot\mathbf{k})^2\right)+\frac{1}{4\gamma^2m^2}\left(-\{\mathbf{v}\cdot\mathbf{k},\,\mathbf{k}^2\}+2(\mathbf{v}\cdot\mathbf{k})^3\right) \\ &\quad +\frac{1}{8\gamma^3m^3}\left(-\mathbf{k}^4+3\left\{\mathbf{k}^2,\,(\mathbf{v}\cdot\mathbf{k})^2\right\}-5(\mathbf{v}\cdot\mathbf{k})^4\right) \;+\; ... \end{aligned} \tag{3.77}$$

Here, we ordered the terms with products of $(\mathbf{v}\cdot\mathbf{k})$ and $\mathbf{k}^2$ in form of anticommutators, since we are now going to replace $\mathbf{k}$ by the operator $-i\mathbf{D}$, and the anticommutator-ordering is what one would have obtained from field redefinitions. Indeed, we get the same results up to $\mathcal{O}(1/m^2)$ and the following $\mathcal{O}(1/m^3)$ term:

$$\mathcal{L}_{\text{kin},m^{-3}}=-\overline{\Psi}_v\,\frac{1}{8\gamma^3m^3}\left(-\mathbf{D}^4+3\left\{\mathbf{D}^2,\,(\mathbf{v}\cdot\mathbf{D})^2\right\}-5(\mathbf{v}\cdot\mathbf{D})^4\right)\Psi_v. \tag{3.78}$$

Note that for heavy-heavy mesons the power counting in mNRQCD is modified when the frame velocity is close to the speed of light (i.e. $|\mathbf{v}|\to 1$ in our units). The details are given in [100]. For the moderate velocities used in the numerical calculations in the following chapters this effect is negligible.

3.5 Euclidean mNRQCD Lagrangian

The Euclidean moving NRQCD Lagrangian can be obtained by following the general procedure discussed in Sec. 2.1. It is also convenient to define the relation between the 3-dimensional chromoelectric field $\mathbf{E}$ and the 4-dimensional field strength tensor $F_{\mu\nu}$ with a different sign in Euclidean space, i.e.

$$E_j=-F_{0j}. \tag{3.79}$$

With this definition, Eq. (3.52) turns into the symmetric form

$$\begin{aligned} \mathbf{B}' &= \gamma\left(\mathbf{B}+i\mathbf{v}\times\mathbf{E}-\frac{\gamma}{1+\gamma}\mathbf{v}\,(\mathbf{v}\cdot\mathbf{B})\right), \\ \mathbf{E}' &= \gamma\left(\mathbf{E}+i\mathbf{v}\times\mathbf{B}-\frac{\gamma}{1+\gamma}\mathbf{v}\,(\mathbf{v}\cdot\mathbf{E})\right). \end{aligned} \tag{3.80}$$

The Euclidean Lagrangian, to which we now also include the $\mathcal{O}(1/m^3)$ relativistic correction term (3.78), reads

$$\begin{aligned}
\mathcal{L} \;=\; & \psi_v^\dagger \Bigg[D_0 - i\mathbf{v}\cdot\mathbf{D} - \frac{\mathbf{D}^2 - (\mathbf{v}\cdot\mathbf{D})^2}{2\gamma m} - \frac{g}{2\gamma m}\boldsymbol{\sigma}\cdot\mathbf{B}' \\
& - \frac{i}{4\gamma^2 m^2}\left(\left\{\mathbf{v}\cdot\mathbf{D},\, \mathbf{D}^2\right\} - 2(\mathbf{v}\cdot\mathbf{D})^3\right) + \frac{g}{8m^2}\Big(i\mathbf{D}^{\mathrm{ad}}\cdot\mathbf{E} + \mathbf{v}\cdot(\mathbf{D}^{\mathrm{ad}}\times\mathbf{B})\Big) \\
& - \frac{g}{8\gamma m^2}\,\boldsymbol{\sigma}\cdot\big(\mathbf{D}\times\mathbf{E}' - \mathbf{E}'\times\mathbf{D}\big) + \frac{g}{8(\gamma+1)m^2}\left\{\mathbf{v}\cdot\mathbf{D},\ \boldsymbol{\sigma}\cdot(\mathbf{v}\times\mathbf{E}')\right\} \\
& - \frac{(2-\mathbf{v}^2)g}{16m^2}\Big(D_0^{\mathrm{ad}} + i\mathbf{v}\cdot\mathbf{D}^{\mathrm{ad}}\Big)(\mathbf{v}\cdot\mathbf{E}) - \frac{ig}{4\gamma^2 m^2}\left\{\mathbf{v}\cdot\mathbf{D},\ \boldsymbol{\sigma}\cdot\mathbf{B}'\right\} \\
& - \frac{1}{8\gamma^3 m^3}\Big(\mathbf{D}^4 - 3\left\{\mathbf{D}^2,\, (\mathbf{v}\cdot\mathbf{D})^2\right\} + 5(\mathbf{v}\cdot\mathbf{D})^4\Big)\Bigg]\,\psi_v \\
& + \xi_v^\dagger \Bigg[D_0 - i\mathbf{v}\cdot\mathbf{D} + \frac{\mathbf{D}^2 - (\mathbf{v}\cdot\mathbf{D})^2}{2\gamma m} + \frac{g}{2\gamma m}\boldsymbol{\sigma}\cdot\mathbf{B}' \\
& - \frac{i}{4\gamma^2 m^2}\left(\left\{\mathbf{v}\cdot\mathbf{D},\, \mathbf{D}^2\right\} - 2(\mathbf{v}\cdot\mathbf{D})^3\right) + \frac{g}{8m^2}\Big(i\mathbf{D}^{\mathrm{ad}}\cdot\mathbf{E} + \mathbf{v}\cdot(\mathbf{D}^{\mathrm{ad}}\times\mathbf{B})\Big) \\
& - \frac{g}{8\gamma m^2}\,\boldsymbol{\sigma}\cdot\big(\mathbf{D}\times\mathbf{E}' - \mathbf{E}'\times\mathbf{D}\big) + \frac{g}{8(\gamma+1)m^2}\left\{\mathbf{v}\cdot\mathbf{D},\ \boldsymbol{\sigma}\cdot(\mathbf{v}\times\mathbf{E}')\right\} \\
& - \frac{(2-\mathbf{v}^2)g}{16m^2}\Big(D_0^{\mathrm{ad}} + i\mathbf{v}\cdot\mathbf{D}^{\mathrm{ad}}\Big)(\mathbf{v}\cdot\mathbf{E}) - \frac{ig}{4\gamma^2 m^2}\left\{\mathbf{v}\cdot\mathbf{D},\ \boldsymbol{\sigma}\cdot\mathbf{B}'\right\} \\
& + \frac{1}{8\gamma^3 m^3}\Big(\mathbf{D}^4 - 3\left\{\mathbf{D}^2,\, (\mathbf{v}\cdot\mathbf{D})^2\right\} + 5(\mathbf{v}\cdot\mathbf{D})^4\Big)\Bigg]\,\xi_v \\
& + \mathcal{O}(1/m^3).
\end{aligned} \tag{3.81}$$

Naturally, the field redefinition (3.74) also needs to be continued to imaginary time. This must be done independently for Ψ and $\overline{\Psi}$.

Note that, as in (3.20), the antiquark action can be obtained from the quark action through the replacements

$$\begin{aligned}
\psi_v &\;\mapsto\; (\xi_v^\dagger)^T, \\
\psi_v^\dagger &\;\mapsto\; (\xi_v)^T, \\
iA_\mu &\;\mapsto\; (iA_\mu)^*, \\
iE_j &\;\mapsto\; (iE_j)^*, \\
iB_j &\;\mapsto\; (iB_j)^*, \\
i\sigma^j &\;\mapsto\; \left(i\sigma^j\right)^*.
\end{aligned} \tag{3.82}$$

Remarkably, in Euclidean space there is also a much simpler prescription:

$$\begin{aligned} \text{replace} \qquad \psi_v &\mapsto (\xi_v^\dagger)^T, \\ \psi_v^\dagger &\mapsto (\xi_v)^T, \\ \mathbf{v} &\mapsto (-\mathbf{v}), \end{aligned}$$

and take the complex conjugate of the whole action kernel. (3.83)

To see that the new prescription (3.83) is equivalent to (3.82), it is convenient to insert factors of $-(i^2) = 1$ into the Euclidean Lagrangian where appropriate such that it is written explicitly in terms of the anti-Hermitian quantities iA_μ, $i\mathbf{E}$, $i\mathbf{B}$ and $i\boldsymbol{\sigma}$. Then one sees that (3.82) is equivalent to taking the complex conjugate of the whole action kernel, *apart from the remaining factors of i*. Now, the crucial point is that precisely those terms with additional factors of i come with an odd power of $\mathbf{v}$. Thus, changing also the sign of the velocity makes the new prescription work.

3.5.1 Euclidean quark and antiquark Green functions in mNRQCD

As shown in the previous section, in Euclidean space the antiquark action kernel equals the complex conjugate of the quark action kernel with the opposite boost velocity,

$$S_{\psi_v} = \int \mathrm{d}^4x \int \mathrm{d}^4x' \ \Big[\psi_v^\dagger(x)\Big]_{cs} \Big[K^{(+\mathbf{v})}(x,\ x')\Big]_{cs\,c's'} \Big[\psi_v(x')\Big]_{c's'}, \tag{3.84}$$

$$\begin{aligned} S_{\xi_v} &= \int \mathrm{d}^4x \int \mathrm{d}^4x' \ \Big[\xi_v(x)\Big]_{cs} \Big[K^{(-\mathbf{v})}(x,\ x')^*\Big]_{cs\,c's'} \Big[\xi_v^\dagger(x')\Big]_{c's'} \\ &= \int \mathrm{d}^4x \int \mathrm{d}^4x' \ \Big[\xi_v(x')\Big]_{c's'} \Big[K^{(-\mathbf{v})}(x',\ x)^*\Big]_{c's'\,cs} \Big[\xi_v^\dagger(x)\Big]_{cs} \\ &= \int \mathrm{d}^4x \int \mathrm{d}^4x' \ \Big[\xi_v^\dagger(x)\Big]_{cs} \Big[-K^{(-\mathbf{v})}(x',\ x)^*\Big]_{c's'\,cs} \Big[\xi_v(x')\Big]_{c's'}. \end{aligned} \tag{3.85}$$

Here, we explicitly introduced the colour and spin indices c, c', s, s'. We define the quark and antiquark Green functions as

$$\begin{aligned} G_{\psi_v}^{(+\mathbf{v})}(x,\ x') &= \langle\, \psi_v(x)\ \psi_v^\dagger(x')\,\rangle, \\ G_{\xi_v}^{(+\mathbf{v})}(x,\ x') &= \langle\, \xi_v(x)\ \xi_v^\dagger(x')\,\rangle. \end{aligned} \tag{3.86}$$

From the relation between the actions S_{ψ_v} and S_{ξ_v} it follows that

$$\begin{aligned} \Big[G_{\xi_v}^{(+\mathbf{v})}(x,\ x')\Big]_{cs\,c's'} &= -\Big[G_{\psi_v}^{(-\mathbf{v})}(x',\ x)^*\Big]_{c's'\,cs} \\ &= -\Big[G_{\psi_v}^{(-\mathbf{v})}(x',\ x)^\dagger\Big]_{cs\,c's'}, \end{aligned} \tag{3.87}$$

that is, the Euclidean antiquark Green function can be obtained from the Euclidean quark Green function with the opposite boost velocity.

Chapter 4

Lattice HQET

Recall from Sec. 3.2.1 that for hadrons containing only a single heavy quark of mass m the contributions from the operators with factors of $1/m^p$ are suppressed by $(\Lambda_{\mathrm{QCD}}/m)^p$. The leading-order Euclidean Lagrangian in the rest frame is simply

$$\mathcal{L}_\psi^{(0)} = \psi^\dagger D_0\, \psi. \tag{4.1}$$

Eichten and Hill [101] suggested a simple lattice discretisation of (4.1), referred to as lattice heavy-quark effective theory (LHQET). In LHQET, higher-order corrections to (4.1) are treated as insertions in correlation function, so that the resulting theory may be renormalisable. Even though LHQET is not used for the calculations in this dissertation, we will discuss it briefly in this chapter. It will be instructive to compare it to lattice nonrelativistic QCD, which will be introduced in Chapter 5.

4.1 Relativistic corrections as operator insertions

We first discuss the continuum theory, working to order $1/m$ and setting $\mathbf{v} = 0$ for simplicity. The effective Lagrangian has the form

$$\mathcal{L}_\psi = \delta m\, \mathcal{L}_\psi^{(-1)} + \mathcal{L}_\psi^{(0)} + \frac{1}{m}\mathcal{L}_\psi^{(1)} \tag{4.2}$$

where $\mathcal{L}_\psi^{(-1)} = \psi^\dagger\psi$ is a mass counterterm, $\mathcal{L}_\psi^{(0)}$ is given by (4.1), and $\mathcal{L}_\psi^{(1)}$ reads

$$\mathcal{L}_\psi^{(1)} = \psi^\dagger \left[-\frac{1}{2}\mathbf{D}^2 - \frac{g}{2}\,\boldsymbol{\sigma}\cdot\mathbf{B}\right]\psi. \tag{4.3}$$

Let us denote by S_{QCD} the relativistic QCD action including the gluons A_μ and the light quarks Ψ, $\overline{\Psi}$. The full path integral with action $S = S_{QCD} + \int \mathrm{d}^4x\, \mathcal{L}_\psi$ for the expectation

value of some observable O is

$$\langle O \rangle = \frac{1}{Z} \int D[A, \Psi, \overline{\Psi}, \psi, \psi^\dagger] \; O \; \exp\left(-S_{QCD} - \delta m \, S_\psi^{(-1)} - S_\psi^{(0)} - \tfrac{1}{m} S_\psi^{(1)} \right). \tag{4.4}$$

However, in HQET one does not work with (4.4), but rather expands the exponential to the given order in $1/m$:

$$\exp\left(-S_{QCD} - S_\psi\right) \;\approx\; \exp\left(-S_{QCD} - \delta m \, S_\psi^{(-1)} - S_\psi^{(0)} \right) \left(1 - \tfrac{1}{m} S_\psi^{(1)} \right). \tag{4.5}$$

Thus, one effectively calculates the expectation value

$$\begin{aligned} \left\langle \left(1 - \tfrac{1}{m} S_\psi^{(1)} \right) O \right\rangle^{(0)} \;&=\; \frac{1}{Z} \int D[A, \Psi, \overline{\Psi}, \psi, \psi^\dagger] \; \left(1 - \tfrac{1}{m} S_\psi^{(1)} \right) O \\ &\quad \times \; \exp\left(-S_{QCD} - \delta m \, S_\psi^{(-1)} - S_\psi^{(0)} \right), \end{aligned} \tag{4.6}$$

where the action used in the path integral is

$$S_{QCD} + \delta m \int \mathrm{d}^4 x \;\; \psi^\dagger \psi + \int \mathrm{d}^4 x \;\; \psi^\dagger D_0 \, \psi. \tag{4.7}$$

Since this action contains all possible operators of dimension ≤ 4 compatible with the symmetries, and no higher-order operators, it is renormalisable according to Weinberg's power-counting theorem [102]. The question then is whether the composite operators in $\left(1 - \frac{1}{m} S_\psi^{(1)} \right) O$ can be renormalised. It is shown in [103] that the renormalisation of a composite operator requires as counterterms only operators of the same or lower dimension. When all these are included, the theory is formally renormalisable. It has been pointed out in [104] that the renormalisation must be performed nonperturbatively. This shows up in power-law divergences when using a momentum cut-off or the lattice regularisation, but is also true when using dimensional regularisation where apparently no power-law divergences exist.

In lattice HQET, nonperturbative renormalisation can be performed using Schrödinger functional methods; see e.g. [72].

4.2 Continuum HQET Green functions

In the following, we consider the continuum HQET propagator to order $1/m$ on a given background gauge-field. For $x = (\tau, \mathbf{x})$, $x' = (\tau', \mathbf{x}')$ and $\tau > \tau'$, we have, according to Eq. (4.6),

$$\begin{aligned} G_\psi^{(1)}(x,\, x') \;&=\; \frac{1}{Z_\psi} \int D[\psi, \psi^\dagger] \;\; \psi(x) \left\{ 1 + \int \mathrm{d}^4 x'' \; \psi^\dagger(x'') \left[\frac{\mathbf{D}^2}{2m} + \frac{g \, \boldsymbol{\sigma} \cdot \mathbf{B}}{2m} \right]_{x''} \psi(x'') \right\} \psi^\dagger(x') \\ &\quad \times \;\; \exp\left\{ - \int \mathrm{d}^4 y \;\; \psi^\dagger(y) \left(D_0 + \delta m \right) \psi(y) \right\}. \end{aligned} \tag{4.8}$$

Let us now perform the functional integral over the heavy-quark fields $\psi, \psi^\dagger$. This gives

$$\begin{aligned} G_\psi^{(1)}(x,\, x') &= G_\psi(\tau, \mathbf{x},\, \tau', \mathbf{x}') \\ &+ \int_{\tau'}^{\tau} \mathrm{d}\tau'' \int \mathrm{d}^3x'' G_\psi(\tau, \mathbf{x},\, \tau'', \mathbf{x}'') \left[\frac{\mathbf{D}^2}{2m} + \frac{g\,\boldsymbol{\sigma}\cdot\mathbf{B}}{2m}\right]_{\tau'',\mathbf{x}''} G_\psi(\mathbf{x}'', \tau'',\, \tau', \mathbf{x}'), \end{aligned} \tag{4.9}$$

where G_ψ denotes the propagator according to the action $\int \mathrm{d}^4x\ \ \psi^\dagger(x)\,(D_0 + \delta m)\,\psi(x)$. Now the question arises what boundary conditions to use. In Minkowski space, the field operator related to $\psi^\dagger$ creates heavy quarks and the field operator related to ψ annihilates heavy quarks. It follows that for ψ the time-ordered Green function equals the *retarded* Green function. In order for Wick rotation to give the correct result, one must also take the retarded Green function in Euclidean space, i.e. consider forward propagation. The propagator G_ψ satisfies the initial condition

$$G_\psi(\tau = \tau', \mathbf{x},\, \tau', \mathbf{x}') = \delta^3(\mathbf{x} - \mathbf{x}') \tag{4.10}$$

and for $\tau > \tau'$ we have

$$(D_0 + \delta m)\, G_\psi(\tau, \mathbf{x},\, \tau', \mathbf{x}') = 0, \tag{4.11}$$

or

$$\partial_\tau G_\psi(\tau, \mathbf{x}, \tau', \mathbf{x}') = -\big[ig\, A_0(\tau, \mathbf{x}) + \delta m\big]\, G_\psi(\tau, \mathbf{x}, \tau', \mathbf{x}'). \tag{4.12}$$

The solution of this differential equation is

$$G_\psi(\tau, \mathbf{x}, \tau', \mathbf{x}') = e^{-\delta m(\tau - \tau')} \delta^3(\mathbf{x} - \mathbf{x}')\, U(\mathbf{x}', \tau, \tau'), \tag{4.13}$$

where $U(\mathbf{x}', \tau, \tau')$ the time-ordered exponential of $-ig\, A_0$ along the line with constant $\mathbf{x}'$:

$$U(\mathbf{x}', \tau, \tau') = \mathscr{T} \exp\left(-ig \int_{\tau'}^{\tau} A_0(\tau'', \mathbf{x}')\ \mathrm{d}\tau''\right). \tag{4.14}$$

Eq. (4.14) is the parallel transporter along the straight line from $(\tau', \mathbf{x}')$ to $(\tau, \mathbf{x}')$. By inserting the solution (4.13) into Eq. (4.9), we finally obtain the following result for the heavy quark propagator with the $1/m$ correction:

$$\begin{aligned} G_\psi^{(1)}(x,\, x') &= e^{-\delta m(\tau - \tau')} \delta^3(\mathbf{x} - \mathbf{x}')\, U(\mathbf{x}', \tau, \tau') \\ &+ e^{-\delta m(\tau - \tau')} \int_{\tau'}^{\tau} \mathrm{d}\tau''\ U(\mathbf{x}, \tau, \tau'')\ \left[\frac{\mathbf{D}^2}{2m} + \frac{g\,\boldsymbol{\sigma}\cdot\mathbf{B}}{2m}\right]_{\tau'',\mathbf{x}} \delta^3(\mathbf{x} - \mathbf{x}')\, U(\mathbf{x}', \tau'', \tau'). \end{aligned} \tag{4.15}$$

4.3 Lattice discretisation

The simplest lattice discretisation of the action $\left(\delta m\, S_\psi^{(-1)} + S_\psi^{(0)}\right)$ is, in lattice units,

$$\sum_x \psi^\dagger(x)\big[(1+\delta m)\psi(x) - U_0^\dagger(x-\hat{0})\psi(x-\hat{0})\big]. \tag{4.16}$$

The corresponding propagator is

$$G_\psi(x,\, x') = \delta_{\mathbf{x},\,\mathbf{x}'}(1+\delta m)^{-(\tau-\tau'+1)} U_{\rm lat}(\mathbf{x}',\tau,\tau'), \tag{4.17}$$

where $U_{\rm lat}(\mathbf{x}',\tau,\tau')$ is given by

$$U_{\rm lat}(\mathbf{x}',\tau,\tau') = \prod_{n=0}^{\tau-\tau'-1} U_0^\dagger(x'+n\hat{0}). \tag{4.18}$$

The lattice expression for the propagator with the $1/m$ correction analogous to (4.15) is then

$$\begin{aligned} G_\psi^{(1)}(x,\, x') &= (1+\delta m)^{-(\tau-\tau'+1)} \\ &\times \Bigg\{ \delta_{\mathbf{x},\,\mathbf{x}'}\, U_{\rm lat}(\mathbf{x}',\tau,\tau') \\ &\quad + \sum_{\tau''=\tau'}^{\tau} U_{\rm lat}(\mathbf{x},\tau,\tau'') \left[\frac{\mathbf{D}^2_{\rm lat}}{2m} + \frac{g\,\boldsymbol{\sigma}\cdot\mathbf{B}_{\rm lat}}{2m}\right]_{\tau,\mathbf{x}''} \delta_{\mathbf{x},\,\mathbf{x}'}\, U_{\rm lat}(\mathbf{x}',\tau'',\tau') \Bigg\}, \end{aligned} \tag{4.19}$$

where $\mathbf{D}^2_{\rm lat}$ and $\mathbf{B}_{\rm lat}$ are lattice discretisations of $\mathbf{D}^2$ and $\mathbf{B}$ (examples are given in Sec. A.2). Of course the operators need to be multiplied by renormalisation factors.

4.4 Signal-to-noise ratio

The simple form of the static action (4.16) leads to a rather bad signal-to-noise ratio in heavy-light correlation functions, exponentially falling as the continuum limit is taken. This has been explained in [105]. In general, the statistical variance in a two-point function

$$C(\tau) = \langle \Phi(\tau)\Phi^\dagger(0)\rangle \tag{4.20}$$

is given by

$$\sigma^2(\tau) = \langle [\Phi(\tau)\Phi^\dagger(0)][\Phi(\tau)\Phi^\dagger(0)]^\dagger\rangle - |\langle \Phi(\tau)\Phi^\dagger(0)\rangle|^2. \tag{4.21}$$

Now, if Φ is an interpolating field for a heavy-light meson, then for large τ we have in the static theory

$$C(\tau)|_{\text{static}} \;\propto\; e^{-E^{\text{st}}_{Q\bar{q}}\tau}, \tag{4.22}$$

where $E^{\text{st}}_{Q\bar{q}}$ is the energy of the heavy-light ground state, which is dominated by a linearly divergent contribution from the static propagator, $E^{\text{st}} \propto g^2/a$.

On the other hand, it turns out that in the variance correlator (4.21) the contributions from the two static propagators cancel each other and hence

$$\sigma^2(\tau)|_{\text{static}} \;\propto\; e^{-m_\pi\tau}. \tag{4.23}$$

It follows that the signal-to noise ratio is

$$\left.\frac{C(\tau)}{\sigma(\tau)}\right|_{\text{static}} \;\propto\; e^{-\left(E^{\text{st}}_{Q\bar{q}}-\frac{1}{2}m_\pi\right)\tau}. \tag{4.24}$$

This decays rapidly with τ. In contrast, when lattice NRQCD (see Chapter 5) is used, the heavy quarks in $\sigma^2(\tau)$ form a $Q\bar{Q}$ (quarkonium) bound state, so that

$$\left.\frac{C(\tau)}{\sigma(\tau)}\right|_{\text{NRQCD}} \;\propto\; e^{-\left(E_{Q\bar{q}}-\frac{1}{2}(E_{Q\bar{Q}}+m_\pi)\right)\tau}. \tag{4.25}$$

The signal-to-noise ratio (4.25) still decays exponentially with τ, but with a much smaller exponent [106].

Note that the signal-to-noise ratio in lattice HQET can be improved significantly by replacing the gauge link $U_0^\dagger(x-\hat{0})$ in (4.16) with a "smeared" link that depends also on the neighbouring gauge links [107].

Chapter 5

Lattice moving NRQCD

In this chapter I will explain how the moving NRQCD Lagrangian (3.81) can be formulated on the lattice such that the resulting theory works for both heavy-heavy and heavy-light hadrons. The method is analogous to non-moving lattice NRQCD, which has been formulated in [9, 10] and used with great success in recent dynamical lattice QCD calculations [108, 109, 11, 110].

According to the power-counting rules derived in Sec. 3.2.2, for heavy-heavy mesons the *lowest-order* moving NRQCD Lagrangian is

$$\mathcal{L}^{(0)} = \psi_v^\dagger \left[D_0 - i\mathbf{v}\cdot\mathbf{D} - \frac{\mathbf{D}^2 - (\mathbf{v}\cdot\mathbf{D})^2}{2\gamma m} \right] \psi_v + \xi_v^\dagger \left[D_0 - i\mathbf{v}\cdot\mathbf{D} + \frac{\mathbf{D}^2 - (\mathbf{v}\cdot\mathbf{D})^2}{2\gamma m} \right] \xi_v. \quad (5.1)$$

The operators $\left(\mathbf{D}^2 - (\mathbf{v}\cdot\mathbf{D})^2\right)/(2\gamma m)$ and $\left(D_0 - i\mathbf{v}\cdot\mathbf{D}\right)$ are both of order $\mathcal{O}(v_{\text{orb.}}^2)$. Thus, the operator $\left(\mathbf{D}^2 - (\mathbf{v}\cdot\mathbf{D})^2\right)/(2\gamma m)$ can not be treated as an operator insertion like in lattice HQET (cf. Chapter 4), but must be kept in the exponential e^{-S} in the path integral. As this operator has dimension 5, the resulting theory will be nonrenormalisable in the standard sense, and power-law divergences occur. However, this does not cause any problems as long as one works with a sufficiently low cutoff, like a sufficiently coarse lattice. In terms of the lattice spacing a, one must have $m\,a > 1$, the opposite of the condition for relativistic heavy quarks on the lattice (cf. Sec. 2.8). The contributions from higher-order operators are then suppressed according to the power-counting rules. Instead of taking the continuum limit, discretisation errors can be reduced using Symanzik improvement.

In lattice moving NRQCD, a lattice version of the full action (3.81) is used in the path integral, in contrast to lattice HQET where only the static action is used. For this reason, lattice mNRQCD can be applied to both heavy-heavy and heavy-light hadrons, and with the action (3.81) it will be accurate to order $\mathcal{O}(v_{\text{orb.}}^4)$ for heavy quarkonium mesons and $\mathcal{O}(\Lambda_{\text{QCD}}^2/m^2)$ for hadrons containing only a single heavy quark.

5.1 Continuum evolution equation

As in Chapter 4, we start by considering the continuum Green function on a given background gauge-field A_μ. Since the antiquark Green function can be obtained from the quark Green function using Eq. (3.87), we consider only the quark field $\psi_v(x)$ in what follows. Recall from Eq. (3.81) that the Euclidean Lagrangian for ψ_v has the form

$$\mathcal{L}_{\psi_v} = \psi_v^\dagger \left(D_0 + H\right) \psi_v. \tag{5.2}$$

As explained above, the full action is used in the weight factor e^{-S} in the path integral. Therefore, the Green function is the inverse of the full heavy-quark action kernel, i.e.

$$\left(D_0 + H\right) G_{\psi_v}(x, x') = \delta^4(x - x'), \tag{5.3}$$

with $x = (\tau, \mathbf{x})$ and $x' = (\tau', \mathbf{x}')$. As already discussed in 4.1 one must take the retarded Green function in Euclidean space:

$$G_{\psi_v}(\tau, \mathbf{x}, \tau', \mathbf{x}') = 0 \quad \text{for} \quad \tau < \tau', \tag{5.4}$$

and for $\tau = \tau'$

$$G_{\psi_v}(\tau = \tau', \mathbf{x}, \tau', \mathbf{x}') = \delta^3(\mathbf{x} - \mathbf{x}'). \tag{5.5}$$

For $\tau > \tau'$, Eq. (5.3) becomes

$$\left(D_0 + H\right) G_{\psi_v}(\tau, \mathbf{x}, \tau', \mathbf{x}') = 0, \tag{5.6}$$

or

$$\partial_0 \, G_{\psi_v}(\tau, \mathbf{x}, \tau', \mathbf{x}') = -(H + ig\, A_0)\, G_{\psi_v}(\tau, \mathbf{x}, \tau', \mathbf{x}'). \tag{5.7}$$

Since H does not contain time derivatives acting on ψ_v, we can integrate this differential equation, so that for $\tau_2 > \tau_1 > \tau'$

$$G_{\psi_v}(\tau_2, \mathbf{x}, \tau', \mathbf{x}') = G_{\psi_v}(\tau_1, \mathbf{x}, , \tau', \mathbf{x}') - \int_{\tau_1}^{\tau_2} (H + ig\, A_0)\, G_{\psi_v}(\tau, \mathbf{x}, \tau', \mathbf{x}') \; \mathrm{d}\tau. \tag{5.8}$$

The solution of (5.8) can be written as a Euclidean-time-ordered exponential function,

$$G_{\psi_v}(\tau_2, \mathbf{x}, \tau', \mathbf{x}') = \mathscr{T} \exp\left(- \int_{\tau_1}^{\tau_2} (H + ig\, A_0) \; \mathrm{d}\tau \right) G_{\psi_v}(\tau_1, \mathbf{x}, \tau', \mathbf{x}'). \tag{5.9}$$

5.2 Lattice evolution equation

On the lattice, the quark Green function evolution Eq. (5.9) is conveniently approximated by

$$\begin{aligned} G_{\psi_v}(\tau,\mathbf{x},\tau',\mathbf{x}') &= \left(1-\frac{\delta H|_\tau}{2}\right)\left(1-\frac{H_0|_\tau}{2n}\right)^n U_0^\dagger(\tau-1,\mathbf{x}) \\ &\quad\times\left(1-\frac{H_0|_{\tau-1}}{2n}\right)^n\left(1-\frac{\delta H|_{\tau-1}}{2}\right) G_{\psi_v}(\tau-1,\mathbf{x},\tau',\mathbf{x}'), \end{aligned} \tag{5.10}$$

which corresponds to the lattice action

$$\begin{aligned} S_{\psi_v} &= \sum_{\mathbf{x},\tau}\psi_v^\dagger(\tau,\mathbf{x})\left[\psi_v(\tau,\mathbf{x})-\left(1-\frac{\delta H|_\tau}{2}\right)\left(1-\frac{H_0|_\tau}{2n}\right)^n U_0^\dagger(\tau-1,\mathbf{x})\right. \\ &\quad\left.\times\left(1-\frac{H_0|_{\tau-1}}{2n}\right)\left(1-\frac{\delta H|_{\tau-1}}{2}\right)^n\psi_v(\tau-1,\mathbf{x})\right]. \end{aligned} \tag{5.11}$$

Here, H_0 contains the leading-order kinetic terms and δH contains all higher-order operators including Symanzik improvement terms. The leading evolution due to H_0 from one lattice time slice to the next is effectively divided into $2n$ smaller steps to avoid instabilities from high-momentum modes [10].

The time-reversal symmetric split into H_0 and δH (albeit with the opposite ordering) was introduced in [10] for non-moving NRQCD. In the following, lattice versions of H_0 and δH are constructed for the full moving NRQCD action (3.81), satisfying the following requirements:

- for $\mathbf{v}=0$, the action reduces to the standard lattice NRQCD action currently in use by the HPQCD collaboration (see e.g. [111]).

- the same order of Symanzik improvement as in the standard HPQCD lattice NRQCD action is retained at non-zero velocity.

Lattice versions of earlier moving NRQCD actions were presented or used in [19, 21, 22, 112, 23, 24, 25, 113]; the following lattice formulation is the result of work done by myself and Eike Müller and is published in [100].

The lattice H_0 and δH are defined as

$$H_0 = -i\mathbf{v}\cdot\boldsymbol{\Delta}^\pm - \frac{\Delta^{(2)}-\Delta_v^{(2)}}{2\gamma m}, \tag{5.12}$$

$$
\begin{aligned}
\delta H \;=\; & -\frac{g}{2\gamma m}\boldsymbol{\sigma}\cdot\tilde{\mathbf{B}}' \\
& -\frac{i}{4\gamma^2 m^2}\left(\left\{\Delta^{(2)},\ \mathbf{v}\cdot\boldsymbol{\Delta}^{\pm}\right\} - 2\Delta_v^{(3)}\right) \\
& +\frac{g}{8m^2}\Big(i(\boldsymbol{\Delta}^{\pm}\cdot\tilde{\mathbf{E}} - \tilde{\mathbf{E}}\cdot\boldsymbol{\Delta}^{\pm}) + \mathbf{v}\cdot(\boldsymbol{\Delta}^{\mathrm{ad}}\times\tilde{\mathbf{B}})\Big) \\
& -\frac{g}{8\gamma m^2}\ \boldsymbol{\sigma}\cdot\left(\tilde{\boldsymbol{\Delta}}^{\pm}\times\tilde{\mathbf{E}}' - \tilde{\mathbf{E}}'\times\tilde{\boldsymbol{\Delta}}^{\pm}\right) \\
& +\frac{g}{8(\gamma+1)m^2}\left\{\mathbf{v}\cdot\tilde{\boldsymbol{\Delta}}^{\pm},\ \boldsymbol{\sigma}\cdot(\mathbf{v}\times\tilde{\mathbf{E}}')\right\} \\
& -\frac{(2-\mathbf{v}^2)g}{16m^2}\left(\Delta_0^{\mathrm{ad}} + i\mathbf{v}\cdot\boldsymbol{\Delta}^{\mathrm{ad}}\right)\left(\mathbf{v}\cdot\tilde{\mathbf{E}}\right) \\
& -\frac{ig}{4\gamma^2 m^2}\left\{\mathbf{v}\cdot\tilde{\boldsymbol{\Delta}}^{\pm},\ \boldsymbol{\sigma}\cdot\tilde{\mathbf{B}}'\right\} \\
& -\frac{1}{8\gamma^3 m^3}\Big(\left(\Delta^{(2)}\right)^2 - 3\left\{\Delta^{(2)},\ \Delta_v^{(2)}\right\} + 5\Delta_v^{(4)}\Big) \\
& \\
& +\delta H_{\mathrm{corr}}\,. \qquad (5.13)
\end{aligned}
$$

The lattice derivative operators and field strength are defined in Appendix A.2. The "$\sim$" is used to denote Symanzik-improved quantities; the boosted fields $\tilde{\mathbf{E}}'$ and $\tilde{\mathbf{B}}'$ are related to the fields $\tilde{\mathbf{E}}$ and $\tilde{\mathbf{B}}$ in the lattice frame through Eq. 3.80.

Note that in the continuum the Leibniz rule $\mathbf{D}^{\mathrm{ad}}\cdot\mathbf{E} = \mathbf{D}\cdot\mathbf{E} - \mathbf{E}\cdot\mathbf{D}$ holds. In order to get agreement with the standard HPQCD lattice NRQCD action at $\mathbf{v} = 0$, the right-hand side of this expression is discretised on the lattice. However, the other adjoint derivatives in the action, which enter only at $\mathbf{v} \neq 0$, are discretised as lattice adjoint derivatives (defined in Eq. (A.14)). This is more efficient and for the term $D_0^{\mathrm{ad}}(\mathbf{v}\cdot\mathbf{E})$ it is crucial since it avoids a time derivative acting on the quark field.

Note that in the static limit ($m \to \infty$) one has $H_0 = -i\mathbf{v}\cdot\boldsymbol{\Delta}^{\pm}$. The symmetric derivative $\boldsymbol{\Delta}^{\pm}$ is used to ensure Hermiticity of the Hamiltonian. It does however lead to doublers, as we have seen for the naive lattice Dirac action in Sec. 2.4. With a finite mass, these doublers are shifted to higher energy due to the second-order derivatives in H_0. However, the second-order derivatives are suppressed by a factor of $1/(2\gamma m)$ and hence γm must not be too large.

The terms in δH_{corr} provide the spatial and temporal lattice spacing improvement for the leading evolution due to H_0. We perform tree-level Symanzik improvement to order $\mathcal{O}(a^2, \mathbf{k}^4)$, as explained in the next section. This means that the we expect the leading errors to be of order $\mathcal{O}(\alpha_s a^2)$.

5.2.1 Symanzik improvement

An $\mathcal{O}(a^2, \mathbf{k}^4)$-improved version of H_0 is given by

$$\tilde{H}_0 \;=\; -i\mathbf{v}\cdot\tilde{\boldsymbol{\Delta}}^{\pm} - \frac{\tilde{\Delta}^{(2)} - \tilde{\Delta}_v^{(2)}}{2\gamma m} \tag{5.14}$$

with the improved derivatives defined in Eq. (A.13) in Appendix A.2. However, we do not simply replace H_0 by $\tilde{H}_0$. Let us first consider the time derivative in the lattice action. Improving it in the standard way would introduce next-to-nearest neighbour couplings, preventing the use of an evolution equation like (5.10). Instead, we try to find an operator $\tilde{H}_0^\star$ such that (explicitly re-introducing the lattice spacing a)

$$\left(1 - \frac{a\tilde{H}_0^\star}{2n}\right)^n \;=\; \exp\left(-\frac{a}{2}\tilde{H}_0\right), \tag{5.15}$$

which yields a more continuum-like behaviour [10]. We obtain

$$a\tilde{H}_0^\star \;=\; 2n\left[1 - \exp\left(-\frac{a\tilde{H}_0}{2n}\right)\right]. \tag{5.16}$$

One could now replace $H_0 \to \tilde{H}_0^\star$ in the lattice action. However, for consistency with previous work, we choose to put all correction terms into δH. We consider the operator on the right-hand side of the temporal link in the lattice action (5.11); the operator acting in the time slice at time $\tau - a$. Then δH_{corr}, the lattice spacing improvement term in (5.13), is defined by

$$\left(1 - \frac{a\tilde{H}_0^\star}{2n}\right)^n = \left(1 - \frac{aH_0}{2n}\right)^n \left(1 - \frac{a\,\delta H_{\mathrm{corr}}}{2}\right). \tag{5.17}$$

This gives

$$\begin{aligned} a\,\delta H_{\mathrm{corr}} \;&=\; 2\left[1 - \left(1 - \frac{aH_0}{2n}\right)^{-n}\left(1 - \frac{a\tilde{H}_0^\star}{2n}\right)^n\right] \\ &=\; 2\left[1 - \left(1 - \frac{aH_0}{2n}\right)^{-n}\exp\left(-\frac{a\tilde{H}_0}{2}\right)\right], \end{aligned} \tag{5.18}$$

and, expanding in powers of a,

$$\begin{aligned} a\,\delta H_{\rm corr} &= a(\tilde{H}_0 - H_0) \\ &\quad + \frac{a^2}{4n}\left(-(1+n)H_0^2 - n\tilde{H}_0^2 + 2nH_0\tilde{H}_0\right) \\ &\quad + \frac{a^3}{24n^2}\left(-(2+3n+n^2)H_0^3 + (3n+3n^2)H_0^2\tilde{H}_0 - 3n^2H_0\tilde{H}_0^2 + n^2\tilde{H}_0^3\right) \\ &\quad + \frac{a^4}{192n^3}\Big(-(6+11n+6n^2+n^3)H_0^4 + (8n+12n^2+4n^3)H_0^3\tilde{H}_0 \\ &\qquad\qquad -(6n^2+6n^3)H_0^2\tilde{H}_0^2 + 4n^3H_0\tilde{H}_0^3 - n^3\tilde{H}_0^4\Big) \\ &\quad + \mathcal{O}(a^5)\,. \end{aligned} \tag{5.19}$$

The term $C \equiv \tilde{H}_0 - H_0$ is of order $|\mathbf{k}|^3$, while H_0 is of order $|\mathbf{k}|$. Neglecting all operators of order $|\mathbf{k}|^5$ and higher, we obtain

$$a\,\delta H_{\rm corr} = a\,C - \frac{a^2}{4n}\left(H_0^2 + n[C,\,H_0]\right) - \frac{a^3H_0^3}{12n^2} - \frac{(2+n)a^4H_0^4}{64n^3}. \tag{5.20}$$

Had we considered the operators on the left-hand side of the temporal link in the lattice action (5.11) instead, the ordering of H_0 and $\tilde{H}_0$ would be interchanged, and this would change the sign of the commutator $[C,\,H_0]$ in (5.20), thereby cancelling the term in the lattice action up to operators of order $|\mathbf{k}|^5$ and higher. We therefore remove this term on both sides.

Let us go back to lattice units now. Writing $H_0 = A + B$ with

$$\begin{aligned} A &= -i\mathbf{v}\cdot\boldsymbol{\Delta}^{\pm}, \\ B &= -\frac{\Delta^{(2)} - \Delta_v^{(2)}}{2\gamma m}, \end{aligned} \tag{5.21}$$

we obtain

$$\begin{aligned} \delta H_{\rm corr} &= \tilde{H}_0 - H_0 - \frac{1}{4n}\left(A^2 + \{A\,,\,B\} + B^2\right) \\ &\quad -\frac{1}{12n^2}\left(A^3 + \left\{A^2\,,\,B\right\} + ABA\right) - \frac{(2+n)}{64n^3}A^4. \end{aligned} \tag{5.22}$$

For performance reasons, we replace some 3rd- and 4th-order derivatives in (5.22) by more

local expressions (the resulting change is of order $|\mathbf{k}|^5$ or higher):

$$\begin{aligned}
(\mathbf{v}\cdot\boldsymbol{\Delta}^{\pm})^3 &\rightarrow \Delta_v^{(3)},\\
\left\{\mathbf{v}\cdot\boldsymbol{\Delta}^{\pm},\,\Delta_v^{(2)}\right\} &\rightarrow 2\Delta_v^{(3)},\\
(\mathbf{v}\cdot\boldsymbol{\Delta}^{\pm})^4 &\rightarrow \Delta_v^{(4)},\\
(\Delta_v^{(2)})^2 &\rightarrow \Delta_v^{(4)},\\
\left\{(\mathbf{v}\cdot\boldsymbol{\Delta}^{\pm})^2\,,\,\Delta^{(2)}\right\} &\rightarrow \left\{\Delta_v^{(2)}\,,\,\Delta^{(2)}\right\},\\
\left\{(\mathbf{v}\cdot\boldsymbol{\Delta}^{\pm})^2\,,\,\Delta_v^{(2)}\right\} &\rightarrow 2\Delta_v^{(4)},\\
(\mathbf{v}\cdot\boldsymbol{\Delta}^{\pm})\Delta_v^{(2)}(\mathbf{v}\cdot\boldsymbol{\Delta}^{\pm}) &\rightarrow \Delta_v^{(4)},\\
(\mathbf{v}\cdot\boldsymbol{\Delta}^{\pm})\Delta^{(2)}(\mathbf{v}\cdot\boldsymbol{\Delta}^{\pm}) &\rightarrow \tfrac{1}{2}(\mathbf{v}\cdot\boldsymbol{\Delta}^{-})\Delta^{(2)}(\mathbf{v}\cdot\boldsymbol{\Delta}^{+})\\
&\quad + \tfrac{1}{2}(\mathbf{v}\cdot\boldsymbol{\Delta}^{+})\Delta^{(2)}(\mathbf{v}\cdot\boldsymbol{\Delta}^{-})\,.
\end{aligned} \tag{5.23}$$

This finally gives

$$\begin{aligned}
\delta H_{\rm corr} \;=\;& \tilde{H}_0 - H_0\\
&-\frac{1}{4n}\Bigg[-(\mathbf{v}\cdot\boldsymbol{\Delta}^{\pm})^2 + \frac{\left\{i\mathbf{v}\cdot\boldsymbol{\Delta}^{\pm},\,\Delta^{(2)}\right\} - 2i\Delta_v^{(3)}}{2\gamma m}\\
&\qquad + \frac{(\Delta^{(2)})^2 - \left\{\Delta^{(2)},\,\Delta_v^{(2)}\right\} + \Delta_v^{(4)}}{4\gamma^2 m^2}\Bigg]\\
&-\frac{1}{12n^2}\Bigg[i\Delta_v^{(3)} + \frac{\left\{\Delta^{(2)},\,\Delta_v^{(2)}\right\} - 3\Delta_v^{(4)}}{2\gamma m}\\
&\qquad + \frac{(\mathbf{v}\cdot\boldsymbol{\Delta}^{-})\Delta^{(2)}(\mathbf{v}\cdot\boldsymbol{\Delta}^{+}) + (\mathbf{v}\cdot\boldsymbol{\Delta}^{+})\Delta^{(2)}(\mathbf{v}\cdot\boldsymbol{\Delta}^{-})}{4\gamma m}\Bigg]\\
&-\frac{(2+n)}{64n^3}\,\Delta_v^{(4)}.
\end{aligned} \tag{5.24}$$

The result (5.24) can of course be simplified further but I show it in this form for clarity. Also, most operators in $\delta H_{\rm corr}$ are already in the Hamiltonian. Note that for $\mathbf{v}=0$, the correction term (5.24) reduces to the standard NRQCD improvement terms as in [111],

$$\delta H_{\rm corr}\Big|_{\mathbf{v}=0} = \frac{1}{24m}\sum_{j=1}^{3}\Delta_j^{+}\Delta_j^{-}\Delta_j^{+}\Delta_j^{-} - \frac{\left(\Delta^{(2)}\right)^2}{16n\,m^2}. \tag{5.25}$$

5.3 Renormalisation

In principle, all terms in the lattice moving NRQCD action must be multiplied by individual renormalisation coefficients c_i, to be determined by matching the effective theory to continuum QCD.

Nonperturbative adjustment of all coefficients is forbiddingly complicated due to the large number of couplings which have to be tuned simultaneously. A simple yet powerful method of including the biggest part of the radiative corrections is tadpole improvement, which was introduced in Sec. 2.7.1. In the present calculations, I use the tree-level values for the couplings, $c_i = 1$, but perform tadpole improvement.

With this choice, the remaining free parameters in the action are the heavy-quark mass and the boost velocity. The bare heavy-quark mass can easily be adjusted nonperturbatively so that the lattice result for a quarkonium mass matches the experimental value. Along with the heavy-quark mass, the boost velocity determines the size of the external momentum. We will discuss this in more detail in Sec. 5.3.2.

When lattice moving NRQCD is used to compute matrix elements of certain currents, these currents must also be matched to continuum QCD. This will be discussed in Sec. 8.5 of Chapter 8.

5.3.1 Tadpole improvement

As explained in Sec. 2.7.1, tadpole improvement is achieved by dividing the gauge links $U_\mu(x)$ in the lattice action by u_0, the mean link in Landau gauge. Before that, any factors of $U_\mu^\dagger(x)U_\mu(x) = 1$ should be cancelled. However, expanding out the whole action (5.11) in terms of products of U's would be too expensive for numerical calculations, and therefore link-pair cancellations are only taken into account separately within H_0 and δH. Also, no extra cancellations are made when derivative operators act on field strengths in δH. These conventions are consistent with the ones in the standard HPQCD lattice (non-moving) NRQCD action. Note that the majority of the link pair cancellations is still correctly accounted for. In appendix D of [100] it is shown that the difference to full cancellation is negligible.

5.3.2 Energy shift and external momentum renormalisation

The factor of $e^{-im\,u\cdot x\,\hat{\gamma}^0}$ in the moving NRQCD field redefinition (3.74) corresponds to a shift in the 4-momentum of a heavy quark by $P = m\,u = (\gamma m, \gamma m\mathbf{v})$. However, the shifts in energy and momentum will get renormalised.

Consider a hadron containing n_Q heavy quarks (here we also count antiquarks positively). On the lattice, an interpolating field for the hadron is constructed from ψ_v and ξ_v (see Chapter 6). This field is given a momentum $\mathbf{k}$ by inserting a phase $e^{i\mathbf{k}\cdot\mathbf{x}}$. The

physical momentum of the hadron is then

$$\mathbf{p} \;=\; n_Q\, Z_p\, \mathbf{P} + \mathbf{k} \quad \text{with} \quad \mathbf{P} = \gamma m \mathbf{v}, \tag{5.26}$$

where

$$Z_p = Z_\gamma Z_m Z_v \tag{5.27}$$

is the renormalisation of the bare external momentum $\mathbf{P}$. Here and in the following we assume that $\mathbf{v}$ points in one of the axis directions, so that only its magnitude is renormalised. Note that Z_γ and Z_v are not independent renormalisation constants; they are related through $\gamma = 1/\sqrt{1-\mathbf{v}^2}$.

The full (physical) energy of the hadron is given by

$$E = E_v(\mathbf{k}) + n_Q\, C_v, \tag{5.28}$$

where $E_v(\mathbf{k})$ is the energy obtained from the large-τ behaviour of the hadron two-point function and C_v is the renormalised energy shift

$$C_v = Z_m Z_\gamma \gamma m + E_0. \tag{5.29}$$

All renormalisation parameters introduced up to here can be written in terms of the three independent quantities Z_m, Z_v, E_0. At tree-level, one has $Z_m = Z_v = 1$ and $E_0 = 0$.

The combinations Z_p and C_v can be determined nonperturbatively from the dispersion relation of a hadron. Given expression (5.26) for the full (physical) momentum, we expect that, up to lattice artifacts,

$$\begin{aligned} E &= \sqrt{\mathbf{p}^2 + M_{\text{kin}}^2} \\ &= \sqrt{(n_Q\, Z_p\, \mathbf{P} + \mathbf{k})^2 + M_{\text{kin}}^2}\;, \end{aligned} \tag{5.30}$$

where M_{kin} is the kinetic mass of the hadron. Using (5.30) one can extract C_v, Z_p and M_{kin} from the energies at various non-zero lattice momenta in combination with the energy at $\mathbf{k} = 0$:

$$C_v \;=\; \frac{\mathbf{k}_\perp^2 - \left[E_v^2(\mathbf{k}_\perp) - E_v^2(0)\right]}{2\, n_Q \left[E_v(\mathbf{k}_\perp) - E_v(0)\right]}, \tag{5.31}$$

$$Z_p \;=\; \frac{E_v^2(\mathbf{k}_\parallel) - E_v^2(-\mathbf{k}_\parallel) + 2\, n_Q\, C_v \left[E_v(\mathbf{k}_\parallel) - E_v(-\mathbf{k}_\parallel)\right]}{4\, n_Q\, \mathbf{k}_\parallel \cdot \mathbf{P}}, \tag{5.32}$$

$$M_{\text{kin}} \;=\; \sqrt{(E_v(\mathbf{k}) + n_Q\, C_v)^2 - (n_Q\, Z_p\, \mathbf{P} + \mathbf{k})^2}. \tag{5.33}$$

Here, $\mathbf{k}_\parallel$ ($\mathbf{k}_\perp$) is a lattice momentum parallel (perpendicular) to $\mathbf{v}$. Equations (5.31) and (5.32) were first derived in [22].

My nonperturbative results for C_v, Z_p, and M_{kin} for the full action (3.81) will be presented in Chapter 6.

5.3.3 Reparametrisation invariance

The renormalisation parameter Z_p is expected to be close to 1 due to an approximate reparametrisation invariance [22], a symmetry that is exact in continuum HQET [97]. The HQET Lagrangian was derived in Sec. 3.3. Denoting the field $\tilde{\Psi}_+$ used there by Q_u, we have[1]

$$\begin{aligned}\mathcal{L} &= \overline{Q}_u \left(i\, u\cdot D - \frac{\not{D}_\perp^2}{2m} \right) Q_u \\ &= \overline{Q}_u \left(i\, u\cdot D - \frac{D_\perp^2}{2m} - \frac{ig}{8m}[\hat{\gamma}^\mu, \hat{\gamma}^\nu] F_{\mu\nu} \right) Q_u. \end{aligned} \tag{5.34}$$

The Lagrangian (5.34) is invariant under the transformation

$$\begin{aligned} u &\mapsto u + \epsilon, \\ Q_u &\mapsto e^{i\, m\, \epsilon\cdot x} \left(1 + \frac{\not{\epsilon}}{2} \right) Q_u, \\ \overline{Q}_u &\mapsto e^{-i\, m\, \epsilon\cdot x}\, \overline{Q}_u \left(1 + \frac{\not{\epsilon}}{2} \right), \end{aligned} \tag{5.35}$$

where ϵ is an infinitesimal change in the 4-velocity, satisfying $\epsilon \cdot u = 0$ so that $u^2 = 1$ is preserved. The symmetry (5.35) requires the coefficient of the operator $-D_\perp^2/(2m)$ to be 1. Absorbing an overall wave function renormalisation into the fields Q_u, $\overline{Q}_u$, there can be no radiative correction to this coefficient provided that the regulator respects reparametrisation invariance.

In moving NRQCD, time and space are not treated on an equal basis, and the truncation of the action at a given order in $1/m$ or $v_{\text{orb.}}$ breaks reparametrisation invariance [100]. However, when only selected terms are included the continuum Lagrangian may still possess an exact symmetry. This is the case for the incomplete Lagrangian

$$\mathcal{L} = \psi_v^\dagger \left(iD_0 + i\mathbf{v}\cdot\mathbf{D} + \frac{\mathbf{D}^2}{2\gamma m} \right) \psi_v, \tag{5.36}$$

which is invariant under

$$\begin{aligned} \mathbf{v} &\mapsto \mathbf{v} + \boldsymbol{\epsilon}, \\ \psi_v &\mapsto e^{-i\gamma m \boldsymbol{\epsilon}\cdot\mathbf{x}}\, \psi_v, \\ \psi_v^\dagger &\mapsto e^{i\gamma m \boldsymbol{\epsilon}\cdot\mathbf{x}}\, \psi_v^\dagger, \end{aligned} \tag{5.37}$$

with infinitesimal $\boldsymbol{\epsilon}$ satisfying $\boldsymbol{\epsilon}\cdot\mathbf{v} = 0$. The symmetry (5.37) implies that the two terms $i\mathbf{v}\cdot\mathbf{D}$ and $\mathbf{D}^2/(2\gamma m)$ in (5.36) must renormalise by the same factor, so that $Z_p = 1$.

[1] No $\perp$ labels are needed in the $[\hat{\gamma}^\mu, \hat{\gamma}^\nu] F_{\mu\nu}$ term, since $\overline{Q}_u u^\mu [\hat{\gamma}^\mu, \hat{\gamma}^\nu] Q_u = 0$.

The operator $-(\mathbf{v}\cdot\mathbf{D})^2/(2\gamma m)$, which was omitted in (5.36), breaks the reparametrisation invariance. An additional breaking in lattice moving NRQCD arises from lattice artefacts. The remaining approximate symmetry still guarantees that Z_p is close to 1 for moderate boost velocities, as is confirmed by my nonperturbative calculations (Chapter 6) and by perturbation theory.

5.3.4 Perturbation theory

The heavy-quark renormalisation parameters Z_ψ (the wave function renormalisation), Z_m, Z_v, E_0, and the corresponding Z_p and C_v have also been calculated in automated one-loop lattice perturbation theory. There, one computes the inverse heavy-quark propagator $G^{-1}(k) = G_0^{-1}(k) - \Sigma(k)$, where $G_0(k)$ is the tree-level propagator and $\Sigma(k)$ is the self-energy at one-loop order. The renormalisation parameters can then be extracted from the expansion of $\Sigma(k)$ in powers of the momentum; the details can be found in [100]. Results for a simple action at order $1/m$ have been obtained in [112]; these calculations have been extended to an action similar to (5.12, 5.13) by Lew Khomskii [113]. New calculations for exactly the action (5.12, 5.13) have then been performed by Eike Müller [114] and are published in [100]. I will compare the perturbative results for C_v and Z_p to my nonperturbative results in Sec. 6.3 of Chapter 6.

Perturbation theory is thought to be a reasonably good approximation as the momenta giving the dominant contributions to the radiative corrections are of the order π/a, and the running coupling α_s is small at this scale. Note that this requires $ma > 1$ and $\Lambda_{\mathrm{QCD}} a \ll 1$ simultaneously. In order to obtain a good convergence, tadpole improvement is crucial [77].

Perturbative calculations of the couplings c_i in the action are also underway. So far, results have been obtained for the coefficients of the 4-th-order derivative operators at $\mathbf{v} = 0$ [115, 116].

5.3.5 High-β methods

Lattice perturbation theory for highly improved actions is already hard at one-loop level due to the extremely complicated Feynman rules, and automated methods are used to derive them (see e.g. [117]). Two-loop calculations for the full lattice moving NRQCD action seem to be out of reach currently.

An alternative approach has been introduced in [118]. There, nonperturbative Monte-Carlo simulations are performed at very weak coupling (high $\beta = 2N_c/g^2$) and in Coulomb

gauge. Results for a short-distance observable are computed at several values of β and then fitted by a polynomial in $\alpha_s = g^2/(4\pi)$. The fit results then give the perturbative coefficients, provided that non-perturbative effects are negligible. The linear term can be constrained by the 1-loop perturbative result, which stabilises the fit. Certain nonperturbative finite-volume effects can be suppressed by using twisted boundary conditions [119].

As the inclusion of dynamical fermions is computationally very expensive, most high-β calculations are done in the quenched limit, i.e. in pure gauge theory. However, at order α_s^2 only a handful of diagrams contain fermion loops and these may be accessible in perturbation theory. The contribution from these diagrams can be combined with the gluonic two-loop coefficient from the high-β simulation to give the full two-loop result.

High-β simulations have been carried out for a simple $\mathcal{O}(1/m)$ lattice moving NRQCD action in [25] and further calculations are currently underway [116].

5.4 Signal-to-noise ratio

The signal-to-noise ratio for correlation functions involving heavy quarks implemented with lattice mNRQCD can be estimated using the same general methods as in Sec. 4.4.

Note that for a hadronic correlation function at arbitrary lattice momentum $\mathbf{k}$ and boost velocity $\mathbf{v}$ the variance correlator always contains contributions from hadrons at rest ($\mathbf{k} = 0$, $\mathbf{v} = 0$). For example, for a B meson two-point function in moving NRQCD one obtains

$$\frac{C(\tau)}{\sigma(\tau)} \propto e^{-\left(E_{Q\bar{q}}(\mathbf{p}) - \frac{1}{2}\left[E_{Q\bar{Q}}(0) + m_\pi\right]\right)\tau}, \tag{5.38}$$

where

$$\mathbf{p} = \mathbf{k} + Z_p \gamma m \mathbf{v}. \tag{5.39}$$

Thus, the noise is expected to grow exponentially as the boost velocity is increased at a fixed $\mathbf{k}$. I do indeed see this behaviour in my numerical calculations (cf. Chapter 6). Note that this is not a disadvantage of moving NRQCD compared to standard NRQCD. The amount of noise depends on $\mathbf{p}$; for a comparable momentum in non-moving NRQCD one gets a similar amount of noise (and higher discretisation and relativistic errors).

Chapter 6

Nonperturbative tests of moving NRQCD

In this chapter, I report on a range of nonperturbative tests of the full lattice moving NRQCD action (5.12, 5.13) that I performed by computing heavy-heavy (bottomonium) and heavy-light (B_s) two-point functions in dynamical 2+1 flavour lattice QCD. These tests include the calculation of renormalisation parameters, decay constants and energy splittings at several values for the boost velocity. Lattice units are used throughout this chapter.

Previous nonperturbative tests of mNRQCD for a simple $\mathcal{O}(1/m)$ action and with quenched gauge field configurations (i.e. without dynamical quarks) were reported in [22, 23, 24, 25].

6.1 Tests with bottomonium

6.1.1 Calculation of the two-point functions

We begin by constructing "smeared" interpolating fields for quarkonium. To demonstrate the effect of the moving NRQCD field redefinition, we start the construction with the QCD fields $\overline{\Psi}$, Ψ. A meson with momentum $\mathbf{p}$ can be obtained from

$$O_\Gamma(\tau, \mathbf{p}) = \frac{1}{\sqrt{V}} \sum_{\mathbf{x},\mathbf{y}} \overline{\Psi}(\tau, \mathbf{x}) \Gamma(\mathbf{x} - \mathbf{y}) \Psi(\tau, \mathbf{y}) e^{-i\mathbf{p}\frac{\mathbf{x}+\mathbf{y}}{2}} \tag{6.1}$$

where $\Gamma(\mathbf{r})$ is a Dirac-matrix-valued smearing function, and $V = L^3$ is the spatial volume. I do not include gauge links in $\Gamma(\mathbf{r})$; instead I work with gauge configurations fixed to

Name	$\Gamma(\mathbf{r})$
$\eta_b(1S)$	$\exp[-\lvert\mathbf{r}\rvert/r_s]\ \hat{\gamma}_5$
$\eta_b(2S)$	$[1-\lvert\mathbf{r}\rvert/(2r_s)]\ \exp[-\lvert\mathbf{r}\rvert/(2r_s)]\ \hat{\gamma}_5$
$\Upsilon(1S)$	$\exp[-\lvert\mathbf{r}\rvert/r_s]\ \hat{\gamma}^j$
$\Upsilon(2S)$	$[1-\lvert\mathbf{r}\rvert/(2r_s)]\ \exp[-\lvert\mathbf{r}\rvert/(2r_s)]\ \hat{\gamma}^j$
$\chi_{b1}(1P)$	$\exp[-\lvert\mathbf{r}\rvert/(2r_s)]\ (\mathbf{r}\times\hat{\gamma})^j/r_s$

Table 6.1: The bottomonium states and corresponding smearing functions used in the nonperturbative tests of moving NRQCD. More details on bottomonium can be found in Sec. 7.1 of Chapter 7.

Coulomb gauge[1]. The bottomonium states and corresponding functions $\Gamma(\mathbf{r})$ used here are listed in Table 6.1. In addition to these, we also consider the local function

$$\Gamma(\mathbf{r}) = \delta_{\mathbf{r},0}\ \hat{\gamma}_5\hat{\gamma}^0, \tag{6.2}$$

which corresponds to the temporal axial current

$$J_5^0(x) = \overline{\Psi}(x)\ \hat{\gamma}_5\hat{\gamma}^0\ \Psi(x). \tag{6.3}$$

The lowest state above the vacuum that couples to (6.3) is also the $\eta_b(1S)$ meson.

We now express $\overline{\Psi}$ and Ψ through the Euclidean version of the tree-level moving NRQCD field redefinition (3.74). To lowest order we have

$$\begin{aligned}
\Psi(x) &= \frac{1}{\sqrt{\gamma}}\ S(\Lambda)\ e^{-i\gamma m(-i\tau-\mathbf{v}\cdot\mathbf{x})\hat{\gamma}^0}\Psi_v(x), \\
\overline{\Psi}(x) &= \frac{1}{\sqrt{\gamma}}\ \overline{\Psi_v}(x)\ e^{i\gamma m(-i\tau-\mathbf{v}\cdot\mathbf{x})\hat{\gamma}^0}\ \overline{S(\Lambda)}.
\end{aligned} \tag{6.4}$$

Note that for calculations of the spectrum no higher-order terms or radiative corrections are needed in the field redefinition; it suffices that the state of interest has a non-vanishing overlap with the interpolating field.

Let us, for example, consider the Υ states with polarisation $j = 1, 2, 3$. We allow different radial smearing at source and sink, so that $\Gamma_{\rm sc}(\mathbf{r}) = \hat{\gamma}^j\ f_{\rm sc}(\mathbf{r})$ and $\Gamma_{\rm sk}(\mathbf{r}) =$

[1]On the lattice, Coulomb gauge is obtained by minimising the functional $F[U] = -\sum_x \sum_{j=1}^3 \mathrm{Tr}\big[U_j(x) + U_j^\dagger(x)\big]$ through gauge transformations (2.38) of the link variables U_j.

$\hat{\gamma}^j\, f_{\rm sk}(\mathbf{r})$. Using

$$\overline{S(\Lambda)}\,\hat{\gamma}^j\, S(\Lambda) = \Lambda^j{}_\mu \hat{\gamma}^\mu, \tag{6.5}$$

we obtain

$$\begin{aligned} O_{\Gamma_{\rm sk}}(\tau,\mathbf{p})O^\dagger_{\Gamma_{\rm sc}}(\tau',\mathbf{p}) &= \frac{1}{V}\frac{1}{\gamma^2}e^{-2\gamma m(\tau-\tau')}\sum_{\mathbf{x},\mathbf{y},\mathbf{x}',\mathbf{y}'} e^{-i\mathbf{k}\frac{\mathbf{x}+\mathbf{y}}{2}} f_{\rm sk}(\mathbf{x}-\mathbf{y}) e^{i\mathbf{k}\frac{\mathbf{x}'+\mathbf{y}'}{2}} f_{\rm sc}(\mathbf{x}'-\mathbf{y}') \\ &\quad\times\ \Lambda^j{}_l \Lambda^j{}_m \xi^\dagger_v(\tau,\mathbf{x})\sigma^l\psi_v(\tau,\mathbf{y})\psi^\dagger_v(\tau',\mathbf{y}')\sigma^m\xi_v(\tau',\mathbf{x}') + \ \ldots \end{aligned} \tag{6.6}$$

(no summation over j here) where the ellipsis denotes terms that do not contribute to the connected meson correlator for $\tau > \tau'$. In Eq. (6.6) we have $\mathbf{k} = \mathbf{p} - 2\gamma m\mathbf{v}$. This is the tree-level mNRQCD momentum shift, as expected. On the lattice the momentum $\mathbf{k}$ rather than $\mathbf{p}$ has a definite value; $k_j = 2\pi\, n_j/L$ where L is the spatial extent of the lattice. The full momentum $\mathbf{p}$ will be given by (5.26) with $n_Q = 2$.

According to Eqs. (2.24)and (2.92), the expectation value of (6.6) can be obtained as

$$\begin{aligned} \langle\, O_{\Gamma_{\rm sk}}\, O^\dagger_{\Gamma_{\rm sc}}\,\rangle &= \frac{1}{N}\sum_U \frac{1}{V}\frac{1}{\gamma^2}e^{-2\gamma m(\tau-\tau')}\sum_{\mathbf{x},\mathbf{y},\mathbf{x}',\mathbf{y}'} e^{-i\mathbf{k}\frac{\mathbf{x}+\mathbf{y}}{2}} f_{\rm sk}(\mathbf{x}-\mathbf{y}) e^{i\mathbf{k}\frac{\mathbf{x}'+\mathbf{y}'}{2}} f_{\rm sc}(\mathbf{x}'-\mathbf{y}') \\ &\quad\times\ \Lambda^j{}_l \Lambda^j{}_m \mathrm{Tr}\left(\sigma^l\left[G^{(+\mathbf{v})}_{\psi_v}(\tau,\mathbf{y},\tau',\mathbf{y}')\right]\sigma^m\left[G^{(-\mathbf{v})}_{\psi_v}(\tau,\mathbf{x},\tau',\mathbf{x}')\right]^\dagger\right), \end{aligned} \tag{6.7}$$

where we average over N gauge configurations U. The trace is in (6.7) is over colour and spin indices. We have also used Eq. (3.87) to express the antiquark green function $G^{(+\mathbf{v})}_{\xi_v}$ in terms of the quark green function $G^{(-\mathbf{v})}_{\psi_v}$ with the opposite boost velocity.

The summations over all quark and antiquark source locations would render the lattice computation too expensive. Therefore, using translation invariance, we remove the summation over the antiquark source location $\mathbf{x}'$, and correspondingly remove the factor of $1/V$.

Note that the mNRQCD field redefinition also introduced the factor of $e^{-2\gamma m(\tau-\tau')}$ in the two-point function, which corresponds to the tree-level energy shift. In the later analysis, only energy differences will be measured, and so we remove this trivial factor. Hence, the quantity

$$\begin{aligned} C(\Gamma_{\rm sk},\Gamma_{\rm sc},\mathbf{k},\tau,\tau') &= \frac{1}{N}\sum_U \frac{1}{\gamma^2}\sum_{\mathbf{x},\mathbf{y}} e^{-i\mathbf{k}\frac{\mathbf{x}+\mathbf{y}}{2}} f_{\rm sk}(\mathbf{x}-\mathbf{y}) \\ &\quad\times\ \Lambda^j{}_l \Lambda^j{}_m\ \mathrm{Tr}\left(\sigma^l\left[\widetilde{G}^{(+\mathbf{v})}_{\psi_v}(\tau,\mathbf{y},\tau',\mathbf{x}')\right]\sigma^m\left[G^{(-\mathbf{v})}_{\psi_v}(\tau,\mathbf{x},\tau',\mathbf{x}')\right]^\dagger\right) \end{aligned} \tag{6.8}$$

with

$$\widetilde{G}^{(+\mathbf{v})}_{\psi_v}(\tau,\mathbf{y},\tau',\mathbf{x}') = \sum_{\mathbf{y}'} e^{i\mathbf{k}\frac{\mathbf{x}'+\mathbf{y}'}{2}} f_{\rm sc}(\mathbf{x}'-\mathbf{y}')\, G^{(+\mathbf{v})}_{\psi_v}(\tau,\mathbf{y},\tau',\mathbf{y}') \tag{6.9}$$

is computed on the lattice. The convoluted Green function (6.9) can be computed efficiently by using the function

$$e^{i\mathbf{k}\frac{\mathbf{x}'+\mathbf{y}'}{2}} f_{\rm sc}(\mathbf{x}'-\mathbf{y}') \tag{6.10}$$

as the initial condition in the mNRQCD evolution Eq. (5.10). The momentum-dependent phase factor $\exp(i\mathbf{k}\cdot(\mathbf{x}'+\mathbf{y}')/2)$ at the source improves the overlap with the momentum considered. I used this factor in my computations; however, note that since there is no sum over $\mathbf{x}'$, one may also omit this factor to allow the calculation of correlators with different momenta from the same source.

To maintain the periodic boundary conditions, I set $f(\mathbf{r})$ to zero for $|\mathbf{r}| > R_s$ with some cut-off radius R_s smaller than half the length of the lattice.

I performed the computations using 400 MILC gauge configurations (fixed to Coulomb gauge) of size $20^3 \times 64$ with 2+1 flavors of rooted staggered light quarks, at $\beta = 6.76$ [120, 121, 87]. The light quark masses were $m_u = m_d = 0.007$ and $m_s = 0.05$ (in the MILC convention for lattice masses). The Goldstone pion mass is about 300 MeV, and the pion taste splittings range from $(m_{\pi_A} - m_{\pi_5}) \approx 110$ MeV to $(m_{\pi_I} - m_{\pi_5}) \approx 240$ MeV [121].

The Landau gauge mean link, used for tadpole improvement in the mNRQCD action, was $u_0 = 0.836$. The inverse lattice spacing of these "coarse" MILC configurations is known to be approximately 1.6 GeV [108].

The bare heavy quark mass was set to $m = 2.8$, which gave the correct Υ kinetic masses using non-moving NRQCD [108]. The boost velocity $\mathbf{v}$ was always pointing in the x-direction. The stability parameter was set to $n = 2$.

In order to increase statistics, on each gauge configuration I computed between 16 and 120 correlators with different origins $(\mathbf{x}', \tau')$ spread over the lattice. These origins were also shifted randomly to reduce autocorrelations. The smearing parameter r_s (see Table 6.1) was set to 1 for the S wave states and 0.5 for the P wave states.

6.1.2 Fitting of the two-point functions

In accordance with Eq. (2.34), I fitted the two-point correlators $C(\Gamma_{\rm sk}, \Gamma_{\rm sc}, \mathbf{k}, \tau, \tau')$ for a given momentum $\mathbf{k}$ by a function of the form

$$\sum_{n=0}^{n_{\rm exp}-1} A_n(\Gamma_{\rm sk})\, A_n^*(\Gamma_{\rm sc})\, e^{-E_{v,n}(\tau-\tau')}, \tag{6.11}$$

where $E_{v,n}$ is the (shifted) energy of n-th state and $A_n(\Gamma)$ is, up to the normalisation factor of $\sqrt{2E_n}$, the (real) amplitude for this state to be created by the operator with smearing function $\Gamma(\mathbf{r})$. For the excited states ($n > 0$) I actually used the quantities

$$\begin{aligned} \Delta E_{v,n} &\equiv E_{v,n+1} - E_{v,n}, \\ B_n(\Gamma) &\equiv A_n(\Gamma)/A_0(\Gamma) \end{aligned} \tag{6.12}$$

as parameters in the fit. In general, a matrix of correlators with different smearings at source and sink was fitted simultaneously. The Bayesian method from [122] was used to stabilise the fits. The number of exponentials n_{exp} in (6.11) was increased until the fit results for the states of interest (the ground state, or the first few low-lying states) become independent of n_{exp}. More details on the fitting are given in Appendix C.

6.1.3 Kinetic mass, energy shift and external momentum renormalisation

Results for the $\eta_b(1S)$ kinetic mass M_{kin} and the renormalisation parameters Z_p, C_v, calculated with Eqs. (5.33), (5.32), and (5.31), are shown in Table 6.2. The energies were obtained from 6-exponential fits to 2×2 matrix correlators with the $\eta_b(1S)$ smearing (cf. Table 6.1) and the local operator given by (6.2). Sample fits at $\mathbf{v} = 0$ and $\mathbf{v} = 0.6$ are shown in Fig. 6.1.

For the calculation of C_v using (5.31), I averaged the results over the 4 different perpendicular lattice momenta

$$\mathbf{k}_\perp \in \left\{ \frac{2\pi}{L}(0, \pm 1, 0),\ \frac{2\pi}{L}(0, 0, \pm 1) \right\}. \tag{6.13}$$

The momentum parallel to the boost velocity in (5.32) was chosen to be $\mathbf{k}_\parallel = \frac{2\pi}{L}(1, 0, 0)$, and in (5.33), for the measurement of M_{kin}, I used $\mathbf{k} = 0$.

In order to fully take into account correlations in the energies at different momenta, I used the bootstrap method. This is described in Appendix C.

Because the lattice is of finite extent, $L = 20$ in this case, the estimates for C_v and Z_p are affected by the choice of momenta in (5.31) and (5.32) since the formulae are accurate only in the limit that the momenta are infinitesimal. Note that the uncertainty due to using non-infinitesimal momenta will decrease for larger lattices for which smaller momenta are available.

To estimate the size of the resulting systematic error I also performed the calculations

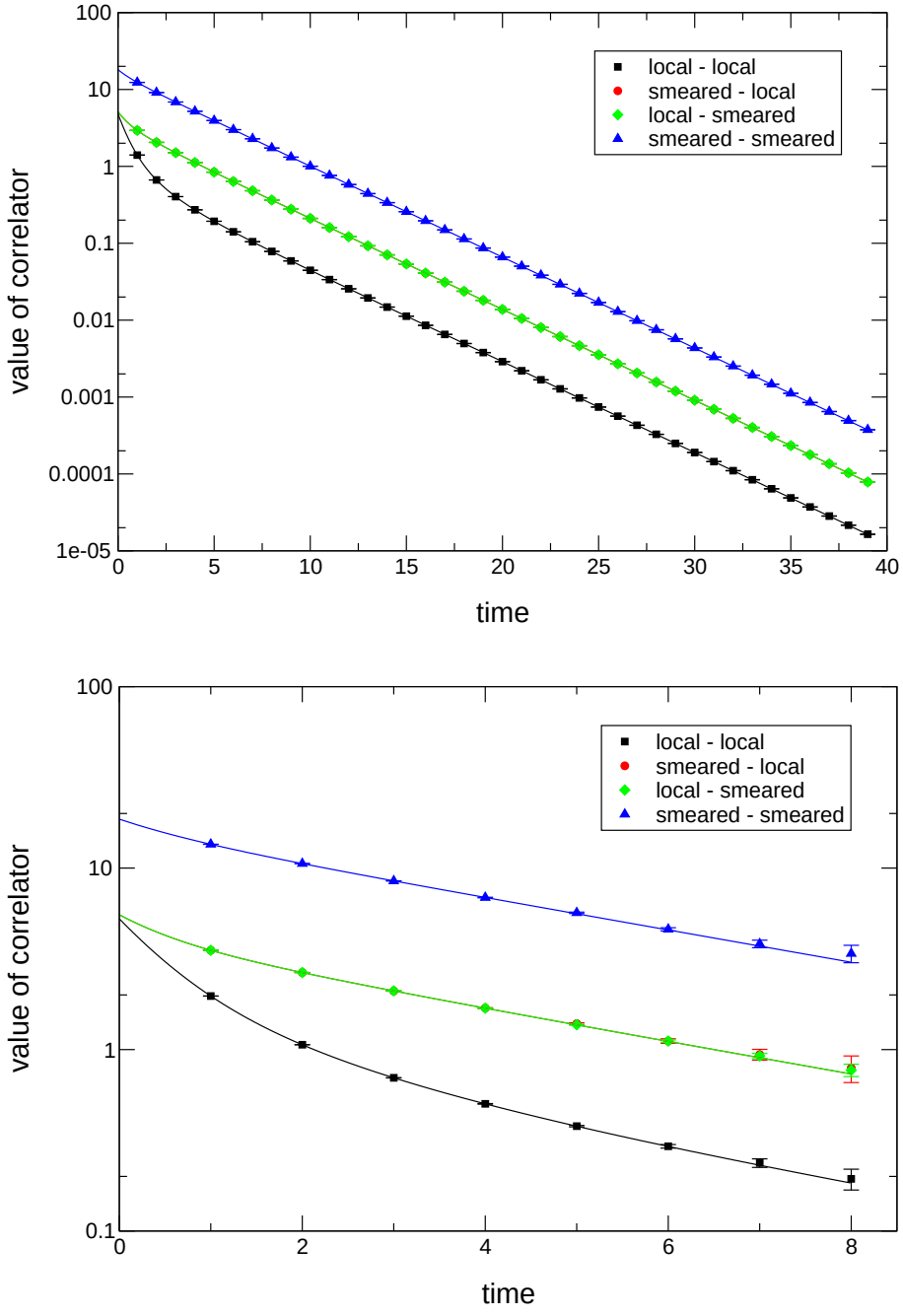

Figure 6.1: Fits to η_b matrix correlators (local and $1S$ smearing) at $\mathbf{k} = 0$ and $\mathbf{v} = 0$ (upper panel), $|\mathbf{v}| = 0.6$ (lower panel). The fits have $n_{\rm exp} = 6$ and $\tau_{\rm min} = 1$. At non-zero momentum $\mathbf{p} = \mathbf{k} + 2Z_p\gamma m\mathbf{v}$ the noise in the two-point function increases exponentially with the Euclidean time. For $|\mathbf{v}| = 0.6$, the errors for the points beyond $\tau \sim 8$ are so large that these points do not give any useful information and hence are not shown here.

	$\lvert\mathbf{k}_\perp\rvert = \lvert\mathbf{k}_\parallel\rvert = 2\pi/L$			$\lvert\mathbf{k}_\perp\rvert = \lvert\mathbf{k}_\parallel\rvert = 4\pi/L$		
$\lvert\mathbf{v}\rvert$	Z_p	M_{kin}	$C_v/(\gamma m)$	Z_p	M_{kin}	$C_v/(\gamma m)$
0	—	5.974(48)	1.0182(86)	—	5.979(37)	1.0190(65)
0.2	1.008(19)	5.95(10)	1.015(18)	1.009(12)	5.969(62)	1.017(11)
0.4	0.9953(78)	5.931(44)	1.0084(77)	0.9830(65)	5.954(40)	1.0101(70)
0.6	0.898(27)	6.22(18)	1.010(28)	0.843(27)	6.37(15)	1.011(21)

Table 6.2: Nonperturbative results (using the $\eta_b(1S)$) for M_{kin}, Z_p, C_v.

with the larger momenta

$$\mathbf{k}_\perp \in \left\{ \frac{2\pi}{L}(0, \pm 2, 0),\ \frac{2\pi}{L}(0, 0, \pm 2) \right\}, \qquad \mathbf{k}_\parallel = \frac{2\pi}{L}(2, 0, 0). \tag{6.14}$$

For C_v, the results from $|\mathbf{k}_\perp| = 2\pi/L$ agree with those obtained from $|\mathbf{k}_\perp| = 4\pi/L$ within statistical errors, indicating that the systematic error is small and does not increase significantly when increasing the momentum perpendicular to $\mathbf{v}$ in the measurement. For the measurement of Z_p at $|\mathbf{v}| = 0.6$ I find a 6% (2σ) change in Z_p when going from $|\mathbf{k}_\parallel| = 2\pi/L$ to $|\mathbf{k}_\parallel| = 4\pi/L$. At $|\mathbf{v}| = 0.4$ and smaller boost velocities the results are equal within statistical errors. For the kinetic mass, which depends on both C_v and Z_p, I again find agreement within statistical errors between the results from the two different momenta for all boost velocities considered. At small velocities, I find that both Z_p and $C_v/(\gamma m)$ are close to their tree-level value of 1, demonstrating that the renormalisations are small.

6.1.4 Decay constant

Moving NRQCD is designed for the calculation of form factors (see Chapter 8). Thus, it is important to perform tests not only for spectral quantities but also for decay constants.

For the $\eta_b(1S)$ meson, I calculated the decay constant f defined by

$$\langle 0|\mathrm{J}_5^\mu(0)|\eta_b(1S), \mathbf{p}\rangle = i f\, p^\mu. \tag{6.15}$$

For simplicity, I only considered the temporal component. Following the discussion in Sec. 2.2, the matrix element (6.15) can be computed from the 2×2 matrix correlators already used in Sec. 6.1.3. These include the local operator given by (6.2), which corresponds to the lowest-order tree-level axial current. With the notation from Sec. 6.1.2, we

define

$$A \equiv A_0(\Gamma)\Big|_{\Gamma(\mathbf{r})=\delta_{\mathbf{r},0}\,\hat{\gamma}_5\hat{\gamma}^0}\,. \tag{6.16}$$

Then, according to Eq. (2.34) we have

$$A^2 = \frac{1}{2E}|\langle 0|\mathsf{J}_5^\mu(0)|\eta_b(1S),\mathbf{p}\rangle|^2 = \frac{1}{2E}f^2E^2, \tag{6.17}$$

and hence

$$f = \frac{2A}{E}, \tag{6.18}$$

where E is the physical energy of the $\eta_b(1S)$ meson. Using Eq. (5.28) with $n_Q = 2$, we finally obtain

$$f = A\sqrt{\frac{2}{E_v(\mathbf{k}) + 2\,C_v}}. \tag{6.19}$$

For the energy shift C_v in (6.19), I used Eq. (5.31) with $|\mathbf{k}_\perp| = 2\pi/L$.

The momentum of the meson is given by $\mathbf{p} = 2Z_p\gamma m\mathbf{v} + \mathbf{k}$. The decay constant is a Lorentz scalar and should ideally be independent of the value of $\mathbf{p}$ used to compute it.

In the following I compare two methods of reaching large $|\mathbf{p}|$. First, at $\mathbf{v} = 0$, i.e. with standard NRQCD, I computed the decay constant at large non-zero lattice momentum $\mathbf{k}$; the results are shown in Table 6.3. Second, I computed the decay constant with $\mathbf{k} = 0$ and three different boost velocities $\mathbf{v}$; the results are shown in Table 6.4. In this case the uncertainty in Z_p (determined nonperturbatively from Eq. (5.32)) leads to an uncertainty in the meson momentum.

A plot of the decay constant against the total momentum (with Z_p from (5.32) with $|\mathbf{k}_\parallel| = 2\pi/L$) for the two methods is shown in Fig. 6.2. With NRQCD we see a strong dependence on $\mathbf{p}$ due to both relativistic and discretisation errors. With moving NRQCD the $\mathbf{p}$-dependence is very small, giving evidence that the formalism works very well. Small deviations from the constant behaviour are still expected here, since only the leading-order current was used; i.e. T_{FWT} and A_{D_t} were set to unity in (3.74) for this calculation.

$\lvert\mathbf{p}\rvert L/(2\pi)$	$\lvert\mathbf{p}\rvert$	f
0	0	0.4724(23)
1	0.31416	0.4731(23)
2	0.62832	0.4755(24)
3	0.94248	0.4772(43)
4	1.25664	0.4835(77)
5	1.57080	0.4971(78)
6	1.88496	0.5209(46)
7	2.19911	0.5527(44)
8	2.51327	0.6006(45)
9	2.82743	0.6740(49)
10	3.14159	0.715(29)

Table 6.3: $\eta_b(1S)$ decay constant with standard NRQCD (i.e. $\mathbf{v} = 0$) computed with several values of meson momentum $|\mathbf{p}|$ by varying $|\mathbf{k}|$.

$\lvert\mathbf{v}\rvert$	$\lvert\mathbf{p}\rvert$	f
0	0	0.4724(23)
0.2	1.152(22)	0.4739(38)
0.4	2.433(19)	0.4810(36)
0.6	3.77(11)	0.499(11)

Table 6.4: $\eta_b(1S)$ decay constant with mNRQCD at $\mathbf{k} = 0$ computed with several values of meson momentum $|\mathbf{p}|$ by varying $|\mathbf{v}|$.

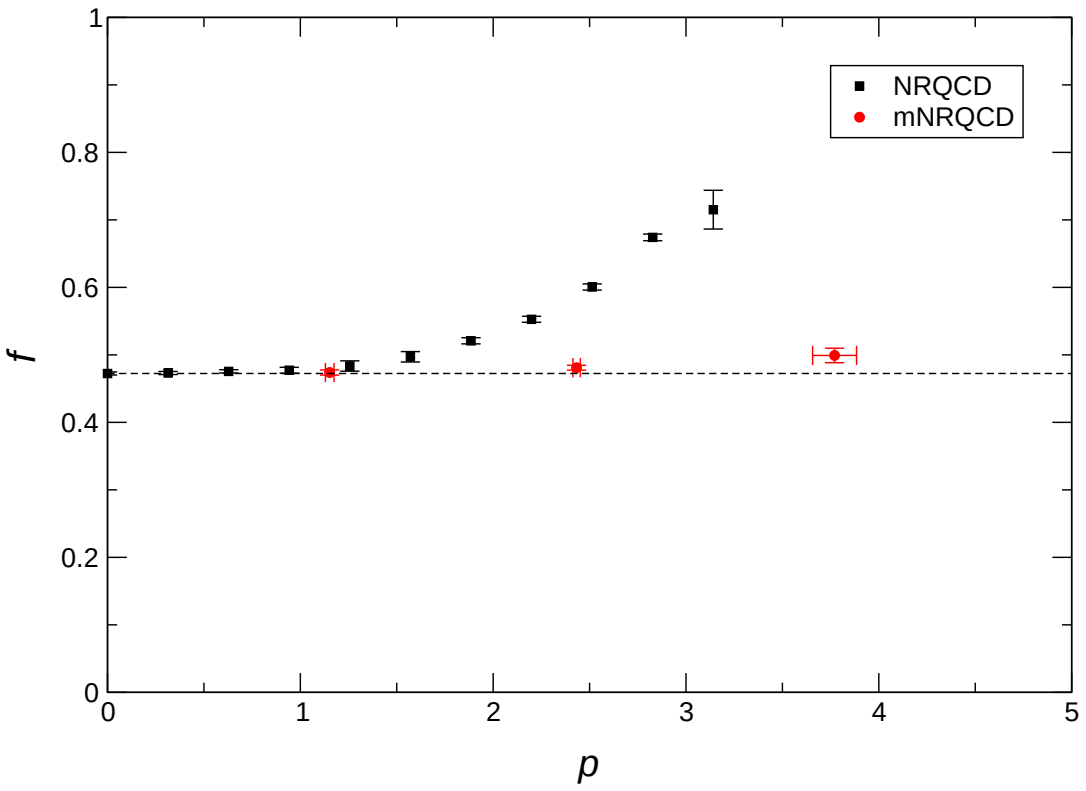

Figure 6.2: Heavy-heavy decay constant in NRQCD and mNRQCD for different values of the meson's momentum, $|\mathbf{p}|/(2\pi/L) = 0 \ldots 10$ (NRQCD) and $\mathbf{p} = Z_p\, 2\gamma m \mathbf{v}$ for $|\mathbf{v}| = 0.2, 0.4, 0.6$ (mNRQCD). The horizontal line indicates the value at $\mathbf{p} = 0$.

$\|\mathbf{v}\|$	$\Delta E_v(0)$	$\frac{\Delta E_v(0)}{\Delta E_0(0)}$
0.0	0.3334(68)	1
0.2	0.329(10)	0.986(37)
0.4	0.320(15)	0.958(48)
0.6	0.20(11)	0.59(33)

Table 6.5: $\Upsilon(2S) - \Upsilon(1S)$ energy splitting as a function of the boost velocity.

$\|\mathbf{v}\|$	$\Delta E_v(0)$	$\frac{\Delta E_v(0)}{\Delta E_0(0)}$
0.0	0.2703(89)	1
0.2	0.264(12)	0.976(56)
0.4	0.270(23)	0.998(91)
0.6	0.227(57)	0.84(21)

Table 6.6: $\chi_{b1}(1P) - \Upsilon(1S)$ energy splitting as a function of the boost velocity.

6.1.5 Energy splittings

I also studied the velocity-dependence of various energy splittings between the bottomonium states listed in Table 6.1. For the Υ and η_b states, I used 6-exponential 2×2 matrix fits with the $1S$ and $2S$ smearings; for the χ_{b1} states a 6-exponential single-correlator fit with the $1P$ smearing at both source and sink was used. The results for the $\Upsilon(2S) - \Upsilon(1S)$, $\chi_{b1}(1P) - \Upsilon(1S)$ and $\Upsilon(1S) - \eta_b(1S)$ splittings are listed in Tables 6.5, 6.6 and 6.7, respectively.

Note that the energy splittings are not Lorentz scalars. Using (5.30), we expect that the splitting between two states A and B at zero lattice momentum is given by

$$\begin{aligned} \Delta E_v(0)|_{\mathbf{v}} \equiv E_v^A(0) - E_v^B(0) &= \sqrt{(2Z_p\gamma m\mathbf{v})^2 + (M_{\rm kin}^A)^2} \\ &\quad - \sqrt{(2Z_p\gamma m\mathbf{v})^2 + (M_{\rm kin}^B)^2}. \end{aligned} \tag{6.20}$$

If we set $Z_p = 1$ and expand the splitting at velocity $\mathbf{v}$ relative to $\mathbf{v} = 0$ in powers of the

$\lvert\mathbf{v}\rvert$	$\Delta E_v(0)\lvert_{\mathbf{v}}$	$\frac{\Delta E_v(0)\lvert_{\mathbf{v}}}{\Delta E_v(0)\lvert_{\mathbf{0}}}$
0.0	0.031469(98)	1
0.2	0.03039(20)	0.9656(71)
0.4	0.02837(85)	0.901(27)
0.6	0.0281(28)	0.894(88)

Table 6.7: $\Upsilon(1S) - \eta_b(1S)$ energy splitting as a function of the boost velocity.

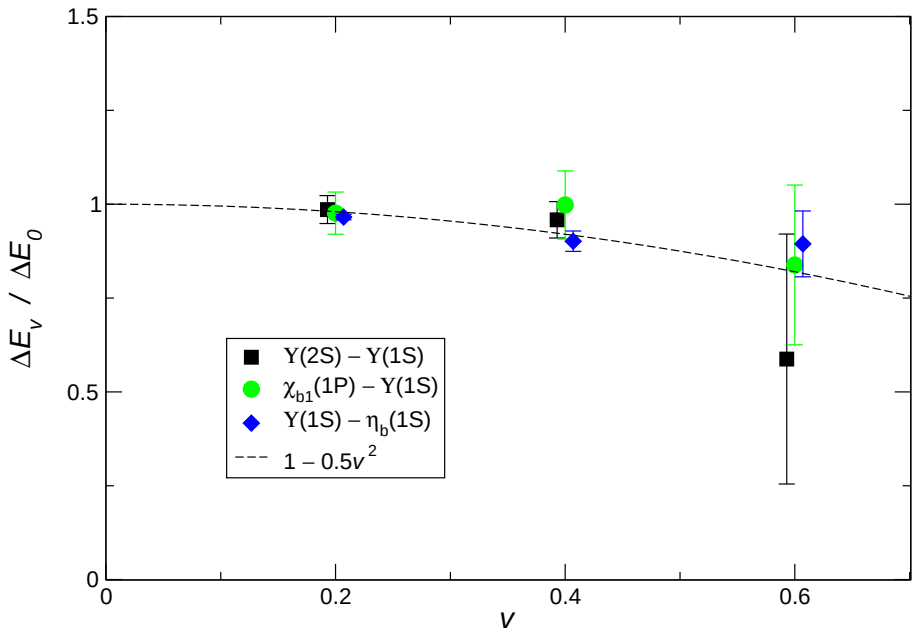

Figure 6.3: Bottomonium energy splittings relative to $\mathbf{v} = 0$ as a function of the boost velocity. Points are offset horizontally for legibility. The data agree with an estimate for the leading $\mathbf{v}^2$ dependence (see text).

$\|\mathbf{v}\|$	$\Delta E_v(0)\|_1$	$\Delta E_v(0)\|_2$	$\Delta E_v(0)\|_3$
0	−0.000009(63)	−0.000039(68)	0.000053(73)
0.2	−0.00012(26)	−0.00005(28)	0.00017(30)
0.4	−0.00046(56)	0.00055(62)	−0.00010(57)
0.6	−0.0176(96)	0.0107(62)	0.0069(75)

Table 6.8: Dependence of the $\Upsilon(1S)$ energy on the polarisation direction. $\Delta E_v(0)|_j$ is the difference between $E_v(0)|_j$ and the polarisation-averaged energy.

boost velocity, we obtain

$$\frac{\Delta E_v(0)|_{\mathbf{v}}}{\Delta E_v(0)|_{\mathbf{0}}} = 1 - \underbrace{\left(\frac{2m^2}{M^A_{\rm kin}\, M^B_{\rm kin}}\right)}_{\approx 0.5} \mathbf{v}^2 + \mathcal{O}(\mathbf{v}^4), \tag{6.21}$$

that is, we expect a quadratic decrease like $1 - 0.5|\mathbf{v}|^2$. The numerical results, shown in Fig. 6.3, are consistent with this estimate as desired.

Finally, for the $\Upsilon(1S)$ meson, I studied the dependence of the energy on the polarisation direction. If moving NRQCD works well, then there should be no difference for polarisations parallel and perpendicular to the boost velocity. In Table 6.8 I show the difference between the energy with definite polarisation direction, $E_v(0)|_j$ and the polarisation-direction-averaged energy $\frac{1}{3}(E_v(0)|_1 + E_v(0)|_2 + E_v(0)|_3)$. No significant dependence on the polarisation direction can be seen (except maybe at $|\mathbf{v}| = 0.6$, where a 1.8σ deviation in the energies was found).

6.2 Tests with B_s mesons

The results given in Sec. 6.1 show that lattice mNRQCD works very well as far as bottomonium is concerned. From bottomonium correlators one can extract mNRQCD renormalisation parameters with high precision.

The main application of mNRQCD is the calculation of heavy-light form factors, and it is therefore important to perform tests of mNRQCD also for heavy-light mesons. In the following, I report on such tests involving B_s mesons.

6.2.1 Calculation of the two-point functions

Starting with the standard Dirac fields, we construct interpolating fields for the B_s and B_s^* mesons with momentum $\mathbf{p}$ from

$$O_\Gamma(\tau,\mathbf{p}) = \frac{1}{\sqrt{V}}\sum_{\mathbf{x},\mathbf{y}} \overline{\Psi}_l(\tau,\mathbf{x})\Gamma(\mathbf{x}-\mathbf{y})\Psi_H(\tau,\mathbf{y})e^{-i\mathbf{p}\cdot\mathbf{y}} \ , \tag{6.22}$$

where Ψ_l is the Dirac spinor for the valence strange quark and Ψ_H is the Dirac spinor for the b quark. I used $\Gamma(\mathbf{r}) = \hat{\gamma}^5\ f(\mathbf{r})$ for the B_s pseudoscalar meson, $\Gamma(\mathbf{r}) = \hat{\gamma}^j\ f(\mathbf{r})$ with $j = 1,2,3$ for the B_s^* vector meson and $\Gamma(\mathbf{r}) = \hat{\gamma}^5\hat{\gamma}^0\ f(\mathbf{r})$ for the computation of the decay constant f_{B_s}. I compute 2×2 matrix correlators with Gaussian and local smearing, $f(\mathbf{r}) = e^{-|\mathbf{r}|^2/r_s^2}$ and $f(\mathbf{r}) = \delta_{\mathbf{r},0}$.

In terms of the standard Dirac propagators, the two-point function reads

$$\begin{aligned}\langle O_{\Gamma_{\rm sk}}(\tau,\mathbf{p})O^\dagger_{\Gamma_{\rm sc}}(\tau',\mathbf{p})\rangle \ &= \ \frac{1}{N}\sum_U \frac{1}{V}\sum_{\mathbf{x},\mathbf{y},\mathbf{x}',\mathbf{y}'} \\ &\times\ {\rm Tr}\left[\ \Gamma_{\rm sk}(\mathbf{x}-\mathbf{y})\, G_l\left(x',\ x\right)\ \Gamma^\dagger_{\rm sc}(\mathbf{x}'-\mathbf{y}')\, G_H\left(y,\ y'\right)\ \right] \\ &\times\ e^{-i\mathbf{p}\cdot\mathbf{y}}e^{i\mathbf{p}\cdot\mathbf{y}'}\ ,\end{aligned} \tag{6.23}$$

with $x = (\tau,\mathbf{x})$, $y = (\tau,\mathbf{y})$, $x' = (\tau',\mathbf{x}')$, $y' = (\tau',\mathbf{y}')$. The tree-level leading-order mNRQCD field redefinition (6.4) leads to the following expression for the b propagator:

$$\begin{aligned}G_H\left(y,\ y'\right) \ &= \ \theta(\tau-\tau')\frac{1}{\gamma}e^{-\gamma m(\tau-\tau')+i\gamma m\mathbf{v}\cdot(\mathbf{y}-\mathbf{y}')}\ S(\Lambda)\begin{pmatrix} G_{\psi_v}(y,\ y') & 0 \\ 0 & 0\end{pmatrix}\overline{S}(\Lambda) \\ &-\theta(\tau'-\tau)\frac{1}{\gamma}e^{+\gamma m(\tau-\tau')-i\gamma m\mathbf{v}\cdot(\mathbf{y}-\mathbf{y}')}\ S(\Lambda)\begin{pmatrix} 0 & 0 \\ 0 & G_{\xi_v}(y,\ y')\end{pmatrix}\overline{S}(\Lambda).\end{aligned} \tag{6.24}$$

For the light quark, I used the ASQTAD (order a^2, tadpole improved) staggered fermion action [123, 124, 125]. The 4-component *naive* light quark propagator [111] can be obtained from the 1-component staggered propagator $G_\chi(x',x)$ via

$$G_l(x',x) = \ G_\chi(x',x)\,\Omega(x')\Omega^\dagger(x) \tag{6.25}$$

with $\Omega(x)$ as defined in Eq. (2.59),

$$\begin{aligned}\Omega(x) \ &= \ (\gamma^0)^{x_0}(\gamma^1)^{x_1}(\gamma^2)^{x_2}(\gamma^3)^{x_3} \\ &= \ (\hat{\gamma}^0)^{x_0}(-i\hat{\gamma}^1)^{x_1}(-i\hat{\gamma}^2)^{x_2}(-i\hat{\gamma}^3)^{x_3}.\end{aligned} \tag{6.26}$$

We also employ $\hat{\gamma}^5$-Hermiticity

$$G_l(x', x) = \hat{\gamma}^5 G_l^\dagger(x, x')\hat{\gamma}^5, \tag{6.27}$$

to interchange the points x and x' for the light quark propagator. As before, we remove the factor of $e^{-\gamma m(\tau-\tau')}$ and the summation over $\mathbf{x}'$.

In the case where $\Gamma_{\rm sk}$ and $\Gamma_{\rm sc}$ contain the same Dirac matrix, we arrive at the following expression (for $\tau > \tau'$):

$$\begin{aligned} C(\Gamma_{\rm sk}, \Gamma_{\rm sc}, \mathbf{k}, \tau, \tau') &= \frac{1}{N}\sum_U \frac{1}{\gamma}\sum_{\mathbf{x},\mathbf{y}} f_{\rm sk}(\mathbf{x}-\mathbf{y}) e^{-i\mathbf{k}\cdot\mathbf{y}} \eta(x, x') \\ &\quad \times \mathrm{Tr}\left[G_\chi^\dagger(x, x')\, \overline{S}(\Lambda)\Omega(x')\Omega^\dagger(x) S(\Lambda) \begin{pmatrix} \widetilde{G}_{\psi_v}(y,\ x') & 0 \\ 0 & 0 \end{pmatrix} \right], \end{aligned} \tag{6.28}$$

with $\mathbf{k} = \mathbf{p} - \gamma m \mathbf{v}$ and

$$\widetilde{G}_{\psi_v}(y,\ x') = \sum_{\mathbf{y}'} f(\mathbf{x}' - \mathbf{y}') e^{i\mathbf{k}\cdot\mathbf{y}'} G_{\psi_v}(y, y'). \tag{6.29}$$

The phase factor $\eta(x, x')$ in (6.28) depends on the Dirac matrix in $\Gamma_{\rm sk}$ and $\Gamma_{\rm sc}$. It is given by

$$\eta(x, x') = \begin{cases} 1 & \text{for } \hat{\gamma}^5, \\ (-1)^{x'_j - x_j} & \text{for } \hat{\gamma}^j, \\ (-1)^{\sum_j (x_j + x'_j)} & \text{for } \hat{\gamma}^5\hat{\gamma}^0. \end{cases} \tag{6.30}$$

As before, I set $f(\mathbf{r})$ to zero for $|\mathbf{r}| > R_s$ with some cut-off radius R_s smaller than half the length of the lattice.

I performed the heavy-light simulations with the same gauge configurations as the heavy-heavy simulations described in Sec. 6.1), using the same heavy-quark action and parameters. Again, the boost velocity was always pointing in x-direction. The valence strange quark mass for the B_s and B_s^* mesons was set to 0.040. I used four staggered propagators with source times $\tau' = 0$, 16, 32, 48 for each gauge configuration. I computed both forward- and backward-propagating meson correlators to increase statistics. The smearing parameter r_s was set to 2.5.

6.2.2 Fitting

The staggered/naive light quark action used here suffers from the doubling problem. As shown in [111] for non-moving NRQCD, the spatial doublers do not contribute to the heavy-light correlators[2]. However, the temporal doubler leads to a coupling to additional

[2] This remains true with moving NRQCD for moderate values of γm; see the remarks in Sec. 5.2

$\|\mathbf{v}\|$	Z_p	$M_{\rm kin}$	$C_v/(\gamma m)$
0		3.37(15)	1.002(52)
0.2	1.05(15)	3.72(47)	1.13(16)
0.4	1.05(18)	3.66(68)	1.10(23)

Table 6.9: B_s results for $M_{\rm kin}$, Z_p, C_v.

opposite-parity states, which manifest themselves as oscillating exponentials in the correlators. I therefore fitted the heavy-light correlators $C(\Gamma_{\rm sk}, \Gamma_{\rm sc}, \mathbf{k}, \tau, \tau')$ for a given momentum $\mathbf{k}$ with a function of the form

$$\sum_{n=0}^{n_{\rm exp}-1} A_n(\Gamma_{\rm sk}) A_n^*(\Gamma_{\rm sc}) e^{-E_{v,n}(\tau-\tau')} + (-1)^{\tau-\tau'+1} \sum_{n=0}^{\widetilde{n}_{\rm exp}-1} \widetilde{A}_n(\Gamma_{\rm sk}) \widetilde{A}_n^*(\Gamma_{\rm sc}) e^{-\widetilde{E}_{v,n}(\tau-\tau')}, \quad (6.31)$$

where the parameters denoted with a "$\sim$" correspond to the opposite-parity states.

6.2.3 Kinetic mass, energy shift and external momentum renormalisation

Results for the B_s kinetic mass $M_{\rm kin}$ and the renormalisation parameters Z_p, C_v computed with Eqs. (5.33), (5.32), (5.31) for $n_Q = 1$ are shown in Table 6.9. The energies and the amplitude required for the calculation of the decay constant were obtained from 8-exponential (4 of which are oscillating) fits to 2×2 matrix correlators with the Gaussian smearing and the local axial current. Examples of fits to these correlators at $\mathbf{v} = 0$ and $|\mathbf{v}| = 0.4$ are shown in Fig. 6.4. These also demonstrate the worsening of the signal-to-noise ratio as the boost velocity increases, in accordance with Eq. (5.38) (for the B_s mesons considered here, one has to replace m_π in (5.38) by $m_{s\bar{s}}$).

For the calculation of C_v, I again averaged the results over the 4 different lattice momenta perpendicular to $\mathbf{v}$

$$\mathbf{k}_\perp = \frac{2\pi}{L}(0, \pm 1, 0), \quad \frac{2\pi}{L}(0, 0, \pm 1), \quad (6.32)$$

and the momentum parallel to the boost velocity required for the determination of Z_p was chosen to be $\mathbf{k}_\parallel = \frac{2\pi}{L}(1, 0, 0)$.

As expected, the statistical errors are larger than for the heavy-heavy mesons. In addition to the generally worse signal-to-noise ratio for heavy-light mesons, a much smaller

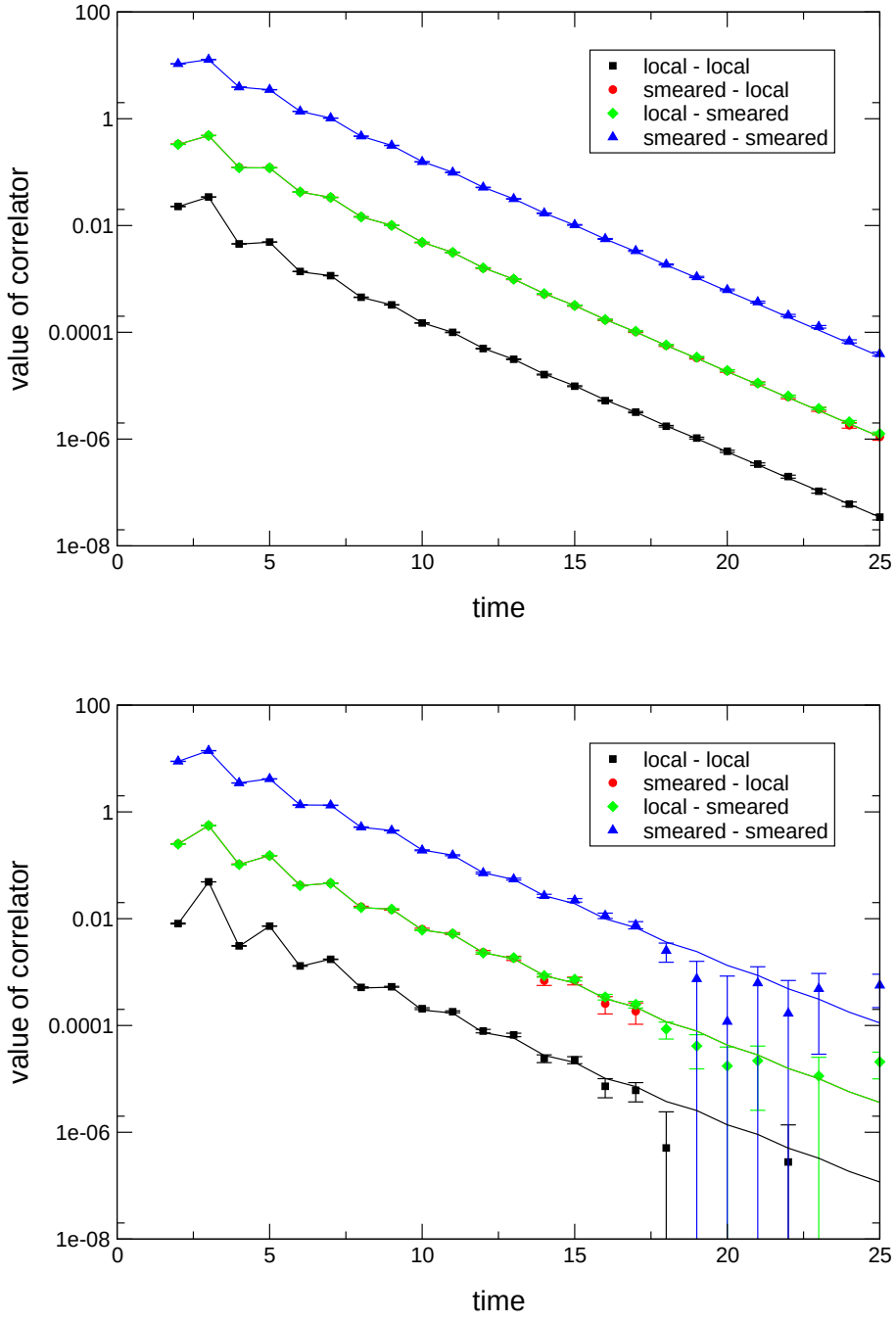

Figure 6.4: Fits to B_s matrix correlators (local and Gaussian smearing) at $\mathbf{k} = 0$ and $\mathbf{v} = 0$ (upper panel), $|\mathbf{v}| = 0.4$ (lower panel). The fits have $n_{\mathrm{exp}} = \widetilde{n}_{\mathrm{exp}} = 4$ and $\tau_{\mathrm{min}} = 2$. The noise in the two-point function increases exponentially with the Euclidean time as expected.

$\|\mathbf{v}\|$	$\|\mathbf{p}\|$	f_{B_s}
0	0	0.1626(27)
0.2	0.576(11)	0.1608(52)
0.4	1.2163(96)	0.1634(94)
0.6	1.885(57)	0.174(17)

Table 6.10: B_s decay constant (unrenormalised, and in lattice units) with mNRQCD at $\mathbf{k} = 0$. The total momentum $\mathbf{p}$ is computed using the nonperturbative result for Z_p from the $\eta_b(1S)$ dispersion relation.

number of origins (four) per gauge configuration was used to save computer time (the computation of light-quark propagators is more expensive than the computation of mNRQCD propagators). The results for Z_p and C_v agree with those obtained using heavy-heavy mesons in section 6.1.3.

6.2.4 Decay constant

The B_s decay constant is defined by

$$\langle 0|\mathsf{J}^\mu_5(0)|B_s, \mathbf{p}\rangle = i f_{B_s}\, p^\mu, \tag{6.33}$$

where $\mathsf{J}^\mu_5(0) = \bar{\mathsf{s}}(0)\hat{\gamma}^\mu\hat{\gamma}_5\mathsf{b}(0)$. I computed f_{B_s} in a similar way as the η_b decay constant in Sec. 6.1.4, using the temporal component of the current. As there is only one heavy quark here, the equation analogous to (6.19) reads

$$f_{B_s} = A\sqrt{\frac{2}{E_v(\mathbf{k}) + C_v}}. \tag{6.34}$$

Here I used C_v determined from the $\eta_b(1S)$ dispersion relation since this is more precise than the result from the B_s dispersion relation.

The results for the decay constant f_{B_s} at $\mathbf{k} = 0$ and $|\mathbf{v}| = 0, 0.2, 0.4, 0.6$ are listed in Table 6.10 and plotted against the total momentum in Fig. 6.5. I find that the decay constant is independent of the boost velocity within statistical errors, which demonstrates that the combination of moving NRQCD and ASQTAD works well at these values of $\mathbf{v}$. I could not obtain reliable fits at large $\mathbf{k}$ and $\mathbf{v} = 0$, and therefore do not show results with non-moving NRQCD here.

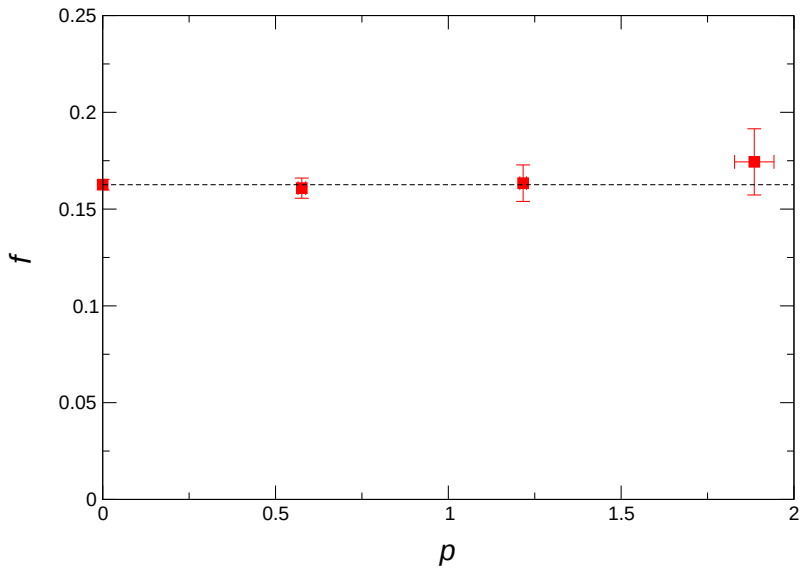

Figure 6.5: The B_s decay constant at $\mathbf{k} = 0$ and $|\mathbf{v}| = 0,\ 0.2,\ 0.4,\ 0.6$ plotted against the total momentum $\mathbf{p} = Z_p \gamma m \mathbf{v} + \mathbf{k}$. The horizontal line indicates the value at $\mathbf{v} = 0$.

6.2.5 Energy splittings

I also computed the $B_s^* - B_s$ energy splitting as a function of $|\mathbf{v}|$; the results are shown in Table 6.11. The statistical errors are so large that no definite statement can be made about the velocity dependence.

$\lvert\mathbf{v}\rvert$	$\Delta E_v(0)$	$\dfrac{\Delta E_v(0)}{\Delta E_0(0)}$
0.0	0.0261(35)	1
0.2	0.0262(65)	1.00(28)
0.4	0.0310(80)	1.18(34)

Table 6.11: $B_s^* - B_s$ energy splitting as a function of the boost velocity.

6.3 Comparison of nonperturbative and perturbative results

In the following I compare my nonperturbative results for Z_p (the renormalisation of the external momentum) and C_v (the energy shift) given in Secs. 6.1.3 and 6.2.3 to predictions from one-loop lattice perturbation theory [114, 100].

The perturbative results have the form

$$Z_p = 1 + \alpha_s \, \delta Z_p, \qquad C_v = 1 + \alpha_s \, \delta C_v, \tag{6.35}$$

where δZ_p and δC_v depend on the form of the heavy-quark and gluon actions as well as the heavy-quark mass and the boost velocity. Results for δZ_p and δC_v for the setup used here (full moving NRQCD action (5.12, 5.13) with $m = 2.8$, $n = 2$, Lüscher-Weisz gluon action) can be found in [114, 100].

To make use of (6.35), a numerical value of the strong coupling constant α_s is needed. In [114, 100], the strong coupling constant was defined in the potential scheme [77], and the momentum scale $q^\star$ was calculated with the Brodsky-Lepage-Mackenzie procedure [126] for each quantity and each value of $\mathbf{v}$. The $q^\star$ values range approximately between $0.5/a$ and $3/a$. The coarse MILC configurations used here have $a^{-1} \approx$1.6 GeV [108]. Using the running of the strong coupling constant $\alpha_V(q)$ [127] this gives, for example, $\alpha_V(2/a) \approx 0.3$.

Figures 6.6 and 6.7, which are taken from [100], show the perturbative and nonperturbative results for Z_p and C_v. Nonperturbative results from both bottomonium and B_s two-point functions are shown, with a slight horizontal offset for legibility. The uncertainties shown on the data points for the perturbative results are purely statistical due to the stochastic integration over the loop momentum. The error band on the perturbative results is obtained by varying the scale in the range $[q^\star/2,\ 2q^\star]$.

The heavy-light results have error bars so large that they agree with the perturbative predictions. In the following, I focus on the statistically much more precise heavy-heavy results. For Z_p, these agree with the perturbative predictions at $|\mathbf{v}| = 0.2$ and $|\mathbf{v}| = 0.4$, while there is a deviation at $|\mathbf{v}| = 0.6$. For $C_v/(\gamma m)$, the (small) correction to the tree-level result $C_v/(\gamma m) = 1$ is in fact found to have the opposite sign for the nonperturbative results compared to the perturbative results at all values of $\mathbf{v}$.

This indicates that there may be sizable higher-loop or nonperturbative contributions. To investigate the two-loop contribution, high-β simulations (cf. Sec. 5.3.5) are currently being performed [116].

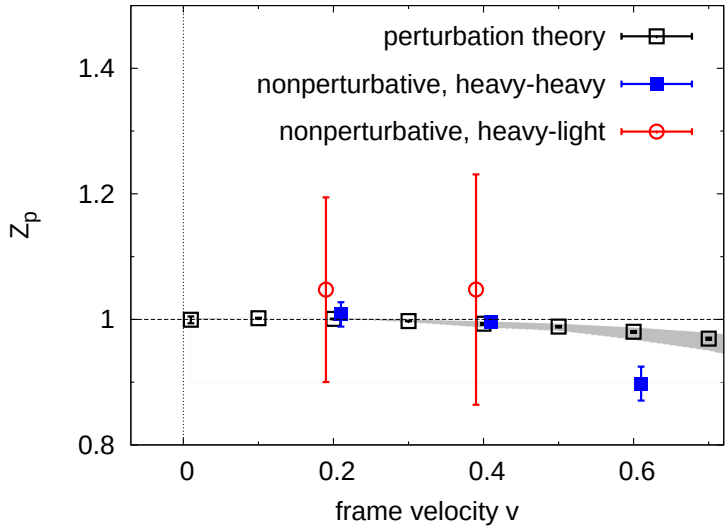

Figure 6.6: Comparison of nonperturbative and perturbative results for the external momentum renormalisation factor Z_p. (Plot by Eike Müller [114], my nonperturbative data.)

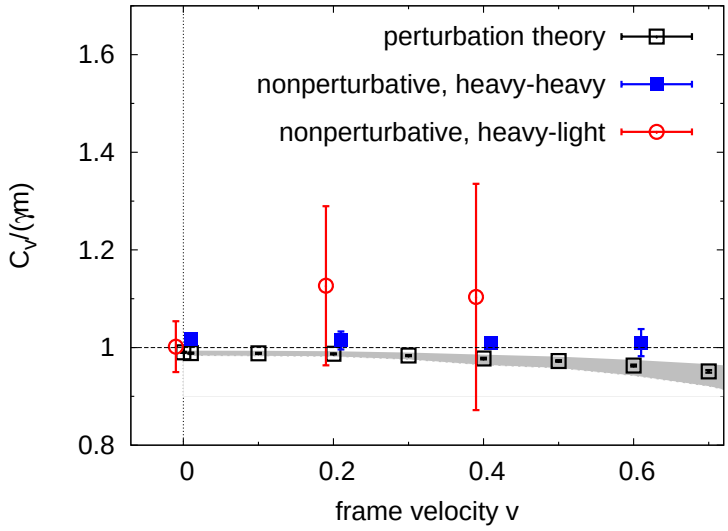

Figure 6.7: Comparison of nonperturbative and perturbative results for the energy shift C_v, relative to the tree-level value γm. (Plot by Eike Müller [114], my nonperturbative data.)

Chapter 7

Heavy-hadron spectroscopy

Before coming to the main application of lattice moving NRQCD, the calculation of B decay form factors in Chapter 8, I will report in the following on a different project: the calculation of masses and excited-state energies of hadrons containing b quarks. Here, the hadrons considered are at rest, and so I use the standard non-moving lattice NRQCD action which is obtained from the action described in Chapter 5 by setting $\mathbf{v} = 0$.

The calculations described in the following make use of gauge field configurations generated by the RBC and UKQCD collaborations [128]. These configurations were created with the renormalisation-group improved Iwasaki gluon action [129, 130] and 2+1 flavours of light quarks described by a domain wall action (see Sec. 2.4.7).

The first part of this chapter (Sec. 7.1) is about bottomonium, i.e. the bound states of bottom quark-antiquark pairs. This work is published in my paper [131]. The spectrum of bottomonium is known very well from experiment [83], as can be seen in the level scheme shown in Fig. 7.1. There are many narrow states and the energy splittings show little dependence on the light quark masses once these are light enough. Thus, the calculation of the bottomonium spectrum is an excellent way of testing the lattice methods used. It also allows independent determinations of the lattice spacing of the RBC/UKQCD gauge field ensembles.

The second part of this chapter (Sec. 7.2) then describes mass-calculations of b-flavoured hadrons, using the domain wall action for the light valence quarks. This is still work in progress; I published my preliminary results in the proceedings of the Lattice 2009 conference [132]. The hadrons considered include B mesons, singly- and doubly-bottom baryons, and for the first time also the triply-bottom baryon Ω_{bbb}. There is currently considerable interest in mass predictions for b-flavoured baryons. A few singly-bottom baryons have been found so far, and more results are expected from the Large Hadron Collider

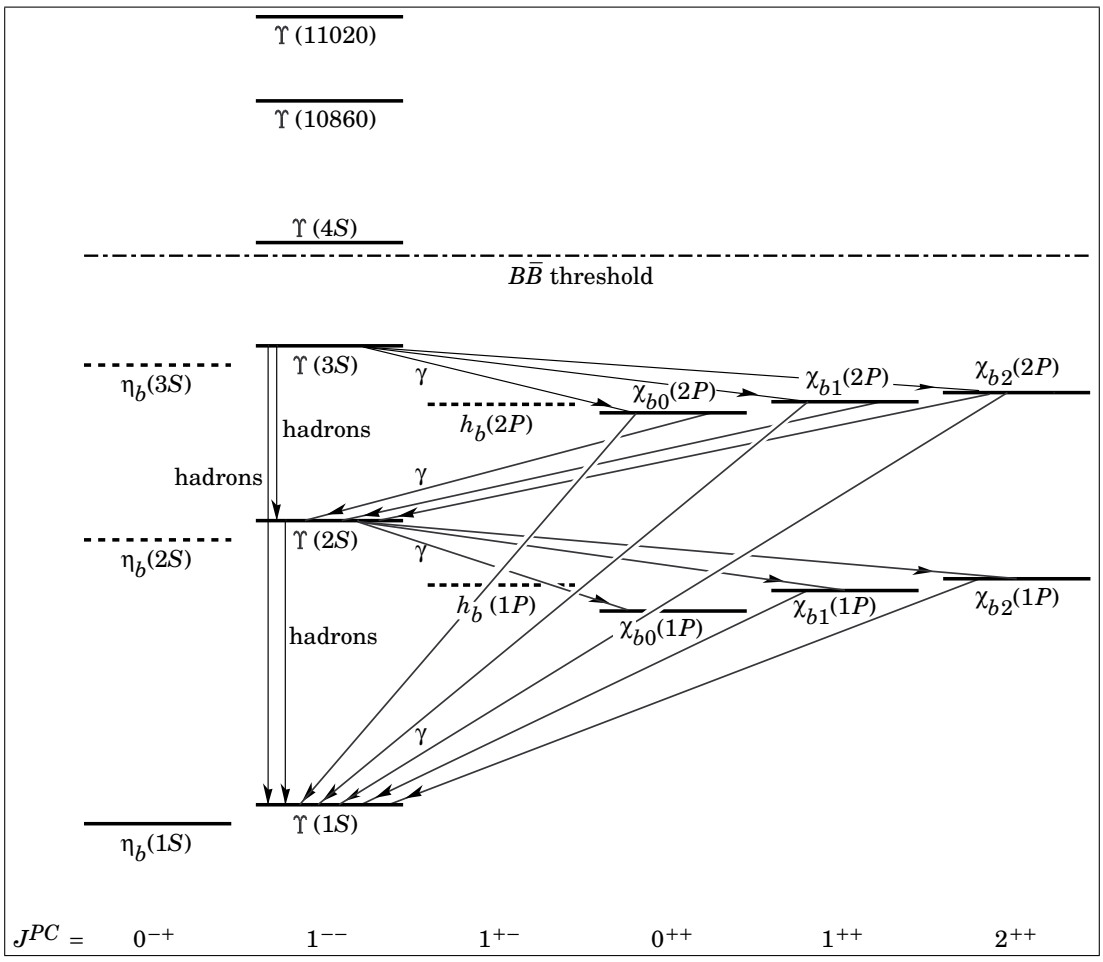

Figure 7.1: Level scheme of $b\bar{b}$ states, from the Particle Data Group [83]

am_l	m_π [MeV]	u_{0L}	MD range (step)	$n_{\rm conf}$
0.005	330	0.8439	915 - 8665 (25)	311
0.01	420	0.8439	1475 - 8525 (25)	283
0.02	560	0.8433	1800 - 3600 (25)	73
0.03	670	0.8428	1275 - 3050 (25)	72

Table 7.1: The ensembles of RBC/UKQCD gauge configurations used for my calculation of the bottomonium spectrum.

at CERN. Most recently, the Ω_b baryon was discovered at Fermilab. There are now two incompatible results for its mass, obtained by the DØ [133] and CDF [134] collaborations. Lattice QCD can contribute to resolve this discrepancy.

7.1 Bottomonium

7.1.1 Lattice details

The details of the domain wall fermion and Iwasaki gauge actions adopted by the RBC and UKQCD collaborations are given in [135]. For the calculation of the bottomonium spectrum I used the gauge configurations of size $24^3 \times 64$ as described in [128]. The size of the fifth dimension in the domain wall action is $L_s = 16$, leading to a residual mass of $am_{\rm res} = 0.00315(2)$ [128]. The strange quark mass is $am_s = 0.04$ and there are ensembles with four different values for the degenerate light (up and down) quark mass am_l corresponding to pion masses in the range from ≈ 330 MeV to ≈ 670 MeV, as shown in Table 7.1.

I started the "measurements" at the same molecular dynamics (MD) time as in [128] to ensure complete thermalisation. Note however that the $am_l = 0.005$ and $am_l = 0.01$ ensembles have since been extended and I included the additional configurations. I performed the measurements every 25 steps of MD time. This is approximately two times the integrated autocorrelation time found in [128] for the 12th time slice of the pion correlator on the $am_l = 0.005$ ensemble. I confirmed that this separation gives sufficiently independent measurements for the observables calculated here by doing a binning analysis.

As discussed in Chapter 5, the lattice NRQCD action is tadpole-improved, using the mean link in Landau gauge u_{0L}. I measured u_{0L} for the different ensembles by transforming subsets of configurations to Landau gauge (using the Chroma software [136]); the results are listed in Table 7.1.

Name	L	S	J	P	C	$\mathcal{R}^{PC}$	$\Gamma(\mathbf{r})$
$\eta_b(nS)$	0	0	0	$-$	$+$	A_1^{-+}	$\phi_{nS}(\mathbf{r})$
$\Upsilon(nS)$	0	1	1	$-$	$-$	T_1^{--}	$\phi_{nS}(\mathbf{r})\,\sigma^j$
$h_b(nP)$	1	0	1	$+$	$-$	T_1^{+-}	$\phi_{nP}(\mathbf{r})\,r^j/r_s$
$\chi_{b0}(nP)$	1	1	0	$+$	$+$	A_1^{++}	$\phi_{nP}(\mathbf{r})\,(\mathbf{r}\cdot\boldsymbol{\sigma})/r_s$
$\chi_{b1}(nP)$	1	1	1	$+$	$+$	T_1^{++}	$\phi_{nP}(\mathbf{r})\,(\mathbf{r}\times\boldsymbol{\sigma})^j/r_s$
$\chi_{b2}(nP)$	1	1	2	$+$	$+$	T_2^{++}	$\phi_{nP}(\mathbf{r})\,(r^j\sigma^k + r^k\sigma^j)/r_s$
$\eta_b(nD)$	2	0	2	$-$	$+$	T_2^{-+}	$\phi_{nD}(\mathbf{r})\,r^j r^k/r_s^2$
$\Upsilon_2(nD)$	2	1	2	$-$	$-$	E^{--}	$\phi_{nD}(\mathbf{r})\,(r^j r^k\sigma^l - r^k r^l\sigma^j)/r_s^2$

Table 7.2: The smearing functions $\Gamma(\mathbf{r})$ (with $j \neq k,\ \ l \neq k$) and the corresponding irreducible representations of the octahedral group.

7.1.2 Calculation of the two-point functions

In Sec. 6.1.1 the computation of bottomonium two-point functions was discussed for moving NRQCD. Here, I use non-moving NRQCD, which is just a special case. The two-point functions are computed as

$$C(\Gamma_{\mathrm{sk}}, \Gamma_{\mathrm{sc}}, \mathbf{k}, \tau, \tau') = \frac{1}{N}\sum_{U}\sum_{\mathbf{x},\mathbf{y}} \mathrm{Tr}\left[G_\psi^\dagger(\tau, \mathbf{x},\ \tau', \mathbf{x}')\,\Gamma_{\mathrm{sk}}^\dagger(\mathbf{x}-\mathbf{y})\,\widetilde{G}_{\mathrm{sc}}(\tau, \mathbf{y},\ \tau', \mathbf{x}')\right] e^{-i\mathbf{k}\frac{\mathbf{x}+\mathbf{y}}{2}} \tag{7.1}$$

where $\tau > \tau'$ and

$$\widetilde{G}_{\mathrm{sc}}(\tau, \mathbf{y},\ \tau', \mathbf{x}') = \sum_{\mathbf{y}'} G_\psi(\tau, \mathbf{y},\ \tau', \mathbf{y}')\,\Gamma_{\mathrm{sc}}(\mathbf{x}'-\mathbf{y}')\,e^{i\mathbf{k}\frac{\mathbf{x}'+\mathbf{y}'}{2}}. \tag{7.2}$$

In Eqs. (7.1) and (7.2), the functions $\Gamma_{\mathrm{sc/sk}}$ are the smearing functions at source and sink, respectively, which are now expressed directly in the non-relativistic spinor basis, i.e. they are (2×2)-matrix-valued in spinor space. The gauge field configurations were fixed to Coulomb gauge using Chroma [136]. In Table 7.2 the bottomonium states considered here are listed, together with their continuum quantum numbers, smearing functions $\Gamma(\mathbf{r})$ and representations of the octahedral group [137].

As can be seen in Table 7.2, all representations are chosen to be different, so that no mixing is expected here. As in [108], the radial functions $\phi_{nS}(\mathbf{r})$, $\phi_{nP}(\mathbf{r})$ and $\phi_{nD}(\mathbf{r})$ for

State	$\phi(\mathbf{r})$
$1S$	$\exp[-\lvert\mathbf{r}\rvert/r_s]$
$2S$	$[1-\lvert\mathbf{r}\rvert/(2r_s)]\ \exp[-\lvert\mathbf{r}\rvert/(2r_s)]$
$3S$	$\left[1-2\lvert\mathbf{r}\rvert/(3r_s)+2\lvert\mathbf{r}\rvert^2/(27r_s^2)\right]\ \exp[-\lvert\mathbf{r}\rvert/(3r_s)]$
$1P$	$\exp[-\lvert\mathbf{r}\rvert/(2r_s)]$
$2P$	$[1-\lvert\mathbf{r}\rvert/(6r_s)]\exp[-\lvert\mathbf{r}\rvert/(3r_s)]$
$1D$	$\exp[-\lvert\mathbf{r}\rvert/(3r_s)]$

Table 7.3: The radial functions $\phi(\mathbf{r})$

the n-th radially excited S-wave ($L=0$), P-wave ($L=1$) and D-wave ($L=2$) states are taken from the corresponding hydrogen atom wave functions and are given in Table 7.3.

The same lattice representations are used at source and sink but the radial smearing functions are allowed to be different. I set the smearing parameters r_s (in lattice units) to 1.0 ($1S$), 0.8 ($2S$), 0.6 ($3S$), 0.5 ($1P$), 0.4 ($2P$) and 0.5 ($1D$), respectively.

As in Sec. 6.1.1, I set the smearing functions to zero outside a ball with radius R smaller than half the spatial lattice dimension, so that the wrapping around the lattice boundaries does not cause any problems. Since the smearing functions decay exponentially with the separation between quark and antiquark, R can be chosen such that the important features remain. To ensure symmetry, the same cut-off radius must be taken at source and sink.

In order to increase statistics, I averaged the correlators (7.1) over eight different spatial origins $\mathbf{x}'$ located at the corners of a cube with side length $L/2=12$. In addition, I used four different source time slices τ' with an equal spacing of 16, so that there are 32 origins per configuration in total. Furthermore, I shifted the locations of the origins on the lattice randomly from configuration to configuration in order to decrease autocorrelations.

7.1.3 Data analysis

After choosing a set of smearing functions $\Gamma(\mathbf{r})$ with equal lattice representations but different radial functions (e.g. $1S$, $2S$ and $3S$), I computed the square matrix of correlators obtained by taking all combinations for source and sink.

As in Sec. 6.1.2, I fitted the matrix of correlators $C(\Gamma_{\mathrm{sk}},\Gamma_{\mathrm{sc}},\mathbf{k},\tau-\tau')$ simultaneously by a function of the form (6.11). Here I took the logarithms of the energy splittings as

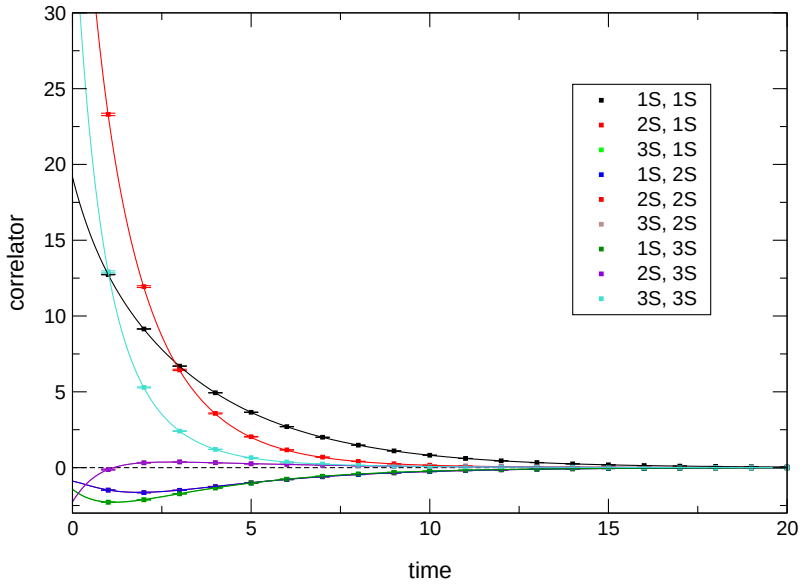

Figure 7.2: Fit of a 3×3 matrix of correlators with the $\{\Upsilon(1S),\ \Upsilon(2S),\ \Upsilon(3S)\}$ smearings. Note that both axes have a linear scale. The fit has $n_{\mathrm{exp}} = 10$ and $\tau_{\mathrm{min}} = 1$.

the fit parameters to ensure the correct ordering of the states.

As before, I used the Bayesian method described in Sec. C.3, where the number of exponentials in the fit is increased until the results for the low-lying states stabilise. This is demonstrated for a 3×3 matrix correlator in the Υ channel in Fig. C.1. A plot of the corresponding fit with $n_{\mathrm{exp}} = 10$ is shown in Fig. 7.2.

I also tested for the presence of autocorrelations in the measurements using the binning method (cf. Sec. C.5). In most cases I did not find significant autocorrelations, but for some quantities the error estimates were slightly corrected upwards. The details can be found in my paper [131].

7.1.4 Tuning of the b quark mass

The bare b quark mass, which is a free parameter in the NRQCD action, was tuned non-perturbatively. I adjusted it such that the kinetic mass of the $\eta_b(1S)$ meson as calculated on the lattice matches the experimental value of 9.389(5) GeV [138]. The tuning was done on the most chiral ($am_l = 0.005$) ensemble of gauge configurations.

I computed the kinetic mass from

$$M_{\mathrm{kin}} = \frac{\mathbf{k}^2 - [E(\mathbf{k}) - E(0)]^2}{2\,[E(\mathbf{k}) - E(0)]}, \tag{7.3}$$

am_b	$aM_{\rm kin}(\eta_b)$	$\Upsilon(2S) - \Upsilon(1S)$ splitting
2.30	4.988(12)	0.3258(47)
2.45	5.281(13)	0.3242(46)
2.60	5.575(13)	0.3231(54)

Table 7.4: Results for the tuning of the bare b quark mass in lattice units. Errors are statistical/fitting only.

where I used the smallest possible lattice momentum $a|\mathbf{k}| = 1 \cdot 2\pi/L$. As shown in the next section, the kinetic mass is very stable and shows no significant dependence on $\mathbf{k}$ even for much larger momenta. In order to increase statistics I averaged the results over the different possibilities for the direction of $\mathbf{k}$.

The comparison with experiment of course requires the knowledge of the lattice spacing, which I determined as the ratio of the experimentally measured $\Upsilon(2S) - \Upsilon(1S)$ mass splitting, 0.56296(40) GeV [83], to the dimensionless lattice result. This will be discussed in more detail in Sec. 7.1.6.

The lattice results for $aM_{\rm kin}$ and the $\Upsilon(2S) - \Upsilon(1S)$ splitting at the three different bare quark masses $am_b = 2.30,\ 2.45$ and 2.60 are shown in Table 7.4. As can be seen, the $\Upsilon(2S) - \Upsilon(1S)$ splitting is very insensitive to the value of the b quark mass. It is also expected to have much smaller lattice discretisation errors than the $1P - 1S$ splitting as discussed in the next section.

I found that in the range considered here, the dependence of the kinetic mass on the bare heavy quark mass is described very well by the linear relation

$$aM_{\rm kin} = A + B \cdot am_b. \tag{7.4}$$

A plot of $aM_{\rm kin}$ as a function of am_b is shown in Fig. 7.3. I performed fits of Eq. (7.4) with the parameters A and B on 500 bootstrap samples for the kinetic masses at $am_b = 2.30,\ 2.45$ and 2.60. The resulting average fit parameters are

$$\begin{aligned} A &= 0.489(25), \\ B &= 1.956(11). \end{aligned} \tag{7.5}$$

To obtain a first result for the lattice spacing of the $am_l = 0.005$ ensemble, I used the $\Upsilon(2S) - \Upsilon(1S)$ mass splitting at $am_b = 2.45$, giving $a^{-1} = 1.736(25)$ GeV (the error is

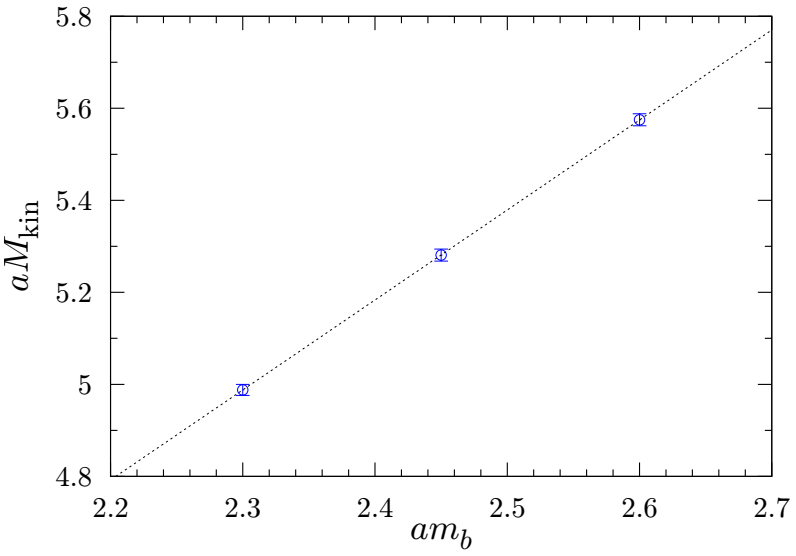

Figure 7.3: The kinetic mass of the $\eta_b(1S)$ meson plotted against the bare heavy quark mass. Errors are statistical/fitting only. The line shows the average over the bootstrap ensemble of linear fit results.

statistical/fitting only). Of course the b quark mass was not yet tuned, but given the relative independence of the $\Upsilon(2S) - \Upsilon(1S)$ splitting on m_b, the value of $am_b = 2.45$ was sufficiently close to the physical value. The final results for the lattice spacing obtained with the correct b quark mass will be presented in Sec. 7.1.6.

Using the preliminary result for a^{-1}, it follows that the $\eta_b(1S)$ mass in lattice units must be tuned to be $aM_{\mathrm{kin}} = 5.407(77)$. Inserting this into (7.4) and solving for am_b gives

$$am_b = 2.514(36). \tag{7.6}$$

The error quoted here is statistical/fitting only and is dominated by the uncertainty in the lattice result for the $\Upsilon(2S) - \Upsilon(1S)$ splitting.

I actually performed all remaining calculations for bottomonium with $am_b = 2.536$. This was an earlier result and the fits have been improved slightly since then. However it is still inside the range of the new value (7.6).

For $am_b = 2.536$ the results were $aM_{\mathrm{kin}} = 5.449(13)$ and $a^{-1} = 1.740(25)$ GeV. This gives $M_{\mathrm{kin}} = 9.48(14)$ GeV which is compatible with the experimental result of 9.389(5) GeV, confirming the successful tuning of the heavy quark mass.

$\mathbf{n}^2$	$aM_{\mathrm{kin}}(\eta_b)$	aC	c^2
1	5.450(17)	2.5913(84)	-
2	5.450(17)	2.5912(85)	1.00003(85)
3	5.450(18)	2.5911(92)	1.0001(16)
4	5.461(22)	2.597(11)	0.9981(21)
5	5.457(20)	2.595(10)	0.9987(24)
6	5.452(20)	2.592(10)	0.9997(27)
8	5.454(22)	2.593(11)	0.9993(35)
9	5.447(20)	2.590(10)	1.0005(35)
12	5.445(21)	2.589(11)	1.0009(42)

Table 7.5: Kinetic mass, NRQCD energy shift and the square of the "speed of light" for various lattice momenta $\mathbf{k} = \mathbf{n} \cdot 2\pi/L$, calculated on the $am_l = 0.005$ ensemble with $am_b = 2.536$.

7.1.5 Speed of light

In order to examine how well the lattice data approximates the relativistic continuum dispersion relation, I computed the kinetic mass of the $\eta_b(1S)$ meson, defined by (7.3), also for larger lattice momenta $\mathbf{k} = \mathbf{n} \cdot 2\pi/L$ up to $\mathbf{n}^2 = 12$. For these calculations, I used the local smearing function $\Gamma(\mathbf{r}) = \delta_{\mathbf{r},0}$ at source and sink so that multiple lattice momenta can be obtained with little computational cost. For each value of $\mathbf{n}^2$, I averaged the results over the possible directions of the vector $\mathbf{n}$, and all components of $\mathbf{n}$ were chosen to be less than or equal to 2.

The results are given in Table 7.5, where also the NRQCD energy shift, calculated as

$$C = \frac{M_{\mathrm{kin}}(\mathbf{k}) - E(0)}{2}, \tag{7.7}$$

and for $\mathbf{n}^2 > 1$ the square of the "speed of light"

$$c^2 \equiv \frac{[E(\mathbf{k}) - E(0) + M_{\mathrm{kin},1}]^2 - M_{\mathrm{kin},1}^2}{\mathbf{k}^2} \tag{7.8}$$

are shown. In Eq. (7.8), $M_{\mathrm{kin},1}$ denotes the kinetic mass calculated with $\mathbf{n}^2 = 1$. In the units used here, one should have $c^2 = 1$. Deviations of c^2 from 1 can be caused by discretisation errors in the NRQCD, gluon and sea quark actions and also by missing higher order relativistic corrections in the NRQCD action. The NRQCD action is highly improved at tree level, and so the most significant errors one expects here are those caused by missing radiative corrections.

As can be seen in the table, in the momentum range considered here the kinetic mass shows no significant dependence on $\mathbf{k}$ within the small statistical/fitting errors. Correspondingly, c^2 remains compatible with 1, with statistical/fitting errors less than 0.5%, indicating that the effect of the errors mentioned above is small.

Analogous calculations for the $\Upsilon(1S)$ meson have been performed in [108] with the same NRQCD action but with the Lüscher-Weisz gluon and the ASQTAD sea quark action. There, the deviation of c^2 from 1 in the same momentum range was also found to be compatible with 1 within statistical errors of less than 1%.

7.1.6 Radial/orbital energy splittings and the lattice spacing

The lattice results for the various radial and orbital energy splittings are listed in Table 7.6. Systematic errors are known to be smallest for the spin-averaged masses, defined as

$$\langle M \rangle = \frac{\sum_J (2J+1) M_J}{\sum_J (2J+1)}. \tag{7.9}$$

However, in most cases not all of the states entering Eq. (7.9) are known from experiment. For the $1S$, $2S$ and $3S$ masses in this section I consider the $J = 1$ states (Υ) instead of the spin-averages. Note that the $J = 0$ S-wave states (η_b) enter the spin-averaged masses only with a weight of 1/4, and so the influence of systematic errors in the hyperfine splittings is negligible here. For the $1P$ and $2P$ masses, I use the spin-averages over the χ_b triplet ($J = 0, 1, 2$) states. The only experimentally known D-wave state [139] is $\Upsilon_2(1D)$ with $J = 2$, and therefore I consider this state here.

In terms of the NRQCD power counting (cf. Sec. 3.2.2), radial and orbital energy splittings are of order $\mathcal{O}(v_{\text{orb.}}^2)$, where $v_{\text{orb.}}$ is the internal speed of the b quarks inside the heavy-heavy meson. Recall that for bottomonium one has $v_{\text{orb.}}^2 \approx 0.1$. The lattice NRQCD action in use includes all relativistic corrections of order $\mathcal{O}(v_{\text{orb.}}^4)$ (at tree-level), and hence the missing relativistic corrections are of order $\mathcal{O}(v_{\text{orb.}}^6)$. Naively this leads to relativistic errors for the radial and orbital splittings of $\mathcal{O}(v_{\text{orb.}}^4) = 1\%$. However, as discussed in [108], for energy splittings one has to consider the *difference* between the expectation values of the missing operators for the two states. This leads to a reduction of the relativistic errors for the $2S - 1S$ splitting to about 0.5%.

Additional systematic errors for the NRQCD action are due to discretisation errors and missing radiative corrections (beyond tadpole improvement). Estimates of these errors for the $2S - 1S$ and $1P - 1S$ splittings are given in Table 7.7. They are taken to be equal to the estimates obtained in [108] for exactly the same lattice NRQCD action on the "coarse" MILC gauge configurations, which have a lattice spacing ($a^{-1} \approx 1.6$ GeV) very similar to

	$am_l = 0.005$	$am_l = 0.01$	$am_l = 0.02$	$am_l = 0.03$
$\Upsilon(2S) - \Upsilon(1S)$	0.3236(46)	0.3270(73)	0.330(18)	0.327(23)
$\Upsilon(3S) - \Upsilon(1S)$	0.517(21)	0.537(23)	-	-
$\langle\chi_b(1P)\rangle - \Upsilon(1S)$	0.2589(30)	0.2572(22)	0.2628(57)	0.2613(61)
$\langle\chi_b(2P)\rangle - \Upsilon(1S)$	0.478(30)	0.502(26)	0.511(39)	0.516(37)
$\langle\chi_b(2P)\rangle - \langle\chi_b(1P)\rangle$	0.219(29)	0.245(24)	0.248(35)	0.255(33)
$\Upsilon_2(1D) - \Upsilon(1S)$	0.4080(46)	0.4194(42)	0.417(12)	0.426(12)

Table 7.6: Results for the radial and orbital energy splittings in lattice units. Errors are statistical/fitting only.

	$2S - 1S$	$1P - 1S$
relativistic	0.5%	1.0%
radiative	0.5%	1.7%
discretisation	0.8%	3.2%
total	1.1%	3.8%

Table 7.7: Estimates of the systematic errors due to the lattice NRQCD action for the $2S - 1S$ radial and $1P - 1S$ orbital splittings [108].

		$am_l = 0.005$	$am_l = 0.01$	$am_l = 0.02$	$am_l = 0.03$
a^{-1}_{2S-1S}	(GeV)	1.740(25)(19)	1.722(38)(19)	1.708(92)(19)	1.72(12)(2)
a^{-1}_{1P-1S}	(GeV)	1.698(19)(65)	1.709(15)(65)	1.673(36)(64)	1.682(40)(64)

Table 7.8: Results for the inverse lattice spacing obtained from the $\Upsilon(2S) - \Upsilon(1S)$ and $\langle\chi_b(1P)\rangle - \Upsilon(1S)$ splittings. The first error given is statistical/fitting and the second is an estimate of the systematic errors (relativistic, radiative and discretisation) due to the NRQCD action. Systematic errors due to the gluon and sea quark actions are not included.

the ensembles considered here. The reader is referred to [108] and [140] for the details. As can be seen in the table, systematic errors are much smaller for the $2S - 1S$ splitting compared to the $1P - 1S$ splitting. This is due to the smaller difference in the wave functions for the $2S$ and $1S$ states. The $2S - 1S$ splitting thus allows a more reliable determination of the lattice spacing.

Note that there are also discretisation errors due to the gluon and sea quark actions. These are difficult to quantify at this stage as only data from one lattice spacing are available. Gauge configurations with a smaller lattice spacing are currently being generated by the RBC and UKQCD collaborations so that a more systematic analysis will become possible in the future. In [128], a preliminary error estimate of $(a\Lambda_{\rm QCD})^2 \approx 4\%$ for the calculations of light hadron properties on the current ensembles was given. The calculations for bottomonium are different in that the domain wall action only enters via the sea quarks. The Iwasaki gluon action [129, 130] is renormalisation-group-improved and is therefore expected to have a better scaling behaviour than the unimproved Wilson action. However, this depends on the observable considered; see e.g. [141] for a scaling study of the critical temperature and glueball masses. The stability of the "speed of light" demonstrated in Sec. 7.1.5 provides some evidence for the smallness of the effect of gluon discretisation errors for bottomonium.

For reference, the discretisation errors in the $2S - 1S$ and $1P - 1S$ splittings on the coarse MILC lattices due to the Lüscher-Weisz gluon action were estimated in [108] to be 0.5% and 1.7%, respectively. These errors are proportional to the difference in the square of the wave function at the origin, which is smaller between the $2S$ and $1S$ states.

My results for the inverse lattice spacings of the four ensembles from both the $\Upsilon(2S) - \Upsilon(1S)$ and the $\langle\chi_b(1P)\rangle - \Upsilon(1S)$ splittings are listed in Table 7.8. For the most chiral ensemble the $2S - 1S$ splitting gives $a^{-1} = 1.740(25)_{\rm stat}(19)_{\rm syst}$ GeV. No significant de-

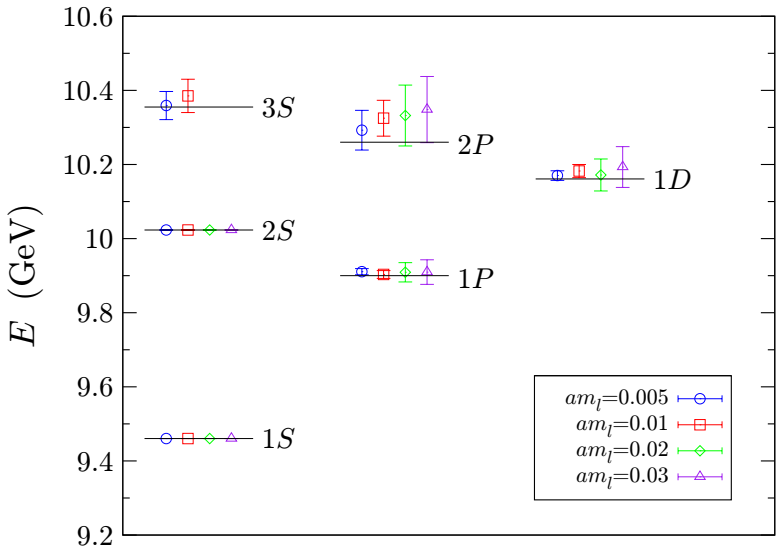

Figure 7.4: Radial and orbital energy splittings compared to the experimental results (indicated by lines). Errors are statistical/fitting only and include the uncertainty in the determination of the lattice spacing. The $1S$ and $2S$ masses, for which no error bars are shown, are not predictions of the lattice calculation as these states are used to determine the lattice scale and the overall energy shift.

pendence on the sea quark mass can be seen within the statistical errors, and therefore I did not attempt an extrapolation. For comparison, the RBC and UKQCD collaborations have obtained $a^{-1} = 1.729(28)_{\text{stat}}$ in the chiral limit, using the Ω^- baryon mass [128]. This is consistent with my results obtained here.

Next, I used the lattice spacing determinations from the $2S - 1S$ splitting to convert the other radial and orbital splittings from Table 7.6 to physical units. The results are plotted in Fig. 7.4. Note that I used the individual results for the lattice spacings of the different ensembles.

Overall, good agreement with experiment is seen, as in [108]. The dependence on the light sea quark mass is found to be weak. This is expected since the typical gluon momenta inside the bottomonium are much larger than all the values for the light quark masses used here. However, note that large deviations between lattice results and experiment were previously seen in quenched simulations ($n_f = 0$), so the inclusion of 2+1 flavors of dynamical light quarks is in fact very important. A comparison between quenched and unquenched results can be found in [6].

	$am_l = 0.005$	$am_l = 0.01$	$am_l = 0.02$	$am_l = 0.03$
$\Upsilon(1S) - \eta_b(1S)$	0.03017(14)	0.03033(16)	0.03102(36)	0.03145(38)
$\Upsilon(2S) - \eta_b(2S)$	0.0137(30)	0.0120(48)	0.013(12)	0.018(16)
$\chi_{b0}(1P) - \langle\chi_b(1P)\rangle$	−0.0207(20)	−0.0206(18)	−0.0231(36)	−0.0175(70)
$\chi_{b1}(1P) - \langle\chi_b(1P)\rangle$	−0.0049(14)	−0.0027(19)	−0.0059(22)	−0.0049(41)
$\chi_{b2}(1P) - \langle\chi_b(1P)\rangle$	0.0071(11)	0.0058(12)	0.0082(17)	0.0064(29)
$h_b(1P) - \langle\chi_b(1P)\rangle$	−0.0026(18)	−0.0002(21)	−0.0014(27)	−0.0058(42)
$\chi_{b1}(1P) - \chi_{b0}(1P)$	0.0158(18)	0.0176(25)	0.0173(40)	0.0126(77)
$\chi_{b2}(1P) - \chi_{b1}(1P)$	0.0120(23)	0.0088(31)	0.0137(38)	0.0113(68)
$h_b(1P) - \chi_{b1}(1P)$	0.0023(16)	0.0027(16)	0.0044(35)	−0.0009(61)
$\Upsilon_2(1D) - \eta_b(1D)$	0.0011(21)	−0.0012(18)	−0.0086(70)	−0.0050(61)

Table 7.9: Spin-dependent energy splittings in lattice units. Errors are statistical/fitting only. Large systematic errors are expected as discussed in the text.

7.1.7 Spin-dependent energy splittings

The spin-dependent energy splittings in bottomonium, i.e. the fine and hyperfine structure, are of order $\mathcal{O}(v^4_{\text{orb.}})$ and hence any sub-leading corrections are missing in the NRQCD action used here. Therefore, the relativistic errors in these splittings are expected to be of order $\mathcal{O}(v^2_{\text{orb.}}) \approx 10\%$. The spin-dependent energy splittings also receive radiative corrections of order $\mathcal{O}(\alpha_s)$, the strong coupling constant at the scale set by the lattice spacing. This may in principle lead to further systematic errors of the order of 20%, although the tadpole improvement used here (see Sec. 2.7.1) reduces the problem. Finally, discretisation errors are also expected to be larger than for the radial and orbital splittings, especially for the S-wave hyperfine splitting as discussed below.

My results for the spin-dependent energy splittings in lattice units are summarised in Table 7.9, where the errors given are statistical/fitting only.

S-wave hyperfine structure

Figure 7.5 shows a plot of the $\Upsilon(1S) - \eta_b(1S)$ and $\Upsilon(2S) - \eta_b(2S)$ energy splittings, where I used the previous lattice spacing determinations from the $2S - 1S$ splittings to convert to physical units.

The errors shown are statistical/fitting only but include the uncertainty in the determination of the lattice spacing. The latter in fact enters with a factor of 2 here, as

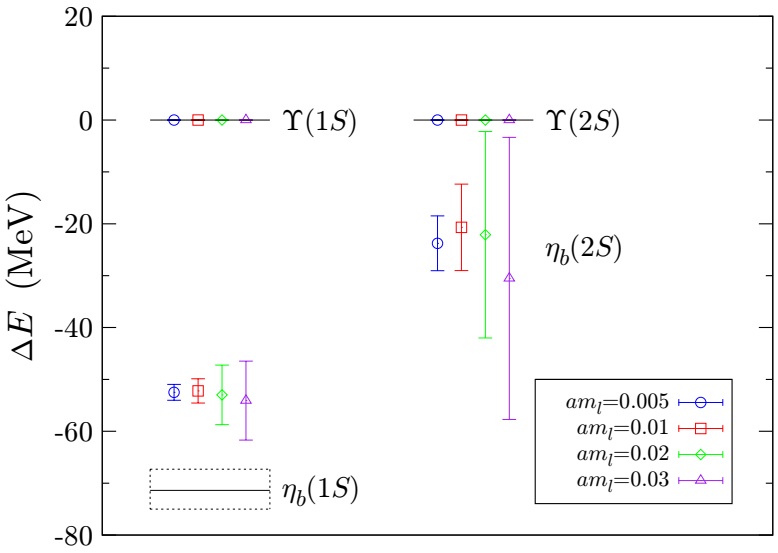

Figure 7.5: S-wave hyperfine splittings (energies relative to the $\Upsilon(1S)$ and $\Upsilon(2S)$ states, respectively) compared to experiment. Errors are statistical/fitting only and include the uncertainty in the determination of the lattice spacing, which enters with a factor of 2. Large systematic errors are expected as discussed in the text.

discussed in [140], due to the resulting uncertainty in the physical heavy quark mass (the hyperfine splitting is approximately proportional to the inverse of that mass). The statistical error in the $1S$ hyperfine splitting is then dominated by far by this uncertainty, while the $2S$ hyperfine splitting has an intrinsically higher statistical error as the state is radially excited.

The $\Upsilon(1S) - \eta_b(1S)$ splitting has recently been measured by the BaBar collaboration [138], who found $71.4^{+2.3}_{-3.1}(\text{stat}) \pm 2.7(\text{syst})$ MeV. This value is indicated in Fig. 7.5. The lattice result in physical units for the $am_l = 0.005$ ensemble is $52.5 \pm 1.5(\text{stat})$ MeV, which is too small by about 25%, in line with the large systematic errors expected. Similarly to the radial and orbital splittings, little dependence on the light sea quark mass is seen, which is expected for the same reason as discussed there.

Note that in [108] and [140] a significant dependence on the lattice spacing was found, with the result increasing toward finer lattices, indicating that a substantial part of the deviation is due to discretisation errors. The hyperfine splitting is indeed expected to be sensitive to very short distances, as the spin-spin interaction potentials in simple models contain a delta function at the origin (see e.g. [142]).

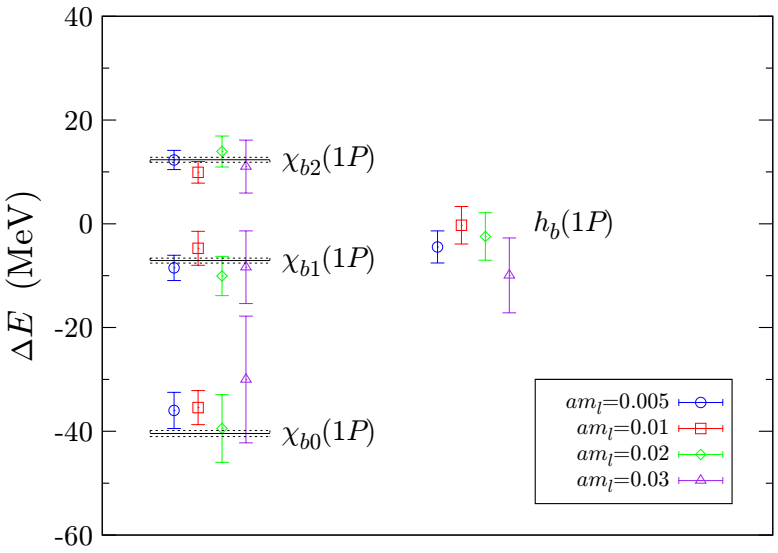

Figure 7.6: P-wave spin splittings (energies relative to the spin-average of the $\chi_b(1P)$ states) compared to experiment. Errors are statistical/fitting only and include the uncertainty in the determination of the lattice spacing. Large systematic errors are expected as discussed in the text.

Finally, note that in [143], where a relativistic heavy-quark action was used, the $\Upsilon(1S) - \eta_b(1S)$ splitting on the same RBC/UKQCD gauge configurations was found to be only 23.7 ± 3.7(stat) MeV. My result obtained with lattice NRQCD is much closer to the experimental value.

P-wave spin-dependent splittings

A plot of the $1P$ spin-dependent splittings, converted to physical units using the previous $2S - 1S$ lattice spacing results, is given in Fig. 7.6.

I show the energy differences of the $\chi_{b0}(1P)$, $\chi_{b1}(1P)$, $\chi_{b2}(1P)$ and $h_b(1P)$ states to the spin-average of the triplet $\langle\chi_b(1P)\rangle$. The experimental results [83] for the triplet states are also indicated in the plot; the h_b states have not yet been observed.

The lattice results are found to be in relatively good agreement with experiment, even within the purely statistical/fitting errors shown in the plot (those include the uncertainty in the lattice spacing). This indicates that discretisation errors may be smaller than for the S-wave hyperfine splittings. Note that in simple potential models the wave function at the origin is zero (cf. the smearing functions in Table 7.2) and hence the P-wave spin

splittings are expected to be not as sensitive to very short distances as the S-wave hyperfine splittings.

My result for the experimentally unknown $h_b(1P) - \langle\chi_b(1P)\rangle$ splitting on the $am_l = 0.005$ ensemble is -4.5 ± 3.1 MeV, where the error quoted is statistical/fitting only and includes the uncertainty from the determination of the lattice spacing.

D-wave spin-dependent splittings

Here, I only calculated the $\Upsilon_2(1D) - \eta_b(1D)$ splitting, using the E^{--} and T_2^{-+} representations as these two states do not mix and can be computed from the same heavy-quark propagators.

My lattice results for the different ensembles are listed in Table 7.9. On the $am_l = 0.005$ ensemble, I find the splitting in physical units to be 1.8 ± 3.7 MeV where the error given is statistical/fitting only and includes the uncertainty from the determination of the lattice spacing. No experimental results are available.

7.2 Bottom hadrons

The results of the previous section demonstrate that the combination of lattice NRQCD for the b quarks and the Iwasaki gluon / domain wall sea quark actions works well at this lattice spacing. The next step is the calculation of heavy-light hadron masses on the same gauge field configurations, using the domain wall action for the light valence quarks. Here, the good chiral properties of the domain wall action will be very useful.

Presently, singly-bottom baryons are the focus of intense experimental and theoretical study. The Λ_b is the first b-baryon discovered [144], followed more recently by the Σ_b and Σ_b^* [145] and the Ξ_b [146, 147]. As already mentioned at the beginning of this chapter, there are two incompatible results for the mass of the most recent discovery, the Ω_b baryon [133, 134]. No baryons with more than one b quark have been observed so far, but they may be discovered at the Large Hadron Collider.

A number of unquenched lattice calculations of bottom baryon masses have been done recently [148, 149, 150, 151, 152]. It is important to perform independent determinations of the same quantities with different lattice formulations in order to test universality, and the combination of NRQCD heavy- and domain wall light quarks has not been used by others. Compared to the static heavy-quark action, which was used in [149, 151, 152], NRQCD has the advantage that it is not restricted to systems containing only a single

b quark. Also, heavy-light spin splittings which would vanish in the static limit can be calculated.

7.2.1 Quark propagators

For the calculation of heavy-light meson and baryon masses, I reuse the u/d and s valence quark domain wall propagators that were computed (using Chroma [136]) and saved during the static-light calculation in [151].

These light-quark propagators have gauge-invariant Gaussian-smeared sources, where APE-smeared gauge links [153, 154] were used in constructing the source. For each of these propagators I also compute a second propagator by smearing the sink in the same way as the source[1].

All calculations are done in the exact isospin limit $m_u = m_d \equiv m_l$. So far, I performed the spectrum calculations only with the propagators on the $am_l = 0.005$, $am_s = 0.04$ ensemble, with valence quark masses equal to the sea quark masses. These quark masses correspond to pion and kaon masses of about 330 and 580 MeV, respectively. Note that not only the u/d quark mass but also the strange quark mass is too large; the physical point corresponds to $am_s \approx 0.034$ [128].

I compute NRQCD bottom quark propagators for point sources (a Kronecker-delta in position-, colour- and spin space) and Gaussian-smeared sources (without link smearing). A Gaussian-smeared source is obtained by applying the operator

$$\left(1 + \frac{\sigma}{n_S}\Delta^{(2)}\right)^{n_S} \tag{7.10}$$

to a point source. In (7.10), $\Delta^{(2)}$ is the covariant lattice Laplacian defined in (A.12). I used $n_S = 10$ steps of smearing and set the width to $\sigma = 1.0$. I also computed sink-smeared b-quark propagators, obtained by applying the operator (7.10) at the sink. The b-quark mass is set to $am_b = 2.514$, as obtained in Sec. 7.1.4.

In order to increase statistics, I compute hadron correlators directed both forward and backward in time. The four-component NRQCD b-quark propagator in the nonrelativistic Dirac gamma matrix-basis is given by

$$G(x,\, x') \;=\; \theta(\tau - \tau') \begin{pmatrix} G_\psi(x,\, x') & 0 \\ 0 & 0 \end{pmatrix} - \theta(\tau' - \tau) \begin{pmatrix} 0 & 0 \\ 0 & G_\xi(x,\, x') \end{pmatrix}. \tag{7.11}$$

Here, G_ψ and G_ξ may include the smearing operator (7.10) at source/and or sink.

[1] The Chroma input XML file for this procedure was provided by W. Detmold.

Note that the light-quark propagators generated by the Chroma software are stored in a chiral gamma matrix basis (the "DeGrand-Rossi" basis). Before combining them with (7.11) to form hadron correlation functions, I convert the light-quark propagators to the nonrelativistic Dirac gamma matrix basis (A.3) by means of a similarity transformation.

In the following, I shall denote the generic light-quark field (in the nonrelativistic Dirac basis) by q and the bottom-quark field by

$$Q = \begin{pmatrix} \psi \\ \xi \end{pmatrix}. \tag{7.12}$$

7.2.2 B mesons

I use interpolating fields of the form $\overline{q}\,\gamma_5\,Q$ for the pseudoscalar B/B_s mesons and $\overline{q}\,\gamma_j\,Q$ for the vector mesons B^*/B_s^*. These fields may include the smearing types discussed in Sec. 7.2.1.

Since all light-quark propagators G_q have a smeared source, there are two possibilities for the meson source, which I denote as `(L,s)` and `(S,s)`. Here, the capital letter denotes a local (`L`) or smeared (`S`) source for the heavy quark; the lower-case letter similarly denotes the source type for the light quark. At the sink, there are the four possibilities `(L,s)`, `(S,s)`, `(L,l)`, `(S,l)`.

Thus, I perform (2×4)-matrix fits of the form (6.11), with four sets of amplitude parameters corresponding to the smearings `(L,s)`, `(S,s)`, `(L,l)`, `(S,l)`. An example of such a fit for the B meson is shown in Fig. 7.7. There, I also show an "effective-energy" plot, where the effective-energy function is defined as

$$E_{\text{eff}}(\tau + 1/2) = \ln\left(\frac{C(\tau)}{C(\tau+1)}\right) \tag{7.13}$$

for a correlator $C(\tau)$. For large Euclidean time separation τ, this approaches the (unphysical, i.e. shifted) ground-state energy. As can be seen in the figure, the various types of smearing all behave similarly. Recall that no completely un-smeared correlators are included here; these would behave very differently (with more contamination from excited states).

My results for the hyperfine splittings in the B mesons are listed in Table 7.10. For the conversion to physical units I used the result for the lattice spacing from Table 7.8. The predicted hyperfine splittings agree well with the experimental values.

To compute the full hadron masses in a way that leads to only weak dependence on the bare b quark mass, one can use the experimental value for the mass of e.g. the $\Upsilon(1S)$

	$a\,\Delta M$ lattice	ΔM (MeV) lattice	ΔM (MeV) experiment
$B^* - B$	0.0277(49)	48(9)	45.78(35)
$B_s^* - B_s$	0.0280(21)	49(4)	46.1(1.5)

Table 7.10: Spin splittings in B mesons for $am_l = 0.005$, $am_s = 0.04$. Errors are statistical/fitting only. Experimental values from [83].

meson as an input parameter in the following way,

$$M = E_{\text{lat.}} + \frac{n_b}{2}\left(M^{\Upsilon}_{\text{exp.}} - E^{\Upsilon}_{\text{lat.}}\right), \tag{7.14}$$

where n_b denotes the number of b quarks in the hadron ($n_b = 1$ for the B mesons considered here) and $E_{\text{lat.}}$ denotes the energy in the lattice calculation.

The results for the full B meson masses computed using (7.14) are plotted together with the experimental values in Fig. 7.8. As expected for the unphysical light-quark masses $am_l = 0.005$, $am_s = 0.04$, the lattice results are found to be slightly above the experimental results. Chiral extrapolations to the physical quark masses will be performed in the future.

7.2.3 Singly-bottom baryons

For baryons containing a single b-quark and two light quarks q, q', I use interpolating fields of the form

$$O_\alpha^{\Gamma\, q\, q'} = \epsilon_{abc}\,(C\Gamma)_{\beta\gamma}\,q_\beta^a\,q_\gamma'^b\,Q_\alpha^c\,, \tag{7.15}$$

where $a, b, ...$ are colour indices running from 1 to 3 and $\alpha, \beta, ...$ are spinor indices running from 1 to 4. In (7.15), $C = \gamma_0\gamma_2$ is the Euclidean charge-conjugation matrix and Γ is a Dirac matrix that determines the total spin of the light degrees of freedom: $\Gamma = \gamma_5$ for $S_l = 0$ and $\Gamma = \gamma_j$ for $S_l = 1$. The total spin of the light degrees of freedom becomes a conserved quantum number in the static limit $m_b \to \infty$.

Note that $(C\gamma_5)^T = -C\gamma_5$ and $(C\gamma_j)^T = C\gamma_j$. This implies

$$O_\alpha^{\Gamma\, q'\, q} = \begin{cases} -O_\alpha^{\Gamma\, q\, q'} & \text{for} \quad \Gamma = \gamma_5, \\ O_\alpha^{\Gamma\, q\, q'} & \text{for} \quad \Gamma = \gamma_j, \end{cases} \tag{7.16}$$

and hence for $q = q'$ one must have $\Gamma = \gamma_j$ and $S_l = 1$.

The singly-bottom baryons in the isospin limit and their interpolating operators are listed in Table 7.11. Note that the operators with $\Gamma = \gamma_j$ have an overlap with both the

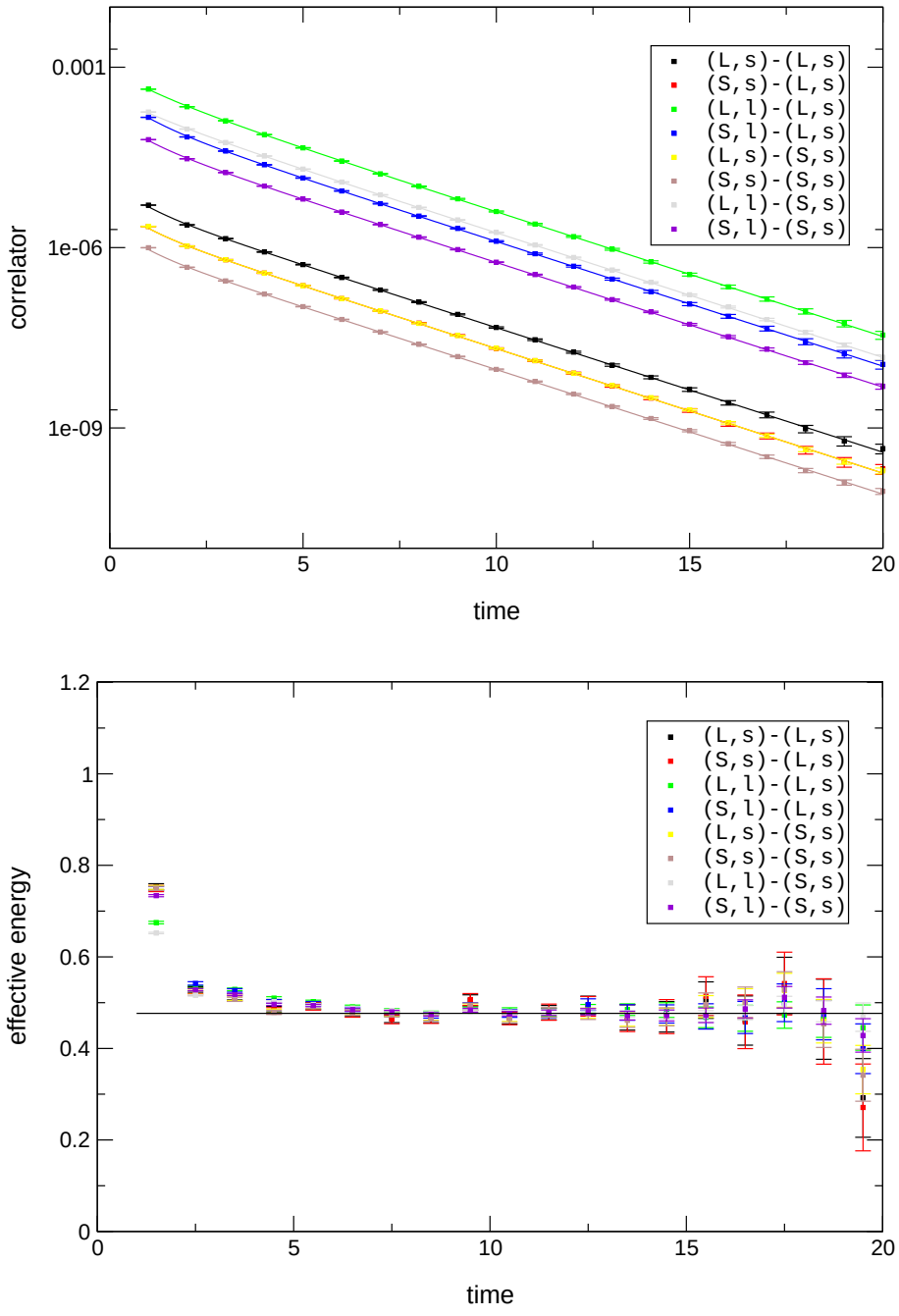

Figure 7.7: Fit to a 2×4 matrix of correlators for the B meson, with $n_{\mathrm{exp}} = 6$ and $\tau_{\mathrm{min}} = 3$. The upper panel shows the correlator data and the fit functions. The lower panel shows an effective-energy plot with the ground-state fit result.

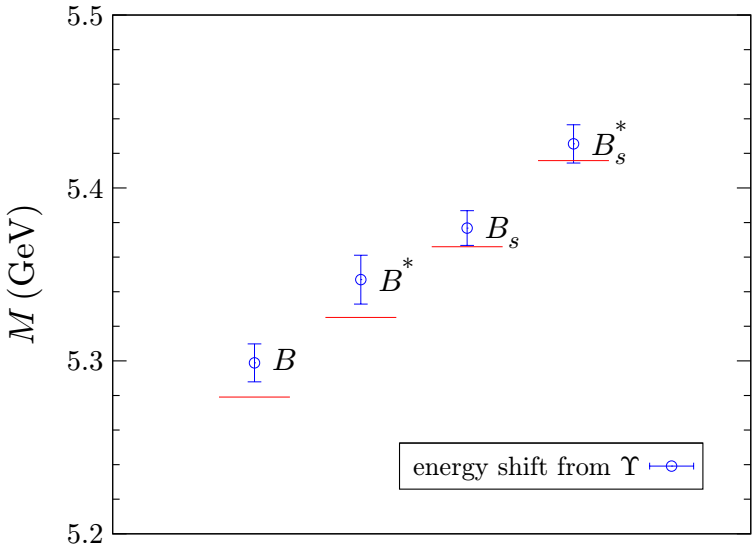

Figure 7.8: Masses of B mesons for $am_l = 0.005$, $am_s = 0.04$. The lines indicate the experimental values [83].

Hadron(s)	J^P	S_l	Operator
Λ_b	$\frac{1}{2}^+$	0	$\epsilon_{abc}\,(C\gamma_5)_{\beta\gamma}\,q^a_\beta\,q'^b_\gamma\,Q^c_\alpha$
Σ_b, Σ_b^*	$\frac{1}{2}^+$, $\frac{3}{2}^+$	1	$\epsilon_{abc}\,(C\gamma_j)_{\beta\gamma}\,q^a_\beta\,q'^b_\gamma\,Q^c_\alpha$
Ξ_b	$\frac{1}{2}^+$	0	$\epsilon_{abc}\,(C\gamma_5)_{\beta\gamma}\,q^a_\beta\,s^b_\gamma\,Q^c_\alpha$
Ξ_b', Ξ_b^*	$\frac{1}{2}^+$, $\frac{3}{2}^+$	1	$\epsilon_{abc}\,(C\gamma_j)_{\beta\gamma}\,q^a_\beta\,s^b_\gamma\,Q^c_\alpha$
Ω_b, Ω_b^*	$\frac{1}{2}^+$, $\frac{3}{2}^+$	1	$\epsilon_{abc}\,(C\gamma_j)_{\beta\gamma}\,s^a_\beta\,s^b_\gamma\,Q^c_\alpha$

Table 7.11: Interpolating fields for baryons containing a single b quark. S_l denotes the total spin of the light degrees of freedom, which becomes a conserved quantum number for $m_b \to \infty$.

$J = \frac{3}{2}$ and $J = \frac{1}{2}$ states. For the correlator $C_{jk}(\tau)$ with $\Gamma = \gamma_j$ at the source and $\Gamma = \gamma_k$ at the sink one has at zero momentum and large $\tau > 0$

$$C_{jk}(\tau) = Z_{3/2}^2\, e^{-E_{3/2}\,\tau}\, \tfrac{1}{2}(1+\gamma_0)(\delta_{jk} - \tfrac{1}{3}\gamma_j\gamma_k) + Z_1^2\, e^{-E_{1/2}\,\tau}\, \tfrac{1}{2}(1+\gamma_0)\tfrac{1}{3}\gamma_j\gamma_k \qquad (7.17)$$

(see [155]). The $J = \frac{3}{2}$ and $J = \frac{1}{2}$ contributions can be disentangled by multiplying with the projectors $(\delta_{ij} - \frac{1}{3}\gamma_i\gamma_j)$ and $\frac{1}{3}\gamma_i\gamma_j$, respectively:

$$\begin{aligned} (\delta_{ij} - \tfrac{1}{3}\gamma_i\gamma_j)\, C_{jk}(\tau) &= Z_{3/2}^2\, e^{-E_{3/2}\,\tau}\, \tfrac{1}{2}(1+\gamma_0)(\delta_{ik} - \tfrac{1}{3}\gamma_i\gamma_k), \\ \tfrac{1}{3}\gamma_i\gamma_j\, C_{jk}(\tau) &= Z_1^2\, e^{-E_{1/2}\,\tau}\, \tfrac{1}{2}(1+\gamma_0)\tfrac{1}{3}\gamma_i\gamma_k. \end{aligned} \qquad (7.18)$$

Note that for $\tau < 0$, one has $\frac{1}{2}(1-\gamma_0)$ instead of $\frac{1}{2}(1+\gamma_0)$ in (7.18).

For the singly-bottom baryons, I use the same type of smearing on both light quarks. Thus, the baryon operators are classified in terms of their smearing in the same way as the B meson operators in Sec. 7.2.2. Again, I perform (2×4)-matrix fits. An example of such a fit for the Λ_b baryon is shown in Fig. 7.9.

Table 7.12 lists the results for the heavy-light spin splittings. An experimental value is known only for $\Sigma_b^* - \Sigma_b$; my lattice result agrees with this but the statistical errors are rather large. It is planned to increase statistics in the future by computing more domain-wall propagators.

Results for the mass differences of the $J = \frac{1}{2}$ singly-bottom baryons to the $B/B_s/\Lambda_b$ hadrons are listed in Table 7.13. To compute the absolute baryon masses, I compare two different methods: (I) using the $\Upsilon(1S)$ mass via Eq. 7.14 with $n_b = 1$ and (II) using the B mass via

$$M = E_{\text{sim.}} + n_b \left(M^B_{\text{exp.}} - E^B_{\text{sim.}}\right) \qquad (7.19)$$

with $n_b = 1$. The results are plotted in Fig. 7.9. The hadron masses at the present unphysically large values for the light quark masses tend to be slightly above the experimental results. Taking into account the overall picture, my lattice result for the Ω_b mass appears to favour the CDF measurement [134] over the DØ measurement [133]. Definitive conclusions can only be made after chiral extrapolation, and, eventually, after the inclusion of different lattice spacings and volumes (finite-volume effects are also known to increase the energy).

Note that the Υ mass shows little dependence on the sea quark masses, while the B has a light valence quark. Thus, (7.14) and (7.19) lead to very different chiral behaviour of M, which likely explains the discrepancies between the two methods seen at the present quark masses.

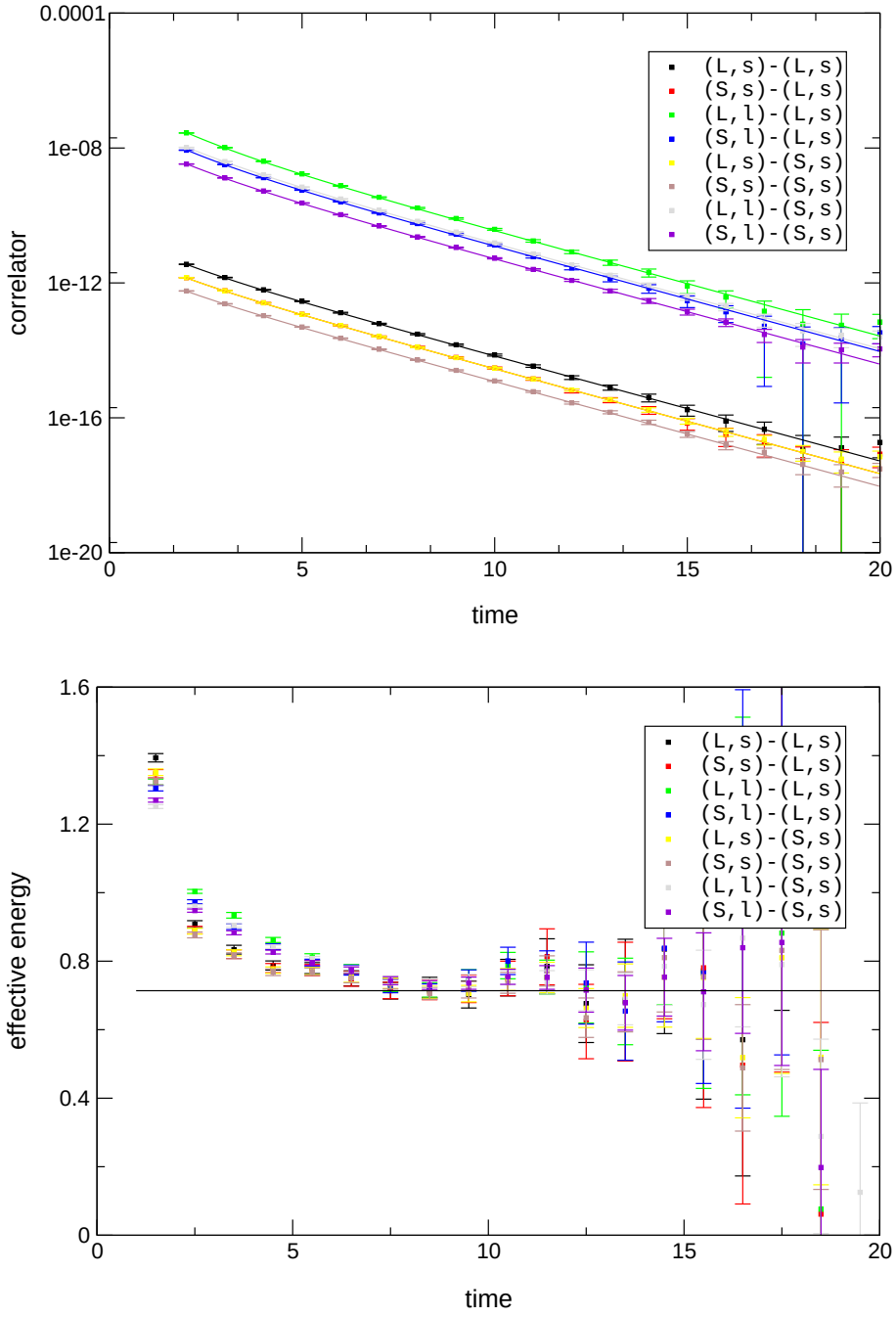

Figure 7.9: Fit to a 2×4 matrix of correlators for the Λ_b baryon, with $n_{\text{exp}} = 6$ and $\tau_{\text{min}} = 3$. The upper panel shows the correlator data and the fit functions. The lower panel shows an effective-energy plot with the ground-state fit result.

	$a\,\Delta M$ lattice	ΔM (MeV) lattice	ΔM (MeV) experiment
$\Sigma_b^* - \Sigma_b$	0.014(14)	25(25)	21.2(2.0)
$\Xi_b^* - \Xi_b'$	0.0105(94)	18(16)	–
$\Omega_b^* - \Omega_b$	0.0108(59)	19(10)	–

Table 7.12: Heavy-light spin splittings in singly-bottom baryons for $am_l = 0.005$, $am_s = 0.04$. Errors are statistical/fitting only. The experimental value for $\Sigma_b^* - \Sigma_b$ is from [83].

	$a\,\Delta M$ lattice	ΔM (GeV) lattice	ΔM (GeV) experiment
$\Lambda_b - B$	0.235(20)	0.408(36)	0.3410(16)
$\Sigma_b - B$	0.350(17)	0.608(31)	0.5286(27)
$\Xi_b - B$	0.320(14)	0.556(25)	0.5132(30)
$\Xi_b' - B$	0.407(10)	0.708(21)	–
$\Omega_b - B$	0.4589(79)	0.798(18)	0.7752(69)
$\Lambda_b - B_s$	0.190(21)	0.330(36)	0.2539(17)
$\Sigma_b - B_s$	0.305(17)	0.530(31)	0.4415(28)
$\Xi_b - B_s$	0.275(14)	0.478(25)	0.4261(31)
$\Xi_b' - B_s$	0.362(10)	0.630(20)	–
$\Omega_b - B_s$	0.4141(68)	0.720(16)	0.6881(69)
$\Sigma_b - \Lambda_b$	0.115(23)	0.200(40)	0.1876(31)
$\Xi_b - \Lambda_b$	0.085(15)	0.148(27)	0.1722(34)
$\Xi_b' - \Lambda_b$	0.172(22)	0.300(38)	–
$\Omega_b - \Lambda_b$	0.224(21)	0.390(37)	0.4342(71)

Table 7.13: Mass differences of the $J = \frac{1}{2}$ singly-bottom baryons to the $B/B_s/\Lambda_b$ for $am_l = 0.005$, $am_s = 0.04$. Errors are statistical/fitting only. Experimental values from [83] and [134].

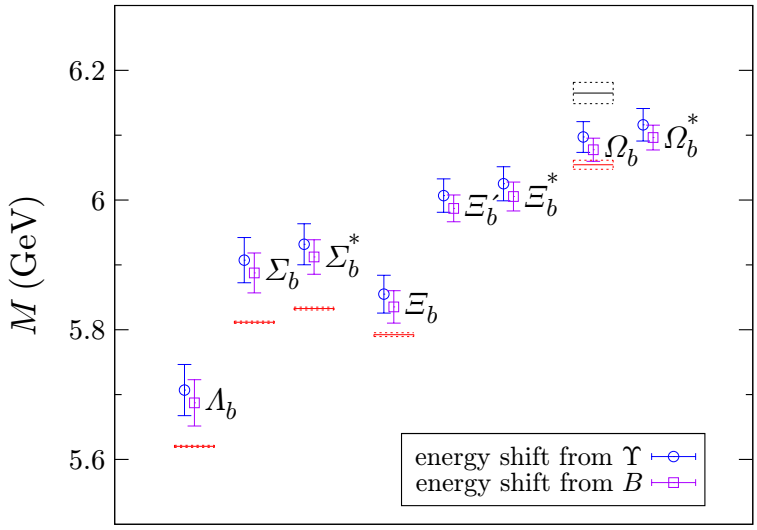

Figure 7.10: Masses of singly-bottom baryons for $am_l = 0.005$, $am_s = 0.04$. The lines indicate the experimental values [83, 133, 134]. The DØ result [133] for the Ω_b mass is indicated in black; the CDF result [134] in red.

Hadrons	J^P	S_{QQ}	Operator
Ξ_{bb}, Ξ^*_{bb}	$\frac{1}{2}^+$, $\frac{3}{2}^+$	1	$\epsilon_{abc}\,(C\gamma_j)_{\beta\gamma}\,Q^a_\beta\,Q^b_\gamma\,q^c_\alpha$
Ω_{bb}, Ω^*_{bb}	$\frac{1}{2}^+$, $\frac{3}{2}^+$	1	$\epsilon_{abc}\,(C\gamma_j)_{\beta\gamma}\,Q^a_\beta\,Q^b_\gamma\,s^c_\alpha$

Table 7.14: Interpolating fields for baryons containing two b quarks. S_{QQ} denotes the total spin of the heavy quarks.

	$a\,\Delta M$ lattice	ΔM (MeV) lattice	ΔM (MeV) experiment
$\Xi^*_{bb} - \Xi_{bb}$	0.0140(75)	24(14)	–
$\Omega^*_{bb} - \Omega_{bb}$	0.0219(54)	38(9)	–

Table 7.15: Heavy-light spin splittings in doubly-bottom baryons for $am_l = 0.005$, $am_s = 0.04$. Errors are statistical/fitting only.

7.2.4 Doubly-bottom baryons

For the doubly-bottom baryons, the role of the light and heavy quarks in (7.15) is interchanged. The interpolating fields for the doubly-bottom baryons are listed in Table 7.14. As for the singly-bottom baryons, I use the spin projection (7.18) to separate the $J = \frac{1}{2}$ and $J = \frac{3}{2}$ states. The energy splittings between these are listed in Table 7.15.

I also use the same smearing for both heavy quarks. A (2×4)-matrix fit for the Ω_{bb} is shown in Fig. 7.11. As can be seen in the effective-energy plot, there is now a more significant difference between the correlators with and without smearing for the heavy quarks. This is expected, as the two heavy quarks can be excited in a similar way as in bottomonium.

Again, I use both methods (7.14) and (7.19) to compute the absolute hadron masses. The results are shown in Fig. 7.12. Here, the differences between the two methods (7.14) and (7.19) for the unphysical quark masses are enhanced since $n_b = 2$.

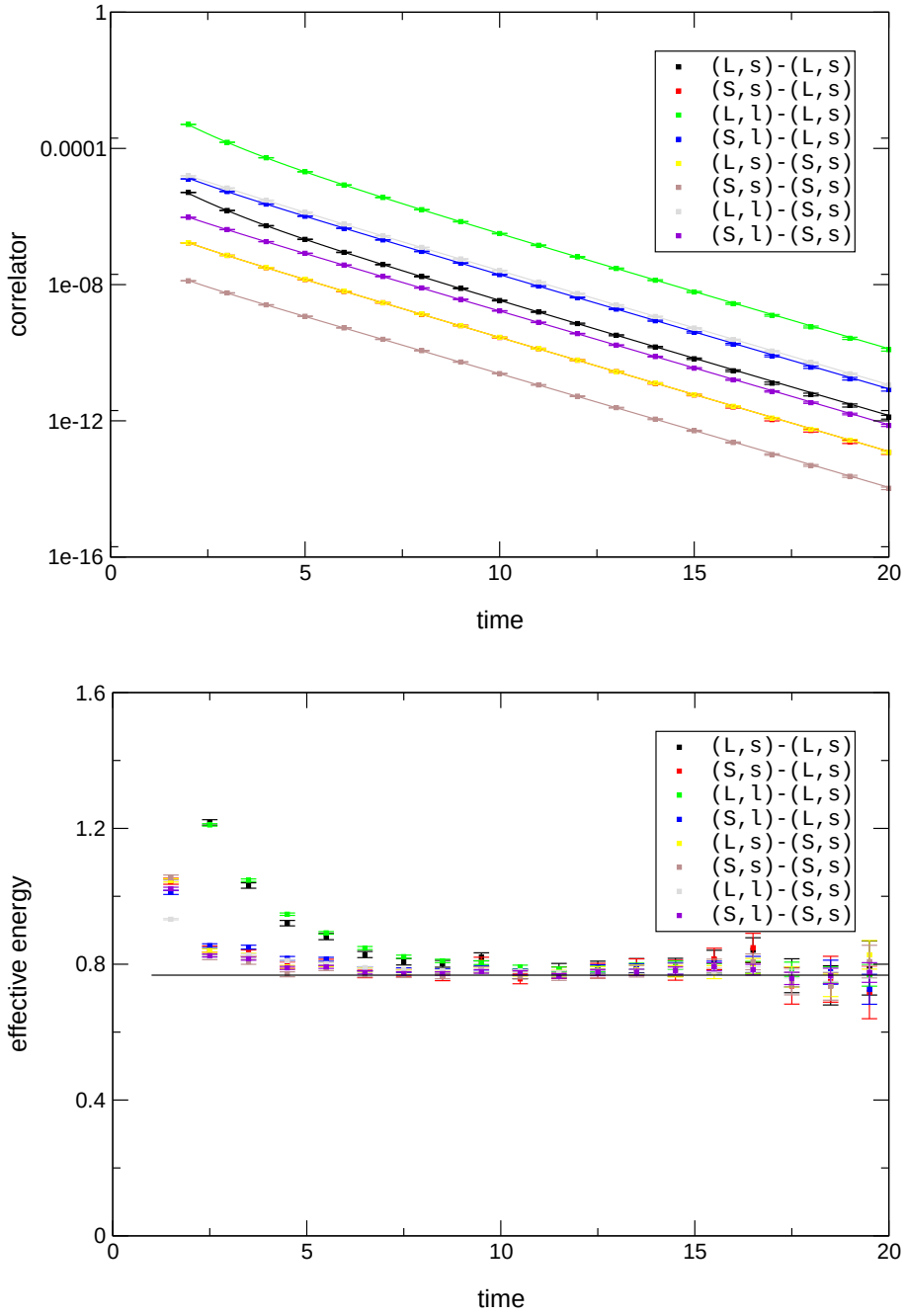

Figure 7.11: Fit to a 2×4 matrix of correlators for the Ω_{bb} baryon, with $n_{\text{exp}} = 6$ and $\tau_{\text{min}} = 3$. The upper panel shows the correlator data and the fit functions. The lower panel shows an effective-energy plot with the ground-state fit result.

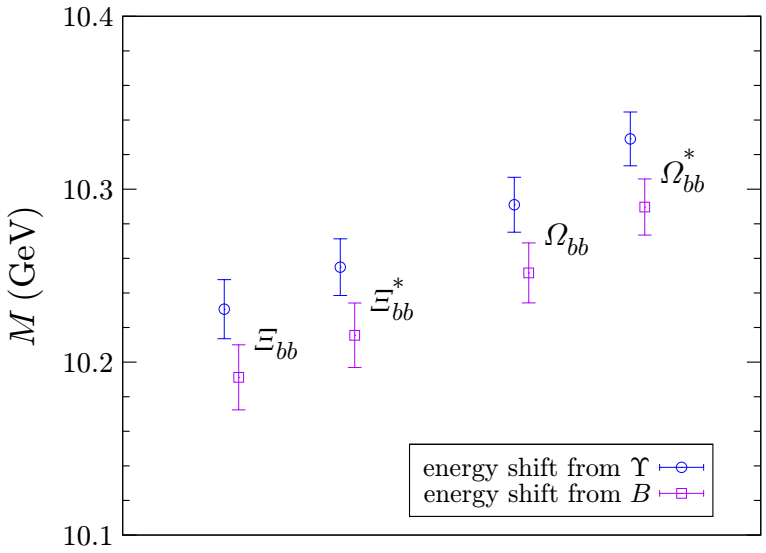

Figure 7.12: Masses of doubly-bottom baryons for $am_l = 0.005$, $am_s = 0.04$.

7.2.5 The Ω_{bbb} baryon

For the Ω_{bbb} baryon, I use interpolating operators of the form

$$\epsilon_{abc}\,(C\gamma_j)_{\beta\gamma}\,Q^a_\beta\,Q^b_\gamma\,Q^c_\alpha. \tag{7.20}$$

The only physical state is the one with $J = \frac{3}{2}$.

As the Ω_{bbb} baryon does not contain light valence quarks, the dependence on the light sea quark masses is expected to be weak once these are light enough, similarly to bottomonium. Thus, Eq. (7.14) is the better method for computing the absolute mass of the Ω_{bbb}, and no chiral extrapolation is required.

Also, since NRQCD is computationally cheap, one can go to very high statistics with little cost. A plot of a (2×2)-matrix correlator from about 10^5 NRQCD propagators on the $am_l = 0.005$, $am_s = 0.04$ ensemble is shown in Fig. 7.13. As can be seen, the signal is very good. The (unphysical) energy obtained from the fit is

$$aE_{\Omega_{bbb}} = 0.5527(12). \tag{7.21}$$

I also computed a high-statistics Υ correlator from the same propagators. Fitting it gives

$$aE_{\Upsilon(1S)} = 0.29786(20). \tag{7.22}$$

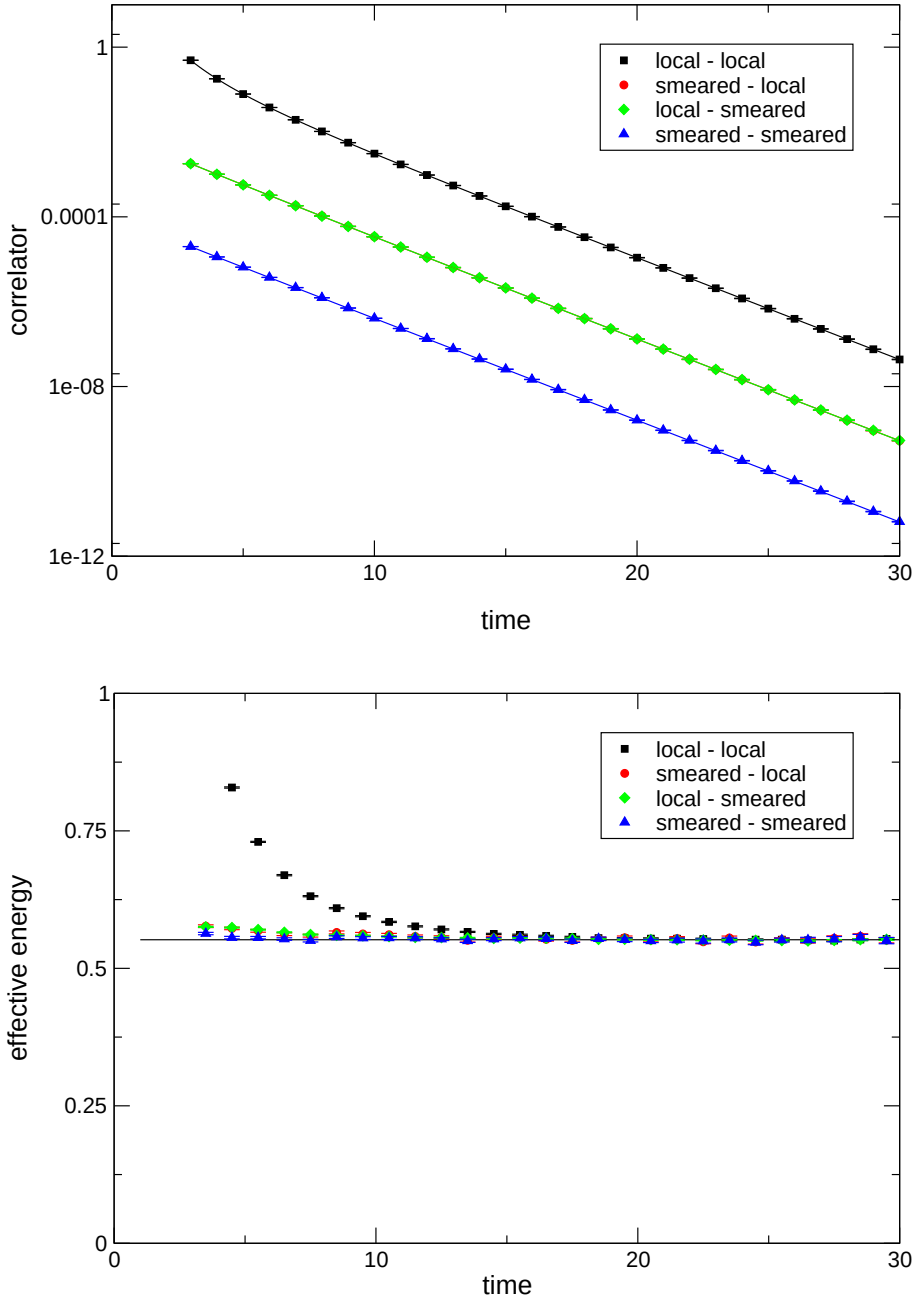

Figure 7.13: Fit to a 2×2 matrix of correlators for the Ω_{bbb} baryon, with $n_{\mathrm{exp}} = 6$ and $\tau_{\mathrm{min}} = 3$. The upper panel shows the correlator data and the fit functions. The lower panel shows an effective-energy plot with the ground-state fit result.

Reference	Method	$M_{\Omega_{bbb}}$ (GeV)
This work	lattice QCD	14.3748(33)
[156]	bag model	14.30
[157]	variational method	14.37(08)
[158]	bag model	14.276
[159]	relativistic quark model	14.569
[160]	sum rules	13.28(10)

Table 7.16: Comparison of my lattice QCD result for the Ω_{bbb} mass to various results from continuum models. The error on my lattice result is statistical/fitting only. See the references given in the table for the details of the errors quoted for the continuum results.

Using the bootstrap method to properly take into account correlations between the Ω_{bbb} and the Υ energies, Eq. (7.14) then leads to

$$M_{\Omega_{bbb}} = 14.3748(33)\ \text{GeV}, \tag{7.23}$$

where the error is statistical only and includes the uncertainty in the lattice spacing (the latter was taken from Table 7.8). To my knowledge, this is the first lattice QCD calculation of the Ω_{bbb} mass.

The Ω_{bbb} mass has been estimated before using various continuum methods. In Table 7.16 I compare my result to these estimates. I find excellent agreement with the value from the variational method given in [157]. The other results are also close, with the notable exception of [160], where QCD sum rules were used.

The production of the Ω_{bbb} at hadron colliders has been studied in [161, 162]. For the LHC at $\sqrt{s} = 14$ TeV, the integrated cross section for direct fragmentation production $b \to \Omega_{bbb}$ was estimated to be about 8 pb.

Chapter 8

Rare B decays

The tests described in Chapter 6 demonstrate the good properties of moving NRQCD. In the following I show how mNRQCD can be applied to the calculation of form factors for B decays and present numerical results.

The interactions with W and Z bosons as well as top quarks are effects at very short distances and can be described by an effective weak Hamiltonian. This method is introduced in Sec. 8.1, where the "tree-level" decay $B \to \pi\ell\nu$ and the rare decay $B \to K^*\gamma$ are considered as examples. The phenomenology of rare decays is rather complex and a complete discussion is beyond the scope of this work. Certain long-distance contributions to rare B decays, which are mentioned in Sec. 8.2, can not be calculated directly in lattice QCD. However, one can choose regions of q^2 where these effects are suppressed. The dominant contributions to the semileptonic and radiative decays then come from operators whose matrix elements can be computed directly in lattice QCD.

These matrix elements are conveniently parametrised in terms of Lorentz-invariant functions called form factors. After giving the definitions of the complete set of B semileptonic form factors in Sec. 8.3, I show how they can be extracted from Euclidean correlation functions in Sec. 8.4.

For the lattice calculation, the heavy-light current in the weak Hamiltonian has to be expressed in terms of the lattice quark fields. This requires the inclusion of several operators multiplied by appropriate matching factors, as discussed in Sec. 8.5.

For a given q^2, the boost velocity $\mathbf{v}$ in the moving NRQCD action should be chosen such that discretisation errors are minimised. Estimates of the optimal choice for $\mathbf{v}$ are shown in Sec. 8.6. Independently of discretisation errors, the heavy-quark effective field theory description of the decay becomes less accurate at low q^2, when the momentum transfer is no longer small compared to m_b. This is discussed in Sec. 8.7.

I then describe in detail the calculation of the two-point and three-point functions with mNRQCD heavy- and staggered light quarks in Sec. 8.8. All constructions are performed for both point- and random-wall sources. The aim of the random-wall source method is to reduce statistical errors. I show in extensive numerical studies to what extent this is possible for the calculation of heavy-to-light decays. Particular emphasis is placed on the analysis of different fitting methods.

Finally, after briefly demonstrating in Sec. 8.9 the contributions of the various operators in the heavy-light current, I present some preliminary form factor results in Sec. 8.10.

8.1 Weak Decays of B Mesons in the Standard Model

8.1.1 Electroweak interactions of quarks

The Lagrange density for the interactions between the quarks and the electroweak gauge bosons $W^{\pm}$, Z and A in the Standard Model has the following form (see e.g. [163, 164]):

$$\mathcal{L}_{\text{q.,e.w.}} = -\frac{g_2}{2\sqrt{2}}\left(J^{\mu}W_{\mu} + J^{\mu\dagger}W_{\mu}^{\dagger}\right) - g_2 \sin\theta_W \; J^{\mu}_{\text{e.m.}} A^{\text{e.m.}}_{\mu} - \frac{g_2}{2\cos\theta_W} J^{\mu}_{\text{n.}} Z_{\mu} \,, \tag{8.1}$$

with the charged weak current

$$J^{\mu} = \begin{pmatrix} \overline{u} & \overline{c} & \overline{t} \end{pmatrix} \; \hat{\gamma}^{\mu}(1-\hat{\gamma}_5) \; V \begin{pmatrix} d \\ s \\ b \end{pmatrix}, \tag{8.2}$$

the electromagnetic current,

$$J^{\mu}_{\text{e.m.}} = -\frac{1}{3}\begin{pmatrix} \overline{d} & \overline{s} & \overline{b} \end{pmatrix} \; \hat{\gamma}^{\mu} \begin{pmatrix} d \\ s \\ b \end{pmatrix} + \frac{2}{3}\begin{pmatrix} \overline{u} & \overline{c} & \overline{t} \end{pmatrix} \; \hat{\gamma}^{\mu} \begin{pmatrix} u \\ c \\ t \end{pmatrix}, \tag{8.3}$$

and the weak neutral current

$$\begin{aligned} J^{\mu}_{\text{n.}} \;=\; & -\frac{1}{2}\begin{pmatrix} \overline{d} & \overline{s} & \overline{b} \end{pmatrix} \; \hat{\gamma}^{\mu}\left(1-\hat{\gamma}_5 - \frac{4}{3}\sin^2\theta_W\right) \begin{pmatrix} d \\ s \\ b \end{pmatrix} \\ & +\frac{1}{2}\begin{pmatrix} \overline{u} & \overline{c} & \overline{t} \end{pmatrix} \; \hat{\gamma}^{\mu}\left(1-\hat{\gamma}_5 - \frac{8}{3}\sin^2\theta_W\right) \begin{pmatrix} u \\ c \\ t \end{pmatrix}. \end{aligned} \tag{8.4}$$

In the charged weak current (8.2), the Cabibbo-Kobayashi-Maskawa matrix

$$V = \begin{pmatrix} V_{ud} & V_{us} & V_{ub} \\ V_{cd} & V_{cs} & V_{cb} \\ V_{td} & V_{ts} & V_{tb} \end{pmatrix}, \tag{8.5}$$

gives rise to a mixing between the quark flavours. In the Standard Model, V is unitary, $V^\dagger V = \mathbb{1}$. After absorbing unobservable phase factors into the definition of the quark fields, 4 free real parameters remain in V. These are three mixing angles and one CP-violating phase. It is known from experiments that V is close to unity; see [83] for the currently known values of the CKM matrix elements and their uncertainties.

Note that the electromagnetic and weak neutral currents (8.3), (8.4) do not change the quark flavour, and therefore transitions within up-type or within down-type quarks like $b \to s$ do not appear at tree-level.

8.1.2 Effective weak Hamiltonians

When describing weak decays of hadrons, it is very useful to separate the short-distance weak interactions from the non-perturbative long-distance dynamics of the hadrons. The heavy W and Z bosons as well as the top quark can be integrated out of the theory, and their effects are then described by new local operators O_n involving the lighter degrees of freedom. The resulting effective Hamiltonian has the general structure

$$\mathcal{H}_{\text{eff}} = \frac{4G_F}{\sqrt{2}} \sum_n V_{CKM}^n \, C_n(\mu) \, O_n, \tag{8.6}$$

where $C_n(\mu)$ are the scale- and renormalisation scheme dependent short-distance coefficients (Wilson coefficients), and V_{CKM}^n stands for the product of CKM matrix elements involved in the weak interactions which yield the effective operator O_n.

The general method to derive the effective Hamiltonian is the operator product expansion. In addition, one must use renormalisation-group methods to evolve the Wilson coefficients from the scale $\mu \sim m_W$ to the scale appropriate to the process under consideration, e.g. $\mu = m_b$ for B decays. For the details, see for example [165, 166].

The operator product expansion can be done in perturbation theory, since asymptotic freedom implies that the QCD coupling is weak at $\mu \sim m_W$. The non-perturbative aspect of the hadron decay then appears in the calculation of the low-energy QCD matrix element $\langle O_n \rangle_\mu$, and this is what can be done on the lattice. Note that the scale- and scheme dependence of this matrix element is cancelled by the corresponding dependence of the Wilson coefficients $C_n(\mu)$, provided that the same renormalisation scheme and scale

is used for both calculations. This means that the lattice results must be converted to the continuum scheme by an appropriate matching calculation (cf. Sec. 8.5).

8.1.3 The decay $B \to \pi\ell\nu$

We will now consider the semileptonic decay $B \to \pi\ell\nu$, from which the magnitude of the CKM matrix element V_{ub} can be determined. Recent experimental results have been published in [12, 13, 14].

The effective Hamiltonian for $b \to u\, e^-\, \bar{\nu}_e$ results from the Feynman diagrams shown in Fig. 8.1.

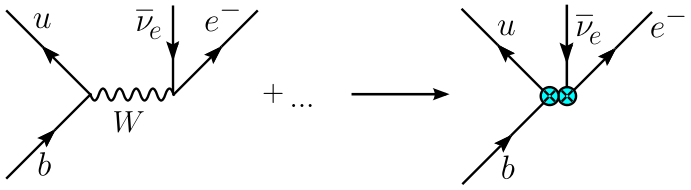

Figure 8.1: Tree-level Feynman diagram contributing to $b \to u\, e^-\, \bar{\nu}_e$

Integrating out the W boson gives the well-known current-current interaction

$$\mathcal{H}_{\text{eff}} = V_{ub} \frac{G_F}{\sqrt{2}}\, C(\mu)\, \overline{u}\hat{\gamma}^\mu(1-\hat{\gamma}_5)b\, \overline{e}\hat{\gamma}_\mu(1-\hat{\gamma}_5)\nu_e \tag{8.7}$$

where $G_F = \sqrt{2}g_2^2/(8m_W^2)$, and up to small loop corrections one has $C(\mu) = 1$. Since the mesons in the initial and final state are both pseudoscalars, only the vector current $\overline{u}\hat{\gamma}^\mu b$ contributes to the hadronic matrix element. The latter can be parametrised by two form factors f_+ and f_-, or equivalently f_+ and f_0, as follows:

$$\begin{aligned} \langle \pi(p')|\, \overline{u}\hat{\gamma}^\mu b\, |B(p)\rangle &= f_+(q^2)\big[p^\mu + p'^\mu\big] + f_-(q^2)\, q^\mu \\ &= f_+(q^2)\left[p^\mu + p'^\mu - \frac{M_B^2 - M_\pi^2}{q^2}\, q^\mu\right] + f_0(q^2)\, \frac{M_B^2 - M_\pi^2}{q^2}\, q^\mu, \end{aligned} \tag{8.8}$$

with $q \equiv p - p'$. Neglecting the lepton masses, the differential decay rate is given by [167]

$$\frac{\mathrm{d}\Gamma}{\mathrm{d}q^2} = \frac{G_F^2 |V_{ub}|^2}{192\pi^3 M_B^3} \left[(M_B^2 + M_\pi^2 - q^2)^2 - 4M_B^2 M_\pi^2\right]^{3/2} |f_+(q^2)|^2. \tag{8.9}$$

Hence, to determine $|V_{ub}|$ from the exclusive measurement of this decay rate, the non-perturbative hadronic matrix element $\langle \pi(p')|\, \overline{u}\hat{\gamma}^\mu b\, |B(p)\rangle$ must be calculated. Two recent unquenched lattice QCD calculations are [11] and [168]. Both works make use of the ASQTAD action for the light quarks. For the b quark, lattice NRQCD was used in [11], while the Fermilab action (cf. Sec. 2.8) was used in [168].

8.1.4 The decay $B \to K^*\gamma$

Among the rare decays, the decay $B \to K^*\gamma$ (first observed by the CLEO collaboration [15]) is the one with the most precise experimental results available [17, 16, 18]. As a loop-mediated flavour-changing neutral current process it is suppressed in the Standard Model, and therefore very sensitive to possible new physics contributions (see for example [169, 170, 171, 172, 173, 174, 175, 176]).

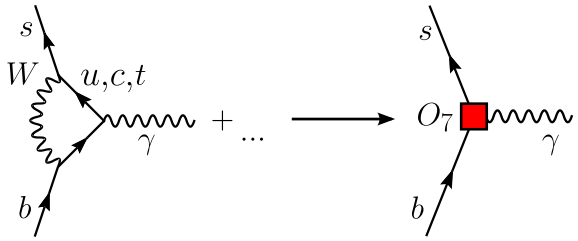

Figure 8.2: Example of a one-loop diagram contributing to O_7

The effective weak Hamiltonian relevant to this radiative decay can be written in the following form,

$$\mathcal{H}_{\text{eff}} = -V_{tb}V_{ts}^* \frac{4G_F}{\sqrt{2}} \sum_{n=1}^{8} C_n(\mu) O_n, \tag{8.10}$$

where O_1, ..., O_6 are 4-quark operators, O_7 is an electromagnetic and O_8 is a chromomagnetic dipole operator [177]. The CKM-matrix dependence has been factored out globally, neglecting $V_{ub} \sim 0$ and using unitarity to replace $V_{cb}V_{cs}^*$ by $-V_{tb}V_{ts}^*$.

The dominant short-distance contribution to $B \to K^*\gamma$ is due to the electromagnetic dipole operator

$$O_7 = \frac{e}{16\pi^2} m_b \, J_{\mu\nu} F^{\mu\nu}_{(\text{e.m.})} \qquad \text{with} \qquad J_{\mu\nu} = \bar{s}\sigma_{\mu\nu}\frac{1+\hat{\gamma}_5}{2} b, \tag{8.11}$$

where $\sigma^{\mu\nu} = \frac{i}{2}[\hat{\gamma}^\mu, \hat{\gamma}^\nu]$. An example of a one-loop Feynman diagram contributing to O_7 is shown in 8.2.

As derived in Sec. B.1, the hadronic matrix element of the tensor current $J_{\mu\nu}$ in O_7 can be parametrised as follows:

$$\begin{aligned} q^\nu \langle K^*(p',\varepsilon)|J_{\mu\nu}|B(p)\rangle \;=\; & 2\,T_1(q^2)\,\epsilon_{\mu\nu\rho\sigma}\;\varepsilon^{*\nu}\,p^\rho\,p'^\sigma \\ & + i\,T_2(q^2)\;\left[\varepsilon^*_\mu\,(M_B^2 - M_{K^*}^2) - (\varepsilon^*\cdot q)(p+p')_\mu\right] \\ & + i\,T_3(q^2)\,(\varepsilon^*\cdot q)\left[q_\mu - \frac{q^2}{M_B^2 - M_{K^*}^2}(p+p')_\mu\right] \end{aligned} \tag{8.12}$$

where $q = p - p'$ and ε is the polarisation vector of the K^* meson. For the physical on-shell photon, one has $q^2 = 0$. Note that $T_1(0) = T_2(0)$.

In Sec. B.2 I give a derivation of the decay rate, with the result

$$\Gamma(B \to K^*\gamma) = \frac{\alpha\, G_F^2}{8\pi^4} C_7(\mu)^2 |V_{tb}V_{ts}^*|^2 m_b^2 M_B^3 \left(1 - \frac{M_{K^*}^2}{M_B^2}\right)^3 |T_1(0)|^2. \tag{8.13}$$

Here, the contributions from the operators other than O_7 are neglected. These contributions will be discussed in Sec. 8.2.

So far, there are no unquenched lattice QCD calculations of the form factors for $B \to K^*\gamma$ by other groups. Quenched calculations can be found [178, 179, 180, 181, 182, 183, 184]. In these works, the b quark was implemented with Wilson-like actions, so that m_b had to be unphysically small. The form factors were then extrapolated in m_b to the physical value. The precise form of the functional dependence on m_b is unknown, which leads to an additional systematic uncertainty.

8.2 More about $b \to s$ decays

Including also $s\,\ell^+\ell^-$ final states, the effective Hamiltonian for $b \to s$ transitions has the form

$$\mathcal{H}_{\text{eff}} = -V_{tb}V_{ts}^* \frac{4G_F}{\sqrt{2}} \sum_{n=1}^{10} C_n(\mu) O_n \tag{8.14}$$

with

$$\begin{aligned}
O_1 &= (\bar{c}_L^b\, \hat{\gamma}^\mu\, b_L^a)\, (\bar{s}_L^a\, \hat{\gamma}_\mu\, c_L^b), \\
O_2 &= (\bar{c}_L^a\, \hat{\gamma}^\mu\, b_L^a)\, (\bar{s}_L^b\, \hat{\gamma}_\mu\, c_L^b), \\
O_3 &= (\bar{s}_L^a\, \hat{\gamma}^\mu\, b_L^a) \textstyle\sum_q (\bar{q}_L^b\, \hat{\gamma}_\mu\, q_L^b), \\
O_4 &= (\bar{s}_L^a\, \hat{\gamma}^\mu\, b_L^b) \textstyle\sum_q (\bar{q}_L^b\, \hat{\gamma}_\mu\, q_L^a), \\
O_5 &= (\bar{s}_L^a\, \hat{\gamma}^\mu\, b_L^a) \textstyle\sum_q (\bar{q}_R^b\, \hat{\gamma}_\mu\, q_R^b), \\
O_6 &= (\bar{s}_L^a\, \hat{\gamma}^\mu\, b_L^b) \textstyle\sum_q (\bar{q}_R^b\, \hat{\gamma}_\mu\, q_R^a), \\
O_7 &= \frac{e}{16\pi^2} m_b\, \bar{s}_L^a\, \sigma_{\mu\nu}\, b_R^a\, F_{(\text{e.m.})}^{\mu\nu}, \\
O_8 &= \frac{g}{16\pi^2} m_b\, \bar{s}_L^a\, \sigma_{\mu\nu}\, F_{ab}^{\mu\nu}\, b_R^b, \\
O_9 &= \frac{e^2}{16\pi^2} (\bar{s}_L^a\, \hat{\gamma}^\mu\, b_L^a) \textstyle\sum_\ell (\bar{\ell}\, \hat{\gamma}_\mu\, \ell), \\
O_{10} &= \frac{e^2}{16\pi^2} (\bar{s}_L^a\, \hat{\gamma}^\mu\, b_L^a) \textstyle\sum_\ell (\bar{\ell}\, \hat{\gamma}_\mu \hat{\gamma}_5\, \ell).
\end{aligned} \tag{8.15}$$

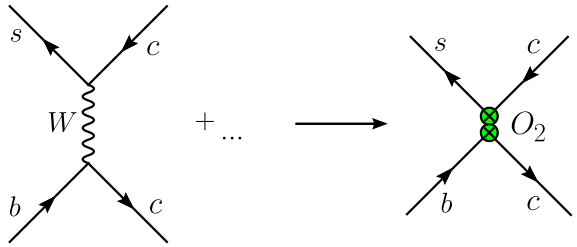

Figure 8.3: Example of a Feynman diagram contributing to O_2.

(see e.g. [177, 165, 185, 166]). Here, $\sum_q$ denotes a sum over the quark flavours u, d, c, s, b and $\sum_\ell$ denotes a sum over the lepton flavours e, μ, τ. The indices a, b are colour indices and are summed over from 1 to 3. Under renormalisation-group running from $\mu = m_W$ down to $\mu = m_b$, the operators mix and their coefficients change significantly.

The operator O_7 was already discussed in Sec. 8.1.4. The operators O_9 and O_{10} give additional short-distance contributions for $b \to s\ell^+\ell^-$; they arise from box diagrams (with two W boson propagators) and penguin diagrams (with a photon or Z decaying to the lepton pair).

At leading order, the operator O_2 is generated by the Feynman diagram shown in Fig. 8.3, so that at this order $C_2(m_W) = 1$. The operator O_1, where the colour structure is changed, is generated from this by QCD corrections and is thus loop-suppressed. In principle, there are also operators analogous to O_1 and O_2, with the replacement $c \mapsto u$. However, since $V_{ub} \approx 0$ is neglected here, these are not included. For the same reason, we also neglect weak annihilation in $B^\pm \to K^{(*)\pm}$ decays.

The hadronic matrix elements of O_2 can be sizable when the $\bar{c}c$ pair forms charmonium resonances (see Figs. 8.4 and 8.5). This is a non-local effect and can not be calculated directly on the lattice. The dominant resonances are the $J/\psi(1S)$ and $\psi(2S)$; their squared masses are 9.591 GeV^2 and 13.587 GeV^2, respectively [83]. Thus, one should keep q^2 away from these values when comparing the theoretical results with experimental data. For $B \to K^*\gamma$, one has $q^2 = 0$, which is far away from the resonances. The remaining effect for $B \to K^*\gamma$ is small [186]. For $B \to K^{(*)}\ell\ell$ decays, one can work at large q^2 (close to $q^2_{\rm max}$), which is also far away from the resonances, so that the long-distance effects are also under control [187]. The lattice calculation works best at large q^2 anyway.

The operators O_3 ... O_6 have very small Wilson coefficients and can be neglected. The chromomagnetic tensor operator O_8 may also lead to non-local contributions like the one shown in Fig. 8.6. The contributions from O_8 to $B \to K^*\gamma$ were estimated in [188] and

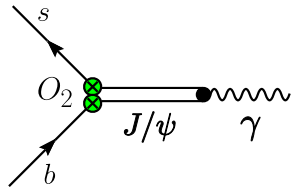

Figure 8.4: Long-distance contribution from charmonium resonances via O_2.

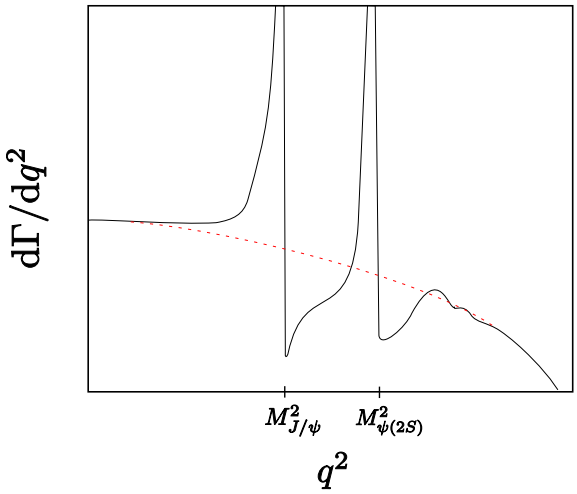

Figure 8.5: Effect of charmonium resonances on the differential decay rate (schematically).

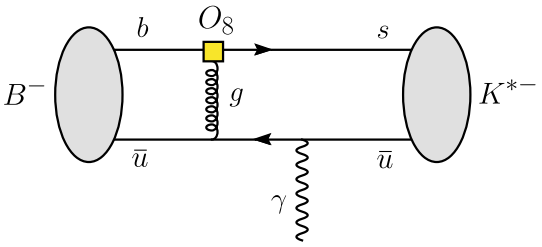

Figure 8.6: Example for a spectator-quark contribution to $B \to K^*\gamma$ due to O_8.

found to be suppressed relative to O_7 by a factor of $(C_8/C_7)\Lambda_{QCD}/M_B \approx 0.05$. See also [189] for a discussion of O_8 for $B \to K^*\ell^+\ell^-$ decays.

Finally, note that the K^* meson decays through the strong interaction into a pseudoscalar kaon and a pion. The width of the K^* is about 50 MeV [83]. For the unphysically large u- and d-quark masses used in the initial lattice calculations, the K^* is stable. However, extrapolations to the physical quark masses will be complicated by threshold effects.

8.3 General definition of semileptonic form factors

As discussed in the previous section, the short-distance contributions for $B \to K^*\gamma$ and $B \to K^{(*)}\ell\ell$ decays are due to the operators O_7, O_9 and O_{10}. The hadronic matrix elements of the bilinear heavy-light quark currents contained in these operators can be parametrised by Lorentz-invariant form factors as follows (see e.g. [190]):

$$\begin{aligned}
\langle P(p')|\bar{q}\hat{\gamma}^\mu b|B(p)\rangle &= f_+(q^2)\left[p^\mu + p'^\mu - \frac{M_B^2 - M_P^2}{q^2}q^\mu\right] \\
&\quad + f_0(q^2)\frac{M_B^2 - M_P^2}{q^2}q^\mu, && (8.16)\\
q_\nu\langle P(p')|\bar{q}\sigma^{\mu\nu} b|B(p)\rangle &= \frac{if_T(q^2)}{M_B + M_P}\left[q^2(p^\mu + p'^\mu) - (M_B^2 - m_P^2)q^\mu\right], && (8.17)\\
\langle V(p',\varepsilon)|\bar{q}\hat{\gamma}^\mu b|B(p)\rangle &= \frac{2iV(q^2)}{M_B + M_V}\,\epsilon^{\mu\nu\rho\sigma}\varepsilon^*_\nu p'_\rho p_\sigma, && (8.18)\\
\langle V(p',\varepsilon)|\bar{q}\hat{\gamma}^\mu\hat{\gamma}_5 b|B(p)\rangle &= 2M_V A_0(q^2)\,\frac{\varepsilon^*\cdot q}{q^2}\,q^\mu \\
&\quad + (M_B + M_V)\,A_1(q^2)\left[\varepsilon^{*\mu} - \frac{\varepsilon^*\cdot q}{q^2}\,q^\mu\right] \\
&\quad - A_2(q^2)\,\frac{\varepsilon^*\cdot q}{M_B + M_V}\left[p^\mu + p'^\mu - \frac{M_B^2 - M_V^2}{q^2}\,q^\mu\right], && (8.19)\\
q^\nu\langle V(p',\varepsilon)|\bar{q}\sigma_{\mu\nu} b|B(p)\rangle &= 4\,T_1(q^2)\epsilon_{\mu\rho\kappa\sigma}\varepsilon^{*\rho}p^\kappa p'^\sigma, && (8.20)\\
q^\nu\langle V(p',\varepsilon)|\bar{q}\sigma_{\mu\nu}\hat{\gamma}_5 b|B(p)\rangle &= 2iT_2(q^2)\left[\varepsilon^*_\mu(M_B^2 - M_V^2) - (\varepsilon^*\cdot q)(p + p')_\mu\right] \\
&\quad + 2iT_3(q^2)(\varepsilon^*\cdot q)\left[q_\mu - \frac{q^2}{M_B^2 - M_V^2}(p + p')_\mu\right]. && (8.21)
\end{aligned}$$

A derivation of (8.20) and (8.21) is given in Sec. B.1.

8.4 Extraction of form factors from correlation functions

The matrix element $\langle F(p')|J|B(p)\rangle$, where F denotes the final pseudoscalar (P) or vector (V) meson, and $J \sim \bar{q}\,\Gamma_J\,b$ is the heavy-light quark current in the effective electroweak

operator, can be extracted from the combination of the Euclidean 3-point function

$$C_{FJB}(\mathbf{p}',\,\mathbf{p},\,x_0,\,y_0,\,z_0) = \sum_{\mathbf{y}}\sum_{\mathbf{z}} \left\langle \Phi_F(x)\,J(y)\,\Phi_B^\dagger(z)\right\rangle e^{-i\mathbf{p}'\cdot(\mathbf{x}-\mathbf{y})}e^{-i\mathbf{p}\cdot(\mathbf{y}-\mathbf{z})} \tag{8.22}$$

with the Euclidean two-point functions

$$C_{BB}(\mathbf{p},\,x_0,\,y_0) = \sum_{\mathbf{x}} \left\langle \Phi_B(x)\,\Phi_B^\dagger(y)\right\rangle e^{-i\mathbf{p}\cdot(\mathbf{x}-\mathbf{y})}, \tag{8.23}$$

$$C_{FF}(\mathbf{p}',\,x_0,\,y_0) = \sum_{\mathbf{x}} \left\langle \Phi_F(x)\,\Phi_F^\dagger(y)\right\rangle e^{-i\mathbf{p}'\cdot(\mathbf{x}-\mathbf{y})}. \tag{8.24}$$

Here, $\Phi_B \sim \bar{q}'\hat{\gamma}_5 b$ and $\Phi_F \sim \bar{q}'\hat{\gamma}_5 q$ $(F=P)$, $\Phi_F \sim \bar{q}'\hat{\gamma}_j q$ $(F=V)$.

In the following we write $\tau = |x_0 - y_0|$ and $T = |x_0 - z_0|$. As in Sec. 2.2, one can show by inserting complete sets of states that at large τ, T, and $T-\tau$, the correlation functions become

$$C_{FJB}(\mathbf{p}',\,\mathbf{p},\,\tau,\,T) \;\to\; A^{(FJB)}e^{-E_F\tau}\,e^{-E_B(T-\tau)}, \tag{8.25}$$

$$C_{FF}(\mathbf{p},\,\tau) \;\to\; A^{(FF)}\,e^{-E_F\tau}, \tag{8.26}$$

$$C_{BB}(\mathbf{p},\,\tau) \;\to\; A^{(BB)}\,e^{-E_B\tau}, \tag{8.27}$$

where

$$A^{(FJB)} = \begin{cases} \dfrac{\sqrt{Z_V}}{2E_V}\dfrac{\sqrt{Z_B}}{2E_B}\displaystyle\sum_s \varepsilon_j(p',s)\,\langle V\left(p',\varepsilon(p',s)\right)\,|\,J\,|B(p)\rangle, & F=V, \\ \dfrac{\sqrt{Z_P}}{2E_P}\dfrac{\sqrt{Z_B}}{2E_B}\,\langle P\left(p'\right)\,|\,J\,|B(p)\rangle, & F=P \end{cases} \tag{8.28}$$

$$A^{(BB)} = \frac{Z_B}{2E_B}, \tag{8.29}$$

$$A^{(FF)} = \begin{cases} \displaystyle\sum_s \frac{Z_V}{2E_V}\,\varepsilon_j^*(p',s)\varepsilon_j(p',s), & F=V \;\;(\text{no sum over } j), \\ \dfrac{Z_P}{2E_P}, & F=P. \end{cases} \tag{8.30}$$

Thus, the matrix elements $\langle P(p')|J|B(p)\rangle$ and $\sum_s \varepsilon_j(p',s)\,\langle V\,(p',\varepsilon(p',s))\,|\,J\,|B(p)\rangle$ can be extracted from (8.28), once the factors Z_B, Z_F have been extracted from the two-point functions (the energies E_B, E_F can be obtained from either the two-point or three-point functions). Note that in Eqs. (8.28) and (8.29), E_B denotes the full, physical energy of the B meson; this is not equal to the energy obtained from the exponential decay in (8.25) or (8.27) when an effective theory like mNRQCD is used for the b quark.

In the next sections I discuss briefly how the form factors can be extracted from the matrix elements. I will only consider the case where all momenta point in x_1-direction.

Then, only certain combinations of operator indices and final state polarisations give non-zero contributions (were appropriate, after contraction with q^ν. There are 21 combinations in total (modulo the antisymmetry of $\sigma_{\mu\nu}$). They are listed in Table 8.1 together with the form factors to which they contribute.

8.4.1 The form factors f_0 and f_+

First, at $\mathbf{p} = \mathbf{q} = 0$, we have from Eq. (8.16)

$$\langle P(p')|\bar{q}\hat{\gamma}^0 b|\bar{B}(p)\rangle = f_0(q^2_{\text{max}})\,[M_B + M_P]\,, \tag{8.31}$$

and hence

$$f_0(q^2_{\text{max}}) = \frac{\langle P(p')|\bar{q}\hat{\gamma}^0 b|\bar{B}(p)\rangle}{M_B + M_P}. \tag{8.32}$$

For non-zero momentum transfer, we define $r \equiv (q^1, q^0, 0, 0)$, so that $r \cdot q = 0$. Then,

$$r_\mu \langle P(p')|\bar{q}\hat{\gamma}^\mu b|\bar{B}(p)\rangle = f_+(q^2) \;\; r \cdot (p + p'). \tag{8.33}$$

Hence, if $q^1 \neq 0$, the form factor $f_+(q^2)$ can be calculated in the following way,

$$f_+(q^2) = \frac{q^1\langle P(p')|\bar{q}\hat{\gamma}^0 b|\bar{B}(p)\rangle - q^0\langle P(p')|\bar{q}\hat{\gamma}^1 b|\bar{B}(p)\rangle}{q^1(p^0 + p'^0) - q^0(p^1 + p'^1)}. \tag{8.34}$$

Once $f_+(q^2)$ has been extracted, we obtain $f_0(q^2)$ from Eq. (8.16) with $\mu = 0$:

$$\langle P(p')|\bar{q}\hat{\gamma}^0 b|\bar{B}(p)\rangle = f_+(q^2)\left[p^0 + p'^0 - \frac{M_B^2 - M_P^2}{q^2}(p^0 - p'^0)\right] + f_0(q^2)\frac{M_B^2 - M_P^2}{q^2}(p^0 - p'^0). \tag{8.35}$$

This gives

$$f_0(q^2) = \frac{\langle P(p')|\bar{q}\hat{\gamma}^0 b|\bar{B}(p)\rangle - f_+(q^2)\left[p^0 + p'^0 - \frac{M_B^2 - M_P^2}{q^2}(p^0 - p'^0)\right]}{\frac{M_B^2 - M_P^2}{q^2}(p^0 - p'^0)}, \tag{8.36}$$

where $p^0 = E_B$, $p'^0 = E_F$.

8.4.2 The form factor f_T

For momenta pointing in 1-direction, it is clear from Eq. (8.17) that only the matrix element with $\sigma^{10} = -\sigma^{01}$ is non-zero. Thus, we obtain

$$f_T(q^2) = -i(M_B + M_P)\frac{(p^0 - p'^0)\langle P(p')|\bar{q}\sigma^{10} b|\bar{B}(p)}{q^2(p^1 + p'^1) - (M_B^2 - m_P^2)(p^1 - p'^1)}. \tag{8.37}$$

Gamma matrix in Φ_F	Gamma matrix in J	$\Re/\Im$	Form factor(s)
$\hat{\gamma}_5$	$\hat{\gamma}^0$	$\Re$	f_+, f_0
$\hat{\gamma}_5$	$\hat{\gamma}^1$	$\Re$	f_+, f_0
$\hat{\gamma}_5$	σ_{01}	$\Im$	f_T
$\hat{\gamma}^2$	$\hat{\gamma}^3$	$\Im$	V
$\hat{\gamma}^3$	$\hat{\gamma}^2$	$\Im$	V
$\hat{\gamma}^0$	$\hat{\gamma}^0\hat{\gamma}_5$	$\Re$	A_0, A_1, A_2
$\hat{\gamma}^0$	$\hat{\gamma}^1\hat{\gamma}_5$	$\Re$	A_0, A_1, A_2
$\hat{\gamma}^1$	$\hat{\gamma}^0\hat{\gamma}_5$	$\Re$	A_0, A_1, A_2
$\hat{\gamma}^1$	$\hat{\gamma}^1\hat{\gamma}_5$	$\Re$	A_0, A_1, A_2
$\hat{\gamma}^2$	$\hat{\gamma}^2\hat{\gamma}_5$	$\Re$	A_1
$\hat{\gamma}^3$	$\hat{\gamma}^3\hat{\gamma}_5$	$\Re$	A_1
$\hat{\gamma}^3$	σ_{02}	$\Re$	T_1
$\hat{\gamma}^2$	σ_{03}	$\Re$	T_1
$\hat{\gamma}^3$	σ_{12}	$\Re$	T_1
$\hat{\gamma}^2$	σ_{13}	$\Re$	T_1
$\hat{\gamma}^2$	$\sigma_{02}\hat{\gamma}_5$	$\Im$	T_2
$\hat{\gamma}^2$	$\sigma_{12}\hat{\gamma}_5$	$\Im$	T_2
$\hat{\gamma}^3$	$\sigma_{03}\hat{\gamma}_5$	$\Im$	T_2
$\hat{\gamma}^3$	$\sigma_{13}\hat{\gamma}_5$	$\Im$	T_2
$\hat{\gamma}^0$	$\sigma_{01}\hat{\gamma}_5$	$\Im$	T_2, T_3
$\hat{\gamma}^1$	$\sigma_{01}\hat{\gamma}_5$	$\Im$	T_2, T_3

Table 8.1: Operators required for form factor calculations with momenta in 1-direction. The table also shows whether the real ($\Re$) or imaginary ($\Im$) part of the three-point function is needed.

8.4.3 The form factor V

Using the following spin sum for massive vector mesons,

$$\sum_{s=1}^{3} \varepsilon_\mu(p',s)\varepsilon^*_\nu(p',s) = \left(g_{\mu\nu} - \frac{p'_\mu p'_\nu}{M_V^2}\right), \tag{8.38}$$

we obtain from Eq. (8.18)

$$\begin{aligned}\sum_s \varepsilon_j(p',s)\,\langle V\left(p',\varepsilon(p',s)\right) \mid \bar{q}\hat{\gamma}^\mu b \mid \bar{B}(p)\rangle &= \frac{2i\,V(q^2)}{M_B+M_V}\,\epsilon^{\mu\nu\rho\sigma}\sum_s \varepsilon_j(p',s)\varepsilon^*_\nu(p',s)\,p'_\rho p_\sigma \\ &= \frac{2i\,V(q^2)}{M_B+M_V}\epsilon^{\mu\nu\rho\sigma}\left(g_{j\nu} - \frac{p'_j p'_\nu}{M_V^2}\right)p'_\rho p_\sigma. \end{aligned} \tag{8.39}$$

If we now set $\mu = 2$, we get

$$\sum_s \varepsilon_j(p',s)\,\langle V\left(p',\varepsilon(p',s)\right) \mid \bar{q}\hat{\gamma}^2 b \mid \bar{B}(p)\rangle = \frac{2i\,V(q^2)}{M_B+M_V}\,g_{j3}\,(p'^0 p^1 - p'^1 p^0), \tag{8.40}$$

and we see that we need to set $j = 3$ in the three-point function. On the other hand, for $\mu = 3$, we need to set $j = 2$ in the three-point function. One can average over these two cases to increase statistics.

8.4.4 The form factors A_0, A_1 and A_2

Setting $\mu = 2$ in (8.19), the only remaining contribution is from A_1. Using (8.38), we get

$$\begin{aligned}\sum_s \varepsilon_j(p',s)\,\langle V\left(p',\varepsilon(p',s)\right) \mid \bar{q}\hat{\gamma}^2\hat{\gamma}_5 b \mid \bar{B}(p)\rangle &= (M_B+M_V)A_1(q^2)\sum_s \varepsilon_j(p',s)\varepsilon^{*2}(p',s) \\ &= (M_B+M_V)A_1(q^2)\delta_j{}^2 \end{aligned} \tag{8.41}$$

and we see that we can extract $A_1(q^2)$ if we set $j = 2$ in the three-point function. For $\mu = 3$, we need to set $j = 3$ in the three-point function.

Next, using the vector r orthogonal to q, as before $r = (q^1, q^0, 0, 0)$, we obtain

$$
\begin{aligned}
r_\mu \sum_s \varepsilon_j(p',s)\,\langle V\left(p',\varepsilon(p',s)\right)\,|\,\bar{q}\hat{\gamma}^\mu\hat{\gamma}_5 b\,|\bar{B}(p)\rangle & \\
&= (M_B+M_V)A_1(q^2)\sum_s \varepsilon_j(p',s)\varepsilon^*_\mu(p',s)\,r^\mu \\
&\quad - \frac{A_2(q^2)}{M_B+M_V}\,r\cdot(p+p')\,\sum_s \varepsilon_j(p',s)\varepsilon^*_\nu(p',s)\,q_\nu \\
&= (M_B+M_V)A_1(q^2)\left(g_{j\mu}-\frac{p'_j p'_\mu}{M_V^2}\right)\,r^\mu \\
&\quad - \frac{A_2(q^2)}{M_B+M_V}\,r\cdot(p+p')\,\left(g_{j\nu}-\frac{p'_j p'_\nu}{M_V^2}\right)\,q_\nu \\
&= (M_B+M_V)A_1(q^2)\left(r_j-\frac{p'\cdot r}{M_V^2}p'_j\right) \\
&\quad - \frac{A_2(q^2)}{M_B+M_V}\,r\cdot(p+p')\,\left(q_j-\frac{p'\cdot q}{M_V^2}p'_j\right).
\end{aligned}
$$

For momenta pointing in 1-direction, this is non-zero only for $j=1$. Since $A_1(q^2)$ is known from (8.41), we can now extract $A_2(q^2)$.

Finally, $A_0(q^2)$ can be extracted by looking at the matrix element for $\mu=0$ or $\mu=1$ and subtracting the now known contributions from A_1 and A_2.

8.4.5 The form factors T_1, T_2 and T_3

We first consider T_1. Using the spin sum (8.38), we obtain from Eq. (8.20)

$$
\begin{aligned}
q^\nu \sum_s \varepsilon_j(p',s)\,\langle V\left(p',\varepsilon(p',s)\right)\,|\,\bar{q}\sigma_{\mu\nu} b\,|\bar{B}(p)\rangle &= 4\,T_1(q^2)\epsilon_{\mu\rho\kappa\sigma}\sum_{s=1}^{3}\varepsilon_j(p',s)\varepsilon^{*\rho}(p',s)p^\kappa p'^\sigma \\
&= 4\,T_1(q^2)\epsilon_{\mu\rho\kappa\sigma}\left(\delta_j{}^\rho-\frac{p'_j p'^\rho}{M_V^2}\right)p^\kappa p'^\sigma.
\end{aligned}
\tag{8.42}
$$

For $\mu=2$, Eq. (8.42) becomes

$$
\sum_s \varepsilon_j(p',s)\,\langle V\left(p',\varepsilon(p',s)\right)\,|\,\bar{q}(q^0\sigma_{20}+q^1\sigma_{21})b\,|\bar{B}(p)\rangle = 4\,T_1(q^2)\delta_j{}^3(p^0p'^1-p^1p'^0), \tag{8.43}
$$

and we see that we need to set $j=3$ in the three-point function to extract T_1. (for $\mu=3$, set $j=2$).

Next, in order to extract T_2, we set $\mu=2$ (or $\mu=3$) in Eq. (8.21), such that there is no

contribution from T_3. This gives

$$\sum_s \varepsilon_j(p',s)\,\langle V\left(p',\varepsilon(p',s)\right)|\,\bar{q}(q^0\sigma_{20}+q^1\sigma_{21})\hat{\gamma}_5 b\,|\bar{B}(p)\rangle$$
$$= 2i\,T_2(q^2)(M_B^2-M_V^2)\sum_{s=1}^{3}\varepsilon_j(p',s)\varepsilon_2^*(p',s)$$
$$= 2i\,T_2(q^2)(M_B^2-M_V^2)\,g_{j2}, \tag{8.44}$$

and we see that we need to set $j=2$ in the three-point function (or $j=3$ for $\mu=3$).

Finally, $T_3(q^2)$ can be extracted by setting $\mu=0$ or $\mu=1$ and subtracting off the now known contributions from T_1 and T_2.

8.5 Matching of heavy-light currents

To compute the three-point function (8.22) on the lattice, the continuum QCD current $J=\bar{q}\,\Gamma_J\,b$ must be replaced by a lattice version. Since we use moving NRQCD for the b quark, we can use the field redefinition (3.74) to express the QCD field in terms of the mNRQCD field.

Depending on the time-ordering in the correlation function, we need either the upper- or lower-component mNRQCD fields for the heavy quark:

$$\Psi_v^{(+)}=\begin{pmatrix}\psi_v\\0\end{pmatrix},\qquad \Psi_v^{(-)}=\begin{pmatrix}0\\\xi_v\end{pmatrix}. \tag{8.45}$$

The tree-level current then is

$$J \;=\; \frac{1}{\sqrt{\gamma}}\;\bar{q}\;\Gamma_J\,S(\Lambda)\;T_{\rm FWT}\;\;A_{D_t}\;\;\Psi_v^{(\pm)}, \tag{8.46}$$

where, to order $1/m$,

$$T_{\rm FWT} \;=\; 1+\frac{i\hat{\gamma}^j\Lambda^\mu{}_j D_\mu}{2m}, \tag{8.47}$$
$$A_{D_t} \;=\; 1+\frac{i}{4\gamma m}\hat{\gamma}^0\left[(\gamma^2-1)D_0+(\gamma^2+1)\mathbf{v}\cdot\mathbf{D}\right]. \tag{8.48}$$

In (8.46), we have removed the factor of $e^{-im\,u\cdot x\,\hat{\gamma}^0}$ in the field redefinition, which corresponds to the tree-level shift in the four-momentum[1]

[1]At first sight, this procedure seems invalid since there are derivative operators on the left-hand

Next, in order to simplify Eq. (8.53) further, we use the relation

$$S(\Lambda)\,\hat{\gamma}^j\,\overline{S(\Lambda)} = (\Lambda^{-1})^j{}_\nu\,\hat{\gamma}^\nu \tag{8.49}$$

to commute the spinorial boost matrix through $T_{\rm FWT}$:

$$\begin{aligned} S(\Lambda)\,T_{\rm FWT} &= \left(1+\frac{i\Lambda^\mu{}_j(\Lambda^{-1})^j{}_\nu\,\hat{\gamma}^\nu D_\mu}{2m}\right) S(\Lambda) \\ &= \left(1+\frac{i\left[\delta^\mu{}_\nu-\Lambda^\mu{}_0(\Lambda^{-1})^0{}_\nu\right]\,\hat{\gamma}^\nu D_\mu}{2m}\right) S(\Lambda) \\ &= \left(1+\frac{i\left[\delta^\mu{}_\nu-u^\mu u_\nu\right]\,\hat{\gamma}^\nu D_\mu}{2m}\right) S(\Lambda). \end{aligned} \tag{8.50}$$

Note that $\hat{\gamma}^0\,\Psi_v^{(\pm)} = \pm\Psi_v^{(\pm)}$. Thus, we get

$$J \;=\; \frac{1}{\sqrt{\gamma}}\,\bar{q}\;\Gamma_J\;\left(1+\frac{i\left[\not{D}-\not{u}\,(u\cdot D)\right]}{2m}\pm\frac{i}{4\gamma m}\left[(\gamma^2-1)D_0+(\gamma^2+1)\mathbf{v}\cdot\mathbf{D}\right]\right) S(\Lambda)\,\Psi_v^{(\pm)}. \tag{8.51}$$

This still contains time derivatives, which is inconvenient for the lattice computation. To eliminate these, we use the leading-order equations of motion

$$D_0\,\Psi_v = -\mathbf{v}\cdot\mathbf{D}\,\Psi_v \tag{8.52}$$

and obtain

$$\begin{aligned} J &= \frac{1}{\sqrt{\gamma}}\,\bar{q}\,\Gamma_J\,\Psi_v^{(\pm)} \;+\; \frac{1}{\sqrt{\gamma}}\,\bar{q}\,\Gamma_J\,\left(\frac{-i\hat{\gamma}^0\mathbf{v}\cdot\mathbf{D}+i\hat{\boldsymbol{\gamma}}\cdot\mathbf{D}}{2m}\pm\frac{i\mathbf{v}\cdot\mathbf{D}}{2\gamma m}\right) S(\Lambda)\,\Psi_v^{(\pm)} \\ &= \frac{1}{\sqrt{\gamma}}\,\bar{q}\,\Gamma_J\,\Psi_v^{(\pm)} \;+\; \frac{1}{2m\sqrt{\gamma}}\,\bar{q}\,\Gamma_J\,\left(-i\hat{\gamma}^0\mathbf{v}+i\hat{\boldsymbol{\gamma}}\pm i\mathbf{v}/\gamma\right)\cdot\mathbf{D}\;\;S(\Lambda)\,\Psi_v^{(\pm)}. \end{aligned} \tag{8.53}$$

On the lattice, the continuum covariant derivative $\mathbf{D}$ has to be replaced by a discrete version $\boldsymbol{\Delta}$. I use the symmetric derivative defined in (A.11).

As before, I use the ASQTAD action for the light quark q. This means that the field q has to be expressed in terms of the staggered field χ_q.

---

side of the factor $e^{-im\,u\cdot x\,\hat{\gamma}^0}$. However, this factor can in fact be moved to the left of $T_{\rm FWT}\,A_{D_t}$ without further changes, for the following reason:

Let us go back to the non-moving case. Equation (3.16) contains a factor of $e^{-imx^0\hat{\gamma}^0}$. Using $\hat{\gamma}^0\,\tilde{\Psi}^{(\pm)} = \pm\tilde{\Psi}^{(\pm)}$, we can replace this by the c-number $e^{\pm imx^0}$.

Now, since the FWT transformation in the non-moving case does not contain time derivatives, the phase $e^{\pm imx^0}$ can be moved to the left of $T_{\rm FWT}$ without any other change.

By doing the transition to non-zero velocity after this step, it follows that the factor $e^{-im\,u\cdot x\,\hat{\gamma}^0}$ can be moved to the left of $T_{\rm FWT}\,A_{D_t}$ also in the case $\mathbf{v}\neq 0$.

Eq. (8.53) does not yet include any radiative corrections. Calculations of radiative corrections to the currents in mNRQCD have been performed by Eike Müller [114, 116] and previously (for a slightly different action) by Lew Khomskii [113].

Due to the complexity of these calculations, radiative corrections have been computed so far only for the first term in (8.53). The second term in (8.53) is suppressed by Λ_{QCD}/m_b and can be included at tree-level (however, one has to define subtracted operators as will be discussed later).

To see the effect of radiative corrections to the first term, note that the spinorial boost is given explicitly by

$$S(\Lambda) = S_+(\Lambda) = \frac{1}{\sqrt{2(1+\gamma)}} \left[(1+\gamma)\mathbb{1} - \gamma\, \mathbf{v}\cdot\hat{\boldsymbol{\gamma}}\, \hat{\gamma}^0\right]. \tag{8.54}$$

As can be seen, (8.54) contains a sum of two different Dirac structures; these will mix under renormalisation. Thus, at order $\mathcal{O}(\alpha_s)$, one also needs to consider the combination with the opposite sign:

$$S_-(\Lambda) \equiv \frac{1}{\sqrt{2(1+\gamma)}} \left[(1+\gamma)\mathbb{1} + \gamma\, \mathbf{v}\cdot\hat{\boldsymbol{\gamma}}\, \hat{\gamma}^0\right].$$

The lattice current through order $\mathcal{O}(\alpha_s)$ then reads

$$J^{(0)\,\mathrm{lat}} = (1 + \alpha_s\, c_+)\, J_+^{(0)} + \alpha_s\, c_-\; J_-^{(0)}, \tag{8.55}$$

with

$$J_+^{(0)} = \frac{1}{\sqrt{\gamma}}\, \bar{q}\; \Gamma\; S_+(\Lambda)\, \Psi_v^{(\pm)}, \qquad J_-^{(0)} = \frac{1}{\sqrt{\gamma}}\, \bar{q}\; \Gamma\; S_-(\Lambda)\, \Psi_v^{(\pm)}.$$

The matching coefficients $c_\pm$ in (8.55) are obtained by requiring that the matrix elements in the lattice theory and in the continuum ($\overline{\mathrm{MS}}$ scheme) are equal to order α_s.

Results for the matching coefficients for the vector ($\Gamma = \hat{\gamma}^\mu$) and tensor ($\Gamma = \sigma^{\mu\nu}$) currents are shown in Figs. 8.7 and 8.8. These were obtained using automated tadpole-improved one-loop lattice perturbation theory by Eike Müller [114, 116]. Here, the bare b quark mass was set to $am_b = 2.8$ and the boost-velocity is pointing in 1-direction. In the figures, the different Lorentz indices of Γ are indicated as 0 (temporal), $\parallel$ (parallel to $\mathbf{v}$) and $\perp$ (perpendicular to $\mathbf{v}$).

We would also like to include the tree-level $\mathcal{O}(\Lambda_{QCD}/m_b)$ correction

$$J_+^{(1)} = \frac{1}{m_b}\frac{1}{\sqrt{\gamma}}\, \bar{q}\; \Gamma\; \frac{(-i\hat{\gamma}^0\mathbf{v} + i\hat{\boldsymbol{\gamma}} \pm i\mathbf{v}/\gamma)\cdot\boldsymbol{\Delta}}{2}\; S_+(\Lambda)\, \Psi_v^{(\pm)} \tag{8.56}$$

to the lattice current. However, this operator mixes with the lower-dimension operators $J_\pm^{(0)}$. As discussed in [191, 192, 11], one should use subtracted higher-order operators. This requires the perturbative calculation of the mixing coefficients.

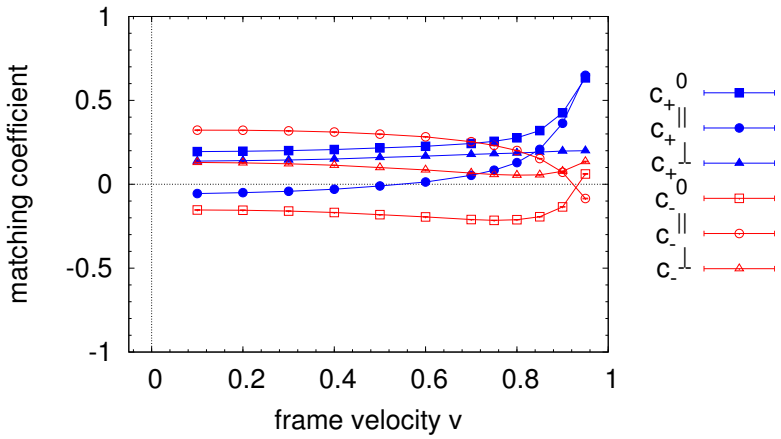

Figure 8.7: Matching coefficients for the vector current, computed by Eike Müller [114, 116].

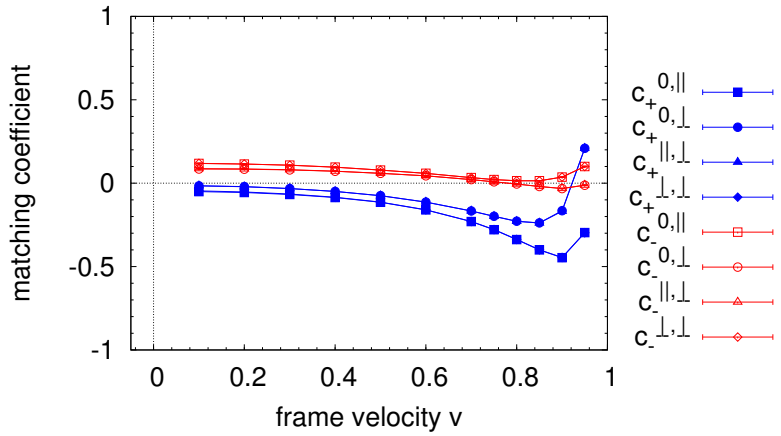

Figure 8.8: Matching coefficients for the tensor current, computed by Eike Müller [114, 116]. The renormalisation scale is $\mu = m_b$.

I have already computed the non-perturbative matrix elements of (8.56), so that I can include them in the form factor results once the necessary mixing coefficients have been calculated.

8.6 Reference frame choice

With moving NRQCD, a non-zero frame velocity is introduced with the objective of reducing discretisation errors. The discretisation errors are determined by the momenta carried by the quarks (and gluons) and are typically proportional to $(a \times \text{momentum})^2$ where a is the lattice spacing. For the b quark described by lattice mNRQCD, the relevant momentum in this relation is the *residual momentum* (see Sec. 3.3).

If the B meson is at rest, the residual momentum of the b quark has a distribution with a width of the order $\Lambda_{\rm QCD}$ (see Sec. 3.2.1) and the residual energy has a distribution with width of the order $\Lambda_{\rm QCD}^2/(2m_b) \ll \Lambda_{\rm QCD}$. Note that momentum conservation implies that the spatial momentum of the light quark in the B meson (the "spectator quark") has a distribution with a width of the same order.

For a B meson moving with velocity $\mathbf{v}$, the momentum distribution is boosted to approximately $\gamma\Lambda_{\rm QCD}$. Let us now consider a decay $B(p) \to F(p')$ where F denotes the light meson in the final state and the 4-momenta are

$$\begin{aligned} p &= (\gamma M_B,\, \gamma M_B \mathbf{v}), \\ p' &= (\sqrt{M_F^2 + |\mathbf{p}'|^2},\, \mathbf{p}'), \end{aligned}$$

where $\mathbf{v}$ is antiparallel to $\mathbf{p}'$. For a given value of $q^2 = (p - p')^2$, we shall determine the optimal velocity of the B meson which minimises discretisation errors. The full lattice mNRQCD action derived in Sec. 5 has no tree-level $\mathcal{O}(a^2\mathbf{k}^2)$-errors, but has $\mathcal{O}(\alpha_s a^2\mathbf{k}^2)$ errors due to radiative corrections. The same is true for highly improved light quark actions such as the ASQTAD action [123, 124, 125] (which I use in this work), or the HISQ action [84].

Thus, the increase in discretisation errors for the quarks in the B meson due to the boost of the momentum distribution when going from zero velocity ($\gamma = 1$) to a non-zero velocity $\mathbf{v}$ is proportional to

$$\gamma^2\Lambda_{\rm QCD}^2 - \Lambda_{\rm QCD}^2. \tag{8.57}$$

Assuming that the quarks in the light meson share the momentum equally, each carrying momentum of order $\mathbf{p}'/2$, we expect that the increase in discretisation errors for the light

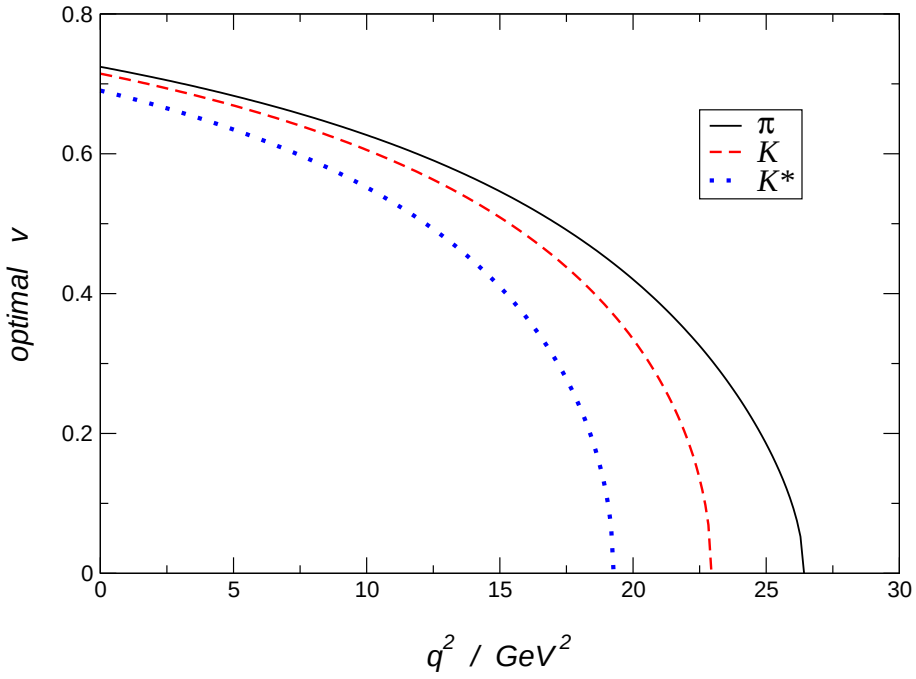

Figure 8.9: Estimate of optimal velocity, minimising discretisation errors, for $B \to F$ form factors (see text) as a function of q^2 for the π, K and K^* light mesons.

meson when going from zero momentum to $\mathbf{p}'$ is proportional to

$$\left(\tfrac{1}{2}|\mathbf{p}'|\right)^2 . \tag{8.58}$$

The total error is the sum of these terms with some coefficients that we presume are of order unity. Investigation with various reasonable choices of coefficients shows that the minimum total error is obtained when the terms (8.57) and (8.58) are approximately equal. The velocity for which these two terms are equal is plotted as a function of q^2 in Figure 8.9 for $F = \pi$, $F = K$ and $F = K^*$. I find that at maximum recoil ($q^2 = 0$) a velocity of $|\mathbf{v}| \approx 0.7$ would minimise discretisation errors. Of course this is only a very crude estimate, and the optimal velocity depends on the details of the lattice computation.

8.7 Heavy-quark expansion of the current

Even in continuum mNRQCD systematic errors for heavy-to-light decays increase when going to lower q^2, since the convergence of the heavy-quark expansion for the current mediating the decay (cf. Sec. 8.5) gets worse. The heavy-quark expansion requires that all

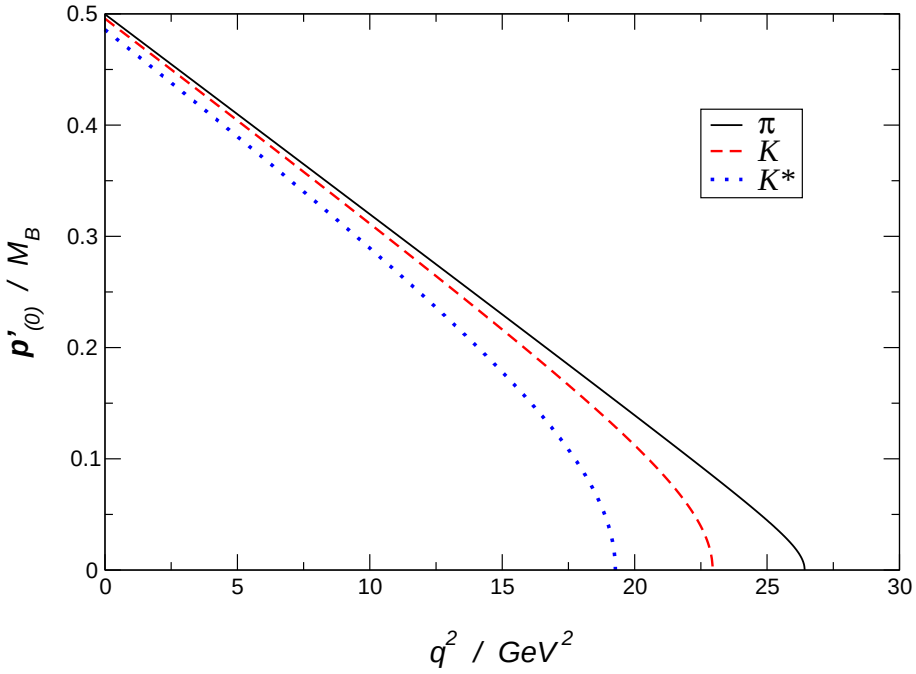

Figure 8.10: The ratio $|\mathbf{p}'_{(0)}|/M_B$ as a function of q^2 for the π, K and K^* light mesons.

momentum scales for the light degrees of freedom are small compared to the mass of the heavy quark, which is approximately equal to the mass of the B meson, M_B. In the low-recoil regime, the only relevant scale is $\Lambda_{\rm QCD} \ll M_B$, but for large recoil the momentum of the light meson in the B rest frame is large.

The light meson energy in the B rest frame can be written in a Lorentz-invariant way as

$$E_{F(0)} = \frac{p \cdot p'}{M_B} = \frac{M_B^2 + M_F^2 - q^2}{2M_B} \,. \tag{8.59}$$

The light meson momentum in this frame is then $|\mathbf{p}'_{(0)}| = \sqrt{E_{F(0)}^2 - M_F^2}$. In Fig. 8.10, I plot the ratio $|\mathbf{p}'_{(0)}|/M_B$ as a function of q^2 for for the π, K and K^* light mesons. This ratio becomes almost 0.5 at $q^2 = 0$, which has to be compared to $\Lambda_{\rm QCD}/M_B \approx 0.1$ in the low-recoil limit.

8.8 Two-point and three-point functions with random-wall sources

In the following sections I give more details about the lattice techniques that I use to calculate the correlation functions (8.22), (8.23), (8.24), and present numerical results. In particular, I investigate the use of stochastic sources (random-wall sources), which provide an approximation to the all-to-all correlators and can therefore potentially reduce statistical errors. For the $B \to \pi\ell\nu$ semileptonic decay in standard NRQCD (i.e. with the B meson at rest), random-wall sources have been tested in Ref. [193]. I now generalise this to include vector-meson final states and moving NRQCD, and also work at smaller light-quark masses (closer to the physical point).

I performed the numerical calculations described in the following sections using the same 400 "coarse" MILC gauge configurations as in Sec. 6. As before, I used the full $\mathcal{O}(1/m_b^2)$ mNRQCD action with $am_b = 2.8$ and $n = 2$ for the b quarks, and the ASQTAD action with $am_u = am_d = 0.007$ and $am_s = 0.04$ for the light valence quarks.

Four source locations per gauge configuration were used, leading to a total of 1600 measurements. The light-quark propagators and light-meson correlators with random-wall sources were generated by Zhaofeng Liu using the MILC code (see `http://physics.utah.edu/~detar/milc.html`). I also thank Zhaofeng Liu for numerous discussions about the fitting of the data. Lattice units are used in the remainder of this section.

8.8.1 Light meson two-point functions

For flavour-non-singlet light pseudoscalar mesons with 3-momentum $\mathbf{p}'$, the two-point function (with naive quarks) from a point source located at x is given by[2]

$$\begin{aligned} C_{55}(\tau = |y_0 - x_0|, \mathbf{p}') &= \frac{1}{16} \sum_{\mathbf{y}} \mathrm{Tr}\big[\hat{\gamma}_5 G_q(y,x) \hat{\gamma}_5 G_{q'}(x,y)\big] e^{-i\mathbf{p}'\cdot(\mathbf{y}-\mathbf{x})} \\ &= \frac{1}{16} \sum_{\mathbf{y}} \mathrm{Tr}\big[G_q(y,x) G^\dagger_{q'}(y,x)\big] e^{-i\mathbf{p}'\cdot(\mathbf{y}-\mathbf{x})} \\ &= \frac{1}{16} \sum_{\mathbf{y}} \mathrm{Tr}\big[G_{\chi_q}(y,x) \underbrace{\Omega^\dagger(x)\Omega(x)}_{=\mathbb{1}} G^\dagger_{\chi_{q'}}(y,x) \underbrace{\Omega^\dagger(y)\Omega(y)}_{=\mathbb{1}}\big] e^{-i\mathbf{p}'\cdot(\mathbf{y}-\mathbf{x})} \\ &= \frac{1}{4} \sum_{\mathbf{y}} \mathrm{Tr}\big[G_{\chi_q}(y,x) G^\dagger_{\chi_{q'}}(y,x)\big] e^{-i\mathbf{p}'\cdot(\mathbf{y}-\mathbf{x})}. \end{aligned} \tag{8.60}$$

[2] All definitions of correlation functions and propagators in this and in the following sections are understood to be on a single background gauge-field configuration. To obtain the full expectation value, an average over the gauge configurations needs to be performed.

The factor of 1/16 has been included to obtain the correct normalisation for a single taste.

To increase statistics, we would like to average (8.60) over all points $\mathbf{x}$, i.e. perform the sum $\frac{1}{L^3}\sum_{\mathbf{x}}$. We shall refer to the two-point function obtained in this way as the *exact all-to-all two-point function*.

The data from different source points are of course correlated with a correlation length of $1/m_\pi$, so one would expect a reduction in the statistical errors by a factor proportional to $\sqrt{m_\pi^3 L^3}$.

Note that for every point $\mathbf{x}$, the lattice Dirac equation would need to be solved again, so the sum $\frac{1}{L^3}\sum_{\mathbf{x}}$ would increase the total computational cost by a factor of L^3. This is forbiddingly expensive. One solution is to only include a few points separated by about $1/m_\pi$.

Another possibility is to compute a stochastic estimator of the exact all-to-all meson two-point function, referred to in the following as the *random-wall* two-point function. Stochastic methods have first been used to estimate all-to all quark propagators (see for example [194]) and later also for meson correlation functions (using the "one-end trick" [195]).

We define

$$\widetilde{G}^p_{\chi_q}(y, x_0, \mathbf{p}') = \sum_{\mathbf{x}} G_{\chi_q}(y, x)\, \xi^p(\mathbf{x})\, e^{i\mathbf{p}'\cdot\mathbf{x}}, \tag{8.61}$$

where $\xi^p(\mathbf{x})$ is a vector in colour space (colour index not shown explicitly), with every colour component at every spatial site an independent $Z_2 \times Z_2$ random number. The index p (not to be confused with the momentum) labels different random samples on a given configuration; additionally it is understood that new random numbers are used on every gauge configuration. The noise fields satisfy

$$\frac{1}{n_Z}\sum_{p=1}^{n_Z} \xi_c^{p*}(\mathbf{x})\xi_d^p(\mathbf{z}) \approx \delta_{cd}\delta_{\mathbf{x}\,\mathbf{z}}, \tag{8.62}$$

where n_Z is the number of random samples (this relation becomes exact in the limit $n_Z \to \infty$). Therefore, an approximation to the all-to-all pseudoscalar two-point function can be obtained as follows:

$$\begin{aligned} C_{55,\mathrm{RW}}(\tau, \mathbf{p}') &= \frac{1}{4L^3}\frac{1}{n_Z}\sum_{p=1}^{n_Z}\sum_{\mathbf{y}} \widetilde{G}^p_{\chi_{q'}}(y, x_0, \mathbf{0})^* \cdot \widetilde{G}^p_{\chi_q}(y, x_0, \mathbf{p}') e^{-i\mathbf{p}'\cdot\mathbf{y}} \\ &\approx \underbrace{\frac{1}{4L^3}\sum_{\mathbf{y},\mathbf{z},\mathbf{x}} G^*_{\chi_{q'}}(y, z)_{ab}\, G_{\chi_q}(y, x)_{ac}\, \delta_{bc}\, \delta_{\mathbf{x}\,\mathbf{z}}\, e^{i\mathbf{p}\cdot\mathbf{x}} e^{-i\mathbf{p}'\cdot\mathbf{y}}}_{= \frac{1}{4L^3}\sum_{\mathbf{x},\mathbf{y}} \mathrm{Tr}\left[G_{\chi_q}(y, x) G^\dagger_{\chi_{q'}}(y, x)\right] e^{-i\mathbf{p}'\cdot(\mathbf{y}-\mathbf{x})}}. \end{aligned} \tag{8.63}$$

In practice, a small number n_Z is sufficient; for the pseudoscalar meson two-point function even $n_Z = 1$ is sufficient to improve the signal compared to point sources.

However, note that for each non-zero value of the momentum $\mathbf{p}'$, new inversions are required. This is not the case for the point source correlator, where arbitrary momenta can be computed without additional inversions.

For a flavour-non-singlet vector meson with interpolating field $\Phi_j = \bar{q}'\hat{\gamma}_j q$, the point-source two-point function is given by

$$\begin{aligned} C_{jj}(\tau, \mathbf{p}') &= \frac{1}{16}\sum_{\mathbf{y}} \mathrm{Tr}\big[\hat{\gamma}_j G_q(y,x)\hat{\gamma}_j\hat{\gamma}_5 G^\dagger_{q'}(y,x)\hat{\gamma}_5\big] e^{-i\mathbf{p}'\cdot(\mathbf{y}-\mathbf{x})} \\ &= \frac{1}{4}\sum_{\mathbf{y}} \mathrm{Tr}\big[G_{\chi_q}(y,x) G^\dagger_{\chi_{q'}}(y,x)\big] (-1)^{x_j+y_j} e^{-i\mathbf{p}'\cdot(\mathbf{y}-\mathbf{x})}, \end{aligned} \tag{8.64}$$

where the phase factor of $(-1)^{x_j+y_j}$ comes from the relation $\Omega^\dagger(x)\hat{\gamma}_5\hat{\gamma}_j\Omega(x) = (-1)^{x_j}\hat{\gamma}_5\hat{\gamma}_j$.

To obtain the random-wall correlator in this case, a factor of $(-1)^{x_j}$ is added to the stochastic source for the zero-momentum quark propagator; we define

$$\widetilde{G}^p_{\chi_{q'}}(y, x_0, j) = \sum_{\mathbf{x}} G_{\chi_{q'}}(y,x)\, \xi^p(\mathbf{x})\, (-1)^{x_j}. \tag{8.65}$$

This means that additional inversions are required for the different polarisations $j = 1, 2, 3$. The random-wall correlator is then

$$C_{jj,\mathrm{RW}}(\tau, \mathbf{p}') = \frac{1}{4L^3}\frac{1}{n_Z}\sum_{p=1}^{n_Z}\sum_{\mathbf{y}} \widetilde{G}^p_{\chi_{q'}}(y, x_0, j)^* \cdot \widetilde{G}^p_{\chi_q}(y, x_0, \mathbf{p}')(-1)^{y_j} e^{-i\mathbf{p}'\cdot\mathbf{y}}. \tag{8.66}$$

Colour dilution

Dilution methods were originally introduced for all-to-all (quark) propagators, where they can lead to a significant reduction in statistical errors [196].

Here we use colour dilution in combination with the one-end trick for the meson correlation functions. With colour dilution, a Kronecker delta in colour space is introduced in the stochastic source, i.e. $\xi^p_a(\mathbf{z})$ is changed to $\delta_{a,a_0}\xi^p(\mathbf{z})$ for each source colour a_0, where $\xi^p(\mathbf{z})$ does not have a colour index. Then for each colour a_0 one needs to perform a separate inversion and in Eqs. (8.63, 8.66) a sum over source colour has to be added.

In the following, I shall denote the random-wall source in combination with colour dilution by "RWcd". All numerical results for the random-wall correlators shown here were obtained with the colour dilution method.

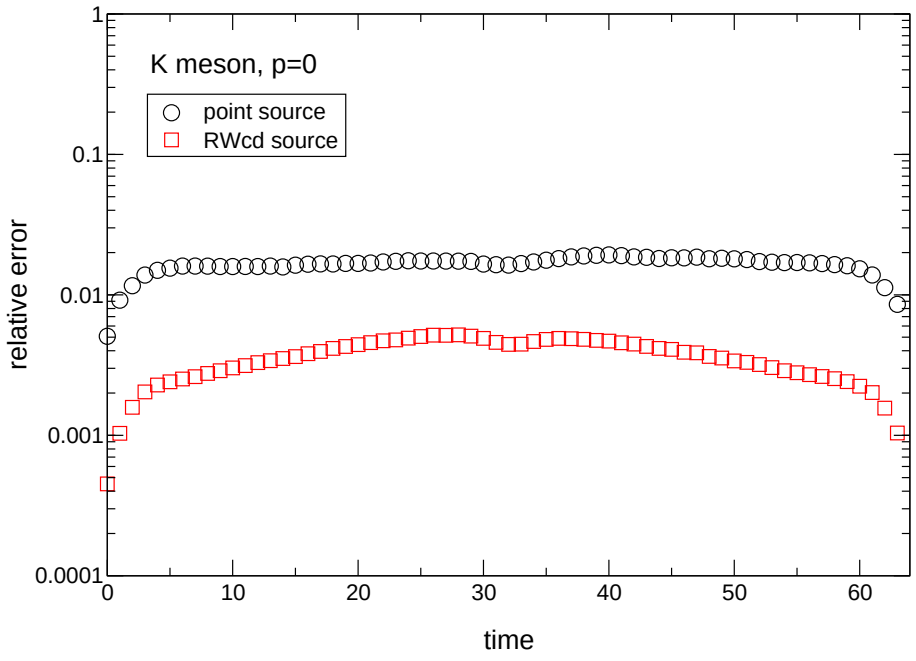

Figure 8.11: Relative errors in the K meson two-point functions at $\mathbf{p}' = 0$.

Numerical results: K-meson two-point functions

Comparisons of the relative errors in the K meson two-point functions from point sources and RWcd sources are shown in Fig. 8.11 (for $\mathbf{p}' = 0$) and Fig. 8.12 (for $\mathbf{p}' = 2\pi/L \cdot (-2, 0, 0)$). As can be seen in the figures[3], the errors are significantly smaller for the RWcd source

At zero momentum, the CPU time used here for the two methods was the same; however, recall that for the random-wall source for each non-zero momentum new propagators have to be computed with the phase $e^{i\mathbf{p}'\cdot\mathbf{x}}$ inserted at the source.

I fit the kaon two-point functions with a function of the form

$$C(\tau, \mathbf{p}') = \sum_{n=0}^{n_{\rm exp}-1} A_n^2 \left[e^{-E_n \tau} + e^{-E_n (L_\tau - \tau)} \right] + (-1)^{\tau+1} \sum_{n=0}^{\widetilde{n}_{\rm exp}-1} \widetilde{A}_n^2 \left[e^{-\widetilde{E}_n \tau} + e^{-\widetilde{E}_n (L_\tau - \tau)} \right], \tag{8.67}$$

where the oscillating terms are required by the naive/staggered light-quark action. To

[3]Note that in contrast to the NRQCD heavy-meson correlation functions encountered so far, the light-meson correlation functions are periodic in τ with a period of $L_\tau = 64$, the temporal extent of the lattice. This is due to the use of a relativistic action for the light quarks, which leads to propagation both forward and backward in time across the lattice boundaries.

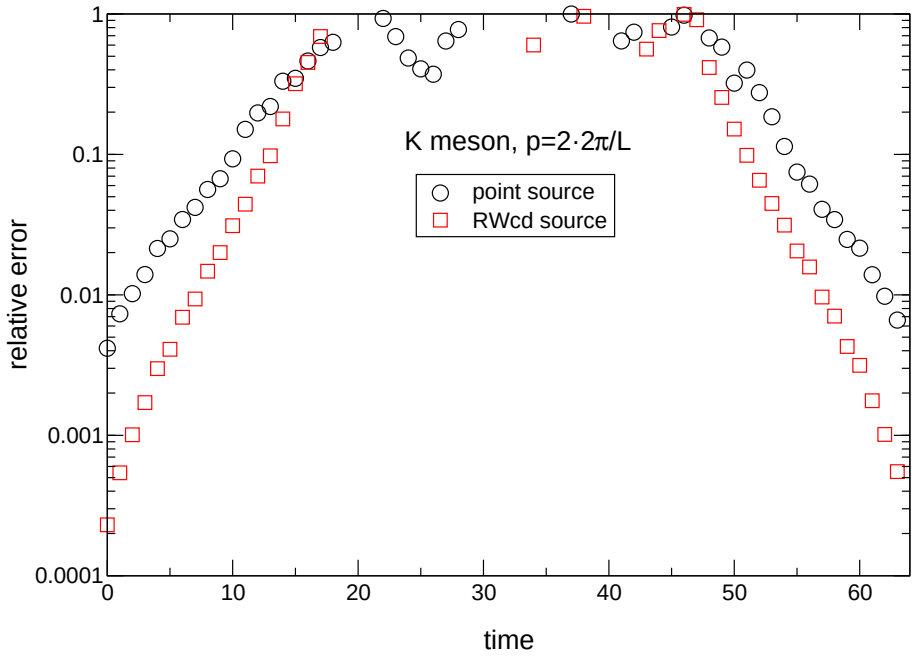

Figure 8.12: Relative errors in the K meson two-point functions at $\mathbf{p}' = 2\pi/L \cdot (-2, 0, 0)$.

ensure the correct ordering of the states, I actually use the logarithms of the energy differences, $\ln(E_n - E_{n-1})$, $\ln(\widetilde{E}_n - \widetilde{E}_{n-1})$ as the fit parameters. Also, I write the amplitudes of the excited states ($n > 0$) as $A_n = B_n A_0$, $\widetilde{A}_n = \widetilde{B}_n \widetilde{A}_0$, and use the relative amplitudes B_n, $\widetilde{B}_n$ as the fit parameters.

Examples of Bayesian fits (cf. Sec. C.3) to the kaon two-point functions are shown in Fig. 8.13 (for $\mathbf{p}' = 0$) and Fig. 8.14 (for $\mathbf{p}' = 2\pi/L \cdot (-2, 0, 0)$). Note that at zero momentum, the oscillating contributions are not detectable and one can set $\widetilde{n}_{\text{exp}} = 0$. At non-zero momentum, I always set $\widetilde{n}_{\text{exp}} = n_{\text{exp}}$.

I chose the priors for the relative amplitudes B_n to be 1 with a width of 2, and the priors for the logarithms of the energy splittings to be (-1) with a width of 1. The fit results from the ground-state energy and amplitude for range of values for n_{exp} are listed in Tables 8.3, 8.5, and 8.7. All fits are performed in the range $\tau = \tau_{\text{min}} \ldots (L_\tau - \tau_{\text{min}})$ with $\tau_{\text{min}} = 2$. As can be seen in the tables, the results are stable for $n_{\text{exp}} \gtrsim 5$. I computed the central values and errors given here using bootstrap, but they agree with those obtained directly from the fit.

For comparison, I also show the results from unconstrained fits with $n_{\text{exp}} = 1$ in Tables 8.2, 8.4, and 8.6 for a range of τ_{min}. Here, one has to choose τ_{min} sufficiently large so that

the contributions from the excited states are negligible. However, the statistical uncertainty of the fit results increases with τ_{min} (especially at non-zero momentum). Usually, one increases τ_{min} until the change in the ground-state fit results becomes smaller than the statistical errors. This is satisfied for $\tau_{\mathrm{min}} \gtrsim 10$.

At zero momentum, I find that the error for the ground-state amplitude from the RWcd correlator is about 4 times smaller than the error from the point source correlator. For the ground-state energy, the improvement factor is only about 1.5. Note that for the point-source correlator, the central values for the ground-state amplitude obtained from Bayesian and unconstrained fits differ by about 2 standard deviations. Additionally, the central values for the ground-state amplitude differ between the two types of sources (RWcd and point), most significantly in the Bayesian fits (3.3 standard deviations). This is despite the apparent stability observed individually for the two methods[4].

I find that the improvement in the ground-state fit results from the RWcd source increases with the momentum. At $\mathbf{p}' = 2\pi/L \cdot (-2, 0, 0)$, the improvement factors are about 7 for both the ground-state amplitude and energy. This is somewhat surprising, given Figs. 8.11 and 8.12 for the relative errors in the correlation functions. However, note that the fits take into account correlations between the data points at different τ, which can be significant. Note that an increase with momentum in the improvement factor for the light pseudoscalar mesons was also observed in [193] (with Bayesian fitting).

[4]Note that (inadvertently) different temporal boundary conditions for the light-quark propagators were used for the two types of sources (periodic for the point source, antiperiodic for the RWcd source). However, we expect the difference caused by this to be suppressed by $e^{-m_\pi L_\tau}$. For the quark masses in use, $m_\pi L_\tau \approx 12$ so that $e^{-m_\pi L_\tau} \approx 6 \cdot 10^{-6}$. Thus, it is unlikely that this can explain the difference seen.

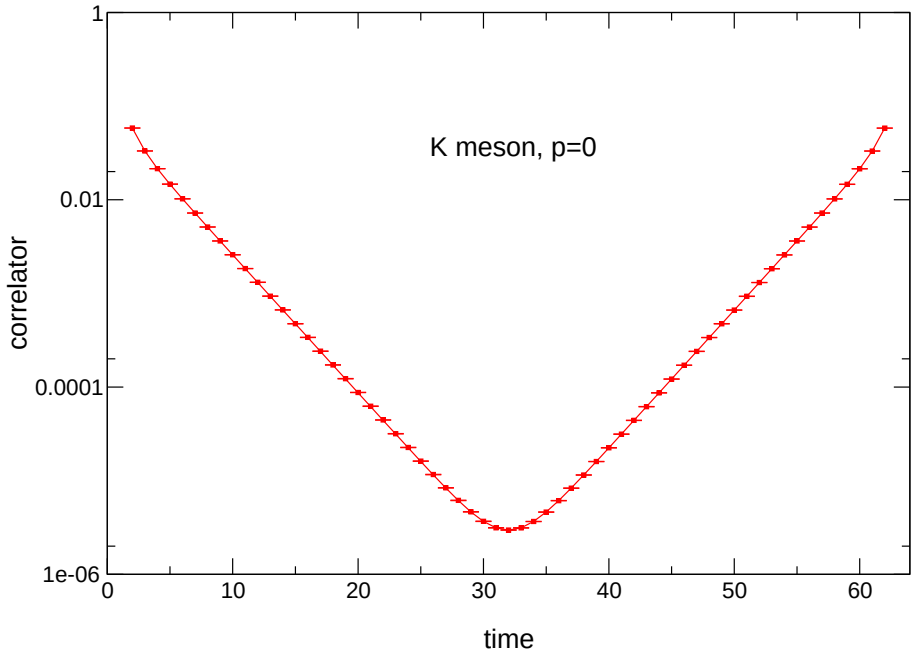

Figure 8.13: Bayesian fit of the K meson two-point function (RWcd source) at $\mathbf{p}' = 0$. The fit has $\tau_{\text{min}} = 2$ and $n_{\text{exp}} = 10$, $\widetilde{n}_{\text{exp}} = 0$.

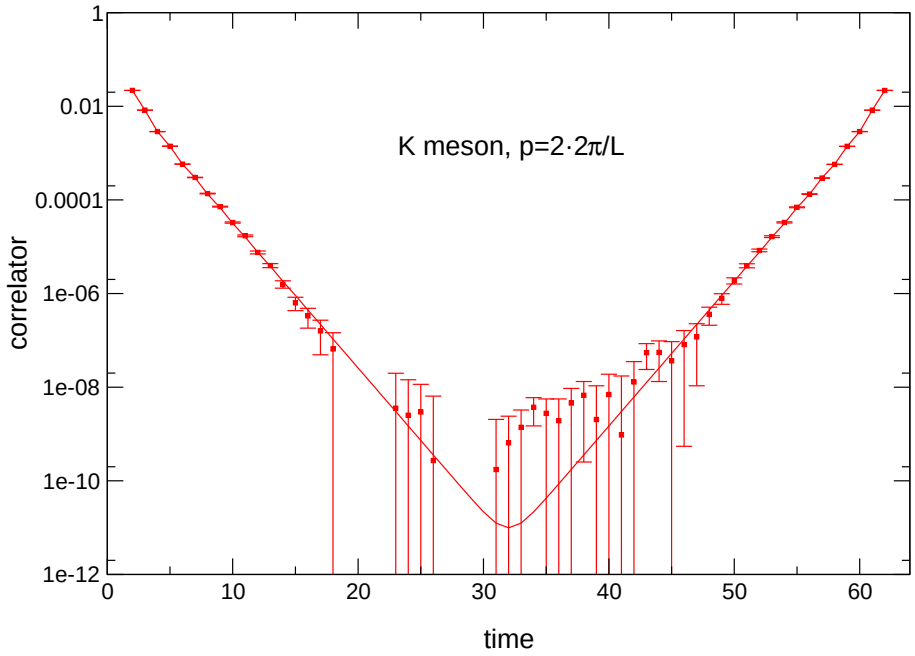

Figure 8.14: Bayesian fit of the K meson two-point function (RWcd source) at $\mathbf{p}' = 2\pi/L \cdot (-2, 0, 0)$. The fit has $\tau_{\text{min}} = 2$ and $n_{\text{exp}} = \widetilde{n}_{\text{exp}} = 10$.

	point source			RWcd source		
$\tau_{\min}$	E	A	χ^2/d.o.f.	E	A	χ^2/d.o.f.
6	0.33989(23)	0.2759(18)	2.59	0.34030(15)	0.27980(32)	4.66
7	0.33951(23)	0.2753(19)	1.41	0.33979(16)	0.27869(34)	2.24
8	0.33931(23)	0.2745(19)	0.89	0.33949(16)	0.27783(36)	1.34
9	0.33924(24)	0.2745(19)	0.82	0.33935(17)	0.27733(38)	1.04
10	0.33924(24)	0.2745(19)	0.83	0.33926(17)	0.27705(41)	1.01
11	0.33914(25)	0.2744(19)	0.79	0.33922(18)	0.27688(44)	1.00
12	0.33910(25)	0.2742(19)	0.79	0.33923(19)	0.27692(48)	1.05

Table 8.2: Results from unconstrained fits to the K meson two-point function at $\mathbf{p}' = 0$. All fits have $n_{\text{exp}} = 1$, $\widetilde{n}_{\text{exp}} = 0$. Central values and errors directly from fit.

	point source		RWcd source	
n_{exp}	E	A	E	A
4	0.33900(27)	0.2702(20)	0.33919(19)	0.27669(47)
5	0.33898(28)	0.2701(21)	0.33918(19)	0.27667(48)
6	0.33898(27)	0.2701(20)	0.33918(19)	0.27668(50)
7	0.33898(29)	0.2701(21)	0.33918(19)	0.27668(47)
8	0.33897(29)	0.2700(21)	0.33918(19)	0.27666(48)
9	0.33898(28)	0.2701(20)	0.33918(19)	0.27666(48)
10	0.33897(28)	0.2700(21)	0.33918(19)	0.27665(50)

Table 8.3: Results from Bayesian fits to the K meson two-point function at $\mathbf{p}' = 0$. All fits have $\tau_{\min} = 2$ and $\widetilde{n}_{\text{exp}} = 0$. Central values and errors from bootstrap.

	point source			RWcd source		
$\tau_{\min}$	E	A	χ^2/d.o.f.	E	A	χ^2/d.o.f.
6	0.4690(13)	0.2421(19)	2.18	0.46866(51)	0.24758(48)	3.63
7	0.4642(15)	0.2362(22)	1.43	0.46531(60)	0.24340(63)	1.71
8	0.4626(15)	0.2347(22)	1.34	0.46396(65)	0.24155(71)	0.99
9	0.4625(17)	0.2346(24)	1.38	0.46304(75)	0.24019(90)	0.90
10	0.4602(19)	0.2307(28)	1.21	0.46263(85)	0.2395(11)	0.90
11	0.4601(21)	0.2305(32)	1.33	0.46177(99)	0.2381(14)	0.87
12	0.4599(23)	0.2302(37)	1.22	0.4619(11)	0.2384(17)	0.91

Table 8.4: Results from unconstrained fits to the K meson two-point function at $\mathbf{p}' = 2\pi/L \cdot (-1, 0, 0)$. All fits have $n_{\text{exp}} = \widetilde{n}_{\text{exp}} = 1$. Central values and errors directly from fit.

	point source		RWcd source	
$n_{\text{exp}} = \widetilde{n}_{\text{exp}}$	E	A	E	A
4	0.4571(37)	0.2206(68)	0.4617(10)	0.2374(17)
5	0.4570(40)	0.2200(75)	0.4615(12)	0.2369(19)
6	0.4570(41)	0.2201(81)	0.4616(11)	0.2372(17)
7	0.4569(42)	0.2197(80)	0.4615(11)	0.2368(17)
8	0.4571(42)	0.2202(78)	0.4616(11)	0.2371(18)
9	0.4571(42)	0.2201(80)	0.4616(11)	0.2373(18)
10	0.4569(43)	0.2195(86)	0.4615(11)	0.2369(19)

Table 8.5: Results from Bayesian fits to the K meson two-point function at $\mathbf{p}' = 2\pi/L \cdot (-1, 0, 0)$. All fits have $\tau_{\min} = 2$. Central values and errors from bootstrap.

	point source			RWcd source		
$\tau_{\min}$	E	A	χ^2/d.o.f.	E	A	χ^2/d.o.f.
6	0.732(14)	0.219(10)	1.10	0.7261(42)	0.2159(28)	1.10
7	0.693(21)	0.186(16)	1.01	0.7125(64)	0.2043(49)	0.97
8	0.722(40)	0.214(40)	1.02	0.716(10)	0.2081(90)	0.98
9	0.728(66)	0.221(78)	1.06	0.721(14)	0.213(14)	0.98
10	–	–	–	0.726(22)	0.219(25)	1.00

Table 8.6: Results from unconstrained fits to the K meson two-point function at $\mathbf{p}' = 2\pi/L \cdot (-2, 0, 0)$. All fits have $n_{\text{exp}} = \widetilde{n}_{\text{exp}} = 1$. Central values and errors directly from fit.

	point source		RWcd source	
$n_{\text{exp}} = \widetilde{n}_{\text{exp}}$	E	A	E	A
4	0.682(23)	0.172(23)	0.7150(47)	0.2021(39)
5	0.677(30)	0.166(33)	0.7134(47)	0.2005(39)
6	0.677(32)	0.166(30)	0.7130(50)	0.2002(41)
7	0.676(32)	0.165(33)	0.7126(49)	0.1999(39)
8	0.676(32)	0.165(32)	0.7123(50)	0.1996(41)
9	0.674(34)	0.164(34)	0.7120(48)	0.1994(40)
10	0.677(29)	0.166(29)	0.7125(50)	0.1998(41)

Table 8.7: Results from Bayesian fits to the K meson two-point function at $\mathbf{p}' = 2\pi/L \cdot (-2, 0, 0)$. All fits have $\tau_{\min} = 2$. Central values and errors from bootstrap.

Numerical results: K^*-meson two-point functions

Comparisons of the relative errors in the K^* meson two-point functions from point sources and RWcd sources are shown in Fig. 8.15 (for $\mathbf{p}' = 0$) and Fig. 8.16 (for $\mathbf{p}' = 2\pi/L \cdot (-1, 0, 0)$). Note that the results are averaged over the polarisation directions $j = 1, 2, 3$ (for $\mathbf{p}' = 0$) and $j = 2, 3$ (for $\mathbf{p}' = 2\pi/L \cdot (-1, 0, 0)$). Recall that all polarisation directions (and momenta) can be obtained from the same point-source propagators, while new random-wall propagators are required for every polarisation direction (and momentum). Thus, at zero momentum, the CPU time used to compute the RWcd two-point function was four times larger for the RWcd source compared to the point source. Despite the additional CPU time, the improvement at zero momentum is smaller than that for the pseudoscalar kaon.

Bayesian fits of the K^* correlators using the function (8.67) with $n_{\text{exp}} = \widetilde{n}_{\text{exp}} = 10$ are shown in Fig. 8.17 (for $\mathbf{p}' = 0$) and Fig. 8.17 (for $\mathbf{p}' = 2\pi/L \cdot (-1, 0, 0)$). Note that in contrast to the K meson, the oscillations are strong even at $\mathbf{p}' = 0$. The priors for the energy splittings and the relative excited-state amplitudes were set to the same values as in Sec. 8.8.1.

The results for the ground-state amplitude and energy from Bayesian fits with various values of n_{exp} and $\tau_{\text{min}} = 1$ are listed in Tables 8.9 and 8.11. In addition, results from unconstrained fits with $n_{\text{exp}} = \widetilde{n}_{\text{exp}} = 1$ for a range of τ_{min} are shown in Tables 8.8 and 8.10.

From the Bayesian fits, at zero momentum I find improvement factors of about 1.5 in the ground-state amplitude and about 1.5 in the ground-state energy. At $\mathbf{p}' = 2\pi/L \cdot (-1, 0, 0)$, these factors are about 2.5 and 4, respectively. For the Bayesian fits I used bootstrap to compute the central values and errors. The errors directly from the fit (not shown) tend to be larger (for the non-Bayesian fit, they agree with the bootstrap errors). I found that the bootstrap results are more stable under changes of the prior widths than the results directly from the fit.

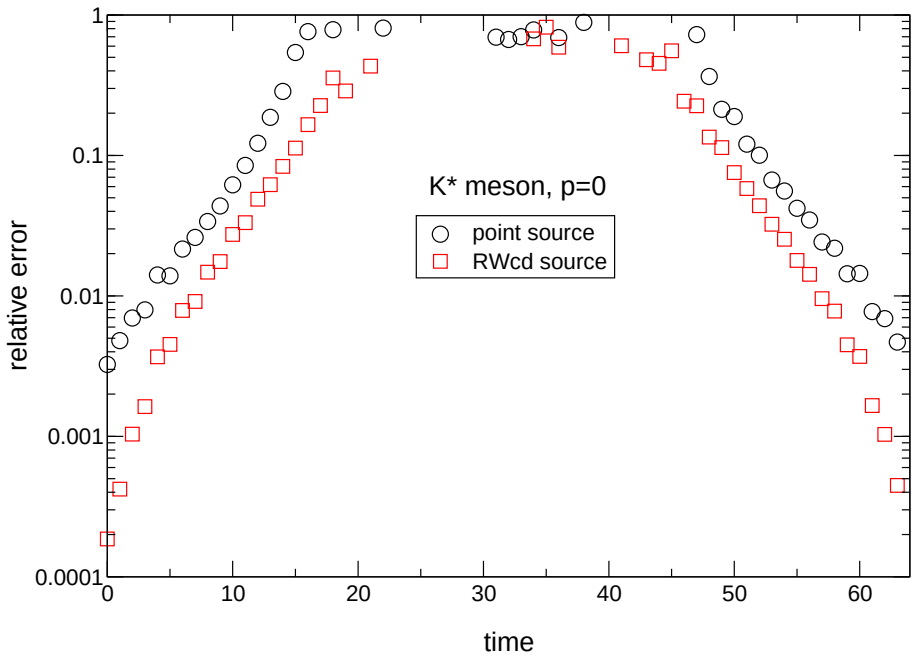

Figure 8.15: Relative errors in the K^* meson two-point functions at $\mathbf{p}' = 0$.

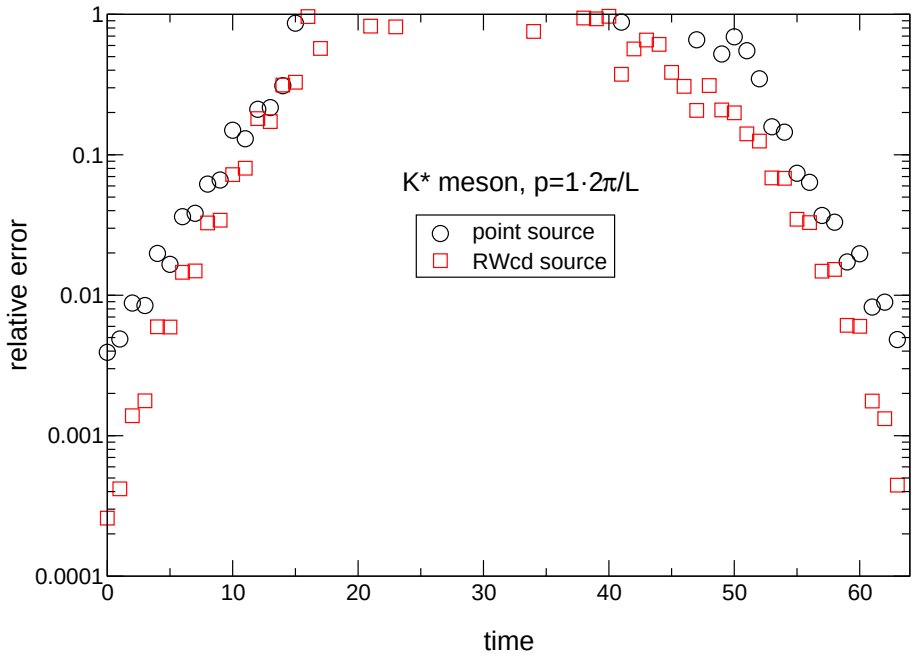

Figure 8.16: Relative errors in the K^* meson two-point functions at $\mathbf{p}' = 2\pi/L \cdot (-1, 0, 0)$.

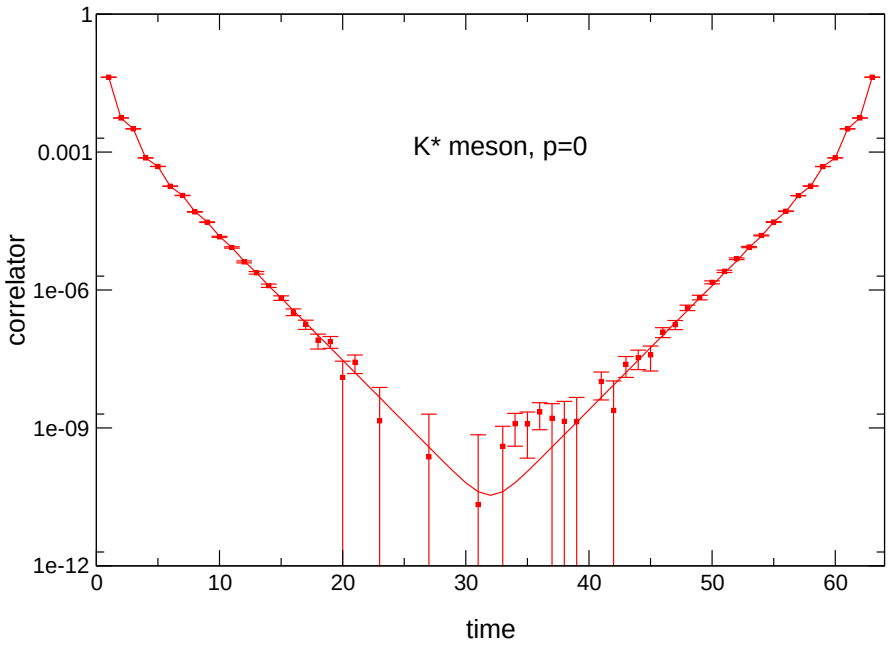

Figure 8.17: Bayesian fit of the K^* meson two-point function (RWcd source) at $\mathbf{p}' = 0$. The fit has $\tau_{\rm min} = 1$ and $n_{\rm exp} = \widetilde{n}_{\rm exp} = 10$.

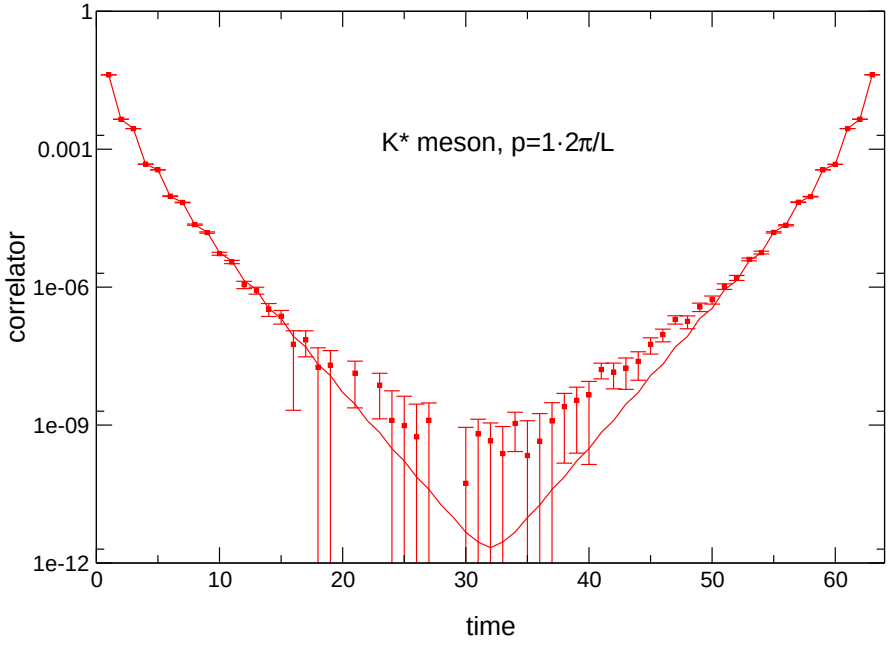

Figure 8.18: Bayesian fit of the K^* meson two-point function (RWcd source) at $\mathbf{p}' = 2\pi/L \cdot (-1, 0, 0)$. The fit has $\tau_{\rm min} = 1$ and $n_{\rm exp} = \widetilde{n}_{\rm exp} = 10$.

	point source			RWcd source		
$\tau_{\min}$	E	A	χ^2/d.o.f.	E	A	χ^2/d.o.f.
4	0.7091(47)	0.1217(14)	2.13	0.7183(19)	0.12476(53)	10.30
5	0.6675(65)	0.1060(21)	0.85	0.6689(28)	0.10703(88)	2.65
6	0.6508(80)	0.0992(28)	0.69	0.6504(34)	0.0998(11)	1.38
7	0.648(11)	0.0983(43)	0.70	0.6328(51)	0.0926(18)	1.02
8	0.655(15)	0.1017(68)	0.71	0.6244(63)	0.0890(24)	0.87
9	0.652(23)	0.100(11)	0.84	0.6183(88)	0.0862(36)	0.86
10	0.649(27)	0.098(14)	0.72	0.617(12)	0.0856(52)	0.91

Table 8.8: Results from unconstrained fits to the K^* meson two-point function at $\mathbf{p}' = 0$. All fits have $n_{\text{exp}} = \widetilde{n}_{\text{exp}} = 1$. Central values and errors directly from fit.

	point source		RWcd source	
$n_{\text{exp}} = \widetilde{n}_{\text{exp}}$	E	A	E	A
4	0.638(10)	0.0924(39)	0.641(11)	0.0950(42)
5	0.636(10)	0.0912(41)	0.6257(67)	0.0887(29)
6	0.635(10)	0.0903(42)	0.6253(68)	0.0886(30)
7	0.634(10)	0.0899(39)	0.6246(76)	0.0882(35)
8	0.633(11)	0.0895(45)	0.6248(66)	0.0883(27)
9	0.633(10)	0.0894(38)	0.6249(58)	0.0886(23)
10	0.633(10)	0.0892(40)	0.6252(55)	0.0889(20)

Table 8.9: Results from Bayesian fits to the K^* meson two-point function at $\mathbf{p}' = 0$. All fits have $\tau_{\min} = 1$. Central values and errors from bootstrap.

	point source			RWcd source		
$\tau_{\min}$	E	A	χ^2/d.o.f.	E	A	χ^2/d.o.f.
4	0.8114(78)	0.1272(23)	1.99	0.8132(34)	0.12855(98)	3.15
5	0.765(11)	0.1098(34)	1.56	0.7685(54)	0.1126(17)	1.56
6	0.716(13)	0.0913(41)	1.14	0.7367(75)	0.1005(25)	1.08
7	0.728(20)	0.0962(75)	1.14	0.729(11)	0.0974(42)	1.08
8	0.723(31)	0.094(12)	1.18	0.699(15)	0.0850(55)	0.99
9	0.676(43)	0.074(16)	1.18	0.686(23)	0.0795(85)	1.01
10	0.712(68)	0.091(33)	1.18	0.669(30)	0.072(11)	1.03

Table 8.10: Results from unconstrained fits to the K^* meson two-point function at $\mathbf{p}' = 2\pi/L \cdot (-1, 0, 0)$. All fits have $n_{\text{exp}} = \widetilde{n}_{\text{exp}} = 1$. Central values and errors directly from fit.

	point source		RWcd source	
$n_{\text{exp}} = \widetilde{n}_{\text{exp}}$	E	A	E	A
4	0.703(21)	0.0846(72)	0.7220(11)	0.0931(35)
5	0.700(21)	0.0827(77)	0.7070(83)	0.0879(27)
6	0.699(19)	0.0824(69)	0.7060(80)	0.0877(25)
7	0.697(20)	0.0818(72)	0.7045(85)	0.0869(27)
8	0.696(20)	0.0814(71)	0.7049(83)	0.0872(24)
9	0.695(22)	0.0810(76)	0.7052(82)	0.0872(25)
10	0.697(21)	0.0816(74)	0.7055(84)	0.0873(24)

Table 8.11: Results from Bayesian fits to the K^* meson two-point function at $\mathbf{p}' = 2\pi/L \cdot (-1, 0, 0)$. All fits have $\tau_{\min} = 1$. Central values and errors from bootstrap.

8.8.2 Heavy-light meson two-point functions

For B mesons, the point-source correlator (without smearing) is

$$\begin{aligned} C_B(\tau,\mathbf{k}) &= \sum_{\mathbf{y}} \mathrm{Tr}\left[G^\dagger_{q'}(y,x)\,G_b(y,x)\right] e^{-i\mathbf{p}\cdot(\mathbf{y}-\mathbf{x})} \\ &= \frac{1}{\gamma}\sum_{\mathbf{y}} \mathrm{Tr}\left[G^\dagger_{\chi_{q'}}(y,x)\,\Omega^\dagger(y)\,S(\Lambda) \begin{pmatrix} G_{\psi_v}(y,x) & 0 \\ 0 & 0 \end{pmatrix} \overline{S}(\Lambda)\,\Omega(x) \right] e^{-i\mathbf{k}\cdot(\mathbf{y}-\mathbf{x})}, \end{aligned} \tag{8.68}$$

for $\tau = y_0 - x_0 > 0$. Here we have used Eq. (6.24) to express $G_b(y,x)$ in terms of the moving-NRQCD propagator.

In order to obtain the random-wall correlator, we define

$$\widetilde{G}^p_H(y,x_0,\mathbf{k}) = \sum_{\mathbf{x}} \begin{pmatrix} G_{\psi_v}(y,x) & 0 \\ 0 & 0 \end{pmatrix} \overline{S}(\Lambda)\, e^{i\mathbf{k}\cdot\mathbf{x}}\, \Omega(x)\, \xi^p(\mathbf{x}). \tag{8.69}$$

We then combine this with the zero-momentum random-wall light-quark propagator from the same ξ^p to obtain the B meson random-wall correlator:

$$C_{B,\mathrm{RW}}(\tau,\mathbf{k}) = \frac{1}{\gamma}\frac{1}{L^3}\frac{1}{n_Z}\sum_{p=1}^{n_Z}\sum_{\mathbf{y}} \widetilde{G}^p_{\chi_{q'}}(y,x_0,\mathbf{0})^* \cdot \mathrm{tr}\left[\Omega^\dagger(y) S(\Lambda) \widetilde{G}^p_H(y,x_0,\mathbf{k})\right]\, e^{-i\mathbf{k}\cdot\mathbf{y}}. \tag{8.70}$$

In (8.70), "tr" denotes a trace over spinor indices only.

I also compute correlators with gauge-invariant Gaussian smearing for the heavy quark at the source and/or sink. The smearing is performed via the operator

$$\left(1 + \frac{\sigma}{n_S}\Delta^{(2)}\right)^{n_S}, \tag{8.71}$$

where $\Delta^{(2)}$ is a covariant lattice Laplacian and σ, n_S are the smearing parameters. The operator (8.71) is inserted in Eq. (8.69) to the left of $\Omega(x)\,\xi^p(\mathbf{x})$ (for source smearing) and/or to the left of $G_{\psi_v}(y,x)$ (for sink smearing).

Numerical results: B meson two-point functions

Figures 8.19 and 8.20 show comparisons of the relative errors (RWcd source vs point source) in the B meson two-point functions (without smearing) at $\mathbf{k}=0$, $\mathbf{v}=0$ and at $\mathbf{k}=0$, $\mathbf{v}=(0.4,0,0)$. As can be seen in the figures, the improvement depends strongly on the separation τ between source and sink, and becomes small at large τ.

I performed fits to (2×1)-matrix correlators with smeared sources and both local and smeared sinks using a function of the form (6.31) with $n_{\mathrm{exp}} = \widetilde{n}_{\mathrm{exp}}$. As for the light-meson

two-point functions, here I also used the logarithms of the energy splittings and the relative amplitudes for the excited states as the fit parameters. I set the priors for the former to (-1) with a width of 1 and for the latter to 0.5 with a width of 2.

Plots of Bayesian fits with $\tau_{\mathrm{min}} = 2$ and $n_{\mathrm{exp}} = \widetilde{n}_{\mathrm{exp}} = 10$ are shown in Figs. 8.21 and 8.22. For the Bayesian fits of the B meson correlators, I show results both directly from the fit and from bootstrap in Tables 8.14, 8.15, 8.16, and 8.17.

At $\mathbf{v} = 0$, the errors from the Bayesian fits are larger for the RWcd source compared to the point source, while the errors from the unconstrained fits are slightly smaller for the RWcd source.

At $\mathbf{v} = (0.4, 0, 0)$, the situation is very different, albeit strongly dependent on the data-analysis method used. With Bayesian fitting and error estimates from bootstrap, I find improvement factors of about 3 for the ground-state energy and about 2 for the ground-state amplitude from the RWcd source. However, from the same fits I see no improvement when considering the errors directly from the fits.

With unconstrained fits, where I see agreement between the direct and the bootstrap results, no significant improvement is observed for the RWcd source compared to the point source, neither at $\mathbf{v} = 0$ nor at $\mathbf{v} = (0.4, 0, 0)$.

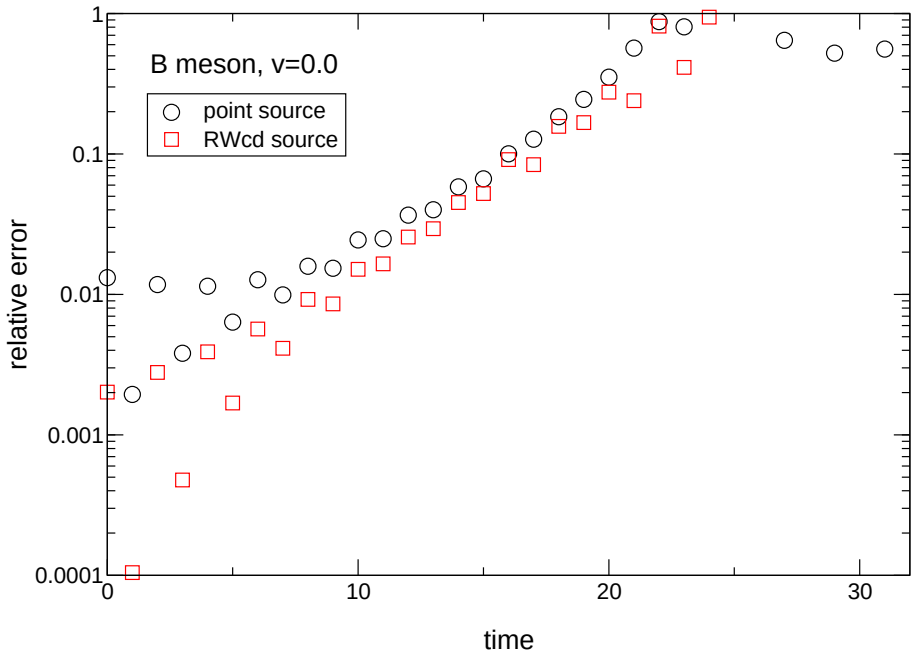

Figure 8.19: Relative errors in the B meson two-point functions (without smearing) at $\mathbf{k} = 0$, $\mathbf{v} = 0$.

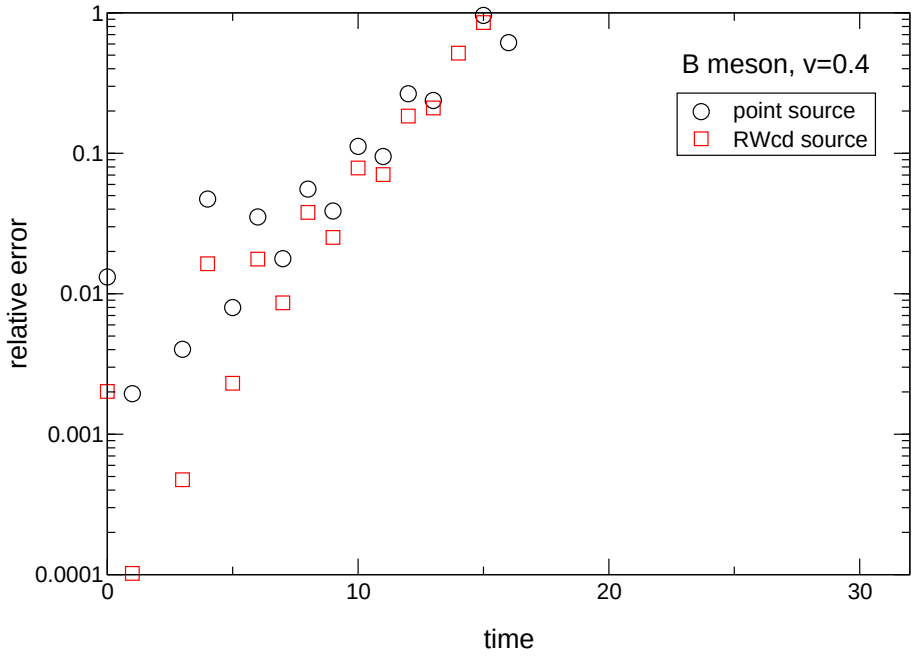

Figure 8.20: Relative errors in the B meson two-point functions (without smearing) at $\mathbf{k} = 0$, $\mathbf{v} = (0.4, 0, 0)$.

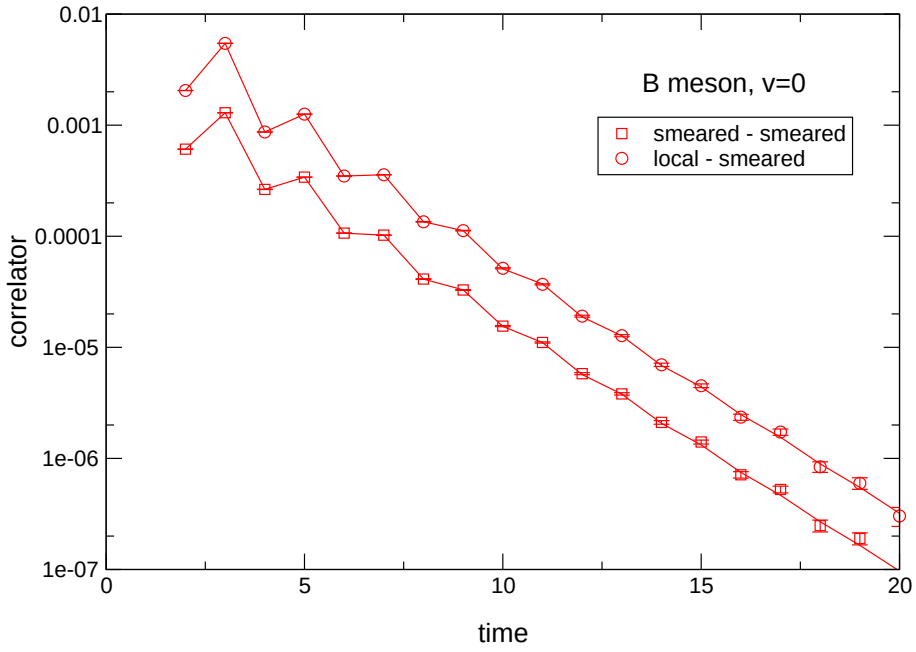

Figure 8.21: Bayesian fit of the B meson (2×1)-matrix correlator (RWcd source) at $\mathbf{k}=0$, $\mathbf{v}=0$. The fit has $\tau_{\rm min}=2$ and $n_{\rm exp}=\widetilde{n}_{\rm exp}=10$.

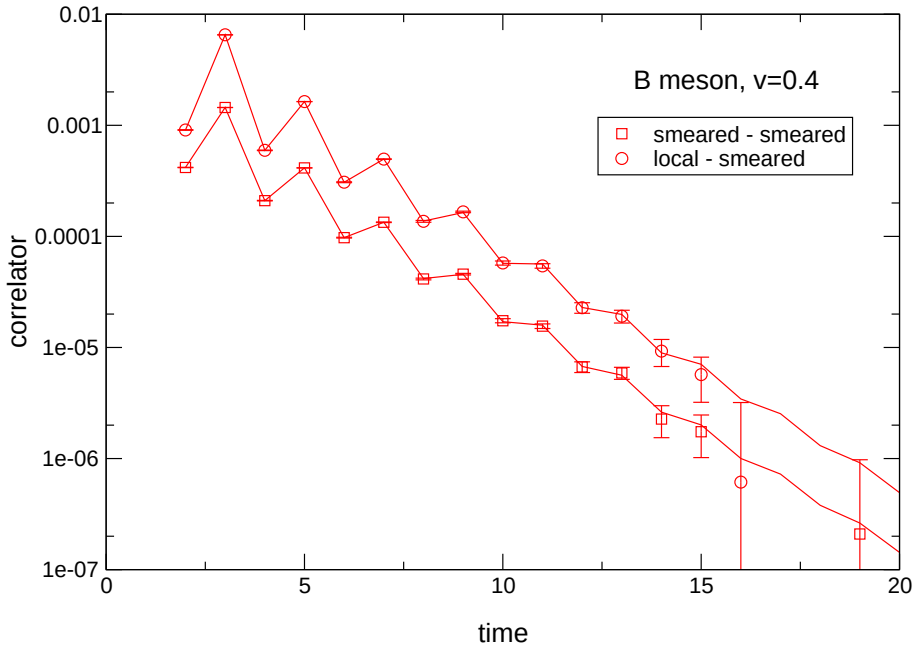

Figure 8.22: Bayesian fit of the B meson (2×1)-matrix correlator (RWcd source) at $\mathbf{k}=0$, $\mathbf{v}=(0.4,0,0)$. The fit has $\tau_{\rm min}=2$ and $n_{\rm exp}=\widetilde{n}_{\rm exp}=10$.

	point source			RWcd source		
$\tau_{\min}$	E	A	χ^2/d.o.f.	E	A	χ^2/d.o.f.
4	0.5776(18)	0.2386(12)	17.70	0.58702(98)	0.24617(58)	64.20
5	0.5603(21)	0.2242(15)	9.58	0.5565(14)	0.22229(90)	17.90
6	0.5396(26)	0.2068(19)	1.87	0.5430(18)	0.2095(13)	3.93
7	0.5426(32)	0.2092(26)	1.33	0.5315(24)	0.1990(19)	1.98
8	0.5362(41)	0.2022(36)	1.11	0.5292(31)	0.1963(27)	1.42
9	0.5260(53)	0.1911(49)	0.87	0.5223(42)	0.1891(40)	1.34
10	0.5243(67)	0.1890(68)	0.90	0.5184(54)	0.1842(53)	0.87
11	0.5308(84)	0.1975(96)	0.85	0.5152(75)	0.1802(79)	0.87
12	0.528(10)	0.193(13)	0.67	0.517(10)	0.183(12)	0.91

Table 8.12: Results from unconstrained fits to the B meson (2×1)-matrix correlator at $\mathbf{k} = 0$, $\mathbf{v} = (0.0, 0, 0)$. All fits have $n_{\text{exp}} = \widetilde{n}_{\text{exp}} = 1$. The local amplitude A is shown. Central values and errors directly from fit.

	point source			RWcd source		
$\tau_{\min}$	E	A	χ^2/d.o.f.	E	A	χ^2/d.o.f.
4	0.5436(37)	0.2398(22)	4.69	0.5382(20)	0.2390(12)	9.28
5	0.5261(52)	0.2258(35)	4.30	0.5163(33)	0.2215(22)	7.11
6	0.5031(76)	0.2029(53)	1.09	0.5082(53)	0.2094(38)	0.96
7	0.499(11)	0.2001(88)	1.13	0.4994(87)	0.2019(68)	0.96
8	0.500(18)	0.199(16)	1.15	0.511(15)	0.212(14)	0.95

Table 8.13: Results from unconstrained fits to the B meson (2×1)-matrix correlator at $\mathbf{k} = 0$, $\mathbf{v} = (0.4, 0, 0)$. All fits have $n_{\text{exp}} = \widetilde{n}_{\text{exp}} = 1$. The local amplitude A is shown. Central values and errors directly from fit.

	point source		RWcd source	
$n_{\text{exp}} = \tilde{n}_{\text{exp}}$	E	A	E	A
4	0.5248(56)	0.1890(60)	0.512(11)	0.174(16)
5	0.5253(55)	0.1897(58)	0.512(11)	0.174(16)
6	0.5260(57)	0.1902(61)	0.513(10)	0.175(14)
7	0.5256(58)	0.1897(63)	0.513(10)	0.175(14)
8	0.5258(59)	0.1899(64)	0.5145(89)	0.178(12)
9	0.5259(58)	0.1900(63)	0.5136(96)	0.177(13)
10	0.5259(59)	0.1900(64)	0.5149(87)	0.178(11)

Table 8.14: Results from Bayesian fits to the B meson (2×1)-matrix correlator at $\mathbf{k} = 0$, $\mathbf{v} = 0$. All fits have $\tau_{\text{min}} = 2$. The local amplitude A is shown. Central values and errors directly from fit.

	point source		RWcd source	
$n_{\text{exp}} = \tilde{n}_{\text{exp}}$	E	A	E	A
4	0.5245(55)	0.1866(72)	0.5113(90)	0.171(13)
5	0.5243(59)	0.1860(78)	0.5112(88)	0.172(12)
6	0.5251(55)	0.1876(71)	0.5117(77)	0.173(11)
7	0.5243(61)	0.1857(90)	0.5110(88)	0.171(12)
8	0.5248(55)	0.1867(75)	0.5107(88)	0.171(13)
9	0.5245(61)	0.1865(85)	0.5101(94)	0.170(14)
10	0.5248(58)	0.1871(74)	0.5109(72)	0.170(14)

Table 8.15: Results from Bayesian fits to the B meson (2×1)-matrix correlator at $\mathbf{k} = 0$, $\mathbf{v} = 0$. All fits have $\tau_{\text{min}} = 2$. The local amplitude A is shown. Central values and errors from bootstrap.

	point source		RWcd source	
$n_{\mathrm{exp}} = \tilde{n}_{\mathrm{exp}}$	E	A	E	A
4	0.491(13)	0.187(12)	0.498(10)	0.1955(95)
5	0.4918(99)	0.1883(82)	0.498(10)	0.1954(98)
6	0.4918(99)	0.1883(83)	0.498(11)	0.1954(99)
7	0.491(14)	0.187(12)	0.511(12)	0.196(12)
8	0.4919(99)	0.1883(83)	0.498(12)	0.196(12)
9	0.491(14)	0.187(12)	0.498(12)	0.196(12)
10	0.491(14)	0.187(12)	0.498(12)	0.196(12)

Table 8.16: Results from Bayesian fits to the B meson (2×1)-matrix correlator at $\mathbf{k} = 0$, $\mathbf{v} = (0.4, 0, 0)$. All fits have $\tau_{\mathrm{min}} = 2$. The local amplitude A is shown. Central values and errors directly from fit.

	point source		RWcd source	
$n_{\mathrm{exp}} = \tilde{n}_{\mathrm{exp}}$	E	A	E	A
4	0.482(20)	0.193(11)	0.4966(72)	0.1943(66)
5	0.480(24)	0.195(14)	0.4971(77)	0.1949(66)
6	0.479(24)	0.197(16)	0.4974(73)	0.1951(69)
7	0.480(24)	0.196(14)	0.4973(78)	0.1955(74)
8	0.480(24)	0.197(15)	0.4973(76)	0.1955(74)
9	0.481(23)	0.195(14)	0.4973(78)	0.1957(76)
10	0.478(27)	0.195(16)	0.4973(81)	0.1949(74)

Table 8.17: Results from Bayesian fits to the B meson (2×1)-matrix correlator at $\mathbf{k} = 0$, $\mathbf{v} = (0.4, 0, 0)$. All fits have $\tau_{\mathrm{min}} = 2$. The local amplitude A is shown. Central values and errors from bootstrap.

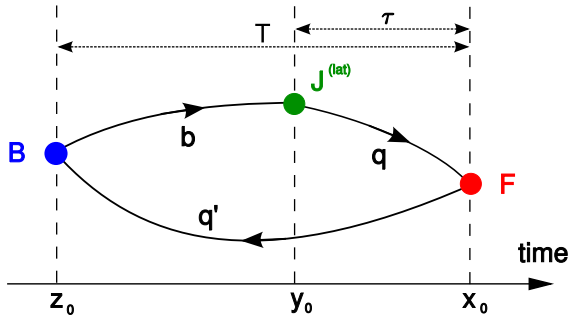

Figure 8.23: Contractions for the three-point functions with point sources.

8.8.3 Heavy-light meson three-point functions

In terms of the standard Dirac propagators, the point-source three-point function at $\tau = |x_0 - y_0|$, $T = |x_0 - z_0|$ is given by

$$C_{FJB}(\tau,\, T,\, \mathbf{p},\, \mathbf{p}') = \sum_{\mathbf{y},\mathbf{z}} e^{-i\mathbf{p}'\cdot\mathbf{x}} e^{-i(\mathbf{p}-\mathbf{p}')\cdot\mathbf{y}} e^{i\mathbf{p}\cdot\mathbf{z}}\ \mathrm{Tr}\big[\Gamma_F\, G_q(x,y)\, \Gamma_J\, G_b(y,z)\, \hat{\gamma}_5\, G_{q'}(z,x)\big], \tag{8.72}$$

where $\Gamma_F = \hat{\gamma}_5$ for $F = P$ and $\Gamma_F = \hat{\gamma}^j$ for $F = V$. See Fig. 8.23 for a diagram showing the contractions. In (8.72) we used the simple form of the heavy-light current $J = \bar{q}\,\Gamma_J b$. When replacing the b quark propagator by the lattice mNRQCD propagator, the current has to be replaced by the lattice current derived in Sec. 8.5. It is convenient to compute and fit the three-point functions for the various terms in the lattice current individually.

Inserting the lattice current, the three-point function becomes

$$\begin{aligned} C_{FJB}(\tau,\, T,\, \mathbf{k},\, \mathbf{p}') \;=\; & \frac{1}{\gamma} \sum_{\mathbf{y},\mathbf{z}} e^{-i\mathbf{p}'\cdot\mathbf{x}} e^{-i(\mathbf{k}-\mathbf{p}')\cdot\mathbf{y}} e^{i\mathbf{k}\cdot\mathbf{z}}\ \mathrm{Tr}\Bigg[G^\dagger_{\chi_q}(y,x)\ F(x)\ \Omega^\dagger(y)\, \hat{\gamma}_5 \\ & \times\ \mathscr{J} \begin{pmatrix} G_{\psi_v}(y,\,z) & 0 \\ 0 & 0 \end{pmatrix} \overline{S}(\Lambda)\, \hat{\gamma}_5\, \Omega(z)\, G_{\chi_{q'}}(z,x) \Bigg] \end{aligned} \tag{8.73}$$

(for $x_0 > y_0 > z_0$). In (8.73), we have $F(x) = 1$ for a pseudoscalar meson in the final state and $F(x) = (-1)^{x_j}\, \hat{\gamma}^j$ for a vector meson in the final state. The symbol $\mathscr{J}$ in (8.73) denotes the gamma matrix / derivative operator content of the heavy-light current:

$$\mathscr{J} \in \Big\{ \Gamma S^+(\Lambda),\ \ \Gamma S^-(\Lambda),\ \ \Gamma\,(-i\hat{\gamma}^0 \mathbf{v} + i\hat{\boldsymbol{\gamma}} \pm i\mathbf{v}/\gamma)\cdot \boldsymbol{\Delta}^{(\pm)} S_+(\Lambda) \Big\}. \tag{8.74}$$

The three-point function (8.73) can be computed by using the spectator-quark (q') propagator as a source for the heavy-quark propagator, so that only the sum over $\mathbf{y}$ remains

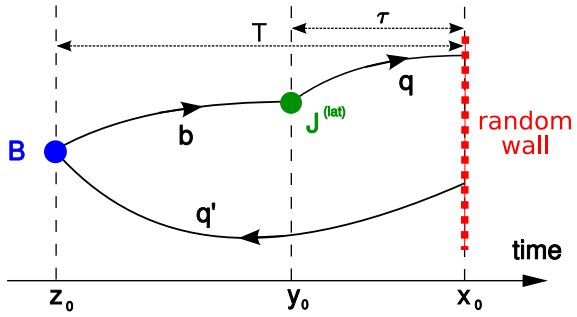

Figure 8.24: Contractions for the three-point functions with random-wall sources.

when the contractions are performed. This is the *sequential-source* method. More precisely, one needs to compute moving-NRQCD propagators from the following source at the time slice z_0,

$$e^{i\mathbf{k}\cdot\mathbf{z}}\,\overline{S}(\Lambda)\,\hat{\gamma}_5\,\Omega(z)\,G_{\chi_{q'}}(z,x), \tag{8.75}$$

evolving them to the sink time-slice y_0. In contrast, both light-quark propagators are computed from the same point source at x.

For smeared three-point functions, I insert the operator (7.10) in the source (8.75), to the left of $\Omega(z)\,G_{\chi_{q'}}(z,x)$.

With the method described here, the point-source three-point functions for arbitrary current operators $\mathscr{J}$, arbitrary polarisations (which enter as $F(x)$) and arbitrary final-state momenta $\mathbf{p}'$ can be obtained with little computational cost, since no new propagators need to be computed when changing any of these.

The situation is somewhat different for the random-wall three-point functions. To obtain these, we now define the sequential-source heavy-quark random-wall propagator:

$$\widetilde{G}^p_H(y,z_0,x_0,\mathbf{k},\mathbf{p}') = \sum_{\mathbf{z}} \begin{pmatrix} G_{\psi_v}(y,z) & 0 \\ 0 & 0 \end{pmatrix} \overline{S}(\Lambda)\,\hat{\gamma}_5\,e^{i\mathbf{k}\cdot\mathbf{z}}\,\Omega(z)\,\widetilde{G}^p_{\chi_{q'}}(z,x_0,-\mathbf{p}'). \tag{8.76}$$

See Fig. 8.24 for a diagram illustrating the method. In (8.76), the spectator-quark random-wall propagator $\widetilde{G}^p_{\chi_{q'}}(z,x_0,-\mathbf{p}')$ is defined as in (8.61).

For a pseudoscalar meson in the final state, the random-wall three-point correlator is then given by

$$\begin{aligned} C_{5JB,\,\mathrm{RW}}(\tau,\,T,\,\mathbf{k},\,\mathbf{p}') \;=\; & \frac{1}{\gamma}\frac{1}{L^3}\frac{1}{n_Z}\sum_{p=1}^{n_Z}\sum_{\mathbf{y}} e^{-i(\mathbf{k}-\mathbf{p}')\cdot\mathbf{y}} \\ & \times \widetilde{G}^p_{\chi_q}(y,x_0,\mathbf{0})^* \cdot \mathrm{tr}\left[\Omega^\dagger(y)\,\hat{\gamma}_5\,\mathscr{J}\,\widetilde{G}^p_H(y,z_0,x_0,\mathbf{k},\mathbf{p}')\right]. \end{aligned} \tag{8.77}$$

In (8.77), the quantity $\widetilde{G}^{p}_{\chi_q}(y, x_0, \mathbf{0})$ is defined as in (8.61) for $\mathbf{p}' = 0$.

Similarly, for a vector meson in the final state, the random-wall three-point correlator is

$$\begin{aligned} C_{jJB,\,\mathrm{RW}}(\tau,\, T,\, \mathbf{k},\, \mathbf{p}') \;&=\; \frac{1}{\gamma}\frac{1}{L^3}\frac{1}{n_Z}\sum_{p=1}^{n_Z}\sum_{\mathbf{y}} e^{-i(\mathbf{k}-\mathbf{p}')\cdot\mathbf{y}} \\ &\quad\times \widetilde{G}^{p}_{\chi_q}(y, x_0, j)^* \cdot \mathrm{tr}\left[\hat{\gamma}^j\,\hat{\gamma}_5\,\Omega^\dagger(y)\,\hat{\gamma}_5\,\not{\mathscr{J}}\,\widetilde{G}^{p}_{H}(y, z_0, x_0, \mathbf{k}, \mathbf{p}')\right], \end{aligned} \tag{8.78}$$

where the quantity $\widetilde{G}^{p}_{\chi_q}(y, x_0, j)$ is defined as in (8.65).

For smeared three-point functions, I insert the operator (7.10) in the equation for the sequential-source heavy-quark propagator (8.76), to the left of $\Omega(z)\,\widetilde{G}^{p}_{\chi_{q'}}(z, x_0, -\mathbf{p}')$. As can be seen from Eqs. (8.77) and (8.78), with the random-wall method, the number of heavy-quark propagators required is proportional to $(\#\mathbf{k}) \times (\#\mathbf{p}')$. The number of light-quark propagators required is proportional to $(\#\mathbf{p}')+(\#j)$. Here, "#" stands for "number different values used".

Simultaneous fitting of two-point and three-point functions

I fit the three-point correlators with functions of the form

$$\begin{aligned} C_{FJB}(\tau,\, T,\, \mathbf{k},\, \mathbf{p}') \;=\;& \sum_{n'=0}^{n^{(F)}_{\mathrm{exp}}-1}\sum_{n=0}^{n^{(B)}_{\mathrm{exp}}-1} A^{(ee)}_{n'\,n}\, e^{-E^{(F)}_{n'}\tau}\, e^{-E^{(B)}_{n}(T-\tau)} \\ &+ (-1)^{\tau} \sum_{n'=0}^{\widetilde{n}^{(F)}_{\mathrm{exp}}-1}\sum_{n=0}^{n^{(B)}_{\mathrm{exp}}-1} A^{(oe)}_{n'\,n}\, e^{-\widetilde{E}^{(F)}_{n'}\tau}\, e^{-E^{(B)}_{n}(T-\tau)} \\ &+ (-1)^{T-\tau} \sum_{n'=0}^{n^{(F)}_{\mathrm{exp}}-1}\sum_{n=0}^{\widetilde{n}^{(B)}_{\mathrm{exp}}-1} A^{(eo)}_{n'\,n}\, e^{-E^{(F)}_{n'}\tau}\, e^{-\widetilde{E}^{(B)}_{n}(T-\tau)} \\ &+ (-1)^{T} \sum_{n'=0}^{\widetilde{n}^{(F)}_{\mathrm{exp}}-1}\sum_{n=0}^{\widetilde{n}^{(B)}_{\mathrm{exp}}-1} A^{(oo)}_{n'\,n}\, e^{-\widetilde{E}^{(F)}_{n'}\tau}\, e^{-\widetilde{E}^{(B)}_{n}(T-\tau)}, \end{aligned} \tag{8.79}$$

again using the logarithms of the energy splittings and the relative amplitudes as the fit parameters for the excited states. In (8.79), the labels "e" and "o" on the amplitude parameters stand for "even" and "odd", respectively.

I find that the results for the form factors are most accurate when the $B(\mathbf{k}, \mathbf{v}) \to F(\mathbf{p}')$ three-point functions are fitted simultaneously with $B(\mathbf{k}, \mathbf{v})$ and $F(\mathbf{p}')$ two-point functions, sharing the energy parameters $E^{(B)}_n$, $\widetilde{E}^{(B)}_n$, $E^{(F)}_{n'}$, and $\widetilde{E}^{(F)}_{n'}$.

Furthermore, I include additional three-point functions to improve the fit as follows:

- For $B(\mathbf{k},\mathbf{v}) \to K(\mathbf{p}')$ at non-zero $\mathbf{p}'$, I also include the three-point function $B(\mathbf{k},\mathbf{v}) \to K(\mathbf{0})$ in the fit, sharing the energy parameters $E_n^{(B)}$ and $\widetilde{E}_n^{(B)}$.
- For $B(\mathbf{k},\mathbf{v}) \to K^*(\mathbf{p}')$ at any $\mathbf{p}'$, I also include the three-point function $B(\mathbf{k},\mathbf{v}) \to K(\mathbf{0})$ in the fit, sharing the energy parameters $E_n^{(B)}$ and $\widetilde{E}_n^{(B)}$.

In both cases, the $B(\mathbf{k},\mathbf{v}) \to K(\mathbf{0})$ three-point function has a much better signal and strongly constrains the B-meson energy and amplitude in the simultaneous fit. As demonstrated in the next section, the results for E_B and A_B are up to about 5 times more accurate compared to equivalent fits of the B-meson two-point function alone.

Numerical results: $B \to K$ three-point functions

So far, I have only analysed the three-point functions without smearing.

Comparisons (RWcd source vs point source) of the relative errors in the $B \to K$ three-point functions with the operator $\mathscr{J} = \hat{\gamma}^0 S^+(\Lambda)$ are shown in Fig. 8.25 (for $\mathbf{v} = 0$, $\mathbf{k} = 0, \mathbf{p}' = 0$) and Fig. 8.26 (for $\mathbf{v} = (0.4, 0, 0)$, $\mathbf{k} = 0, \mathbf{p}' = 2\pi/L \cdot (-1, 0, 0)$). In both figures, the three-point functions are evaluated at $T = 12$. The improvement from the RWcd source is found to decrease with increasing momentum transfer; it is also found to decrease when increasing T.

For the $B \to K$ three-point functions, I performed unconstrained fits including a wide range of T, setting $n_{\text{exp}}^{(B)} = \widetilde{n}_{\text{exp}}^{(B)} = n_{\text{exp}}^{(K)} = 1$ and $\widetilde{n}_{\text{exp}}^{(K)} = 0$ (for $\mathbf{p}' = 0$) or $\widetilde{n}_{\text{exp}}^{(K)} = 1$ (for $\mathbf{p}' \neq 0$). The fitting ranges for τ are chosen such that contaminations from excited states are negligible.

In Fig. 8.27 I show a fit of the $B \to K$ three-point function with $\mathscr{J} = \hat{\gamma}^0 S^+(\Lambda)$ at zero recoil, i.e. $\mathbf{v} = 0$, $\mathbf{k} = 0, \mathbf{p}' = 0$. This is the case with the best signal-to-noise ratio. The fit was performed simultaneously with the K-meson two-point function and the (2×1)-matrix B-meson two-point function. I chose the following fitting ranges: $T = 18 \,...\, 26$ and $\tau = 6 \,...\, (T - 12)$ in the three-point function; $\tau = 12 \,...32$ in the B-meson two-point function and $\tau = 10 \,...\, 54$ in the K-meson two-point function. To confirm that for these fitting ranges the contaminations from excited states are negligible, I varied the values for $\tau_{\text{min}}^{(B\,2\text{pt})}$, $\tau_{\text{min}}^{(K\,2\text{pt})}$, $\tau_{\text{min}}^{(B\,3\text{pt})}$ and $\tau_{\text{min}}^{(K\,3\text{pt})}$ in the fit. The latter two specify the range of τ in the three-point function, which is

$$\tau = \tau_{\text{min}}^{(K\,3\text{pt})} \,...\, \left[T - \tau_{\text{min}}^{(B\,3\text{pt})}\right]. \tag{8.80}$$

The fit results for the non-oscillating states are shown in Table 8.18 (for the point-source data) and Table 8.19 (for the RWcd-source data).

Note in particular that the results for the B-meson energy and amplitude with the simultaneous fits are about 5 times more accurate than the results from fits to the B meson two-point function alone (with the same τ_{min}). The results from unconstrained fits to the two-point functions with $\tau_{\text{min}} = 12$ (see Table 8.12) are

$$\begin{aligned} &\text{point source}: \quad E_B = 0.528(10),\ A_B = 0.193(13), \\ &\text{RWcd source}: \quad E_B = 0.517(10),\ A_B = 0.183(12). \end{aligned} \tag{8.81}$$

When the fit is performed simultaneously with the $B \to K$ three-point function at zero recoil (also setting $\tau_{\text{min}}^{(B\,3\text{pt})} = 12$) and the K-meson two-point function, the results are

$$\begin{aligned} &\text{point source}: \quad E_B = 0.5177(27),\ A_B = 0.1822(35), \\ &\text{RWcd source}: \quad E_B = 0.5158(19),\ A_B = 0.1803(26). \end{aligned} \tag{8.82}$$

The results for the three-point amplitude are

$$\begin{aligned} &\text{point source}: \quad A_{KJB} = 0.0747(24), \\ &\text{RWcd source}: \quad A_{KJB} = 0.0761(17). \end{aligned} \tag{8.83}$$

The improvement factor in the statistical error of A_{KJB} (RWcd source compared to point source) is about 1.4. The findings for the other operators $\mathscr{J}$ are similar.

Figure 8.28 shows a fit of the $B \to K$ three-point function with $\mathscr{J} = \hat{\gamma}^0 S^+(\Lambda)$ at $\mathbf{v} = (0.4, 0, 0)$, $\mathbf{k} = 0, \mathbf{p}' = 2\pi/L \cdot (-1, 0, 0)$. This corresponds to the lowest value in q^2 (the highest recoil) considered here. As can be seen in the plot, the signal-to noise ratio is much smaller than at zero recoil. The fit shown here is simultaneous with the $B \to K$ three-point function at $\mathbf{v} = (0.4, 0, 0)$, $\mathbf{k} = 0, \mathbf{p}' = 0$, the K meson two-point functions at both $\mathbf{p}' = 2\pi/L \cdot (-1, 0, 0)$ and $\mathbf{p}' = 2\pi/L \cdot (0, 0, 0)$, as well as the (2×1)-matrix two-point function for the B meson at $\mathbf{v} = (0.4, 0, 0)$, $\mathbf{k} = 0$. The fitting ranges are $\tau_{\text{min}}^{(B\,2\text{pt})} = \tau_{\text{min}}^{(B\,3\text{pt})} = 10$, $\tau_{\text{min}}^{(K\,2\text{pt})} = 10$, $\tau_{\text{min}}^{(K\,3\text{pt})} = 6$.

The fit results for several fitting ranges are shown in Table 8.20 (for the point-source data) and Table 8.21 (for the RWcd-source data). As can be seen in the tables, the results are not as stable under changes of the fitting ranges as at zero recoil, and the results for the three-point amplitudes from the point- and RWcd sources with the same fitting ranges do not quite agree. It is planned for the future to perform Bayesian fits, which might be more stable.

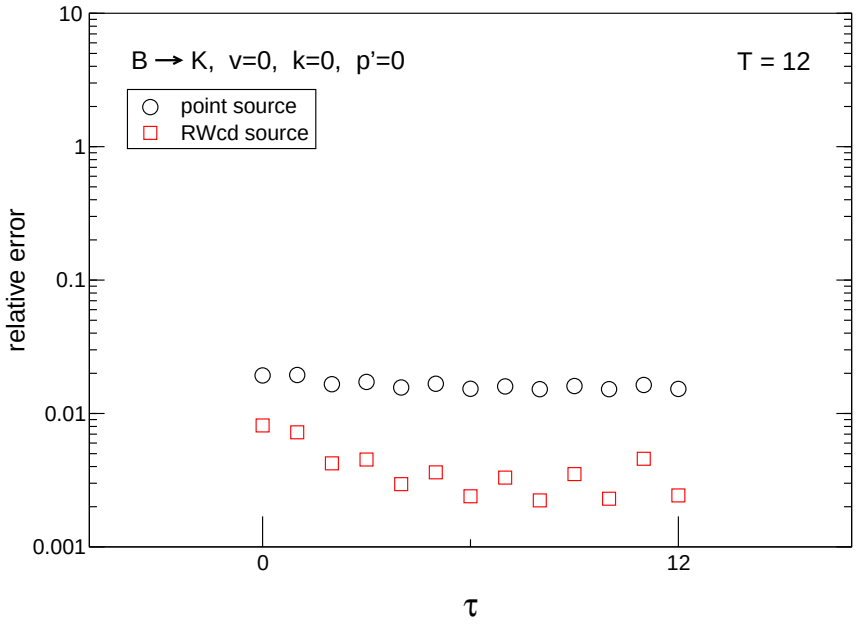

Figure 8.25: Relative errors in the $B \to K$ three-point function with $\mathscr{J} = \hat{\gamma}^0 S^+(\Lambda)$ at $\mathbf{v} = 0$, $\mathbf{k} = 0, \mathbf{p}' = 0$.

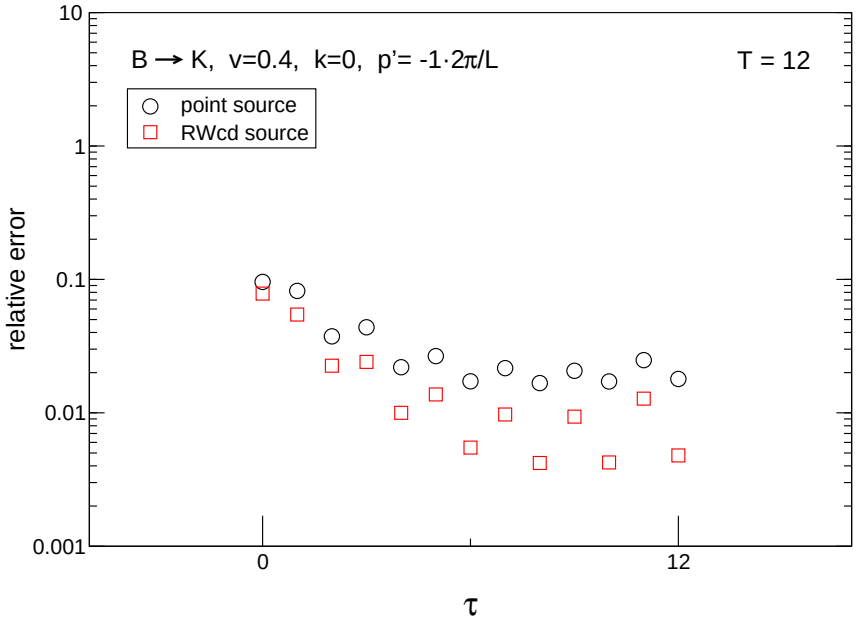

Figure 8.26: Relative errors in the $B \to K$ three-point function with $\mathscr{J} = \hat{\gamma}^0 S^+(\Lambda)$ at $\mathbf{v} = (0.4, 0, 0)$, $\mathbf{k} = 0, \mathbf{p}' = 2\pi/L \cdot (-1, 0, 0)$.

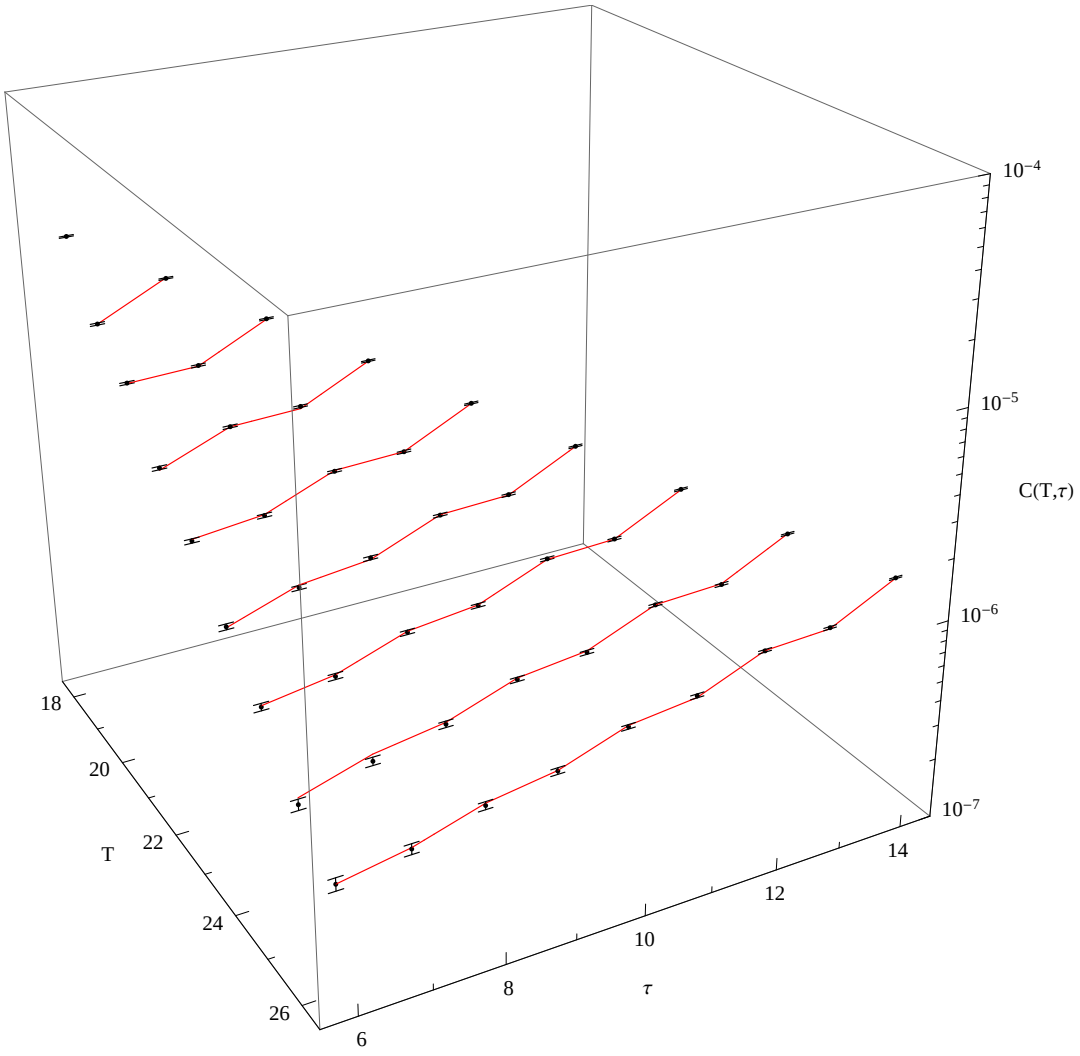

Figure 8.27: Unconstrained fit of the $B \to K$ three-point function with $\mathscr{J} = \hat{\gamma}^0 S^+(\Lambda)$ at $\mathbf{v} = 0$, $\mathbf{k} = 0, \mathbf{p}' = 0$. The numbers of exponentials are $n_{\rm exp}^{(B)} = \widetilde{n}_{\rm exp}^{(B)} = n_{\rm exp}^{(K)} = 1$, $\widetilde{n}_{\rm exp}^{(K)} = 0$. The fitting range is $T = 18 \ldots 26$ and $\tau = 6 \ldots (T - 12)$. The fit is simultaneous with the B and K two-point functions. The data shown are from the RWcd source. The fit has $\chi^2/\text{d.o.f.} = 0.92$.

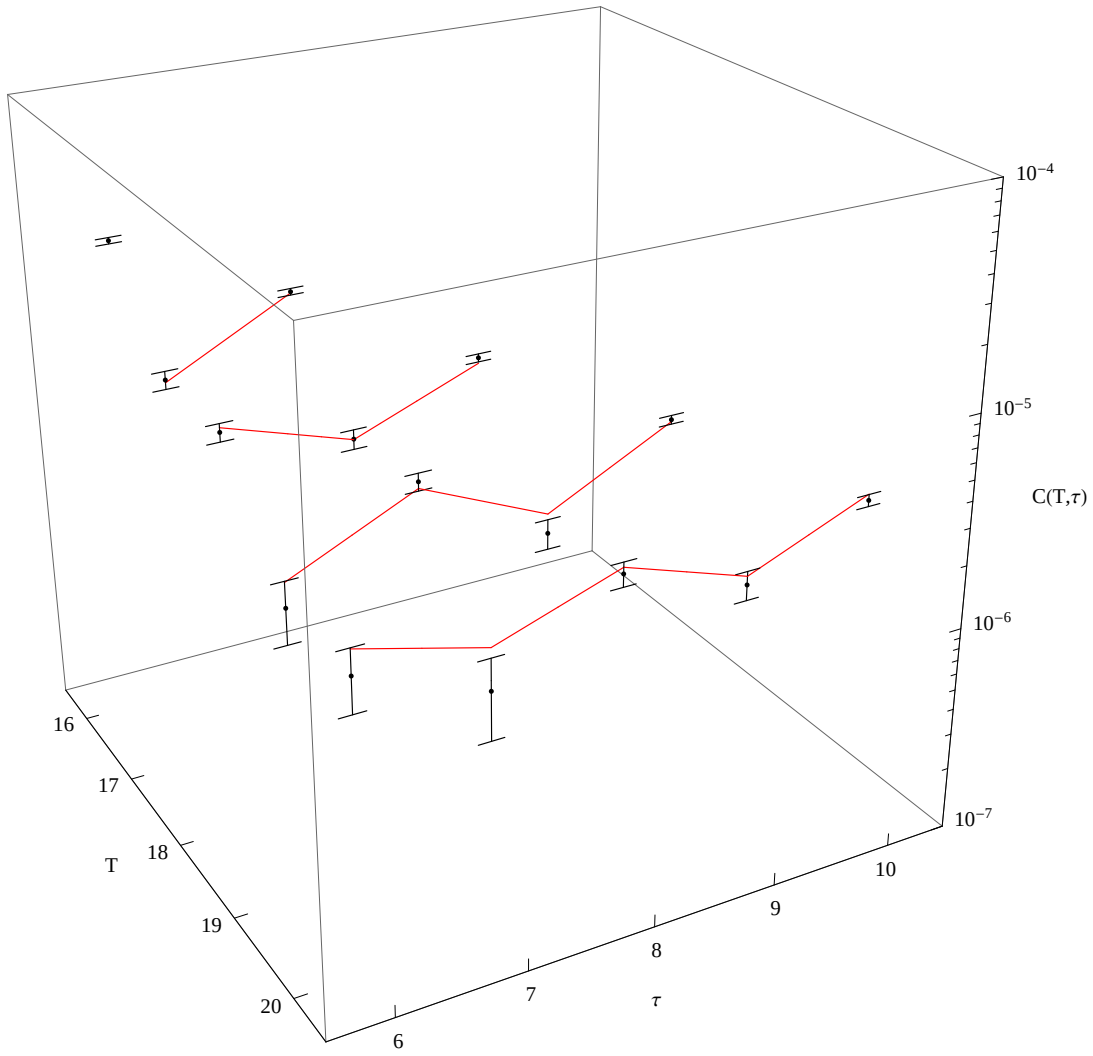

Figure 8.28: Unconstrained fit of the $B \to K$ three-point function with $\mathscr{J} = \hat{\gamma}^0 S^+(\Lambda)$ at $\mathbf{v} = (0.4, 0, 0)$, $\mathbf{k} = 0, \mathbf{p}' = 2\pi/L \cdot (-1, 0, 0)$. The numbers of exponentials are $n_{\text{exp}}^{(B)} = \widetilde{n}_{\text{exp}}^{(B)} = n_{\text{exp}}^{(K)} = \widetilde{n}_{\text{exp}}^{(K)} = 1$. The fitting range is $T = 16 \ldots 20$ and $\tau = 6 \ldots (T - 10)$. The fit is simultaneous with the B and K two-point functions and with the $B \to K$ three-point function at $\mathbf{p}' = 0$. The data shown are from the RWcd source. The fit has $\chi^2/\text{d.o.f.} = 1.04$.

$\tau_{\rm min}^{(B\ 2{\rm pt})}$	$\tau_{\rm min}^{(B\ 3{\rm pt})}$	$\tau_{\rm min}^{(K\ 2{\rm pt})}$	$\tau_{\rm min}^{(K\ 3{\rm pt})}$	A_{KJB}	E_K	A_K	E_B	A_B	χ^2/d.o.f.
12	12	10	10	0.0747(37)	0.33926(24)	0.2739(18)	0.5164(40)	0.1807(47)	0.88
12	12	10	8	0.0754(28)	0.33930(24)	0.2726(18)	0.5181(31)	0.1828(39)	1.00
12	12	10	6	0.0747(24)	0.33935(24)	0.2723(17)	0.5177(27)	0.1822(35)	0.94
12	12	10	4	0.0747(22)	0.33945(23)	0.2719(17)	0.5180(24)	0.1824(32)	0.97
12	12	10	2	0.0734(20)	0.33956(22)	0.2716(16)	0.5165(22)	0.1807(29)	0.95
12	12	10	10	0.0747(37)	0.33926(24)	0.2739(18)	0.5164(40)	0.1807(47)	0.88
12	12	9	9	0.0725(31)	0.33927(23)	0.2737(18)	0.5141(35)	0.1785(42)	0.85
12	12	8	8	0.0755(28)	0.33938(23)	0.2726(17)	0.5184(31)	0.1836(39)	1.03
12	12	7	7	0.0750(25)	0.33961(22)	0.2732(17)	0.5177(28)	0.1839(36)	1.22
12	12	10	6	0.0747(24)	0.33935(24)	0.2723(17)	0.5177(27)	0.1822(35)	0.94
11	11	10	6	0.0720(16)	0.33942(23)	0.2721(17)	0.5146(19)	0.1797(24)	1.00
10	10	10	6	0.0709(12)	0.33952(23)	0.2710(17)	0.5140(14)	0.1787(18)	1.06
12	12	10	6	0.0747(24)	0.33935(24)	0.2723(17)	0.5177(27)	0.1822(35)	0.94
12	11	10	6	0.0720(16)	0.33940(23)	0.2723(17)	0.5145(19)	0.1784(28)	0.96
12	10	10	6	0.0711(13)	0.33951(23)	0.2711(17)	0.5141(14)	0.1778(23)	1.04
12	12	10	6	0.0747(24)	0.33935(24)	0.2723(17)	0.5177(27)	0.1822(35)	0.94
11	12	10	6	0.0747(24)	0.33937(24)	0.2722(17)	0.5178(27)	0.1834(32)	0.98
10	12	10	6	0.0740(23)	0.33935(24)	0.2722(17)	0.5170(25)	0.1817(27)	0.98
9	12	10	6	0.0747(23)	0.33936(24)	0.2721(17)	0.5181(25)	0.1847(25)	1.04
8	12	10	6	0.0793(20)	0.33942(23)	0.2722(17)	0.5233(21)	0.1912(18)	1.14

Table 8.18: Results from unconstrained simultaneous fits of the $B \to K$ three-point function with $\mathscr{J} = \hat{\gamma}^0 S^+(\Lambda)$ at $\mathbf{v} = 0$, $\mathbf{k} = 0, \mathbf{p}' = 0$. Data from point source. $n_{\rm exp}^{(B)} = \widetilde{n}_{\rm exp}^{(B)} = n_{\rm exp}^{(K)} = 1$, $\widetilde{n}_{\rm exp}^{(K)} = 0$. Central values and errors directly from fit.

$\tau_{\text{min}}^{(B\,2\text{pt})}$	$\tau_{\text{min}}^{(B\,3\text{pt})}$	$\tau_{\text{min}}^{(K\,2\text{pt})}$	$\tau_{\text{min}}^{(K\,3\text{pt})}$	A_{KJB}	E_K	A_K	E_B	A_B	χ^2/d.o.f.
12	12	10	10	0.0764(28)	0.33922(17)	0.27701(41)	0.5163(31)	0.1808(37)	0.96
12	12	10	8	0.0764(21)	0.33919(17)	0.27695(40)	0.5161(23)	0.1806(29)	0.94
12	12	10	6	0.0761(17)	0.33921(17)	0.27698(40)	0.5158(19)	0.1803(26)	0.92
12	12	10	4	0.0756(14)	0.33922(17)	0.27693(40)	0.5151(17)	0.1790(23)	0.99
12	12	10	2	0.0750(13)	0.33923(17)	0.27697(39)	0.5141(15)	0.1774(21)	1.18
12	12	10	10	0.0764(28)	0.33922(17)	0.27701(41)	0.5163(31)	0.1808(37)	0.96
12	12	9	9	0.0769(24)	0.33930(16)	0.27728(38)	0.5167(26)	0.1814(32)	0.93
12	12	8	8	0.0772(21)	0.33941(16)	0.27772(35)	0.5168(23)	0.1813(29)	1.09
12	12	7	7	0.0772(19)	0.33972(15)	0.27863(33)	0.5165(21)	0.1813(27)	1.49
12	12	10	6	0.0761(17)	0.33921(17)	0.27698(40)	0.5158(19)	0.1803(26)	0.92
11	11	10	6	0.0752(11)	0.33920(17)	0.27700(40)	0.5149(14)	0.1799(17)	0.92
10	10	10	6	0.07328(71)	0.33917(17)	0.27697(39)	0.5126(10)	0.1783(12)	1.07
12	12	10	6	0.0761(17)	0.33921(17)	0.27698(40)	0.5158(19)	0.1803(26)	0.92
12	11	10	6	0.0751(11)	0.33920(17)	0.27700(40)	0.5147(14)	0.1791(21)	0.93
12	10	10	6	0.07307(72)	0.33917(17)	0.27695(39)	0.5123(10)	0.1761(17)	1.07
12	12	10	6	0.0761(17)	0.33921(17)	0.27698(40)	0.5158(19)	0.1803(26)	0.92
11	12	10	6	0.0763(17)	0.33921(17)	0.27698(40)	0.5161(19)	0.1812(22)	0.91
10	12	10	6	0.0764(16)	0.33920(17)	0.27698(40)	0.5161(18)	0.1818(18)	0.92
9	12	10	6	0.0771(16)	0.33917(17)	0.27683(40)	0.5171(18)	0.1852(17)	1.24
8	12	10	6	0.0786(14)	0.33918(17)	0.27686(40)	0.5188(15)	0.1874(13)	1.25

Table 8.19: Results from unconstrained simultaneous fits of the $B \to K$ three-point function with $\mathscr{J} = \hat{\gamma}^0 S^+(\Lambda)$ at $\mathbf{v} = 0$, $\mathbf{k} = 0, \mathbf{p}' = 0$. Data from RWcd source. $n_{\text{exp}}^{(B)} = \widetilde{n}_{\text{exp}}^{(B)} = n_{\text{exp}}^{(K)} = 1$, $\widetilde{n}_{\text{exp}}^{(K)} = 0$. Central values and errors directly from fit.

$\tau_{\min}^{(B\,2\text{pt})}$	$\tau_{\min}^{(B\,3\text{pt})}$	$\tau_{\min}^{(K\,2\text{pt})}$	$\tau_{\min}^{(K\,3\text{pt})}$	A_{KJB}	E_K	A_K	E_B	A_B	χ^2/d.o.f.
10	10	10	6	0.0280(34)	0.4607(16)	0.2279(24)	0.466(11)	0.169(10)	1.16
10	10	10	5	0.0292(30)	0.4599(16)	0.2272(23)	0.4713(95)	0.1741(94)	1.14
10	10	10	4	0.0317(27)	0.4597(16)	0.2261(23)	0.4775(82)	0.1767(86)	1.21
11	11	10	6	0.0303(78)	0.4602(16)	0.2279(24)	0.470(21)	0.181(22)	1.07
10	10	10	6	0.0280(34)	0.4607(16)	0.2279(24)	0.466(11)	0.169(10)	1.16
9	9	10	6	0.0339(21)	0.4604(16)	0.2277(24)	0.4778(63)	0.1794(59)	1.18
10	11	10	6	0.0310(81)	0.4603(16)	0.2280(24)	0.472(21)	0.175(21)	1.08
10	10	10	6	0.0280(34)	0.4607(16)	0.2279(24)	0.466(11)	0.169(10)	1.16
10	9	10	6	0.0328(21)	0.4606(16)	0.2278(24)	0.4745(65)	0.1758(76)	1.16
11	10	10	6	0.0321(42)	0.4605(16)	0.2277(24)	0.479(12)	0.190(15)	1.18
10	10	10	6	0.0280(34)	0.4607(16)	0.2279(24)	0.466(11)	0.169(10)	1.16
9	10	10	6	0.0281(35)	0.4605(16)	0.2278(24)	0.467(11)	0.1693(99)	1.17

Table 8.20: Results from unconstrained simultaneous fits of the $B \to K$ three-point function with $\mathscr{J} = \hat{\gamma}^0 S^+(\Lambda)$ at $\mathbf{v} = (0.4, 0, 0)$, $\mathbf{k} = 0, \mathbf{p}' = 2\pi/L \cdot (-1, 0, 0)$. Data from point source. $n_{\text{exp}}^{(B)} = \widetilde{n}_{\text{exp}}^{(B)} = n_{\text{exp}}^{(K)} = \widetilde{n}_{\text{exp}}^{(K)} = 1$. Central values and errors directly from fit.

$\tau_{\text{min}}^{(B\,2\text{pt})}$	$\tau_{\text{min}}^{(B\,3\text{pt})}$	$\tau_{\text{min}}^{(K\,2\text{pt})}$	$\tau_{\text{min}}^{(K\,3\text{pt})}$	A_{KJB}	E_K	A_K	E_B	A_B	χ^2/d.o.f.
10	10	10	6	0.0395(36)	0.46280(79)	0.2395(10)	0.4849(84)	0.1799(82)	1.09
10	10	10	5	0.0402(31)	0.46289(79)	0.2396(10)	0.4856(72)	0.1807(73)	1.07
10	10	10	4	0.0387(26)	0.46291(78)	0.2397(10)	0.4807(63)	0.1768(65)	1.11
11	11	10	6	0.050(11)	0.46280(79)	0.2395(10)	0.503(18)	0.211(23)	1.06
10	10	10	6	0.0395(36)	0.46280(79)	0.2395(10)	0.4849(84)	0.1799(82)	1.09
9	9	10	6	0.0384(18)	0.46270(79)	0.2393(10)	0.4783(45)	0.1832(42)	1.13
10	11	10	6	0.050(11)	0.46278(79)	0.2395(10)	0.503(18)	0.210(21)	1.05
10	10	10	6	0.0395(36)	0.46280(79)	0.2395(10)	0.4849(84)	0.1799(82)	1.09
10	9	10	6	0.0371(18)	0.46276(79)	0.2395(10)	0.4750(46)	0.1720(53)	1.09
11	10	10	6	0.0394(38)	0.46281(79)	0.2395(10)	0.4845(89)	0.181(11)	1.10
10	10	10	6	0.0395(36)	0.46280(79)	0.2395(10)	0.4849(84)	0.1799(82)	1.09
9	10	10	6	0.0395(36)	0.46273(79)	0.2394(10)	0.4853(84)	0.1898(80)	1.15

Table 8.21: Results from unconstrained simultaneous fits of the $B \to K$ three-point function with $\mathscr{J} = \hat{\gamma}^0 S^+(\Lambda)$ at $\mathbf{v} = (0.4, 0, 0)$, $\mathbf{k} = 0, \mathbf{p}' = 2\pi/L \cdot (-1, 0, 0)$. Data from RWcd source. $n_{\text{exp}}^{(B)} = \widetilde{n}_{\text{exp}}^{(B)} = n_{\text{exp}}^{(K)} = \widetilde{n}_{\text{exp}}^{(K)} = 1$. Central values and errors directly from fit.

Numerical results: $B \to K^*$ three-point functions

The relative errors in the $B \to K^*$ three-point functions with $\mathscr{J} = \sigma_{0j}\hat{\gamma}_5 S^+(\Lambda)$ from the RWcd and point sources are shown in Fig. 8.29 (at zero recoil) and Fig. 8.30 (at $\mathbf{v} = (0.4, 0, 0)$, $\mathbf{k} = 0, \mathbf{p}' = 2\pi/L \cdot (-1, 0, 0)$). The improvement from the RWcd source is small (and gets even smaller at larger T), despite the higher computational cost.

Here I performed simultaneous Bayesian fits with the range $\tau = 1 \,...\, (T-2)$ and $T = 14 \,...\, 16$ or $T = 15 \,...\, 16$ in the the $B \to K^*$ three-point functions, $\tau = 2 \,...\, 32$ in the B-meson (2×1)-matrix two-point function and $\tau = 1 \,...\, 63$ in the K^* two-point function. For all these correlators I used the same number of exponentials, $n_{\text{exp}}^{(B)} = \widetilde{n}_{\text{exp}}^{(B)} = n_{\text{exp}}^{(K^*)} = \widetilde{n}_{\text{exp}}^{(K^*)} = n_{\text{exp}}$, varying n_{exp} in the range $4 \,...\, 10$. I set the priors for the logarithms of the energy splittings to (-1) with a width of 1, and the priors for the relative excited-state amplitudes to 1 with a width of 2 (for the K^*) and 0.5 with a width of 2 (for the B two-point function and for the $B \to K^*$ three-point function).

As already mentioned in Sec. 8.8.3, I also included the $B \to K$ three-point function (with $\mathscr{J} = \hat{\gamma}^0 S^+(\Lambda)$) and the K two-point function for $\mathbf{p}' = 0$ in the fit in order to improve the results for the B meson. For these correlators I used $n_{\text{exp}}^{(B)} = \widetilde{n}_{\text{exp}}^{(B)} = n_{\text{exp}}^{(K)} = 1$, $\widetilde{n}_{\text{exp}}^{(K)} = 0$ and the same fitting ranges as given in Sec. 8.8.3, so that the contamination from excited states is negligible.

A plot of a fit to the $B \to K^*$ three-point function with $\mathscr{J} = \sigma_{j0}\hat{\gamma}_5 S^+(\Lambda)$ at $\mathbf{v} = 0$, $\mathbf{k} = 0, \mathbf{p}' = 0$ is shown in Fig. 8.31. Fit results are given in Table 8.22 (point source data) and Table 8.23 (RWcd source data). For the point source, I used $T = 14 \,...\, 16$. For the RWcd source, the range $T = 15 \,...\, 16$ gave more reliable fits.

As can be seen in the tables, the errors in A_{K^*JB} are comparable for the RWcd and point source data, while the RWcd source gives more precise results for E_{K^*} and A_{K^*}, compared to the fits of the K^* two-point function alone (cf. Sec. 8.8.1).

The findings for non-zero $\mathbf{p}'$ and for the other operators $\mathscr{J}$ are similar.

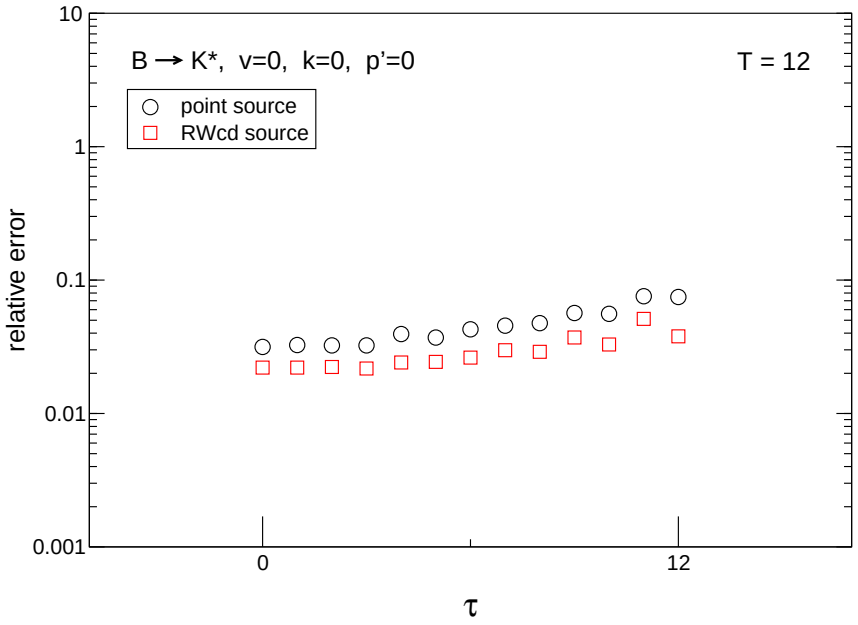

Figure 8.29: Relative errors in the $B \to K^*$ three-point function with $\mathscr{J} = \sigma_{0j}\hat{\gamma}_5 S^+(\Lambda)$ at $\mathbf{v} = 0$, $\mathbf{k} = 0, \mathbf{p}' = 0$.

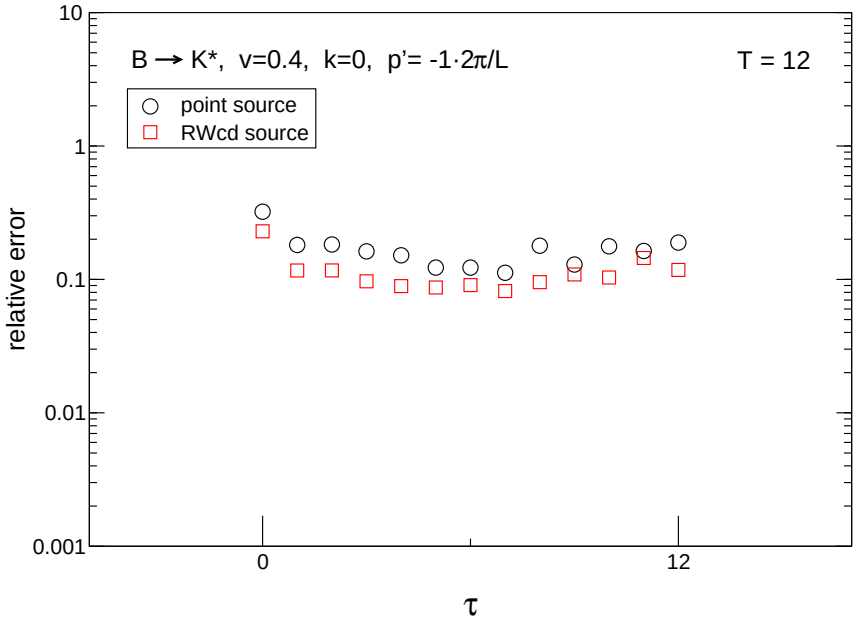

Figure 8.30: Relative errors in the $B \to K^*$ three-point function with $\mathscr{J} = \sigma_{0j}\hat{\gamma}_5 S^+(\Lambda)$ at $\mathbf{v} = (0.4, 0, 0)$, $\mathbf{k} = 0, \mathbf{p}' = 2\pi/L \cdot (-1, 0, 0)$.

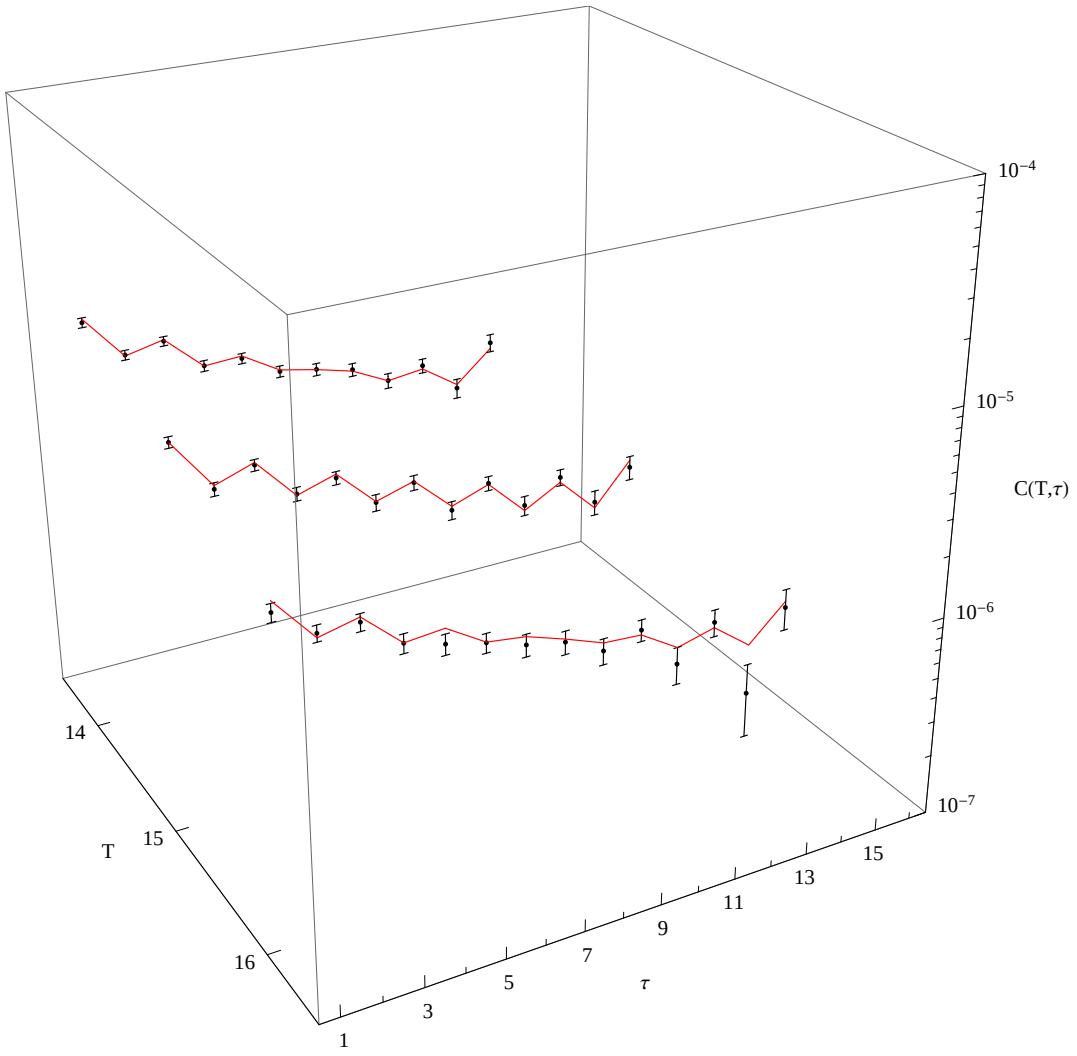

Figure 8.31: Bayesian fit of the $B \to K^*$ three-point function with $\mathscr{J} = \sigma_{j0}\hat{\gamma}_5 S^+(\Lambda)$ at $\mathbf{v} = 0$, $\mathbf{k} = 0, \mathbf{p}' = 0$. The fitting range is $T = 14 \ldots 16$ and $\tau = 1 \ldots (T-2)$. The numbers of exponentials are $n_{\text{exp}}^{(B)} = \widetilde{n}_{\text{exp}}^{(B)} = n_{\text{exp}}^{(K^*)} = \widetilde{n}_{\text{exp}}^{(K^*)} = 8$. The fit is simultaneous with the B and K^* two-point functions and with the $B \to K$ three-point function and K two-point function. The data shown are from the point source.

n_{exp}	A_{K^*JB}	E_{K^*}	A_{K^*}	E_B	A_B
4	0.01261(88)	0.6330(58)	0.0906(23)	0.5172(19)	0.1803(15)
5	0.0124(12)	0.6363(91)	0.0915(30)	0.5167(25)	0.1793(25)
6	0.0125(15)	0.6361(87)	0.0915(38)	0.5168(22)	0.1791(27)
7	0.0123(12)	0.6360(72)	0.0914(31)	0.5166(26)	0.1789(31)
8	0.0127(14)	0.6363(74)	0.0916(33)	0.5167(22)	0.1792(30)
9	0.0124(14)	0.6355(76)	0.0915(36)	0.5165(27)	0.1793(35)
10	0.0120(16)	0.6348(91)	0.0906(39)	0.5167(17)	0.1794(23)

Table 8.22: Results from simultaneous Bayesian fits of the $B \to K^*$ three-point function with $\mathscr{J} = \sigma_{j0}\hat{\gamma}_5 S^+(\Lambda)$ at $\mathbf{v} = 0$, $\mathbf{k} = 0, \mathbf{p}' = 0$. The fitting range in the $B \to K^*$ three-point function is $T = 14 \,...\, 16$ and $\tau = 1 \,...\, (T-2)$. The numbers of exponentials are $n_{\mathrm{exp}}^{(B)} = \widetilde{n}_{\mathrm{exp}}^{(B)} = n_{\mathrm{exp}}^{(K^*)} = \widetilde{n}_{\mathrm{exp}}^{(K^*)} = n_{\mathrm{exp}}$. Data from point source. Central values and errors from bootstrap.

n_{exp}	A_{K^*JB}	E_{K^*}	A_{K^*}	E_B	A_B
4	0.0164(20)	0.680(33)	0.1067(99)	0.5166(13)	0.18011(65)
5	0.01342(98)	0.6302(64)	0.0908(17)	0.5155(20)	0.1790(26)
6	0.01314(79)	0.6282(51)	0.0902(15)	0.5158(16)	0.1789(23)
7	0.01316(80)	0.6274(47)	0.0898(11)	0.5156(17)	0.1782(27)
8	0.01305(85)	0.6262(44)	0.0895(14)	0.5152(21)	0.1775(30)
9	0.0131(12)	0.6257(49)	0.0894(17)	0.5153(17)	0.1779(29)
10	0.0130(12)	0.6255(40)	0.0893(10)	0.5155(19)	0.1784(24)

Table 8.23: Results from simultaneous Bayesian fits of the $B \to K^*$ three-point function with $\mathscr{J} = \sigma_{j0}\hat{\gamma}_5 S^+(\Lambda)$ at $\mathbf{v} = 0$, $\mathbf{k} = 0, \mathbf{p}' = 0$. The fitting range in the $B \to K^*$ three-point function is $T = 15 \,...\, 16$ and $\tau = 1 \,...\, (T-2)$. The numbers of exponentials are $n_{\mathrm{exp}}^{(B)} = \widetilde{n}_{\mathrm{exp}}^{(B)} = n_{\mathrm{exp}}^{(K^*)} = \widetilde{n}_{\mathrm{exp}}^{(K^*)} = n_{\mathrm{exp}}$. Data from RWcd source. Central values and errors from bootstrap.

$\mathscr{J}$	$A_{KJB}(\Gamma_J = \hat{\gamma}^0)$	$A_{KJB}(\Gamma_J = \hat{\gamma}^1)$	$A_{KJB}(\Gamma_J = \sigma_{10})$
$\Gamma\, S^+(\Lambda)$	0.0280(34)	0.0063(11)	0.0218(25)
$\Gamma\, S^-(\Lambda)$	0.0368(43)	0.0218(25)	0.0065(11)
$\frac{i}{2m_b}\, \hat{\boldsymbol{\gamma}} \cdot \boldsymbol{\Delta}^{(\pm)}\, \Gamma\, S^+(\Lambda)$	−0.00177(26)	0.00177(31)	−0.00148(29)
$-\frac{i}{2m_b}\, \hat{\gamma}^0\, \mathbf{v} \cdot \boldsymbol{\Delta}^{(\pm)}\, \Gamma\, S^+(\Lambda)$	−0.000084(55)	0.000139(59)	0.000189(57)
$\pm\frac{i}{2\gamma m_b}\, \mathbf{v} \cdot \boldsymbol{\Delta}^{(\pm)}\, \Gamma\, S^+(\Lambda)$	0.000143(51)	−0.000168(51)	−0.000123(53)

Table 8.24: Fit results for the $B \to K$ ground-state amplitudes of the individual terms in the heavy-light lattice vector and tensor currents. The boost velocity is $\mathbf{v} = (0.4, 0, 0)$ and the momenta are $\mathbf{k} = 0$, $\mathbf{p}' = 2\pi/L \cdot (-1, 0, 0)$. Data from the point source. Central values and errors directly from fit.

8.9 Size of the $1/m$ corrections

The construction of the heavy-light lattice currents was discussed in Sec. 8.5. Now I give examples for the contributions of the individual terms in the current at $\mathbf{v} = (0.4, 0, 0)$. I consider the pseudoscalar kaon in the final state as the results are more precise compared to the vector-meson.

Fit results for A_{KJB} from the different operators $\mathscr{J}$ are shown in Table 8.24. Results are given for $\Gamma_J = \hat{\gamma}^0$, $\Gamma_J = \hat{\gamma}^1$, and $\Gamma_J = \sigma_{10}$.

It should be noted that the $\mathcal{O}(1/m_b)$ corrections considered here are the unsubtracted operators that mix with the lower-dimension operators. For the vector current in non-moving NRQCD it was found in [11] that the matrix elements of the subtracted operators are significantly smaller.

8.10 Preliminary form factor results

In the following I give some preliminary results for the form factors f_0, f_+, f_T and T_1, T_2 obtained with the fitting methods described in Sec. 8.8. I computed the form factors from the formulae in Sec. 8.4, using bootstrap to take into account the correlations between the different quantities entering the formula. For the hadron masses and energies I also

used the lattice results. I computed the full B-meson energies using the non-perturbative results for the mNRQCD energy shift C_v obtained from the η_b dispersion relation (see Sec. 6.1.3). I set $Z_p = 1$, which is compatible with the result obtained in Sec. 6.1.3. For the lattice spacing I used $a^{-1} = 1.6$ GeV [108]. The values of q^2 given in the tables correspond to the experimental values for the hadron masses.

All form factor results shown in the following include the one-loop radiative corrections to the leading-order heavy-light currents, i.e. the lattice currents are given by (8.55). I used the matching coefficients calculated by Eike Müller [114, 116] and set the value of the strong coupling constant to $\alpha_s = 0.3$, which is approximately equal to $\alpha_V(2/a)$ (cf. Sec. 6.3).

8.10.1 The form factors f_0, f_+, and f_T

The preliminary results for f_0, f_+, and f_T for $B \to K$ are listed in Table 8.25 and plotted against q^2 in Figs. 8.32, 8.33. At $|\mathbf{v}| = 0.4$ I added to the error estimates a systematic uncertainty resulting from the choice of $\tau_{\mathrm{min}}^{(B\,3\mathrm{pt})}$, taken as the shift in the central value of the form factor when $\tau_{\mathrm{min}}^{(B\,3\mathrm{pt})}$ is changed by 1.

At zero recoil I find that the statistical error in f_0 is smaller for the RWcd-source data compared to the point-source data by a factor of about 1.4. At the largest recoil considered here, corresponding to $\mathbf{v} = (0.4, 0, 0)$, $\mathbf{k} = 0, \mathbf{p}' = 2\pi/L \cdot (-1, 0, 0)$, the estimated error for the RWcd-source result is larger than that for the point-source data.

Overall, the central values of the results from the RWcd-source data tend to be above those from the point-source data, sometimes outside the one-standard-deviation interval. As already discussed in Sec. 8.8, the fit results are not very stable and systematic uncertainties may be underestimated. It is planned to perform new Bayesian fits of the $B \to K$ data in the future.

I find that the results for f_T and f_+ are very close to each other. Calculations using light-cone sum-rules [197], albeit applicable only at low q^2, give $f_T > f_+$ and show that the difference between f_T and f_+ vanishes as the mass of the pseudoscalar meson in the final state is taken to zero.

Unquenched lattice QCD results for f_0 and f_+ for $B \to \pi$ can be found in [11] and [168]. For $B \to K$, preliminary results for f_0 and f_+ computed using the Fermilab action for the b quark can be found in [198]. No previous lattice results for f_T are available.

	point source			RWcd source		
q^2 (GeV^2)	f_0	f_+	f_T	f_0	f_+	f_T
22.91	0.869(17)	–	–	0.889(12)	–	–
20.68	0.746(19)	1.951(78)	1.852(82)	0.780(15)	1.980(55)	1.858(61)
18.22	0.617(45)	1.21(12)	1.37(20)	0.715(61)	1.40(19)	1.58(29)

Table 8.25: Preliminary results for the form factors f_0, f_+, f_T for $B \to K$ decays, obtained from simultaneous unconstrained fits. The error estimates are statistical/fitting only.

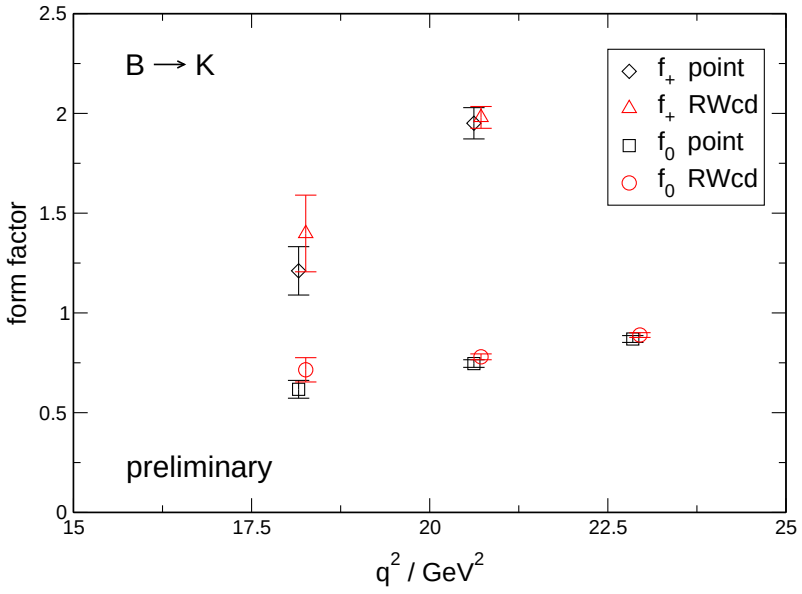

Figure 8.32: Preliminary results for the form factors f_0, f_+ for $B \to K$ decays, obtained from simultaneous unconstrained fits. The left-most points have $\mathbf{v} = (0.4, 0, 0)$, $\mathbf{k} = 0$ and $\mathbf{p}' = 2\pi/L \cdot (-1, 0, 0)$. The error estimates are statistical/fitting only.

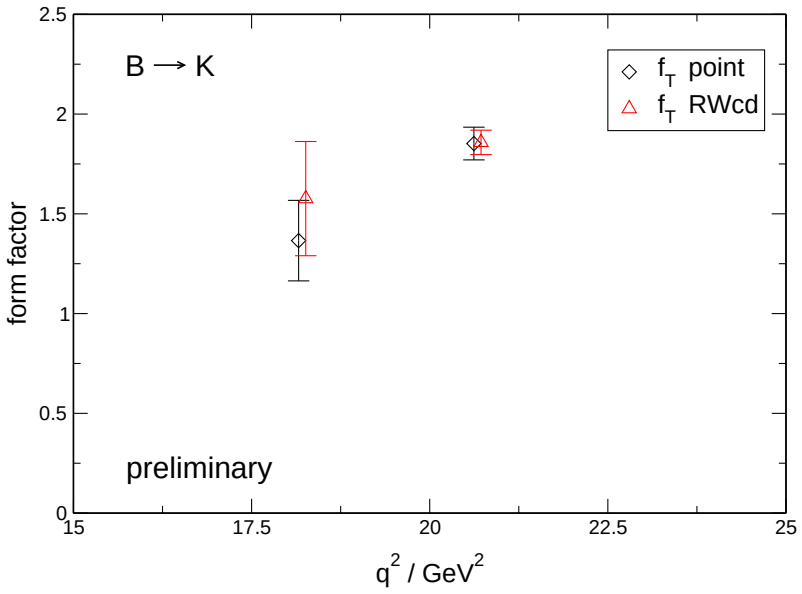

Figure 8.33: Preliminary results for the form factor f_T for $B \to K$ decays, obtained from simultaneous unconstrained fits. The left-most points have $\mathbf{v} = (0.4, 0, 0)$, $\mathbf{k} = 0$ and $\mathbf{p}' = 2\pi/L \cdot (-1, 0, 0)$. The error estimates are statistical/fitting only.

	point source		RWcd source	
q^2 (GeV^2)	T_1	T_2	T_1	T_2
19.25	–	0.285(26)	–	0.305(19)
17.85	0.65(16)	0.246(38)	0.69(12)	0.272(50)

Table 8.26: Preliminary results for the form factors T_1, T_2 for $B \to K^*$ decays, obtained from simultaneous Bayesian fits with with $T = 15, 16$ (RWcd source), $T = 14, 15, 16$ (point source). The error estimates are statistical/fitting only.

Reference	Result
[179]	$T_2(q^2_{\rm max}) = 0.269^{+0.017}_{-0.009} \pm 0.011$
[182]	$T_2(q^2_{\rm max}) = 0.325 \pm 0.033 \pm 0.065$
[183]	$T_2(q^2_{\rm max}) = 0.25 \pm 0.02, \;\; 0.22 \pm 0.02$
[181]	$T_2(q^2_{\rm max}) = 0.25 \pm 0.1$
[184]	$T_2(18.3\ {\rm GeV}^2) = 0.38 \pm 0.05^{+0.00}_{-0.03}$

Table 8.27: Quenched lattice results for T_2 from the literature, obtained by extrapolation in the heavy-quark mass. The two results cited from [183] correspond to two different extrapolation methods. For [184], the result from the finest lattice spacing is shown. See the original works for the meaning of the error estimates.

8.10.2 The form factors T_1 and T_2

Preliminary results for the form factors T_1 and T_2 for $B \to K^*$ are listed in Table 8.26 and are plotted against q^2 in Fig. 8.34. The points with the lower value of q^2 have $\mathbf{v} = 0$, $\mathbf{k} = 0$ and $\mathbf{p}' = 2\pi/L \cdot (-1, 0, 0)$. The data at significantly lower values of q^2 are very noisy and have not yet been analysed.

For $T_2(q^2_{\rm max})$ and T_1 at the lower value of q^2 the errors for the RWcd-source data are smaller by a factor of about 1.3; however, recall that the computational cost for the RWcd method is higher.

For comparison with the literature, Table 8.27 shows results for T_2 at or near $q^2_{\rm max}$ from quenched lattice calculations. All of these calculations were performed with Wilson-like actions for the b quark with unphysically light values for m_b, and were extrapolated in m_b.

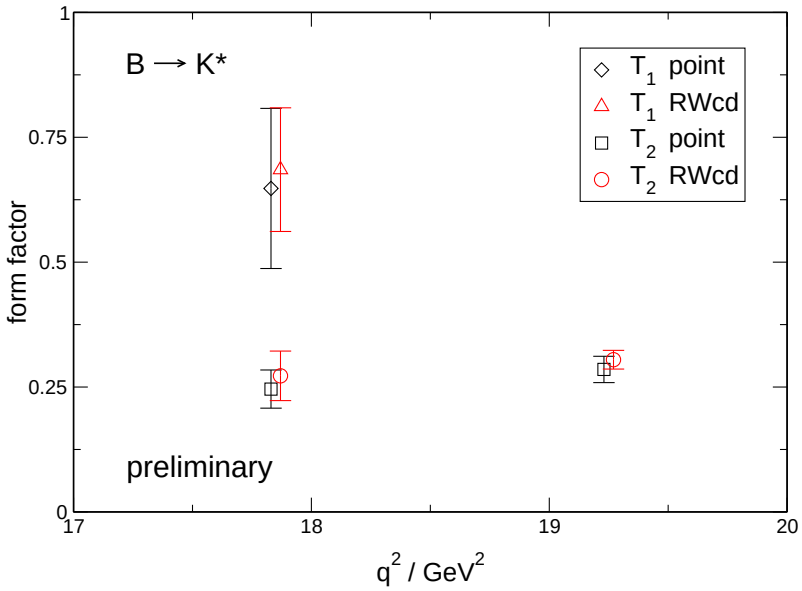

Figure 8.34: Preliminary results for the form factors T_1, T_2 for $B \to K^*$ decays, obtained from simultaneous Bayesian fits with $T = 15, 16$ (RWcd source), $T = 14, 15, 16$ (point source). The left-most points have $\mathbf{v} = 0$, $\mathbf{k} = 0$ and $\mathbf{p}' = 2\pi/L \cdot (-1, 0, 0)$. The error estimates are statistical/fitting only.

Chapter 9

Conclusions

Moving NRQCD is a method for the lattice computation of heavy-to-light form factors. It enables the calculation in a reference frame where the momentum of the light hadron in the final state is reduced, and thereby leads to a reduction of lattice discretisation errors. In this dissertation, I have independently derived an $\mathcal{O}(1/m_b^2, v_{\text{orb.}}^4)$ mNRQCD action in the continuum, and performed nonperturbative tests of a lattice action with the same accuracy for the first time. These tests confirm the reduction of systematic errors compared to non-moving NRQCD (cf. Fig. 6.2). I have then carried out the first calculations of form factors with mNRQCD. The computer programs I have written for this purpose will be used in future large-scale computations. This work will allow further tests of the Standard Model of elementary particles, and will help in searches for new physics.

In the course of this dissertation I have also performed calculations of the heavy-hadron spectrum in lattice QCD with dynamical domain wall fermions, including the spectrum of excited states in bottomonium and the ground-state masses of baryons containing one, two, or three b quarks. Several of these heavy baryons have not yet been observed experimentally but might be discovered in the future at the Tevatron or the Large Hadron Collider.

In the following I shall discuss some open issues and give directions for future work related to the various parts of this dissertation.

9.1 Renormalisation of the lattice mNRQCD action

In Sec. 6.3 I compared my nonperturbative determinations of Z_p (the renormalisation of the external momentum) and C_v (the mNRQCD energy shift) to predictions from one-loop lattice perturbation theory. In both cases I considered the deviations from the tree-level

values. For Z_p good agreement is seen between the perturbative and nonperturbative corrections at moderate boost velocities. However, for C_v the full nonperturbative correction was found to have a sign opposite to the sign of the one-loop correction. Note that this does not impose any practical problems, as the corrections are both small and the nonperturbative results for C_v and Z_p can be used. Assuming that no mistakes were made in either calculation, these findings do however demonstrate that one-loop perturbation theory is somewhat limited. To go beyond one-loop perturbation theory one can use high-β methods, as discussed in Sec. 5.3.5.

In the present calculations, all couplings in the lattice mNRQCD action are set to their tree-level values, and tadpole-improvement is used to account for radiative corrections. As demonstrated by the numerical results, this is already a good approximation. However, if very high precision is to be achieved, eventually one has to go beyond this approximation.

9.2 Heavy-hadron spectroscopy

The heavy-light spectrum calculations described in Sec. 7.2 are not yet complete. Other light-quark masses need to be included, and chiral extrapolations to the physical point need to be performed. The statistical errors can be reduced by computing more propagators.

All calculations presented in Chapter 7 are only for one lattice spacing. A more systematic analysis of discretisation errors will be performed once new ensembles of gauge field configurations with a finer lattice spacing are made available by the RBC and UKQCD collaborations.

Using NRQCD I have achieved high statistical accuracy for the Ω_{bbb} baryon, similarly to bottomonium. I am therefore planning to study excited states also for the Ω_{bbb}. Given how much insight into the strong interaction has been gained by analysing the spectrum of bottomonium, it will be highly interesting to perform similar work for the Ω_{bbb}, where three heavy quarks form a colour singlet.

9.3 Calculation of form factors for B decays

In Chapter 8 I have developed and tested the methods necessary for the numerical calculation of B decay form factors with lattice mNRQCD. Now, further computer time is required to consider more points in q^2, perform calculations with different light-quark masses and also different lattice spacings. After more points in q^2 have been included, the q^2-dependence of the form factors can be fitted by suitable models [199, 184]. In

particular, for $B \to K^*\gamma$ the form factors need to be extrapolated to $q^2 = 0$.

The statistical errors must be reduced further. I found that the reduction in statistical errors when comparing the random-wall-source method to the point-source method is small for the final form factor results. Due to the lower computational cost, the point-source method may lead to more precise results than the random-wall-source method for the same amount of computer time.

The fitting methods for the three-point functions have not yet been finalised and there is still room for optimisations. In particular, the effect of using a "smeared" interpolating field for the B meson in the three-point function has not yet been analysed, and Bayesian fits need to be performed where only unconstrained fits have been done so far.

The contributions of the tree-level $1/m_b$ corrections in the heavy-light currents have not yet been included in the form factor results as the necessary mixing coefficients are not yet known. A calculation of these coefficients would be useful. So far, the matching calculation for the heavy-light currents was performed in one-loop lattice perturbation theory. It would be desirable to go beyond this approximation, using for example high-β methods.

The study of rare B decays is complicated by long-distance effects and, for $B \to K^*$ transitions, by the instability of the K^* under the strong interactions. These issues require further investigation.

Appendix A

Conventions

A.1 Notation

- I use units in which $c = \hbar = 1$.
- Space-time coordinates: $x = (t, \mathbf{x}) = (x^0, x^1, x^2, x^3)$ in Minkowski space, $x = (\tau, \mathbf{x}) = (x^0, x^1, x^2, x^3)$ in Euclidean space
- Indices $\mu, \nu, ...$ run from 0 to 3; indices $j, k, ...$ run from 1 to 3.
- Indices appearing twice (and only twice) in a single term are summed over all allowed values, except where otherwise stated.
- The Minkowski metric is $(g_{\mu\nu}) = \mathrm{diag}(1, -1, -1, -1)$.
- The Lorentz boost of the coordinates is defined in terms of the 3-velocity $\mathbf{v}$ as:

$$\Lambda = \begin{pmatrix} \gamma & \gamma\, v^k \\ \gamma\, v^j & \delta^{jk} + \frac{\gamma^2}{1+\gamma}\, v^j v^k \end{pmatrix}, \tag{A.1}$$

  with $\gamma = (1 - \mathbf{v}^2)^{-1/2}$.

- Gamma matrices in Minkowski space are denoted with a hat, to distinguish them from $\gamma = (1 - \mathbf{v}^2)^{-1/2}$. I use

$$\begin{aligned} \hat{\gamma}^0 &= \begin{pmatrix} \sigma^0 & 0 \\ 0 & -\sigma^0 \end{pmatrix}, \quad \hat{\gamma}^j = \begin{pmatrix} 0 & \sigma^j \\ -\sigma^j & 0 \end{pmatrix}, \\ \hat{\gamma}_5 &= i\hat{\gamma}^0\hat{\gamma}^1\hat{\gamma}^2\hat{\gamma}^3 = \begin{pmatrix} 0 & \sigma^0 \\ \sigma^0 & 0 \end{pmatrix}, \end{aligned} \tag{A.2}$$

with the Pauli matrices σ^j. I define $\sigma^0 = \mathbb{1}_{2\times 2}$. Note that in calculations with moving NRQCD, the Minkowski space gamma matrices are also used in Euclidean space for convenience.

- Euclidean gamma matrices are denoted without a hat:

$$\begin{aligned} \gamma^0 &= \hat{\gamma}^0 = \begin{pmatrix} \sigma^0 & 0 \\ 0 & -\sigma^0 \end{pmatrix}, \quad \gamma^j = -i\hat{\gamma}^j = \begin{pmatrix} 0 & -i\sigma^j \\ i\sigma^j & 0 \end{pmatrix}, \\ \gamma_5 &= \gamma^0\gamma^1\gamma^2\gamma^3 = \hat{\gamma}_5 = \begin{pmatrix} 0 & \sigma^0 \\ \sigma^0 & 0 \end{pmatrix}. \end{aligned} \tag{A.3}$$

- The spinorial Lorentz boost is defined in terms of the 3-velocity $\mathbf{v}$ as:

$$S(\Lambda) = \frac{1}{\sqrt{2(1+\gamma)}}\left[(1+\gamma)\mathbb{1} - \gamma\,\mathbf{v}\cdot\hat{\boldsymbol{\gamma}}\,\hat{\gamma}^0\right] = \frac{1}{\sqrt{2(1+\gamma)}}\begin{pmatrix} 1+\gamma & \gamma\,\boldsymbol{\sigma}\cdot\mathbf{v} \\ \gamma\,\boldsymbol{\sigma}\cdot\mathbf{v} & 1+\gamma \end{pmatrix}. \tag{A.4}$$

- Feynman slash notation:

$$\not{u} = u^\mu\hat{\gamma}_\mu. \tag{A.5}$$

- Covariant derivatives and field strength tensor:

$$D_\mu = \frac{\partial}{\partial x^\mu} + igA_\mu, \tag{A.6}$$

$$[D_\mu, D_\nu] = igF_{\mu\nu}, \tag{A.7}$$

$$D_\mu F_{\rho\sigma} = D^{\mathrm{ad}}_\mu F_{\rho\sigma} + F_{\rho\sigma}D_\mu \qquad \text{with} \qquad D^{\mathrm{ad}}_\mu F_{\rho\sigma} = (\partial_\mu F_{\rho\sigma}) + ig[A_\mu, F_{\rho\sigma}]. \tag{A.8}$$

- Chromoelectric and chromomagnetic fields in Minkowski space:

$$E_k = F_{0k}, \qquad B_j = -\frac{1}{2}\epsilon_{jkl}F_{kl}. \tag{A.9}$$

- Chromoelectric and chromomagnetic fields in Euclidean space:

$$E_k = -F_{0k}, \qquad B_j = -\frac{1}{2}\epsilon_{jkl}F_{kl}. \tag{A.10}$$

A.2 Lattice derivatives and field strength

In this section I give explicit expressions for the discretised derivatives I use in the lattice action, Eqs. (5.12, 5.13). All expressions are constructed from the elementary forward, backward and symmetric derivatives

$$\begin{aligned}
\Delta_\mu^+\psi(x) &= U_\mu(x)\psi(x+\hat{\mu}) - \psi(x), \\
\Delta_\mu^-\psi(x) &= \psi(x) - U_{-\mu}(x)\psi(x-\hat{\mu}), \\
\Delta_\mu^\pm\psi(x) &= \frac{1}{2}\left[U_\mu(x)\psi(x+\hat{\mu}) - U_{-\mu}(x)\psi(x-\hat{\mu})\right].
\end{aligned} \tag{A.11}$$

For performance reasons, I construct higher-order operators to be maximally local by balancing the occurrence of these three types. I also symmetrise the expressions.

- Unimproved derivatives:

$$\begin{aligned}
\Delta^{(2)} &= \sum_{j=1}^{3} \Delta_j^+\Delta_j^- , \\
\Delta_v^{(2)} &= \frac{1}{2}\sum_{j,k=1}^{3} v^j v^k \left(\Delta_j^+\Delta_k^- + \Delta_j^-\Delta_k^+\right), \\
\Delta_v^{(3)} &= \frac{1}{2}\sum_{j,k,l=1}^{3} v^j v^k v^l \left(\Delta_j^+\Delta_k^\pm\Delta_l^- + \Delta_j^-\Delta_k^\pm\Delta_l^+\right), \\
\Delta_v^{(4)} &= \frac{1}{2}\sum_{j,k,l,m=1}^{3} v^j v^k v^l v^m \left(\Delta_j^+\Delta_k^-\Delta_l^+\Delta_m^- + \Delta_j^-\Delta_k^+\Delta_l^-\Delta_m^+\right).
\end{aligned} \tag{A.12}$$

- Improved derivatives:

$$\begin{aligned}
\tilde{\Delta}_j^\pm &= \Delta_j^\pm - \frac{1}{6}\Delta_j^+\Delta_j^\pm\Delta_j^- , \\
\tilde{\Delta}^{(2)} &= \Delta^{(2)} - \frac{1}{12}\sum_{j=1}^{3} \Delta_j^+\Delta_j^-\Delta_j^+\Delta_j^- , \\
\tilde{\Delta}_v^{(2)} &= \Delta_v^{(2)} + \frac{1}{4}\sum_{j,k=1}^{3} v^j v^k \Delta_j^+\Delta_j^-\Delta_k^+\Delta_k^- \\
&\quad -\frac{1}{12}\sum_{j,k=1}^{3} v^j v^k \Big(\Delta_j^+\Delta_j^-\Delta_j^+\Delta_k^- + \Delta_j^-\Delta_j^+\Delta_j^-\Delta_k^+ \\
&\qquad\qquad +\Delta_j^+\Delta_k^-\Delta_k^+\Delta_k^- + \Delta_j^-\Delta_k^+\Delta_k^-\Delta_k^+\Big).
\end{aligned} \tag{A.13}$$

- Unimproved adjoint derivative:

$$\Delta_\mu^{\rm ad}\tilde{F}_{\rho\sigma}(x) \;=\; \frac{1}{2}\Big[U_\mu(x)\tilde{F}_{\rho\sigma}(x+\hat{\mu})U_\mu^\dagger(x) - U_{-\mu}(x)\tilde{F}_{\rho\sigma}(x-\hat{\mu})U_{-\mu}^\dagger(x)\Big]. \quad \text{(A.14)}$$

- Improved field strength tensor:

$$\begin{aligned}\tilde{F}_{\mu\nu}(x) \;=\;& \frac{5}{3}F_{\mu\nu}(x) \\ & -\frac{1}{6}\Big(U_\mu(x)F_{\mu\nu}(x+\hat{\mu})U_\mu^\dagger(x) + U_{-\mu}(x)F_{\mu\nu}(x-\hat{\mu})U_{-\mu}^\dagger(x) - (\mu\leftrightarrow\nu)\Big),\end{aligned} \quad \text{(A.15)}$$

where

$$\begin{aligned}F_{\mu\nu}(x) \;&=\; \frac{-i}{2g}\left(\Omega_{\mu\nu}(x) - \Omega_{\mu\nu}^\dagger(x)\right), \\ \Omega_{\mu\nu}(x) \;&=\; \tfrac{1}{4}\sum_{\{(\alpha,\beta)\}_{\mu\nu}} U_\alpha(x)U_\beta(x+\hat{\alpha})U_{\text{-}\alpha}(x+\hat{\alpha}+\hat{\beta})U_{\text{-}\beta}(x+\hat{\beta}),\end{aligned} \quad \text{(A.16)}$$

with

$$\{(\alpha,\beta)\}_{\mu\nu} = \{(\mu,\nu),(\nu,\text{-}\mu),(\text{-}\mu,\text{-}\nu),(\text{-}\nu,\mu)\} \;\text{ for }\; \mu\neq\nu\,. \quad \text{(A.17)}$$

Appendix B

Form factors and decay rate for $B \to K^*\gamma$

B.1 Derivation of form factors

The invariant matrix element for the exclusive decay $B \to K^*\gamma$ is

$$\mathcal{M} = -\langle \gamma(q,r),\ K^*(p',s)\,|\mathcal{H}_{\rm eff}|B(p)\rangle, \tag{B.1}$$

where $r = 1,2$ denotes two possible photon polarisations and $s = 1,2,3$ denotes three possible K^* polarisations. The relevant part of the effective Hamiltonian is given by (cf. Sec. 8.1.4)

$$\mathcal{H}_{\rm eff} = -V_{tb}V_{ts}^*\frac{4G_F}{\sqrt{2}}C_7(\mu)\frac{e}{16\pi^2}m_b\ J_{\mu\nu}F^{\mu\nu}_{\rm (e.m.)} \qquad \text{with} \qquad J_{\mu\nu} = \bar{b}\sigma_{\mu\nu}\frac{1+\gamma_5}{2}s, \tag{B.2}$$

where $C_7(\mu)$ is the Wilson coefficient at the renormalisation scale μ.

Upon contracting the external photon with $F^{\mu\nu}_{\rm (e.m.)}$, we obtain

$$\begin{aligned}\langle \gamma(q,r),\ K^*(p',s)\,|J_{\mu\nu}F^{\mu\nu}_{\rm (e.m.)}|B(p)\rangle &= i\Big[q^\mu\varepsilon^{*\nu}_{(\gamma)}(q,r) - q^\nu\varepsilon^{*\mu}_{(\gamma)}(q,r)\Big]\langle K^*(p',s)\,|J_{\mu\nu}|B(p)\rangle \\ &= 2i\ q^\mu\varepsilon^{*\nu}_{(\gamma)}(q,r)\,\langle K^*(p',s)\,|J_{\mu\nu}|B(p)\rangle,\end{aligned} \tag{B.3}$$

where $\varepsilon_{(\gamma)} = \varepsilon_{(\gamma)}(q,r)$ is the polarisation vector of the photon. We shall now derive the general structure of the matrix element $\langle K^*(p',s)\,|J_{\mu\nu}|B(p)\rangle$. The operator $J_{\mu\nu}$ contains both a tensor and a pseudotensor part, and it is convenient to consider them separately. Let us start with the tensor part of $J_{\mu\nu}$, so we need to look at

$$\langle K^*(p',\varepsilon)\,|\bar{b}\sigma_{\mu\nu}s|B(p)\rangle, \tag{B.4}$$

where $\varepsilon = \varepsilon(p', s)$ now denotes the K^* polarisation vector. Under parity and time reversal, the states transform as follows:

$$\begin{aligned} \mathsf{P}|B(p)\rangle &= -|B(p_P)\rangle, \\ \mathsf{P}|K^*(p',\varepsilon)\rangle &= |K^*(p'_P,\varepsilon_P)\rangle, \\ \mathsf{T}|B(p)\rangle &= -|B(p_T)\rangle, \\ \mathsf{T}|K^*(p',\varepsilon)\rangle &= |K^*(p'_T,\varepsilon_T)\rangle \end{aligned} \tag{B.5}$$

with $p_P = p_T = (p^0, -\mathbf{p})$ etc. Since QCD is invariant under these transformations, we must have for $i, j = 1, 2, 3$

$$\begin{aligned} \langle K^*(p',\varepsilon)\,|\bar{b}\,\sigma_{0j}\,s|B(p)\rangle &= +\langle K^*(p'_P,\varepsilon_P)\,|\bar{b}\,\sigma_{0j}\,s|B(p_P)\rangle, \\ \langle K^*(p',\varepsilon)\,|\bar{b}\,\sigma_{ij}\,s|B(p)\rangle &= -\langle K^*(p'_P,\varepsilon_P)\,|\bar{b}\,\sigma_{ij}\,s|B(p_P)\rangle, \\ \langle K^*(p',\varepsilon)\,|\bar{b}\,\sigma_{0j}\,s|B(p)\rangle^* &= +\langle K^*(p'_T,\varepsilon_T)\,|\bar{b}\,\sigma_{0j}\,s|B(p_T)\rangle, \\ \langle K^*(p',\varepsilon)\,|\bar{b}\,\sigma_{ij}\,s|B(p)\rangle^* &= -\langle K^*(p'_T,\varepsilon_T)\,|\bar{b}\,\sigma_{ij}\,s|B(p_T)\rangle. \end{aligned} \tag{B.6}$$

Here, we have made a choice of phase.

There are three Lorentz-vectors available: the momenta p, p' and the polarisation vector $\varepsilon = \varepsilon(p', s)$. Since the K^* meson is in the final state, ε must appear as its complex conjugate. Let us use the basis vectors $p_+ \equiv p + p'$, $p_- \equiv p - p'$ and ε^*. From the transformation law under parity, Eq. (B.6), it follows that there are three possible basis pseudotensors:

$$\epsilon_{\mu\nu\rho\sigma}\varepsilon^{*\rho}p_+^\sigma, \qquad \epsilon_{\mu\nu\rho\sigma}\varepsilon^{*\rho}p_-^\sigma \qquad \text{and} \qquad \epsilon_{\mu\nu\rho\sigma}p_-^\rho p_+^\sigma. \tag{B.7}$$

Each of them can come with a function of Lorentz-scalar quantities as a prefactor. We can build the following basic Lorentz scalars:

$$p_+^2, \quad p_-^2, \quad \varepsilon^{*2}, \quad p_- \cdot p_+, \quad \varepsilon^* \cdot p_- \quad \text{and} \quad \varepsilon^* \cdot p_+. \tag{B.8}$$

However, since ε is a polarisation vector, we have $\varepsilon^2 = -1$ and $\varepsilon \cdot p' = 0$. The latter implies that both $\varepsilon^* \cdot p_-$ and $\varepsilon^* \cdot p_+$ reduce to the single quantity $\varepsilon^* \cdot p$. Furthermore, since $p^2 = M_B$ and $p'^2 = M_{K^*}$, we have

$$\begin{aligned} p_- \cdot p_+ &= M_B^2 - M_{K^*}^2, \\ p_+^2 &= M_B^2 + M_{K^*}^2 + 2p \cdot p', \\ p_-^2 &= M_B^2 + M_{K^*}^2 - 2p \cdot p'. \end{aligned} \tag{B.9}$$

Hence, it suffices to consider functions of $\varepsilon^* \cdot p$ and p_-^2 only. Another restriction is that the matrix element must be linear in the polarisation vector ε^*. It follows that we can write the matrix element in the form

$$\begin{aligned}\langle K^*(p',\varepsilon)\,|\bar{b}\sigma_{\mu\nu}s|B(p)\rangle &= f_+(p_-^2)\epsilon_{\mu\nu\rho\sigma}\varepsilon^{*\rho}p_+^\sigma \;+\; f_-(p_-^2)\epsilon_{\mu\nu\rho\sigma}\varepsilon^{*\rho}p_-^\sigma \\ &\quad + g(p_-^2)(\varepsilon^*\cdot p)\epsilon_{\mu\nu\rho\sigma}p_-^\rho p_+^\sigma\,, \end{aligned} \tag{B.10}$$

with unknown functions f_+, f_- and g. The transformation law under time reversal, Eq. (B.6), implies that these functions are real.

Let us now consider the part of $J_{\mu\nu}$ containing γ_5. The identity

$$\sigma_{\mu\nu}\gamma_5 = \frac{i}{2}\epsilon_{\mu\nu\rho\sigma}\sigma^{\rho\sigma} \tag{B.11}$$

allows us to relate the matrix element to (B.10):

$$\begin{aligned}\langle K^*(p',\varepsilon)\,|\bar{b}\,\sigma_{\mu\nu}\gamma_5\,s|B(p)\rangle &= \frac{i}{2}\epsilon_{\mu\nu\rho\sigma}\langle K^*(p',\varepsilon)\,|\bar{b}\sigma^{\rho\sigma}s|B(p)\rangle \\ &= \frac{i}{2}\epsilon_{\mu\nu\rho\sigma}\Big[f_+(p_-^2)\epsilon^{\rho\sigma\alpha\beta}\varepsilon^*_\alpha p_{+\beta} + f_-(p_-^2)\epsilon^{\rho\sigma\alpha\beta}\varepsilon^*_\alpha p_{-\beta} \\ &\qquad + g(p_-^2)(\varepsilon^*\cdot p)\epsilon^{\rho\sigma\alpha\beta}p_{-\alpha}p_{+\beta}\Big]. \end{aligned} \tag{B.12}$$

Using

$$\epsilon_{\mu\nu\rho\sigma}\epsilon^{\rho\sigma\alpha\beta} = -2\left(\delta_\mu^\alpha\delta_\nu^\beta - \delta_\mu^\beta\delta_\nu^\alpha\right), \tag{B.13}$$

Eq. (B.12) simplifies to

$$\begin{aligned}\langle K^*(p',\varepsilon)\,|\bar{b}\,\sigma_{\mu\nu}\gamma_5\,s|B(p)\rangle &= if_+(p_-^2)\left[\varepsilon^*_\nu p_{+\mu} - \varepsilon^*_\mu p_{+\nu}\right] + if_-(p_-^2)\left[\varepsilon^*_\nu p_{-\mu} - \varepsilon^*_\mu p_{-\nu}\right] \\ &\quad + ig(p_-^2)(\varepsilon^*\cdot p)\left[p_{+\nu}p_{-\mu} - p_{+\mu}p_{-\nu}\right]. \end{aligned} \tag{B.14}$$

Next, recall that the full matrix element (B.3) contains a contraction with the photon momentum $q = p_-$. We have

$$\begin{aligned} q^\mu\langle K^*(p',\varepsilon)\,|\bar{b}\sigma_{\mu\nu}s|B(p)\rangle &= f_+(q^2)\epsilon_{\mu\nu\rho\sigma}p_-^\mu\varepsilon^{*\rho}p_+^\sigma \\ &= 2\,f_+(q^2)\epsilon_{\nu\mu\rho\sigma}\varepsilon^{*\mu}p^\rho p'^\sigma \end{aligned} \tag{B.15}$$

and

$$\begin{aligned} q^\mu\langle K^*(p',\varepsilon)\,|\bar{b}\sigma_{\mu\nu}\gamma_5 s|B(p)\rangle &= if_+(q^2)\left[\varepsilon^*_\nu(M_B^2 - M_{K^*}^2) - (\varepsilon^*\cdot q)(p+p')_\nu\right] \\ &\quad + if_-(q^2)\left[\varepsilon^*_\nu q^2 - (\varepsilon^*\cdot q)q_\nu\right] \\ &\quad + ig(q^2)(\varepsilon^*\cdot q)\left[q^2\,(p+p')_\nu - (M_B^2 - M_{K^*}^2)q_\nu\right]. \end{aligned} \tag{B.16}$$

In order to disentangle (B.15) and (B.16), we now define the new form factors

$$\begin{aligned} T_1(q^2) &= -\frac{1}{2} f_+(q^2), \\ T_2(q^2) &= -\frac{1}{2}\left[f_+(q^2) + \frac{q^2}{M_B^2 - M_{K^*}^2} f_-(q^2)\right], \\ T_3(q^2) &= \frac{1}{2}\left[f_-(q^2) + (M_B^2 - M_{K^*}^2) g(q^2)\right], \end{aligned} \tag{B.17}$$

so that

$$\begin{aligned} f_+(q^2) &= -2\, T_1(q^2), \\ f_-(q^2) &= \frac{2\left[T_1(q^2) - T_2(q^2)\right](M_B^2 - M_{K^*}^2)}{q^2}, \\ g(q^2) &= \frac{2\, T_3(q^2)}{M_B^2 - M_{K^*}^2} - \frac{2\left[T_1(q^2) - T_2(q^2)\right]}{q^2}. \end{aligned} \tag{B.18}$$

This results in

$$q^\mu \langle K^*(p',\varepsilon)\, |\bar{b}\sigma_{\mu\nu} s| B(p)\rangle = -4\, T_1(q^2) \epsilon_{\nu\mu\rho\sigma} \varepsilon^{*\mu} p^\rho p'^\sigma \tag{B.19}$$

and

$$\begin{aligned} q^\mu \langle K^*(p',\varepsilon)\, |\bar{b}\sigma_{\mu\nu}\gamma_5 s| B(p)\rangle &= -2iT_2(q^2)\left[\varepsilon_\nu^*(M_B^2 - M_{K^*}^2) - (\varepsilon^* \cdot q)(p+p')_\nu\right] \\ &\quad -2iT_3(q^2)(\varepsilon^* \cdot q)\left[q_\nu - \frac{q^2}{M_B^2 - M_{K^*}^2}(p+p')_\nu\right], \end{aligned} \tag{B.20}$$

so that the tensor- and pseudotensor contributions are now separated. Note that at the physical point $q^2 = 0$, the second line of (B.17) implies

$$T_1(0) = T_2(0). \tag{B.21}$$

B.2 Calculation of decay rate

We shall now express the decay rate

$$\mathrm{d}\Gamma = \frac{1}{2M_B} \frac{\mathrm{d}^3 p'}{(2\pi)^3 2E_{K^*}} \frac{\mathrm{d}^3 q}{(2\pi)^3 2E_\gamma} \sum_{r=1}^{2} \sum_{s=1}^{3} |\mathcal{M}|^2 (2\pi)^4 \delta^{(4)}(p - p' - q) \tag{B.22}$$

in terms of the form factor at $q^2 = 0$.

Equation (B.3) becomes

$$\begin{aligned}\langle\gamma(q,r),\, K^*(p',s)\,|J_{\mu\nu}F^{\mu\nu}_{(\mathrm{e.m.})}|B(p)\rangle &= i\,T_1(0)\Big\{-4\,\epsilon_{\nu\mu\rho\sigma}\varepsilon^{*\nu}(q,r)\varepsilon^{*\mu}(p',s)p^\rho p'^\sigma \\ &\quad -2i\varepsilon^*(q,r)\cdot\varepsilon^*(p',s)\,(M_B^2-M_{K^*}^2) \\ &\quad +2i\left[\varepsilon^*(p',s)\cdot q\right]\left[\varepsilon^*(q,r)\cdot(p+p')\right]\Big\}. \end{aligned} \tag{B.23}$$

Working in the B rest frame and using momentum conservation, we have

$$\begin{aligned} p &= (M_B,\mathbf{0}), \\ q &= (|\mathbf{q}|,\mathbf{q}), \\ p' &= (M_B-|\mathbf{q}|,-\mathbf{q}), \\ |\mathbf{q}| &= \frac{M_B^2-M_{K^*}^2}{2M_B}. \end{aligned} \tag{B.24}$$

We can also set $\varepsilon^0(q,r)=0$, which implies

$$\varepsilon^*(q,r)\cdot(p+p') = \boldsymbol{\varepsilon}^*(q,r)\cdot\mathbf{q} = 0. \tag{B.25}$$

Therefore, (B.23) reduces to

$$\begin{aligned}\langle\gamma(q,r),\, K^*(p',s)\,|J_{\mu\nu}F^{\mu\nu}_{(\mathrm{e.m.})}|B(p)\rangle &= i\,T_1(0)\Big[4\,M_B\,\epsilon_{jkl}\varepsilon^{*j}(q,r)\varepsilon^{*k}(p',s)q^l \\ &\quad +2i\boldsymbol{\varepsilon}^*(q,r)\cdot\boldsymbol{\varepsilon}^*(p',s)(M_B^2-M_{K^*}^2)\Big]. \end{aligned} \tag{B.26}$$

The spin-summed absolute square of the amplitude becomes

$$\begin{aligned}&\sum_{r,s}|\langle\gamma(q,r),\, K^*(p',s)\,|J_{\mu\nu}F^{\mu\nu}_{(\mathrm{e.m.})}|B(p)\rangle|^2 \\ &\quad= 16\,|T_1(0)|^2M_B^2\sum_{r,s}\epsilon_{jkl}\epsilon_{mno}\,\varepsilon^{*j}(q,r)\varepsilon^m(q,r)\varepsilon^{*k}(p',s)\varepsilon^n(p',s)q^lq^o \\ &\qquad+\,4\,|T_1(0)|^2(M_B^2-M_{K^*}^2)^2\sum_{r,s}\varepsilon^{*j}(q,r)\varepsilon^k(q,r)\varepsilon^{*j}(p',s)\varepsilon^k(p',s) \\ &\quad= 16\,|T_1(0)|^2M_B^2\epsilon_{jkl}\epsilon_{mno}\left(\delta^{jm}-\frac{q^jq^m}{|\mathbf{q}|^2}\right)\left(\delta^{kn}+\frac{q^kq^n}{M_{K^*}^2}\right)q^lq^o \\ &\qquad+4\,|T_1(0)|^2(M_B^2-M_{K^*}^2)^2\left(\delta^{jk}-\frac{q^jq^k}{|\mathbf{q}|^2}\right)\left(\delta^{jk}+\frac{q^jq^k}{M_{K^*}^2}\right) \\ &\quad= 16\,|T_1(0)|^2(M_B^2-M_{K^*}^2)^2. \end{aligned} \tag{B.27}$$

Finally, the total decay rate is

$$\begin{aligned}
\Gamma &= \frac{1}{2M_B}\int \frac{\mathrm{d}^3 q}{(2\pi)^3 2|\mathbf{q}|} \\
&\quad \times \frac{1}{(2\pi)^3 2\sqrt{M_{K^*}^2+|\mathbf{q}|^2}}\,(2\pi)^4\delta\left(M_B-\sqrt{M_{K^*}^2+|\mathbf{q}|^2}-|\mathbf{q}|\right)\sum_{r,s}|\mathcal{M}|^2 \\
&= \frac{1}{2M_B}\int \frac{4\pi|\mathbf{q}|^2\mathrm{d}|\mathbf{q}|}{(2\pi)^2 2|\mathbf{q}|}\frac{1}{2\sqrt{M_{K^*}^2+|\mathbf{q}|^2}}\delta\left(M_B-\sqrt{M_{K^*}^2+|\mathbf{q}|^2}-|\mathbf{q}|\right)\sum_{r,s}|\mathcal{M}|^2 \\
&= \frac{1}{2M_B}\frac{4\pi|\mathbf{q}|^2}{(2\pi)^2 2|\mathbf{q}|}\frac{1}{2\sqrt{M_{K^*}^2+|\mathbf{q}|^2}}\left(1+\frac{|\mathbf{q}|}{\sqrt{M_{K^*}^2+|\mathbf{q}|^2}}\right)^{-1}\sum_{r,s}|\mathcal{M}|^2\Bigg|_{|\mathbf{q}|=\frac{M_B^2-M_{K^*}^2}{2M_B}} \\
&= \frac{M_B^2-M_{K^*}^2}{16\pi M_B^3}\sum_{r,s}|\mathcal{M}|^2 \\
&= \frac{M_B^2-M_{K^*}^2}{16\pi M_B^3}\left|V_{tb}V_{ts}^*\frac{4G_F}{\sqrt{2}}C_7(\mu)\frac{e}{16\pi^2}m_b\right|^2 16\,|T_1(0)|^2(M_B^2-M_{K^*}^2)^2 \\
&= \frac{\alpha\,G_F^2}{8\pi^4}|C_7(\mu)|^2|V_{tb}V_{ts}^*|^2 m_b^2 M_B^3\left(1-\frac{M_{K^*}^2}{M_B^2}\right)^3|T_1(0)|^2. \qquad \text{(B.28)}
\end{aligned}$$

Appendix C

Data analysis methods

C.1 Correlated least-squares fitting

Suppose that we have real-valued "observables" y_i where $i = 1, 2, ...$ is a generic label; an example will be given in Sec. C.2. In this notation, the total number of observables equals the total number of degrees of freedom in the fit.

Suppose further that we have N statistically independent measurements (for example data from N independent gauge field configurations) for all of these observables. We denote a data point by y_i^n, where $n = 1 \dots N$. We define the average of the i-th observable as

$$\overline{y_i} = \frac{1}{N} \sum_{n=1}^{N} y_i^n, \tag{C.1}$$

and the data correlation matrix as

$$C_{ij} = \frac{1}{N(N-1)} \sum_{n=1}^{N} (y_i^n - \overline{y_i})(y_j^n - \overline{y_j}). \tag{C.2}$$

We would like to describe the data by smooth model functions $f_i(\mathbf{a})$ depending on P real-values parameters $a_1, a_2, ..., a_P$. The aim is to find those values of the parameters that minimise the following χ^2 function[1]:

$$\chi^2(\mathbf{a}) = \sum_{i,j} (C^{-1})_{ij} \left[\overline{y_i} - f_i(\mathbf{a})\right] \left[\overline{y_j} - f_j(\mathbf{a})\right]. \tag{C.3}$$

[1] This definition, which contains C^{-1}, requires the number of measurements N to be much larger than the number of degrees of freedom, so that the data correlation matrix is well-determined and invertible. If this is not the case, one can work with a pseudo-inverse of C instead, which is computed using singular value decomposition.

This is the standard least-squares fitting procedure for correlated data points [33, 34].

An efficient method for finding the minimum of (C.3) numerically is the Levenberg-Marquardt algorithm [200, 201, 202]. A good fit should have $\chi^2/\text{dof} \approx 1$, where "dof" denotes the number of degrees of freedom.

Let $\mathbf{a}^{(0)} = (a_1^{(0)}, a_2^{(0)}, ..., a_P^{(0)})$ be the point in parameter space (we assume that it exists and is unique) that minimises $\chi^2(\mathbf{a})$. The error estimate for a parameter a_p in the quadratic approximation is then given by

$$a_p = a_p^{(0)} \pm \sqrt{\left[\alpha^{-1}(\mathbf{a}^{(0)})\right]_{p\,p}}\,, \tag{C.4}$$

(no sum over the repeated index p here) where the matrix $\alpha_{p\,q}$ is defined as follows:

$$\alpha_{p\,q}(\mathbf{a}) = \frac{1}{2}\,\frac{\partial^2\chi^2(\mathbf{a})}{\partial a_p \partial a_q}. \tag{C.5}$$

Note that in the definition (C.5), second derivatives of the functions f_i are usually neglected. The inverse of $\alpha_{p\,q}$ is the parameter covariance matrix.

When evaluating some smooth function $g(\mathbf{a})$ of the parameters, the error estimate in the quadratic approximation is

$$g(\mathbf{a}) = g(\mathbf{a}^{(0)}) \pm \sqrt{\sum_{p,\,q} \left[\alpha^{-1}(\mathbf{a}^{(0)})\right]_{p\,q} \frac{\partial g(\mathbf{a}^{(0)})}{\partial a_p} \frac{\partial g(\mathbf{a}^{(0)})}{\partial a_q}}. \tag{C.6}$$

In this work, I refer to results and error estimates computed with (C.4) or (C.6) as "obtained directly from the fit", as opposed to results and error estimates from bootstrap (see Sec. C.4).

C.2 Simultaneous fitting of multiple correlation functions

The general principle introduced in Sec. C.1 also allows simultaneous fits of multiple correlation functions in lattice QCD. As an example, we consider a simultaneous fit of the following model functions:

- a three-point function with model $C_{FJB}(T, \tau)$ and data in the range $T = 15$, 16 and $\tau = 6 \,...\, (T - 6)$,
- a two-point function with model $C_{FF}(\tau)$ and data in the range $\tau = 10 \,...\, 54$,
- a two-point function with model $C_{BB}(\tau)$ and data in the range $\tau = 12 \,...\, 32$.

The model functions $C_{FJB}(T,\tau)$, $C_{FF}(\tau)$, and $C_{BB}(\tau)$ depend on a set of parameters, here various energies and amplitudes. In this example, $C_{FJB}(T,\tau)$ could share the energy parameters describing the state F and its excitations with the two-point function $C_{FF}(\tau)$, and $C_{FJB}(T,\tau)$ could share the energy parameters describing the state B and its excitations with the two-point function $C_{BB}(\tau)$.

To perform the simultaneous fit we would use the following model functions f_i in the notation of Sec. C.1:

$$\begin{aligned}
f_1 &= C_{FJB}(T=15,\tau=6),\\
&\vdots\\
f_4 &= C_{FJB}(T=15,\tau=9),\\
f_5 &= C_{FJB}(T=16,\tau=6),\\
&\vdots\\
f_9 &= C_{FJB}(T=16,\tau=10),\\
f_{10} &= C_{FF}(\tau=10),\\
&\vdots\\
f_{54} &= C_{FF}(\tau=54),\\
f_{55} &= C_{BB}(\tau=12),\\
&\vdots\\
f_{75} &= C_{FF}(\tau=32).
\end{aligned} \tag{C.7}$$

The simultaneous fit in this example has 75 degrees of freedom.

C.3 Bayesian fitting

Bayesian (constrained) fitting of lattice QCD data has been introduced in [122, 203]. The use of the Bayesian method is best illustrated for the fitting of a Euclidean two-point function to extract energies and amplitudes. It is known from the theory (see Sec. 2.2) that a two-point function has the form of an infinite sum of exponentials. For a matrix of two-point functions with a (finite) set of operators labelled by Γ, we have

$$C(\Gamma_{\rm sk},\Gamma_{\rm sc},\tau) = \sum_{n=0}^{\infty} A_n(\Gamma_{\rm sk})\, A_n^*(\Gamma_{\rm sc})\, e^{-E_n\,\tau}, \tag{C.8}$$

where we assume that the energies are ordered so that $E_n > E_{n-1}$. We would like to extract the amplitudes $A_n(\Gamma)$ and energies E_n from a fit of (C.8) for a range of points

$\tau_{\min} \leq \tau \leq \tau_{\max}$. However, there is an infinite number of parameters but only a finite number of data points. Therefore, when unconstrained fits are used, one has to truncate the sum in (C.8) and keep only a finite number of exponentials: $0 \leq n < n_{\exp}$. Since the contributions from higher excited states fall exponentially with τ, one has to choose $\tau_{\min}$ large, so that the contributions from the states with $n \geq n_{\exp}$ are negligible. However, when $\tau_{\min}$ is chosen too large, statistical errors in the fit results are too big; when $\tau_{\min}$ is too small, the contributions from excited states introduce systematic errors in the results. This behaviour can be seen for example in Table 8.10. The precise value one should choose for $\tau_{\min}$ is not well-determined.

Ideally, we would like to include the data at small τ, since it is statistically very precise. We would like to increase $n_{\exp}$ until the systematic errors in the fits results for the low-lying states are negligible. However, the fit becomes soon unstable when $n_{\exp}$ is increased. If the fit converges at all, one typically obtains unphysically large values for the amplitudes at large n, such as 100 times the amplitude for the ground state, which also destabilises the results for the low-lying states. From quark models it is expected that the amplitudes of the excited states are smaller than or of a similar magnitude as the ground-state amplitude.

The solution for this problem is to constrain the parameters to physically reasonable ranges. This can be achieved through augmenting the χ^2 function (C.3) by

$$\chi^2 \;\rightarrow\; \chi^2 + \chi^2_{\text{prior}} \tag{C.9}$$

with a Gaussian prior

$$\chi^2_{\text{prior}} = \sum_p \frac{(a_p - \widetilde{a}_p)^2}{\widetilde{\sigma}^2_{a_p}}. \tag{C.10}$$

The term χ^2_{prior} favours parameter values in the ranges $a_p = \widetilde{a}_p \pm \widetilde{\sigma}_{a_p}$; the values for $\widetilde{a}_p$ and $\widetilde{\sigma}_{a_p}$ are chosen based on prior knowledge.

In the following discussion of the prior choices $\{\widetilde{a}_p, \widetilde{\sigma}_{a_p}\}$ we will distinguish between parameters for low-lying and high-lying states. For example, the 3×3 matrix fit shown in Fig. 7.2 contains operators optimised for the $\Upsilon(1S)$, $\Upsilon(2S)$ and $\Upsilon(3S)$ states. These three states are referred to as low-lying for this fit, since their energies and amplitudes are well-determined by the data. Higher excitations are referred to as high-lying.

I typically choose the prior widths for the parameters of the low-lying states to be about 10 times larger than the resulting error estimates (C.4) from the fit. This ensures that the influence of the priors on these parameters is negligible. I obtain initial guesses for the central values from unconstrained fits including only a small number of exponentials

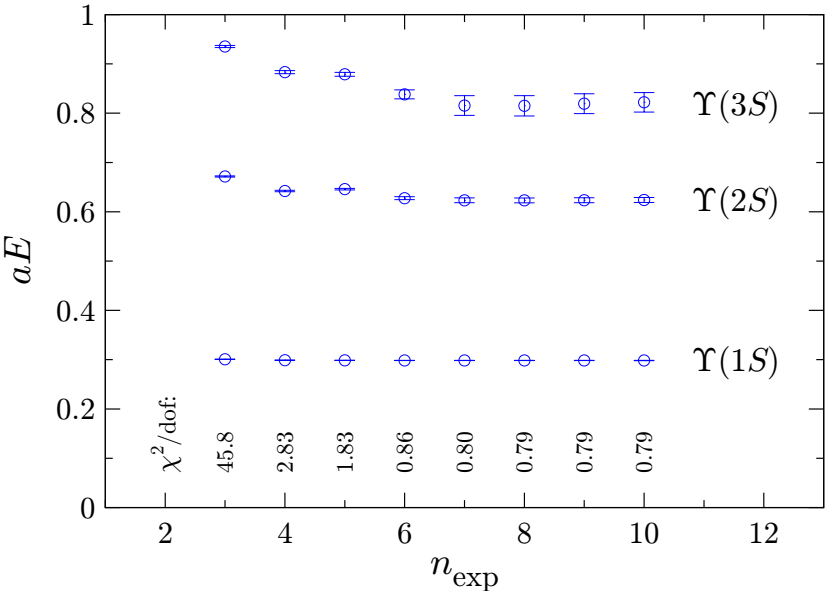

Figure C.1: Bayesian fit results for a 3×3 matrix correlator with the $\{\Upsilon(1S),\ \Upsilon(2S),\ \Upsilon(3S)\}$ smearings as a function of the number of exponentials. The values of χ^2 divided by the number of degrees of freedom are also shown.

at large Euclidean time.

For the fit shown in Fig. 7.2, I used the logarithms of the energy splittings $l_n \equiv \ln(E_{n+1} - E_n)$ and the relative amplitudes $B_n(\Gamma) \equiv A_n(\Gamma)/A_0(\Gamma)$ as the fit parameters for $n > 0$. I set $\widetilde{l}_n = -1.4$ and $\widetilde{\sigma}_{l_n} = 1$. This corresponds to energy splittings of about 400 MeV, with a prior uncertainty of about 100 percent. For the relative amplitudes I set $\widetilde{B}_n = 0$ and $\widetilde{\sigma}_{B_n} = 5$.

With the Bayesian method, one can increase n_{exp} arbitrarily without destabilising the fit. One has to increase n_{exp} until the results and error estimates for the low-lying states of interest become independent of n_{exp}. This is demonstrated in Fig. C.1.

C.4 Bootstrap method

Equation (C.6) provides a method for taking into account correlations when computing quantities that depend on more than one parameter of a single fit. However, in many cases one also needs to compute quantities that depend on parameters from multiple non-simultaneous fits of data from the same gauge field configurations.

An alternative technique for taking into account correlations that is applicable in both

cases is the statistical bootstrap method [33, 34]. Recall from Sec. C.1 that we considered N independent measurements. A single bootstrap sample is obtained by picking N out of these N measurements randomly (with allowed repetition). One generates a large number of such bootstrap samples, and performs the fits as in Sec. C.1 for each of these bootstrap samples.

The function of the fit parameters that one is interested in is then computed for the fit results from each bootstrap sample. In this way, a distribution for the function is obtained. One computes the average and takes the 68% width of the distribution as the error estimate.

Note that the bootstrap method must be modified for Bayesian fitting [122] such that not only the data sets are resampled randomly, but also the central values $\widetilde{a}_p$ of the priors in (C.10) are drawn from Gaussian random distributions with widths $\widetilde{\sigma}_{a_p}$ for every fit.

C.5 Autocorrelations

The methods described above all require that the N measurements are statistically independent. However, in lattice QCD the gauge field configurations are generated using a Markov process with a non-zero autocorrelation time. In addition, when different measurements are performed on a single gauge field configuration, these are also not completely independent. In general, autocorrelations lead to underestimates of statistical errors. A detailed discussion can be found in [34].

A simple method to reduce autocorrelations is the binning method. "Neighbouring" measurements (in terms of Markov-chain time and/or position on a single gauge field configuration) are grouped into bins of size B, and the average is computed for each bin. The N/B bin-averages are then taken as the new measurements, which are statistically more independent. The bin size B is increased until the error estimates become stable.

Acknowledgements

I would like to thank my supervisor Matt Wingate for his continued support and encouragement throughout this work. I thank all those who contributed through useful discussions, including Christine Davies, Will Detmold, Alistair Hart, Ron Horgan, Lew Khomskii, Andrew Lee, Peter Lepage, David Lin, Zhaofeng Liu, Eike Müller, Heechang Na, Junko Shigemitsu and Laurent Storoni. I also thank the lecturers of the two summer schools where I have learned so much: the school on "Lattice QCD and its applications" in 2007 at the Institute for Nuclear Theory in Seattle, USA, and the school on "Modern perspectives in lattice QCD: Quantum field theory and high performance computing" in 2009 at the École de Physique in Les Houches, France.

I am deeply grateful to my parents for all their support. I would also like to thank my friends, who made my stay in Cambridge very enjoyable.

I thank St John's College Cambridge, the Cambridge European Trust and the Engineering and Physical Sciences Research Council for financial support.

This work has made use of high performance computing resources provided by the Fermilab Lattice Gauge Theory Computational Facility (`http://www.usqcd.org/fnal`), the University of Cambridge High Performance Computing Service (`http://www.hpc.cam.ac.uk`), the National Energy Research Scientific Computing Center (`http://www.nersc.gov/`), the National Center for Supercomputing Applications (`http://www.ncsa.illinois.edu/`) and Teragrid (`http://www.teragrid.org/`).

List of publications

1. "Form factors for rare B decays: strategy, methodology, and numerical study"
   Z. Liu, S. Meinel, A. Hart, R. R. Horgan, E. H. Müller and M. Wingate
   PoS **LAT2009** (2009) 242, arXiv:0911.2370 [hep-lat]

2. "Radiative corrections to the m(oving)NRQCD action and heavy-light operators"
   E. H. Müller, C. T. H. Davies, A. Hart, G. M. von Hippel, R. R. Horgan, I. Kendall, A. Lee, S. Meinel, C. Monahan and M. Wingate
   PoS **LAT2009** (2009) 241, arXiv:0909.5126 [hep-lat]

3. "Bottom hadrons from lattice QCD with domain wall and NRQCD fermions"
   S. Meinel, W. Detmold, C.-J. D. Lin and M. Wingate
   PoS **LAT2009** (2009) 105, arXiv:0909.3837 [hep-lat]

4. "Moving NRQCD for heavy-to-light form factors on the lattice"
   R. R. Horgan, L. Khomskii, S. Meinel, M. Wingate, K. M. Foley, G. P. Lepage, G. M. von Hippel, A. Hart, E. H. Müller, C. T. H. Davies, A. Dougall and K. Y. Wong
   Phys. Rev. **D80** (2009) 074505, arXiv:0906.0945 [hep-lat]

5. "Bottomonium spectrum from lattice QCD with 2+1 flavors of domain wall fermions"
   S. Meinel
   Phys. Rev. **D79** (2009) 094501, arXiv:0903.3224 [hep-lat]

6. "Rare B decays with moving NRQCD and improved staggered quarks"
   S. Meinel, E. H. Müller, L. Khomskii, A. Hart, R. R. Horgan and M. Wingate
   PoS **LAT2008** (2008) 280, arXiv:0810.0921 [hep-lat]

7. "Moving NRQCD and $B \to K^*\gamma$"
   S. Meinel, R. Horgan, L. Khomskii, L. C. Storoni and M. Wingate
   PoS **LAT2007** (2007) 377, arXiv:0710.3101 [hep-lat]

Bibliography

[1] M. Kobayashi and T. Maskawa, "CP violation in the renormalizable theory of weak interaction," *Prog. Theor. Phys.* **49** (1973) 652–657.

[2] S. W. Herb *et al.*, "Observation of a dimuon resonance at 9.5 GeV in 400-GeV proton-nucleus collisions," *Phys. Rev. Lett.* **39** (1977) 252–255.

[3] **CLEO** Collaboration, S. Behrends *et al.*, "Observation of exclusive decay modes of b-flavored mesons," *Phys. Rev. Lett.* **50** (1983) 881–884.

[4] **Heavy Flavor Averaging Group** Collaboration, E. Barberio *et al.*, "Averages of b-hadron and c-hadron properties at the end of 2007," `arXiv:0808.1297 [hep-ex]`. `http://www.slac.stanford.edu/xorg/hfag/`.

[5] K. G. Wilson, "Confinement of quarks," *Phys. Rev.* **D10** (1974) 2445–2459.

[6] **HPQCD** and **MILC** and **UKQCD** and **Fermilab Lattice** Collaboration, C. T. H. Davies *et al.*, "High-precision lattice QCD confronts experiment," *Phys. Rev. Lett.* **92** (2004) 022001, `arXiv:hep-lat/0304004`.

[7] K. Jansen, "Lattice QCD: a critical status report," *PoS* **LAT2008** (2008) 010, `arXiv:0810.5634 [hep-lat]`.

[8] C. Jung, "Status of dynamical ensemble generation," *PoS* **LAT2009** (2010) 002, `arXiv:1001.0941 [hep-lat]`.

[9] B. A. Thacker and G. P. Lepage, "Heavy-quark bound states in lattice QCD," *Phys. Rev.* **D43** (1991) 196–208.

[10] G. P. Lepage, L. Magnea, C. Nakhleh, U. Magnea, and K. Hornbostel, "Improved nonrelativistic QCD for heavy quark-physics," *Phys. Rev.* **D46** (1992) 4052–4067, `arXiv:hep-lat/9205007`.

[11] E. Gulez *et al.*, "B meson semileptonic form factors from unquenched lattice QCD," *Phys. Rev.* **D73** (2006) 074502, arXiv:hep-lat/0601021.

[12] **CLEO** Collaboration, S. B. Athar *et al.*, "Study of the q^2 dependence of $B \to \pi\ell\nu$ and $B \to \rho(\omega)\ell\nu$ decay and extraction of $|V_{ub}|$," *Phys. Rev.* **D68** (2003) 072003, arXiv:hep-ex/0304019.

[13] **BELLE** Collaboration, T. Hokuue *et al.*, "Measurements of branching fractions and q^2 distributions for $B \to \pi\ell\nu$ and $B \to \rho\ell\nu$ decays with $B \to D^{(*)}\ell\nu$ decay tagging," *Phys. Lett.* **B648** (2007) 139–148, arXiv:hep-ex/0604024.

[14] **BABAR** Collaboration, B. Aubert *et al.*, "Measurement of the $B^0 \to \pi^-\ell^+\nu$ form-factor shape and branching fraction, and determination of $|V_{ub}|$ with a loose neutrino reconstruction technique," *Phys. Rev. Lett.* **98** (2007) 091801, arXiv:hep-ex/0612020.

[15] **CLEO** Collaboration, R. Ammar *et al.*, "Evidence for penguin-diagram decays: first observation of $B \to K^*(892)\gamma$," *Phys. Rev. Lett.* **71** (1993) 674–678.

[16] **BELLE** Collaboration, M. Nakao *et al.*, "Measurement of the $B \to K^*\gamma$ branching fractions and asymmetries," *Phys. Rev.* **D69** (2004) 112001, arXiv:hep-ex/0402042.

[17] **BABAR** Collaboration, B. Aubert *et al.*, "Measurement of branching fractions and CP and isospin asymmetries for $B \to K^*\gamma$," *Phys. Rev.* **D70** (2004) 112006, arXiv:hep-ex/0407003.

[18] **BABAR** Collaboration, B. Aubert *et al.*, "Measurement of branching fractions and CP and isospin asymmetries in $B \to K^*\gamma$," arXiv:0808.1915 [hep-ex].

[19] S. Hashimoto and H. Matsufuru, "Lattice heavy quark effective theory and the Isgur-Wise function," *Phys. Rev.* **D54** (1996) 4578–4584, arXiv:hep-lat/9511027.

[20] J. H. Sloan, "Moving NRQCD," *Nucl. Phys. Proc. Suppl.* **63** (1998) 365–367, arXiv:hep-lat/9710061.

[21] K. M. Foley and G. P. Lepage, "Moving NRQCD for B form factors at high recoil," *Nucl. Phys. Proc. Suppl.* **119** (2003) 635–637, arXiv:hep-lat/0209135.

[22] K. M. Foley, *The quest for flavor physics parameters: Highly improved lattice algorithms for heavy quarks.* PhD thesis, Cornell University, 2004. UMI-31-40868.

[23] K. M. Foley, G. P. Lepage, C. T. H. Davies, and A. Dougall, "Moving NRQCD: B mesons at high velocities," *Nucl. Phys. Proc. Suppl.* **140** (2005) 470–472.

[24] A. Dougall, K. M. Foley, C. T. H. Davies, and G. P. Lepage, "B meson decays at high velocity from mNRQCD," *PoS* **LAT2005** (2006) 219, arXiv:hep-lat/0509108.

[25] C. T. H. Davies, K. Y. Wong, and G. P. Lepage, "B meson decays from moving-NRQCD on fine MILC lattices," *PoS* **LAT2006** (2006) 099, arXiv:hep-lat/0611009.

[26] D. B. Kaplan, "A method for simulating chiral fermions on the lattice," *Phys. Lett.* **B288** (1992) 342–347, arXiv:hep-lat/9206013.

[27] Y. Shamir, "Chiral fermions from lattice boundaries," *Nucl. Phys.* **B406** (1993) 90–106, arXiv:hep-lat/9303005.

[28] V. Furman and Y. Shamir, "Axial symmetries in lattice QCD with Kaplan fermions," *Nucl. Phys.* **B439** (1995) 54–78, arXiv:hep-lat/9405004.

[29] M. Creutz, "Quarks, gluons and lattices," *Cambridge Monogr. Math. Phys.* (1984) .

[30] I. Montvay and G. Münster, "Quantum fields on a lattice," *Cambridge Monogr. Math. Phys.* (1994) .

[31] J. Smit, "Introduction to quantum fields on a lattice: A robust mate," *Cambridge Lect. Notes Phys.* **15** (2002) .

[32] H. J. Rothe, "Lattice gauge theories: An introduction," *World Sci. Lect. Notes Phys.* **74** (2005) .

[33] T. DeGrand and C. DeTar, "Lattice methods for quantum chromodynamics," *World Sci.* (2006) .

[34] C. Gattringer and C. Lang, "Quantum chromodynamics on the lattice - an introductory presentation," *Springer Lect. Notes Phys.* **788** (2009) .

[35] L. Maiani and M. Testa, "Final state interactions from Euclidean correlation functions," *Phys. Lett.* **B245** (1990) 585–590.

[36] M. Lüscher, "Volume dependence of the energy spectrum in massive quantum field theories. 2. Scattering states," *Commun. Math. Phys.* **105** (1986) 153–188.

[37] M. Lüscher, "Two-particle states on a torus and their relation to the scattering matrix," *Nucl. Phys.* **B354** (1991) 531–578.

[38] C. Bernard, M. Golterman, and Y. Shamir, "Observations on staggered fermions at non-zero lattice spacing," *Phys. Rev.* **D73** (2006) 114511, arXiv:hep-lat/0604017.

[39] Y. Shamir, "Renormalization-group analysis of the validity of staggered-fermion QCD with the fourth-root recipe," *Phys. Rev.* **D75** (2007) 054503, arXiv:hep-lat/0607007.

[40] C. Bernard, "Staggered chiral perturbation theory and the fourth-root trick," *Phys. Rev.* **D73** (2006) 114503, arXiv:hep-lat/0603011.

[41] C. Bernard, M. Golterman, and Y. Shamir, "Effective field theories for QCD with rooted staggered fermions," *Phys. Rev.* **D77** (2008) 074505, arXiv:0712.2560 [hep-lat].

[42] M. Creutz, "Chiral anomalies and rooted staggered fermions ," *Phys. Lett.* **B649** (2007) 230–234, arXiv:hep-lat/0701018.

[43] M. Creutz, "Reply to: "Comment on: 'Chiral anomalies and rooted staggered fermions' "," *Phys. Lett.* **B649** (2007) 241–242, arXiv:0704.2016 [hep-lat].

[44] M. Creutz, "Comment on "'t Hooft vertices, partial quenching, and rooted staggered QCD' "," *Phys. Rev.* **D78** (2008) 078501, arXiv:0805.1350 [hep-lat].

[45] C. Bernard, M. Golterman, Y. Shamir, and S. R. Sharpe, "Comment on 'Chiral anomalies and rooted staggered fermions'," *Phys. Lett.* **B649** (2007) 235–240, arXiv:hep-lat/0603027.

[46] C. Bernard, M. Golterman, Y. Shamir, and S. R. Sharpe, "'t Hooft vertices, partial quenching, and rooted staggered QCD," *Phys. Rev.* **D77** (2008) 114504, arXiv:0711.0696 [hep-lat].

[47] C. Bernard, M. Golterman, Y. Shamir, and S. R. Sharpe, "Reply to: 'Comment on: ' 't Hooft vertices, partial quenching, and rooted staggered QCD' '," *Phys. Rev.* **D78** (2008) 078502, arXiv:0808.2056 [hep-lat].

[48] D. H. Adams, "Rooting issue for a lattice fermion formulation similar to staggered fermions but without taste mixing," *Phys. Rev.* **D77** (2008) 105024, arXiv:0802.3029 [hep-lat].

[49] F. Wilczek, "Lattice fermions," *Phys. Rev. Lett.* **59** (1987) 2397.

[50] L. H. Karsten, "Lattice fermions in Euclidean space-time," *Phys. Lett.* **B104** (1981) 315.

[51] H. B. Nielsen and M. Ninomiya, "Absence of neutrinos on a lattice. 1. Proof by homotopy theory," *Nucl. Phys.* **B185** (1981) 20.

[52] H. B. Nielsen and M. Ninomiya, "Erratum: Absence of neutrinos on a lattice. 1. Proof by homotopy theory," *Nucl. Phys.* **B195** (1982) 541.

[53] H. B. Nielsen and M. Ninomiya, "Absence of neutrinos on a lattice. 2. Intuitive topological proof," *Nucl. Phys.* **B193** (1981) 173.

[54] K. Fujikawa, "Path-integral measure for gauge invariant fermion theories," *Phys. Rev. Lett.* **42** (1979) 1195.

[55] L. H. Karsten and J. Smit, "Lattice fermions: species doubling, chiral invariance, and the triangle anomaly," *Nucl. Phys.* **B183** (1981) 103.

[56] H. S. Sharatchandra, H. J. Thun, and P. Weisz, "Susskind fermions on a Euclidean lattice," *Nucl. Phys.* **B192** (1981) 205.

[57] T. D. Kieu, "Axial anomaly and staggered fermions in the coordinate space interpretation," *Phys. Rev.* **D38** (1988) 636.

[58] M. Lüscher, "Exact chiral symmetry on the lattice and the Ginsparg-Wilson relation," *Phys. Lett.* **B428** (1998) 342–345, arXiv:hep-lat/9802011.

[59] P. H. Ginsparg and K. G. Wilson, "A remnant of chiral symmetry on the lattice," *Phys. Rev.* **D25** (1982) 2649.

[60] H. Neuberger, "Exactly massless quarks on the lattice," *Phys. Lett.* **B417** (1998) 141–144, arXiv:hep-lat/9707022.

[61] H. Neuberger, "More about exactly massless quarks on the lattice," *Phys. Lett.* **B427** (1998) 353–355, arXiv:hep-lat/9801031.

[62] H. Neuberger, "A practical implementation of the overlap Dirac operator," *Phys. Rev. Lett.* **81** (1998) 4060–4062, arXiv:hep-lat/9806025.

[63] D. B. Kaplan, "Chiral symmetry and lattice fermions," *Modern perspectives in lattice QCD: Quantum feld theory and high performance computing (Les Houches, 2009)* , arXiv:0912.2560 [hep-lat].

[64] P. M. Vranas, "Chiral symmetry restoration in the Schwinger model with domain wall fermions," *Phys. Rev.* **D57** (1998) 1415–1432, arXiv:hep-lat/9705023.

[65] H. Neuberger, "Vectorlike gauge theories with almost massless fermions on the lattice," *Phys. Rev.* **D57** (1998) 5417–5433, arXiv:hep-lat/9710089.

[66] S. R. Sharpe, "Future of chiral extrapolations with domain wall fermions," arXiv:0706.0218 [hep-lat].

[67] A. S. Kronfeld, "Uses of effective field theory in lattice QCD," *World Sci., Handbook of QCD, Vol. 4, Ch. 39* (2002) 2411, arXiv:hep-lat/0205021.

[68] G. Martinelli, C. Pittori, C. T. Sachrajda, M. Testa, and A. Vladikas, "A general method for nonperturbative renormalization of lattice operators," *Nucl. Phys.* **B445** (1995) 81–108, arXiv:hep-lat/9411010.

[69] M. Lüscher, P. Weisz, and U. Wolff, "A numerical method to compute the running coupling in asymptotically free theories," *Nucl. Phys.* **B359** (1991) 221–243.

[70] M. Lüscher, R. Sommer, P. Weisz, and U. Wolff, "A precise determination of the running coupling in the $SU(3)$ Yang-Mills theory," *Nucl. Phys.* **B413** (1994) 481–502, arXiv:hep-lat/9309005.

[71] **ALPHA** Collaboration, M. Della Morte *et al.*, "Non-perturbative quark mass renormalization in two-flavor QCD," *Nucl. Phys.* **B729** (2005) 117–134, arXiv:hep-lat/0507035.

[72] **ALPHA** Collaboration, J. Heitger and R. Sommer, "Non-perturbative heavy quark effective theory," *JHEP* **02** (2004) 022, arXiv:hep-lat/0310035.

[73] S. Schäfer, R. Sommer, and F. Virotta, "Investigating the critical slowing down of QCD simulations," arXiv:0910.1465 [hep-lat].

[74] L. Del Debbio, H. Panagopoulos, and E. Vicari, "θ dependence of $SU(N)$ gauge theories," *JHEP* **08** (2002) 044, arXiv:hep-th/0204125.

[75] L. Del Debbio, G. M. Manca, and E. Vicari, "Critical slowing down of topological modes," *Phys. Lett.* **B594** (2004) 315–323, arXiv:hep-lat/0403001.

[76] G. P. Lepage, "Lattice QCD for small computers," arXiv:hep-lat/9403018.

[77] G. P. Lepage and P. B. Mackenzie, "On the viability of lattice perturbation theory," *Phys. Rev.* **D48** (1993) 2250–2264, arXiv:hep-lat/9209022.

[78] S. R. Sharpe, "Applications of chiral perturbation theory to lattice QCD," arXiv:hep-lat/0607016.

[79] M. Golterman, "Applications of chiral perturbation theory to lattice QCD," *Modern perspectives in lattice QCD: Quantum feld theory and high performance computing (Les Houches, 2009)* , arXiv:0912.4042 [hep-lat].

[80] J. Gasser and H. Leutwyler, "Chiral perturbation theory: Expansions in the mass of the strange quark," *Nucl. Phys.* **B250** (1985) 465.

[81] J. Gasser and H. Leutwyler, "Light quarks at low temperatures," *Phys. Lett.* **B184** (1987) 83.

[82] J. Gasser and H. Leutwyler, "Spontaneously broken symmetries: Effective Lagrangians at finite volume," *Nucl. Phys.* **B307** (1988) 763.

[83] **Particle Data Group** Collaboration, C. Amsler *et al.*, "Review of particle physics," *Phys. Lett.* **B667** (2008) 1.

[84] **HPQCD** Collaboration, E. Follana *et al.*, "Highly improved staggered quarks on the lattice, with applications to charm physics," *Phys. Rev.* **D75** (2007) 054502, arXiv:hep-lat/0610092.

[85] **HPQCD** Collaboration, E. Follana, C. T. H. Davies, G. P. Lepage, and J. Shigemitsu, "High-precision determination of the π, K, D and D_s decay constants from lattice QCD," *Phys. Rev. Lett.* **100** (2008) 062002, arXiv:0706.1726 [hep-lat].

[86] C. McNeile *et al.*, "Towards precise relativistic b quarks on the lattice," arXiv:0910.2921 [hep-lat].

[87] A. Bazavov *et al.*, "Full nonperturbative QCD simulations with 2+1 flavors of improved staggered quarks," arXiv:0903.3598 [hep-lat].

[88] M. G. Alford, T. R. Klassen, and G. P. Lepage, "Improving lattice quark actions," *Nucl. Phys.* **B496** (1997) 377–407, arXiv:hep-lat/9611010.

[89] T. R. Klassen, "Non-perturbative improvement of the anisotropic Wilson QCD action," *Nucl. Phys. Proc. Suppl.* **73** (1999) 918–920, arXiv:hep-lat/9809174.

[90] J. Harada, A. S. Kronfeld, H. Matsufuru, N. Nakajima, and T. Onogi, "$\mathcal{O}(a)$-improved quark action on anisotropic lattices and perturbative renormalization of heavy-light currents," *Phys. Rev.* **D64** (2001) 074501, arXiv:hep-lat/0103026.

[91] S. Hashimoto and M. Okamoto, "Perturbative study of anisotropic lattice actions for heavy quarks," *Phys. Rev.* **D67** (2003) 114503, arXiv:hep-lat/0302012.

[92] A. X. El-Khadra, A. S. Kronfeld, and P. B. Mackenzie, "Massive fermions in lattice gauge theory," *Phys. Rev.* **D55** (1997) 3933–3957, arXiv:hep-lat/9604004.

[93] A. S. Kronfeld, "Application of heavy-quark effective theory to lattice QCD. I: Power corrections," *Phys. Rev.* **D62** (2000) 014505, arXiv:hep-lat/0002008.

[94] J. Harada *et al.*, "Application of heavy-quark effective theory to lattice QCD. II: Radiative corrections to heavy-light currents," *Phys. Rev.* **D65** (2002) 094513, arXiv:hep-lat/0112044.

[95] J. Harada, S. Hashimoto, A. S. Kronfeld, and T. Onogi, "Application of heavy-quark effective theory to lattice QCD. III: Radiative corrections to heavy-heavy currents," *Phys. Rev.* **D65** (2002) 094514, arXiv:hep-lat/0112045.

[96] W. E. Caswell and G. P. Lepage, "Effective Lagrangians for bound state problems in QED, QCD, and other field theories," *Phys. Lett.* **B167** (1986) 437.

[97] A. V. Manohar and M. B. Wise, "Heavy quark physics," *Camb. Monogr. Part. Phys. Nucl. Phys. Cosmol.* **10** (2000) .

[98] J. G. Körner and G. Thompson, "The heavy mass limit in field theory and the heavy quark effective theory," *Phys. Lett.* **B264** (1991) 185–192.

[99] M. A. Shifman and M. B. Voloshin, "On production of D and D^* mesons in B meson decays," *Sov. J. Nucl. Phys.* **47** (1988) 511.

[100] R. R. Horgan *et al.*, "Moving nonrelativistic QCD for heavy-to-light form factors on the lattice," *Phys. Rev.* **D80** (2009) 074505, arXiv:0906.0945 [hep-lat].

[101] E. Eichten and B. R. Hill, "Renormalization of heavy-light bilinears and f_B for Wilson fermions," *Phys. Lett.* **B240** (1990) 193.

[102] S. Weinberg, "The quantum theory of fields. Vol. 1: Foundations," *Cambridge Univ. Pr.* (1995) .

[103] J. C. Collins, "Renormalization," *Camb. Monogr. Math. Phys.* (1984) .

[104] L. Maiani, G. Martinelli, and C. T. Sachrajda, "Nonperturbative subtractions in the heavy quark effective field theory," *Nucl. Phys.* **B368** (1992) 281–292.

[105] G. P. Lepage, "Simulating heavy quarks," *Nucl. Phys. Proc. Suppl.* **26** (1992) 45–56.

[106] S. Hashimoto, "Computation of the heavy-light decay constant using nonrelativistic lattice QCD," *Phys. Rev.* **D50** (1994) 4639–4648, `arXiv:hep-lat/9403028`.

[107] **ALPHA** Collaboration, M. Della Morte *et al.*, "Lattice HQET with exponentially improved statistical precision," *Phys. Lett.* **B581** (2004) 93–98, `arXiv:hep-lat/0307021`.

[108] A. Gray *et al.*, "The Υ spectrum and m_b from full lattice QCD," *Phys. Rev.* **D72** (2005) 094507, `arXiv:hep-lat/0507013`.

[109] **HPQCD** Collaboration, A. Gray *et al.*, "The B meson decay constant from unquenched lattice QCD," *Phys. Rev. Lett.* **95** (2005) 212001, `arXiv:hep-lat/0507015`.

[110] **HPQCD** Collaboration, E. Gamiz, C. T. H. Davies, G. P. Lepage, J. Shigemitsu, and M. Wingate, "Neutral B meson mixing in unquenched lattice QCD," *Phys. Rev.* **D80** (2009) 014503, `arXiv:0902.1815 [hep-lat]`.

[111] M. Wingate, J. Shigemitsu, C. T. H. Davies, G. P. Lepage, and H. D. Trottier, "Heavy-light mesons with staggered light quarks," *Phys. Rev.* **D67** (2003) 054505, `arXiv:hep-lat/0211014`.

[112] A. Dougall, C. T. H. Davies, K. M. Foley, and G. P. Lepage, "The heavy quark's self energy from moving NRQCD on the lattice," *Nucl. Phys. Proc. Suppl.* **140** (2005) 431–433, `arXiv:hep-lat/0409088`.

[113] L. Khomskii, *Perturbation theory for quarks and currents in moving NRQCD on a lattice*. PhD thesis, University of Cambridge, 2008.

[114] E. Müller, *Heavy-to-light decays on the lattice*. PhD thesis, University of Edinburgh, 2009.

[115] C. J. Morningstar, "Radiative corrections to the kinetic couplings in nonrelativistic lattice QCD," *Phys. Rev.* **D50** (1994) 5902–5911, arXiv:hep-lat/9406002.

[116] E. H. Müller *et al.*, "Radiative corrections to the m(oving)NRQCD action and heavy-light operators," arXiv:0909.5126 [hep-lat].

[117] A. Hart, G. M. von Hippel, R. R. Horgan, and E. H. Müller, "Automated generation of lattice QCD Feynman rules," *Comput. Phys. Commun.* **180** (2009) 2698–2716, arXiv:0904.0375 [hep-lat].

[118] W. Dimm, G. P. Lepage, and P. B. Mackenzie, "Nonperturbative 'lattice perturbation theory'," *Nucl. Phys. Proc. Suppl.* **42** (1995) 403–405, arXiv:hep-lat/9412100.

[119] H. D. Trottier, N. H. Shakespeare, G. P. Lepage, and P. B. Mackenzie, "Perturbative expansions from Monte Carlo simulations at weak coupling: Wilson loops and the static-quark self-energy," *Phys. Rev.* **D65** (2002) 094502, arXiv:hep-lat/0111028.

[120] C. W. Bernard *et al.*, "The QCD spectrum with three quark flavors," *Phys. Rev.* **D64** (2001) 054506, arXiv:hep-lat/0104002.

[121] **MILC** Collaboration, C. Aubin *et al.*, "Light pseudoscalar decay constants, quark masses, and low energy constants from three-flavor lattice QCD," *Phys. Rev.* **D70** (2004) 114501, arXiv:hep-lat/0407028.

[122] G. P. Lepage *et al.*, "Constrained curve fitting," *Nucl. Phys. Proc. Suppl.* **106** (2002) 12–20, arXiv:hep-lat/0110175.

[123] **MILC** Collaboration, K. Orginos and D. Toussaint, "Testing improved actions for dynamical Kogut-Susskind quarks," *Phys. Rev.* **D59** (1999) 014501, arXiv:hep-lat/9805009.

[124] G. P. Lepage, "Flavor-symmetry restoration and Symanzik improvement for staggered quarks," *Phys. Rev.* **D59** (1999) 074502, arXiv:hep-lat/9809157.

[125] **MILC** Collaboration, K. Orginos, D. Toussaint, and R. L. Sugar, "Variants of fattening and flavor symmetry restoration," *Phys. Rev.* **D60** (1999) 054503, arXiv:hep-lat/9903032.

[126] S. J. Brodsky, G. P. Lepage, and P. B. Mackenzie, "On the elimination of scale ambiguities in perturbative quantum chromodynamics," *Phys. Rev.* **D28** (1983) 228.

[127] **HPQCD** Collaboration, Q. Mason *et al.*, "Accurate determinations of α_s from realistic lattice QCD," *Phys. Rev. Lett.* **95** (2005) 052002, arXiv:hep-lat/0503005.

[128] **RBC and UKQCD** Collaboration, C. Allton *et al.*, "Physical results from 2+1 flavor domain wall QCD and $SU(2)$ chiral perturbation theory," *Phys. Rev.* **D78** (2008) 114509, arXiv:0804.0473 [hep-lat].

[129] Y. Iwasaki, "Renormalization group analysis of lattice theories and improved lattice action. 2. Four-dimensional nonabelian $SU(N)$ gauge model,". UTHEP-118.

[130] Y. Iwasaki and T. Yoshie, "Renormalization group improved action for $SU(3)$ lattice gauge theory and the string tension," *Phys. Lett.* **B143** (1984) 449.

[131] S. Meinel, "Bottomonium spectrum from lattice QCD with 2+1 flavors of domain wall fermions," *Phys. Rev.* **D79** (2009) 094501, arXiv:0903.3224 [hep-lat].

[132] S. Meinel, W. Detmold, C. J. D. Lin, and M. Wingate, "Bottom hadrons from lattice QCD with domain wall and NRQCD fermions," *PoS* **LAT2009** (2009) 105, arXiv:0909.3837 [hep-lat].

[133] **D0** Collaboration, V. M. Abazov *et al.*, "Observation of the doubly strange b baryon Ω_b^-," *Phys. Rev. Lett.* **101** (2008) 232002, arXiv:0808.4142 [hep-ex].

[134] **CDF** Collaboration, T. Aaltonen *et al.*, "Observation of the Ω_b^- and measurement of the properties of the Ξ_b^- and Ω_b^-," *Phys. Rev.* **D80** (2009) 072003, arXiv:0905.3123 [hep-ex].

[135] **RBC and UKQCD** Collaboration, D. J. Antonio *et al.*, "First results from 2+1-flavor domain wall QCD: Mass spectrum, topology change and chiral symmetry with $L_s = 8$," *Phys. Rev.* **D75** (2007) 114501, arXiv:hep-lat/0612005.

[136] **SciDAC** Collaboration, R. G. Edwards and B. Joo, "The Chroma software system for lattice QCD," *Nucl. Phys. Proc. Suppl.* **140** (2005) 832, arXiv:hep-lat/0409003.

[137] R. C. Johnson, "Angular momentum on a lattice," *Phys. Lett.* **B114** (1982) 147.

[138] **BABAR** Collaboration, B. Aubert *et al.*, "Observation of the bottomonium ground state in the decay $\Upsilon(3S) \to \gamma\, \eta_b$," *Phys. Rev. Lett.* **101** (2008) 071801, arXiv:0807.1086 [hep-ex].

[139] **CLEO** Collaboration, G. Bonvicini *et al.*, "First observation of a $\Upsilon(1D)$ state," *Phys. Rev.* **D70** (2004) 032001, arXiv:hep-ex/0404021.

[140] C. T. H. Davies *et al.*, "Scaling of the Υ spectrum in lattice NRQCD," *Phys. Rev.* **D58** (1998) 054505, arXiv:hep-lat/9802024.

[141] S. Necco, "Universality and scaling behavior of RG gauge actions," *Nucl. Phys.* **B683** (2004) 137–167, arXiv:hep-lat/0309017.

[142] W. Buchmüller (ed.), "Quarkonia," *Amsterdam: North-Holland (Current physics-sources and comments, Vol. 9)* (1992) .

[143] **RBC and UKQCD** Collaboration, M. Li, "Bottom spectroscopy on dynamical 2+1 flavor domain wall fermion lattices with a relativistic heavy quark action," *PoS* **LAT2008** (2008) 120, arXiv:0810.0040 [hep-lat].

[144] **UA1** Collaboration, C. Albajar *et al.*, "First observation of the beauty baryon Λ_b in the decay channel $\Lambda_b \to J/\psi\, \Lambda$ at the CERN proton - anti-proton collider," *Phys. Lett.* **B273** (1991) 540–548.

[145] **CDF** Collaboration, T. Aaltonen *et al.*, "Observation of the heavy baryons Σ_b and Σ_b^*," *Phys. Rev. Lett.* **99** (2007) 202001, arXiv:0706.3868 [hep-ex].

[146] **D0** Collaboration, V. M. Abazov *et al.*, "Direct observation of the strange b baryon Ξ_b^-," *Phys. Rev. Lett.* **99** (2007) 052001, arXiv:0706.1690 [hep-ex].

[147] **CDF** Collaboration, T. Aaltonen *et al.*, "Observation and mass measurement of the baryon Ξ_b^-," *Phys. Rev. Lett.* **99** (2007) 052002, arXiv:0707.0589 [hep-ex].

[148] R. Lewis and R. M. Woloshyn, "Bottom baryons from a dynamical lattice QCD simulation," *Phys. Rev.* **D79** (2009) 014502, arXiv:0806.4783 [hep-lat].

[149] T. Burch, C. Hagen, C. B. Lang, M. Limmer, and A. Schafer, "Excitations of single-beauty hadrons," *Phys. Rev.* **D79** (2009) 014504, arXiv:0809.1103 [hep-lat].

[150] H. Na and S. Gottlieb, "Heavy baryon mass spectrum from lattice QCD with 2+1 dynamical sea quark flavors," *PoS* **LAT2008** (2008) 119, arXiv:0812.1235 [hep-lat].

[151] W. Detmold, C. J. D. Lin, and M. Wingate, "Bottom hadron mass splittings in the static limit from 2+1 flavour lattice QCD," *Nucl. Phys.* **B818** (2009) 17–27, arXiv:0812.2583 [hep-lat].

[152] H.-W. Lin, S. D. Cohen, N. Mathur, and K. Orginos, "Bottom-hadron mass splittings from static-quark action on 2+1-flavor lattices," *Phys. Rev.* **D80** (2009) 054027, arXiv:0905.4120 [hep-lat].

[153] M. Teper, "An improved method for lattice glueball calculations," *Phys. Lett.* **B183** (1987) 345.

[154] **APE** Collaboration, M. Albanese *et al.*, "Glueball masses and string tension in lattice QCD," *Phys. Lett.* **B192** (1987) 163–169.

[155] **UKQCD** Collaboration, K. C. Bowler *et al.*, "Heavy baryon specroscopy from the lattice," *Phys. Rev.* **D54** (1996) 3619–3633, arXiv:hep-lat/9601022.

[156] P. Hasenfratz, R. R. Horgan, J. Kuti, and J. M. Richard, "Heavy baryon spectroscopy in the QCD bag model," *Phys. Lett.* **B94** (1980) 401.

[157] Y. Jia, "Variational study of weakly coupled triply heavy baryons," *JHEP* **10** (2006) 073, arXiv:hep-ph/0607290.

[158] A. Bernotas and V. Simonis, "Heavy hadron spectroscopy and the bag model," arXiv:0808.1220 [hep-ph].

[159] A. P. Martynenko, "Ground-state triply and doubly heavy baryons in a relativistic three-quark model," *Phys. Lett.* **B663** (2008) 317–321, arXiv:0708.2033 [hep-ph].

[160] J.-R. Zhang and M.-Q. Huang, "Deciphering triply heavy baryons in terms of QCD sum rules," *Phys. Lett.* **B674** (2009) 28–35, arXiv:0902.3297 [hep-ph].

[161] M. A. Gomshi Nobary and R. Sepahvand, "Fragmentation of triply heavy baryons at the CERN LHC," *Phys. Rev.* **D71** (2005) 034024, arXiv:hep-ph/0406148.

[162] M. A. Gomshi Nobary and R. Sepahvand, "An investigation of triply heavy baryon production at hadron colliders," *Nucl. Phys.* **B741** (2006) 34–41, arXiv:hep-ph/0508115.

[163] B. C. Allanach, "The Standard Model: D. Electro-weak gauge theory," *Lecture notes, Part III of the Mathematical Tripos, University of Cambridge* . http://users.hepforge.org/~allanach/teaching.html.

[164] T. P. Cheng and L. F. Li, "Gauge theory of elementary particle physics," *Oxford Univ. Pr.* (1984) .

[165] G. Buchalla, A. J. Buras, and M. E. Lautenbacher, "Weak decays beyond leading logarithms," *Rev. Mod. Phys.* **68** (1996) 1125–1144, arXiv:hep-ph/9512380.

[166] A. J. Buras, "Weak Hamiltonian, CP violation and rare decays," arXiv:hep-ph/9806471.

[167] F. J. Gilman and R. L. Singleton, "Analysis of semileptonic decays of mesons containing heavy quarks," *Phys. Rev.* **D41** (1990) 142.

[168] J. A. Bailey *et al.*, "The $B \to \pi \ell \nu$ semileptonic form factor from three-flavor lattice QCD: a model-independent determination of $|V_{ub}|$," *Phys. Rev.* **D79** (2009) 054507, arXiv:0811.3640 [hep-lat].

[169] S. Bertolini, F. Borzumati, A. Masiero, and G. Ridolfi, "Effects of supergravity-induced electroweak breaking on rare B decays and mixings," *Nucl. Phys.* **B353** (1991) 591–649.

[170] M. Gronau and D. London, "New physics in CP asymmetries and rare B decays," *Phys. Rev.* **D55** (1997) 2845–2861, arXiv:hep-ph/9608430.

[171] J. L. Hewett and J. D. Wells, "Searching for supersymmetry in rare B decays," *Phys. Rev.* **D55** (1997) 5549–5560, arXiv:hep-ph/9610323.

[172] G. Degrassi, P. Gambino, and G. F. Giudice, "$B \to X_s \gamma$ in supersymmetry: large contributions beyond the leading order," *JHEP* **12** (2000) 009, arXiv:hep-ph/0009337.

[173] M. S. Carena, D. Garcia, U. Nierste, and C. E. M. Wagner, "$b \to s\gamma$ and supersymmetry with large $\tan(\beta)$," *Phys. Lett.* **B499** (2001) 141–146, arXiv:hep-ph/0010003.

[174] K. Agashe, N. G. Deshpande, and G. H. Wu, "Universal extra dimensions and $b \to s\gamma$," *Phys. Lett.* **B514** (2001) 309–314, arXiv:hep-ph/0105084.

[175] T. Besmer, C. Greub, and T. Hurth, "Bounds on supersymmetric flavour violating parameters from $B \to X_s\gamma$," *Nucl. Phys.* **B609** (2001) 359–386, arXiv:hep-ph/0105292.

[176] A. J. Buras, A. Poschenrieder, M. Spranger, and A. Weiler, "The impact of universal extra dimensions on $B \to X_s\gamma$, $B \to X_s$ gluon, $B \to X_s\mu^+\mu^-$, $K_L \to \pi^0 e^+ e^-$, and ϵ'/ϵ," *Nucl. Phys.* **B678** (2004) 455–490, arXiv:hep-ph/0306158.

[177] B. Grinstein, R. P. Springer, and M. B. Wise, "Strong-interaction effects in weak radiative $\bar{B}$ meson decay," *Nucl. Phys.* **B339** (1990) 269–309.

[178] **UKQCD** Collaboration, K. C. Bowler *et al.*, "$B \to K^*\gamma$: penguins on the lattice," *Phys. Rev. Lett.* **72** (1994) 1398–1401, arXiv:hep-lat/9311004.

[179] **UKQCD** Collaboration, K. C. Bowler *et al.*, "Probing with penguins: A lattice calculation of the branching ratio for some of the exclusive modes of $b \to s\gamma$," *Phys. Rev.* **D51** (1995) 4955–4970, arXiv:hep-lat/9407013.

[180] **UKQCD** Collaboration, D. R. Burford *et al.*, "Form factors for $B \to \pi\ell\bar{\nu}_\ell$ and $B \to K^*\gamma$ decays on the lattice," *Nucl. Phys.* **B447** (1995) 425–440, arXiv:hep-lat/9503002.

[181] **UKQCD** Collaboration, L. Del Debbio, J. M. Flynn, L. Lellouch, and J. Nieves, "Lattice-constrained parametrizations of form factors for semileptonic and rare radiative B decays," *Phys. Lett.* **B416** (1998) 392–401, arXiv:hep-lat/9708008.

[182] C. W. Bernard, P. Hsieh, and A. Soni, "$B \to K^*\gamma$ and $B_s \to \phi\gamma$ on the lattice," *Phys. Rev. Lett.* **72** (1994) 1402–1405, arXiv:hep-lat/9311010.

[183] **APE** Collaboration, A. Abada *et al.*, "A lattice study of the exclusive $B \to K^*\gamma$ decay amplitude, using the clover action at $\beta = 6.0$," *Phys. Lett.* **B365** (1996) 275–284, arXiv:hep-lat/9503020.

[184] D. Becirevic, V. Lubicz, and F. Mescia, "An estimate of the $B \to K^*\gamma$ form factor," *Nucl. Phys.* **B769** (2007) 31–43, arXiv:hep-ph/0611295.

[185] K. G. Chetyrkin, M. Misiak, and M. Munz, "Weak radiative B-meson decay beyond leading logarithms," *Phys. Lett.* **B400** (1997) 206–219, arXiv:hep-ph/9612313.

[186] A. Khodjamirian, R. Ruckl, G. Stoll, and D. Wyler, "QCD estimate of the long-distance effect in $B \to K^*\gamma$," *Phys. Lett.* **B402** (1997) 167–177, arXiv:hep-ph/9702318.

[187] B. Grinstein and D. Pirjol, "Exclusive rare $B \to K^*\ell^+\ell^-$ decays at low recoil: controlling the long-distance effects," *Phys. Rev.* **D70** (2004) 114005, arXiv:hep-ph/0404250.

[188] C. E. Carlson and J. Milana, "Penguins leaving the pole: bound state effects in $B \to K^*\gamma$," *Phys. Rev.* **D51** (1995) 4950–4954, arXiv:hep-ph/9405344.

[189] M. Beneke, T. Feldmann, and D. Seidel, "Systematic approach to exclusive $B \to V\ell^+\ell^-$, $V\gamma$ decays," *Nucl. Phys.* **B612** (2001) 25–58, arXiv:hep-ph/0106067.

[190] M. Beneke and T. Feldmann, "Symmetry-breaking corrections to heavy-to-light B meson form factors at large recoil," *Nucl. Phys.* **B592** (2001) 3–34, arXiv:hep-ph/0008255.

[191] S. Collins *et al.*, "Scaling and further tests of heavy meson decay constant determinations from NRQCD," *Phys. Rev.* **D63** (2001) 034505, arXiv:hep-lat/0007016.

[192] E. Dalgic, J. Shigemitsu, and M. Wingate, "One-loop matching of the heavy-light A_0 and V_0 currents with NRQCD heavy and improved naive light quarks," *Phys. Rev.* **D69** (2004) 074501, arXiv:hep-lat/0312017.

[193] C. T. H. Davies, E. Follana, K. Y. Wong, G. P. Lepage, and J. Shigemitsu, "B semileptonic decays at high recoil momentum," *PoS* **LAT2007** (2007) 378, arXiv:0710.0741 [hep-lat].

[194] S.-J. Dong and K.-F. Liu, "Stochastic estimation with Z_2 noise," *Phys. Lett.* **B328** (1994) 130–136, arXiv:hep-lat/9308015.

[195] **UKQCD** Collaboration, M. Foster and C. Michael, "Quark mass dependence of hadron masses from lattice QCD," *Phys. Rev.* **D59** (1999) 074503, arXiv:hep-lat/9810021.

[196] J. Foley *et al.*, "Practical all-to-all propagators for lattice QCD," *Comput. Phys. Commun.* **172** (2005) 145–162, arXiv:hep-lat/0505023.

[197] P. Ball and R. Zwicky, "New results on $B \to \pi, K, \eta$ decay formfactors from light-cone sum rules," *Phys. Rev.* **D71** (2005) 014015, arXiv:hep-ph/0406232.

[198] **Fermilab Lattice QCD** Collaboration, R. D. Jain, "The form factors for the rare decay $B \to K\ell^+\ell^-$ from three-flavor lattice QCD," *PoS* **LAT2006** (2006) 085.

[199] D. Becirevic and A. B. Kaidalov, "Comment on the heavy $\to$ light form factors," *Phys. Lett.* **B478** (2000) 417–423, arXiv:hep-ph/9904490.

[200] K. Levenberg, "A method for the solution of certain non-linear problems in least-squares," *Quarterly of Applied Mathematics* **2** (1944) 164–168.

[201] D. W. Marquardt, "An algorithm for the least-squares estimation of nonlinear parameters," *SIAM Journal of Applied Mathematics* **11** (1963) 431–441.

[202] W. H. Press *et al.*, "Numerical Recipes in C," *Cambridge Univ. Pr.* (1992) .

[203] C. Morningstar, "Bayesian curve fitting for lattice gauge theorists," *Nucl. Phys. Proc. Suppl.* **109A** (2002) 185–191, arXiv:hep-lat/0112023.